Development of a Solid State Planar Carbon Dioxide Sensor

Steven MUDENDA

Institute for Materials Research

School of Chemical and Process Engineering

University of Leeds

Submitted in accordance with the requirements for the degree of

Doctor of Philosophy

July 2015

Declaration

The candidate confirms that the work submitted is his own, except where work which has formed part of jointly authored publications has been included. The contribution of the candidate and the other authors to this work has been explicitly indicated below. The candidate confirms that appropriate credit has been given within the thesis where reference has been made to the work of others.

All the results that are presented in the papers were obtained and analysed by the author of the thesis except for the following contributions; (a) Dr. Girish M. Kale - offered technical advice and editing of manuscripts both in language and technical content. (b) Dr.Yotamu R.S Hara - offered help to use his furnace, operated the furnace and offered technical advice on non ambient calcinations.

1. S. Mudenda, Girish M. Kale and Yotamu R.S. Hara. *Rapid synthesis and electrical transition in p-type delafossite $CuAlO_2$, Journal of Materials Chemistry C, 2014, 2,9233.*

2. S. Mudenda and Girish M. Kale. *New insight into the electrical properties and ion dynamics of screen printed NASICON thick films, Journal of Materials Chemistry A, 2015,3, 12268.*

rial and that no quotation from the thesis may be published without proper acknowledgment.

Acknowledgments

My profound gratitude goes to my supervisor Dr. Girish M. Kale for bringing me into this interesting area of research. His continuous encouragement and sagacious guidance during my study is greatly appreciated and treasured. His advice both in science and language and his pickiness refined my write-upand can never be over-emphasised, thank you!

I also extend my thanks to Dr. Tim Comyn for all the XRD help, Mr. John Harrington and Stuart Micklethwaite from LEMAS for help and advice in SEM/EDS measurements, Dr. Yotamu R.S Hara for the help in the non-ambient calcination experiments using his furnace, Mrs. Diane Cochrane for all the technical and health/safety advice in my labs. I know I made too much trouble for you Di.

Thanks go to the Commonwealth Scholarship Council and the Institute for Materials Research of the University of Leeds for their financial support during my study. Thanks also go the University of Zambia for the paid study leave. It enabled me visit my family frequently.

I am also very grateful to the following colleagues: Aurang Zeb, Saeed, Terry Makanyire, Muhammed Adamu, Steven Parirenyatwa, Phillip Masimba, Kennedy Phiri and James Manchisi for the valuable scientific discussions with me related to my work. My friends, I refer to as my Zambian family in Leeds, Leonard Nonde, Evans Silavwe, Hilda Nyambe Silavwe and Evaristo Musonda for their

friendship. A special mention also goes to Mr David Tembo from Malawi, thank you for the friendship and the valuable academic discussions. A shout out to Etambuyu Wamunyima Phiri and her family whose doors were always open for me at their home in Chesterfield for weekend breathers and some plenty of home cooked meals. A special thanks also go to my elder sister Cathy Bili and my nephew Wezzy Bili Mulenga, those trips to the Emirates stadium on match days where refreshing away from my hectic work. Thank you all!

Dedication

This is to my two sons, Maluba and Maleele, my wife Kasamba for being patient with me during my PhD work. You had to put up with my absence, just for this to be done. Thank you. To my late mum, and my family members thank you for nurturing a scientist/engineer in me, this is yours.

◆◆◆◆◆◆◆◆◆

Abstract

Aspects relating to and including the development of thick film screen printed CO_2 sensors were investigated. Modified sensor structures with potential for preventing sensor degradation due to humidity and solid electrolyte/alumina substrate interaction have been developed and hence tested. Sensor testing characteristics such as the response and recovery times, repeatability and importantly sensor stability and humidity cross-sensitivity were thus determined and investigated.

Firstly, in the quest to lower the cost of sensor production, new and superior synthesis procedures for sensor components (NASICON-solid electrolyte and $CuAlO_2$-oxygen buffer) have been developed which require low thermal input. Bespoke inks from the functional powders were also developed. Sintering schedule optimisation of the NASICON thick films demonstrated that 1100 °C for 60 minutes was the optimal recipe to obtaining a perfectly sintered NASICON film.

To investigate the electrical properties of NASICON having commonly used electrode configurations in sensors, the effect of film thickness and film electrode configurations on electrical properties was explored. No significant dependence on thickness at high temperatures is observed while lower temperature conductivity is dominated by extrinsic behaviour. The film whose electrode configuration was in a basal plane showed superior conductivity properties than when the electrodes were place across the film.

Thermodynamics of reference electrodes using the EMF method using cells (-)Pt, NT6-TiO_2(or NT6 - NT3) | NASICON | ($\alpha + \beta$) - Al_2O_3, Pt(+) revealed new information that may have been ignored by other workers; the existence of two temperature regimes and phase transformation of $Na_2Ti_6O_{13}$ to higher(lower sodium content) titanates ($Na_2Ti_7O_{15}$ and $Na_2Ti_9O_{19}$). This data presents the first indications from EMF thermodynamic studies for the possible transformation as was proposed by other workers.

Three types of sensor structures were developed; (a)the conventional planar sensor architecture(PSA)- fabricated by printing sensing and reference electrodes side by side on the electrolyte (b) the modified planar sensor architecture(M-PSA)- a PSA with an oxygen buffer material deposited on top of the reference electrode and (c) a multi-layered structure referred to as stacked sensor architecture (SSA)- fabricated by first depositing the oxygen buffer on the alumina substrate followed by the reference electrode then NASICON and finally the sensing electrode.

A new sensing material combination (Na_2CO_3-Li_2CO_3-$BaCO_3$) used on the PSA improved sensing response and recovery times of the sensors as well as sensor stability. The new sensing electrodes were used in the multi-layered structure (SSA) and performed just as well in terms of response and recovery times as well as stability.

Both the modified sensors(M-PSA and SSA) demonstrated long term signal stability as well as humidity immunity. The sensors also demonstrated that they could operate even at as low a temperature as 225 °C and sensor performance improved as the operating temperature was increased demonstrating how wide a temperature they can operate at. The measurements in this study were done up to 430 °C. Furthermore, since the CO_2 concentrations measured were < 500 ppm, it demonstrates how robust the sensors are as they were responsive to such low

concentration changes.

List of Abbreviations

1DS **1** **D**ouble **S**troke

2DS **2** **D**ouble **S**trokes

3DS **3** **D**ouble **S**trokes

AP **A**cross the **P**lane

CAO **C**opper **A**luminium **O**xide

DSC **D**ifferential **S**canning **C**alorimetry

EDS **E**nergy **D**ispersive **S**pectroscopy

FEGSEM **F**ield **E**mission **G**un **S**canning **E**lectron **M**icroscopy

IP **I**n **P**lane

IPB **I**n **P**lane **B**ottom

HT **H**igh **T**emperature

HTXRD **H**igh **T**emperature **XRD**

LT **L**ow **T**emperature

M-PSA **M**odified **P**lanar **S**ensor **A**rchitecture

NaBa Sodium(**Na**) carbonate + Barium(**Ba**) carbonate

NaLiBa Sodium(**Na**) carbonate + Lithium(**Li**) carbonate + Barium(**Ba**) carbonate

NBA Sodium(**N**a) **B**eta **A**lumina

NI TC **N**ational **I**nstruments **T**hermo**C**ouple

NT3 $\mathbf{N}a_2\mathbf{T}i_3O_7$

NT6 $\mathbf{N}a_2\mathbf{T}i_6O_{13}$

PSA **P**lanar **S**ensor **A**rchitecture

RT **R**oom **T**emperature

SEM **S**canning **E**lectron **M**icroscopy

SSA **S**tacked **S**ensor **A**rchitecture

TGA **T**hermo**G**ravimetric **A**nalysis

Nomenclature

E_a - activation energy

F - Farad

H - Henry (SI -Inductance)

μ_o - magnetic permeability of free space

μ_r - relative magnetic permeability of conductor

ω- angular frequency (rad)

ω_H- hopping frequency

σ- electrical conductivity

k - Boltzmann costant

m - meter (SI)

Contents

List of Figures

List of Tables

Chapter 1

Introduction

Carbon dioxide, one of the greenhouse gases can vibrate upon absorbing infrared radiation in the process passing heat to its surroundings. This consequently increases the ambient temperature. If the concentration of carbon dioxide increases in the atmosphere, the temperature increases too. It is widely accepted, with an exception of a few sceptics that the recent increase in carbon dioxide concentrations is to a large extent due to human activities (such as combustion of hydrocarbons and other carbon containing fuels)[1, 2].

The Keeling curve[1] indicates a progressive increase of the concentration from 315.62 ppm in 1959, 393.09 ppm in Jan 2012 and 402.8 ppm in June 2015. This trend is expected to carry on rising as long as humans satisfy their thirst for combusting fossil fuels. The safe limit is considered to be 350 ppm [3].

Given this background and the alarming increase of pollutants and combustible gas exhausts in the global environment, a continuous monitoring and control of carbon dioxide (CO_2) would require accurate, reliable carbon dioxide sensors.

[1] A graph that plots ongoing change in carbon dioxide concentration in the Earth's atmosphere.

Although the commonly used spectroscopic analysers are quite exact, a more portable and low cost device capable of working under extreme conditions such as at high temperatures, particulate matter, toxic gases or micro-organisms has become a necessity.

Carbon dioxide can also cause substantial negative health effects in high concentration exposures ranging from headaches ($\geq 2\%$(20000 ppm) to death (for $\geq 20\%$ concentrations)[4]. The maximum average time of exposure recommended by the United States Occupational Safety and Health Administration is 5000 ppm over eight hours [5].

Furthermore, fire detection can be improved beyond the conventional smoke detection system by concurrently monitoring the chemical nature of a fire. One possible signature to determine fire condition is the CO/CO_2 ratio[6, 7]. As such it is highly desirable to be able to measure and monitor carbon dioxide in order to control indoor air quality in buildings, cars as well as in aircraft. For this reason carbon dioxide sensors are indispensable.

In the quest for a better, robust and portable sensor, a number of investigators have developed sensors such as ones employing solid electrolytes, mixed oxides, zeolites and polymers [8, 9, 10, 11, 12, 13]. All potentiometric sensors using solid state electrolytes have drawn attention because of their good selectivities, low cost, technological simplicity and potentially excellent sensing performance.

A great deal of cells have been prepared from bulk ceramic pellets or tubes but their usefulness in real world applications is limited; for instance since they work at elevated temperatures, homogeneous heating can only be achieved in a furnace. In

view of their good sensing performance and because sensor response (EMF) is an intensive property, the sensor concept can be transferred to thick film technology providing a basis for miniaturisation and integration of further accessories such as temperature sensors, on-board heaters and wireless technology within a single sensor device.

One of the major issues in the ongoing development of a solid electrolyte based screen printed potentiometric CO_2 sensor is long-term stability. Although many attempts have been reported by several research groups towards sensor improvements, and most to changes in material combinations in the electrodes such as replacing of Na_2CO_3 with Na_2CO_3-$BaCO_3$, Na_2CO_3-$CaCO_3$ or Li_2CO_3-$BaCO_3$, little is known on the influence of basic technological aspects on degradation effects and signal drifts that are usually observed. In this study the characterisation of electrolyte/substrate interface and its condition after high temperature treatment highlights some thermodynamic aspects contributing to sensor signal (EMF) drifting that is common feature in thick film sensors when NASICON as electrolyte and alumina as substrate are coupled. A new auxiliary sensing material combination is also tried.

Thick film sensors come in two configurations, one is called the planar sensor architecture (PSA)[14, 15] which is a commonly used sensor and the other is a multi-layered structure called a stacked sensor architecture (SSA) demonstrated by Choi et al. [16]. A PSA sensor is fabricated by printing sensing and reference electrodes side by side on the electrolyte. Despite its reported good performance, usual issues of stability and EMF drifting have been reported. A multi-layered structure has also been explored with similar results even though authors claim this architecture is better than the PSA because it does not need a reference electrode[16, 17].

However, contrary to the positive claims, the inherent problems with this SSA are; (a) sensor oxygen dependence because one side is a closed reference. (b) NASICON/alumina substrate interface conditions at high temperatures do not allow fixed sodium or sodium oxide potential and this may lead to drifting or unstable equilibrium. This sensor therefore can not be relied upon. In this study, a modified multi-layered structure which isolates NASICON from the substrate using a buffer system with the potential to prevent oxygen cross-sensitivity has been developed and tested.

In a bid to lower the cost of sensor production through high throughput deposition techniques such as the screen printing technology, new and cheaper synthesis methods of sensor components are also required; and this study attempts both quests. Detailed characterisation of the synthesised materials and deposited bespoke inks is also presented. The common reference electrodes that have been used in NASICON based sensors and have proven successful in providing stable equilibrium are the biphasic oxides such as $Na_2Ti_6O_{13}$ - TiO_2 and $Na_2Ti_6O_{13}$ - $Na_2Ti_3O_7$. Despite their use, there is quite limited and contradictory information on the high temperature stability of these oxides when in contact with NASICON or sodium beta alumina. This research provides new findings on the thermodynamics of these materials and provide a basis for further research.

1.1 Objectives

The overall objective of the study was to demonstrate the feasibility of fabricating a practical, low cost, multilayered planar CO_2 sensor using thick film screen printing technology.

To achieve this, the following aspects of investigations were performed:

1. New and low cost synthesis methods of the solid electrolyte, NASICON.
2. Improved synthesis procedure for the buffer material $CuAlO_2$-$CuAl_2O_4$-Al_2O_3.
3. Use of the EMF method to study the thermodynamics and chemical stability of the reference electrodes at high temperatures.
4. Preparation of bespoke thick film pastes, screen printing and optimising layer by layer sintering schedule through characterisation of the printed films using X-Ray Diffraction (XRD), Scanning Electron Microscopy (SEM).
5. Detailed electrical characterisation of the sensor component materials that is, NASICON (bulk and thick films) and the buffer component material.
6. Fabrication of the sensor and sensing characterisation in terms of sensitivity, response time, stability and humidity cross-sensitivity.

1.2 Structure of the Thesis

Chapter 2 of this thesis will outline the background theory and surveyed literature. Background theory on electrochemical sensing, conductivity mechanisms of solid electrolytes will be presented whilst great emphasis of the literature survey will hinge on CO_2 sensors and more importantly potentiometric sensors.

Experimental techniques will be contained in Chapter 3. This will include materials synthesis procedures as well as the techniques used to characterise them. The chapter will be concluded with the art of screen printing technology and how the thick film pastes were prepared.

Chapter 4 and 5 discusses Materials Characterisation of NASICON and the Electrodes respectively. Furthermore, heat treatment optimisation of screen

printed films and characterisation of their electrical properties is presented.

Thermodynamics studies using the EMF method is contained in Chapter 6. This will investigate the stability of electrode materials at high temperatures.

Chapter 7 discusses layer by layer sensor fabrication, sensor measurements and characterisation.

The final chapter of this study, Chapter 8 discusses the conclusions and recommendations. Chapter 9 is a peripheral chapter that consists of a list of publications, potential publications, and conferences attended. The appendix finally completes the write up.

Chapter 2

Theoretical Background and Literature survey

This chapter concerns the theoretical models of the research as well as a literature survey. Other dedicated literature surveys are contained in the introductory parts of the relevant chapters.

2.1 Sensor

A sensor is a device that receives a signal or stimulus and responds with an electrical signal. By signal it is meant a signal that can be channeled, amplified and modified by electrical devices **[18].** Therefore a chemical sensor responds to stimuli produced by various chemicals (or chemical reactions). A gas sensor (or array of sensors) is a human analogy of a nose. An odour signal is picked up in the nostrils by olfactory receptors and then transmitted via sensory nerves in the form of ions, processed by the brain and then identified[19]. See Figure 2.1 as adapted from Arshak et al. [19]

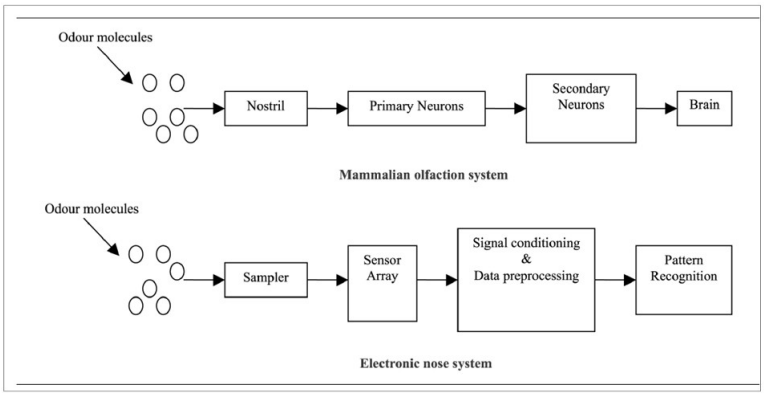

Figure 2.1 – Electronic nose system[18].

From this analogy, it is clear that, for example in the case of an electrochemical sensor, there should be: (a) a sensing material to handshake with the physical world (or sensing the analyte gas), which we call a sensing electrode, (b) a medium of ion transport, in this case an electrolyte (c) a reference electrode to fix the potential constant at that electrode and complete the circuit and (d) interface electronics and display to grab the signal, condition it and display it.

Sensors are categorized into two: Passive sensors, and active sensors. Passive sensors convert the stimulus directly into an electrical signal without any energy input. Examples are, a thermocouple, piezoelectric sensor.

On the other hand, active sensors require an excitation energy (external power) to convert a stimulus into an electrical signal. Examples include; thermistors, a potentiometric (requires thermal energy for ionic conduction in solid electrolytes), amperometric and conductometric sensors (require a voltage to drive current).

Below are some of the important parameters that are used to characterise sensor performance.

Sensitivity

This is defined as the change in sensor output per unit change in measurand.

Full Scale Output

Full-scale output (FSO) is the algebraic difference between the electrical output signals measured with maximum input stimulus and the lowest input stimulus applied (also known as the baseline)[18].

Accuracy

An important characteristic of a sensor is accuracy which really means inaccuracy. Inaccuracy is measured as a highest deviation of a value represented by the sensor from the ideal or true value at its input. The true value is attributed to the object of measurement and accepted as having a specified uncertainty[18].

Hysteresis

A hysteresis error is a deviation of the sensor's output at a specified point of the input signal when it is approached from the opposite direction[18].

Selectivity

This is a measure of how selective a sensor is when exposed to different stimuli. This means that the sensor should be able to respond to only one analyte with little or no interference from other gases [18, 20].

Response Time (t_{90})

The is a measure of how fast the response is when a new level of stimulus is applied. The response time therefore is the time taken to achieve 90% of the stable EMF value and is denoted as t_{90}.

Recovery time

This is the time for signal to return to its baseline or the lower steady state output when the stimulus is removed. It is the time that it takes the sensor to be within 10% of the value it had before exposure to the measurand.

Resolution

Resolution describes the smallest increments of stimulus or input signal that can be sensed. To have a meaningful output some sensors may only resolve decade scales.

2.2 Solid State Electrochemical Gas Sensors

The fundamental principles of electrochemical gas sensors with solid electrolytes are the electrochemical reactions that take place in the electrochemical cells. These cells comprise a dense solid electrolyte (that is highly conductive) and two porous electrodes which are separated by the solid electrolyte. These sensors are able to measure the concentration, partial pressure or thermodynamic activity of the analytes.

There are three working modes of electrochemical sensors namely potentiometric, amperometric and conductometric[18].

For potentiometric sensors, a local equilibrium is established at the sensor interface, where the electrode potential is measured, and information about the composition of a sample is obtained from the potential difference (voltage) between two electrodes due to the redox reactions which takes place at the electrode interfaces. The voltage is measured under conditions of essentially zero current. The voltage is logarithmically dependent on the concentration of the analyte. Consider an electrode reaction in Equation (2.1), where Ox denotes an oxidant and Red denotes a reduced product

$$\mathrm{Ox} + \mathrm{ne} \rightarrow \mathrm{Red} \tag{2.1}$$

The electromotive force (EMF) developed at the electrode interface under equilibrium conditions follows the Nernstian law, that is

$$E = E^{\circ} - \frac{RT}{nF} \ln\left(\frac{C_O}{C_R}\right), \tag{2.2}$$

or thermodynamically, under isothermal conditions of known temperatures, the EMF can also be described as activity dependent, that is

$$E = E^{\circ} - \frac{RT}{nF} \sum v_i \ln a_i \tag{2.3}$$

where E_o is the standard electrode potential, F is the Faraday constant, R is the gas constant, n is the number of electrons transferred in the external circuit to the other electrode and T is the absolute temperature, v_i are the stoichiometric numbers, positive for products (reduced species) and negative for reagents (oxidised species) while a_i are the activities[21]. The concentrations of Ox and Red are C_O

and C_R respectively. The relation between activity and concentration is given by

$$a = \gamma_c C \tag{2.4}$$

where γ_c is the activity coefficient for unit concentrations[21]. Therefore, by measuring the activity at the reference electrode and employing (2.3), the unkown activity of the analyte can be determined. Substituting this activity into (2.4) the concentration can be obtained.

It should be noted that two half reactions take place simultaneously at the electrodes and only one of the two reactions will involve the sensing. The other half is non interfering, reversible and known. In short, the EMF measured that is representative of the concentration of the analyte is the difference between the potentials generated by the reactions on the two electrodes.

Amperometric sensors exploit the use of a potential applied between a reference and a working electrode, to cause the oxidation or reduction of an electroactive species. The applied voltage drives the electron transfer reaction of the electroactive species. The resulting current is a direct measure of the rate of the electron transfer reaction. It is thus reflecting the rate of the recognition event, and is proportional to the concentration of the target analyte. One drawback of amperometric sensors is that they respond to the chemical potential of the element being measured and not directly to the concentration[22]. This is because in process control (which requires direct measurements), concentration is the one being measured and not chemical potential. Therefore an amperometric sensor may not be very well suited for such actuating activities.

On the other hand, conductometric sensors are involved with the measurement of conductivity at a series of frequencies. Charge transfer processes causes polarization hence the capacitative impedance is obtained. The concentration of charge is obtained through measurement of electrolyte resistance and is therefore not species-selective.

As has been already alluded to, this review focuses on the potentiometric sensors especially carbon dioxide sensors based on solid electrolytes. Details of sensing mechanisms of amperometric and conductometric sensors is well established knowledge and found in many text books and reviews elsewhere.[18, 23, 24, 25, 26, 20, 7, 27, 28]

2.3 History of CO_2 Electrochemical Sensors (ECS)

Solid state based carbon dioxide sensors have been capturing interest since the first potentiomentric CO_2 sensor was reported in 1977, a finding which was merely a preliminary measurement [8]. It was based on the K_2CO_3 and 1% mole fraction $AgSO_4$ electrolyte with Ag/Ag^+ reference electrode, i.e. Pt,CO_2,O_2 | K_2CO_3-$AgSO_4$ | Ag/Ag^+.

Cote et al. [29] followed up with a more dedicated investigation where they used K_2CO_3 as the electrolyte with Ag/Ag^+ replaced by a controlled CO_2/O_2 gas mixture and used Au as the electrode instead of Pt since Pt tends to react with K_2CO_3 at high temperatures using the cell Au,CO_2,O_2 | K_2CO_3 | O_2, CO_2. From then on, the pursuit for a "better sensor" with attributes of high sensitivity, fast response, highly stable, low cross-sensitivity and selectivity gathered momentum. For example, metal carbonates are difficult to sinter and have a low conductivity, hence more highly conductive electrolytes were suggested, such as sodium

zirconium silicophosphate and commonly called Sodium Super Ionic Conductor (NASICON: which is a Na^+ ion conductor) and beta alumina [9]. In this research, we shall focus on NASICON as a solid electrolyte as this has very high electrical properties at high temperatures comparable to liquid electrolytes.

2.3.1 Basic Components ECS

There are three major components of an electrochemical sensor. The working electrode, the reference electrode and the ion conductive electrolyte.

The ion selective electrode is an indicator electrode capable of selectively measuring the activity of a particular ionic species. One electrode is the working (or sensing) electrode whose potential is determined by its environment. The second electrode is a reference electrode whose potential is fixed by the material containing the ion of interest at a constant activity. Since the potential of the reference electrode is constant, the value of the potential difference (cell potential) can be related to the concentration of the dissolved ion[30].

The quality, reliability and operation of a sensor hinges its foundation on a good quality ion conductive electrolyte. Beta alumina or β-alumina (NBA) and NASICONs are the better suited electrolytes because of their ideal properties such as being superionic and being sinterable to a good density. The next section discusses the NASICON and its conductivity mechanism.

2.4 Solid Electrolytes

It has been well known for a long time that electrical conductivity in solids is due to mobile species such electrons and holes as observed in semiconductors and metals. However, there are solids in which mobile species are only ions. These are

called solid electrolytes or ionic conducting solids. Na-β- alumina (NBA) with structure $((Na_2O)_{1+x} \cdot 11\,Al_2O_3)$ has been known as one of the solid electrolytes for secondary batteries [31] It has a maximum conductivity at $x = 0.2 - 0.3$ [32] . The Na^+ ion conduction in NBA is, however, restricted to the 2-D plane of the hexagonal structure consisting of spinel-type blocks of closed packed oxygen and aluminium ions separated by loosely packed planes of Na^+ and O^{2-} ions inside which there is space for Na^+ to move.

Hong [33] found a new system $Na_{1+x}Zr_xSi_xP_{3-x}O_{12}$ ($0 \leq x \leq 3$) formed by tetrahedral SiO_4 and PO_4, and also hexagonal ZrO_6 polyhedra, linked by oxide ions to form 3-D network structure, which is suitable for ion migration in all the three dimensions. The compound $Na_3Zr_2Si_2PO_{12}$ ($x = 2$) of monoclinic symmetry shows Na^+ ion conductivity comparable to that of NBA. The new solid electrolyte was then named NASICON (for Na SuperIonic Conductor).

The average symmetry system of NASICON material is rhombohedral with space group $R\bar{3}c$ except in the interval $1.8 \leq x \leq 2.2$ where a small distortion to monoclinic occurs [34, 33]. NASICON phase is also gradually formed between the temperature range of $800 \leq T \leq 1050$ °C.

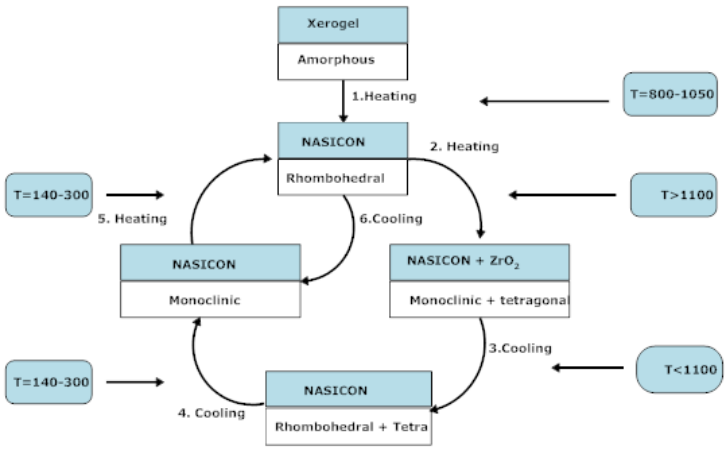

Figure 2.2 – Phase transition of NASICON upon heating and cooling

The rhombohedral to monoclinic transition is only observed above 1100 °C where traces of monoclinic zirconia appear [35, 36]. Also, upon cooling to room temperature, it transits from rhombohedral to monoclinic. In situ high temperature XRD (HTXRD), calorimetric and dilatometric measurements point to the transition temperature being 140-300 °C [36, 35]. Figure 2.2 represents the phase transition temperatures.

von Alpen [37] did a comprehensive work on the phase transition of NASICON, ($x = 2$), and found a change of activation energy from high to low at 152 °C (implying an increase in conductivity at 152 °C). This was also complimented by calorimetric measurements where he found a clear phase transition at 147 °C. HTXRD also confirmed a transition from rhombohedral to monoclinic shown by the splitting of peaks at lower temperatures.

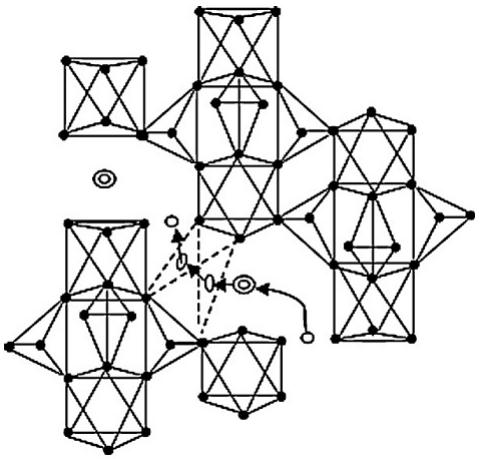

Figure 2.3 – NASICON structure: The two sites of Na^+ ions are represented as follows; Na_1 by double circles and Na_2 by open circles. Oxygen atoms are denoted by closed circles and the bottleneck is shown by dotted lines.

Regarding the location and movement of sodium ions, there are two main sodium lattice sites. They are denoted as Na_1 and Na_2. Na_1 is located along the c-axis

between 2-octahedra polyhedron while the Na_2 site is midway between Na_1 sites along the a-axis[38]. The Na sites are connected through triangular bottlenecks formed by three oxygen atoms whose centres make up an isosceles triangle. See Figure 2.3 as adapted from [39].

2.4.1 Mechanism for ionic conduction

With regard to conduction mechanisms for ionic motion in solid electrolytes three types are regarded as important; these are vacancy diffusion, interstitial mobility and interstitialcy motion. The general theory is contained in many reviews and books[40, 41]. The description here is dedicated to ion conduction in NASICON.

The movement of Na^+ ions from one interstitial site to another through bottlenecks constitutes ionic conduction. The diffusion pathway of ions from Na_1 to Na_2 occurs in a zigzag fashion through the bottlenecks whose diameter (2.12Å) is comparable to the diameter of Na^+ ions ($\sim$ 2.02Å) and widens to a maximum when $x = 2$ [42, 43]. Variation of x would imply a partial substitution of P by Si thereby modifying the orientation of the tetrahedral polyhedron and increasing the bottleneck. Therefore the diffusion (and hence ionic conduction) depends on the size of the bottleneck(activation energy). The widening also increases with temperature.

Solid electrolyte ion conductivity is generally described by the Arrhenius relation in Equation (2.6)[43, 44];

$$\sigma = \left(\frac{C}{kT}\right) \exp\left(-\frac{E_a}{kT}\right) \tag{2.5}$$

where C is pre-exponential factor, E_a is the activation[1] energy of ionic motion, k

[1] **Activation energy** is an energy barrier that the charge carrying ions must overcome to conduct through the material.

is the Boltzmann constant and T is the absolute temperature.

Furthermore, the constant C in (2.6) is given by

$$C = \frac{1}{3}(Ze)^2 nd^2\omega_o \tag{2.6}$$

where n is the defect density (intersticials in intersticial diffusion or vacancies in vacancy diffusion), d is the unit jump distance of an ion, ω_o is the attempt frequency while the total charge is Ze. The temperature dependence of the microscopic, mobile species diffusion coefficient D is correspondingly represented by an Arrhenius equation of the form $D = D_o \exp\left(-\frac{E_a}{kT}\right)$ where $D_o = C/\left(Z^2e^2n\right)$ so that the conductivity becomes

$$\sigma = n(Ze)^2\left(\frac{D}{kT}\right). \tag{2.7}$$

Equation (2.7) is called the Nernst-Einstein equation.

Different researches have pinpointed $x = 2$ as the 'gold parameter' because some unique properties occur here. NASICON has a maximum conductivity at $x = 2$ found it to be 2.1×10^{-1}S/cm at 300 °C [45]. The quality of NASICON and synthesis procedures have improved such that higher conductivities have actually been achieved and reported such as 0.236 S/cm by Dhas and Patil [46] and 0.45 S/cm by Kang and Cho [47].

Kale and Jacob [48] in their study on the thermodynamic activity of Na_2O in NASICON found that the maximum deviation of Na_2O entropy from the linear line (a composition weighted line relative to the end members) occurred at $x = 2$ that is, partial enthalpy exhibited a maximum at $x = 2$ indicating a low binding

enthalpy or that Na^+ is weakly bonded with other oxides hence it is more mobile thereby contributing to high conductivity in the solid solution.

Apart from the fact that NASICON has a higher conductivity than the close counterpart NBA, carbon dioxide sensors made out of NASICON are able to sense a wider range of partial pressure of carbon dioxide up to as high as 10^5 Pa [9]. This is because of the low Na_2O activity in NASICON than in NBA hence it has a wider sensing range than NBA [9]. See Figure 2.4. NASICON is thermodynamically stable as a result it does not react with carbon dioxide to form sodium carbonate (unless at very high partial pressures) at the reference electrode. This can be deleterous to the sensor as it might form a symmetrical cell and thereby short circuiting the sensor and basically giving a zero or unusually low EMF.

From the fundamental finding of Kale and Jacob [48] on the activity of Na_2O in NASICON, shown in Equation 2.8

$$\log a_{Na_2O} = -\frac{12050}{T} - 2.15 \tag{2.8}$$

increasing the operation temperature reduces the Na_2O activity hence giving the sensor a wider range of detection and the reverse is true for low operating temperatures. However, very low activities give higher EMF voltages which in turn decrease sensitivity, $\left(\frac{\Delta E}{E}\right)$, to the change in partial pressure of carbon dioxide. This is one of the reasons why operation temperatures for CO_2 sensors are in the range of 500 °C and above[12]. Because of this wide bandwidth of detection, NASICON is the best candidate for fast response and stable carbon dioxide sensors.

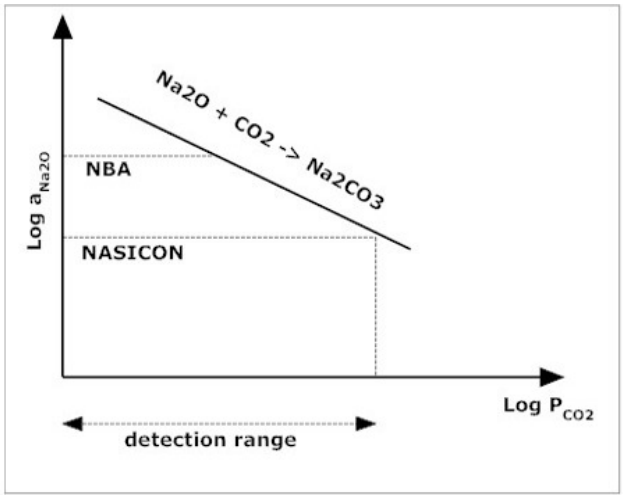

Figure 2.4 – Stabilities of NASICON and NBA upon exposure to carbon dioxide at high temperatures

2.5 Sensing Electrodes.

The sensing electrode is sometimes synonymously regarded as an auxiliary electrode as this is usually a combination of auxiliary phase such as alkali carbonates and a gold or platinum probe. Instead of just a metal lead, such as platinum, a material that contains the compound to be measured and the species ionically mobile is coated on the surface of the electrode, which will then be the sensing side. It therefore provides a chemical coupling between the species being measured and the conducting ion. For example, in the detection of CO_2, Na_2CO_3 is normally used [10, 12, 49, 9, 11, 50].

In the detection of SO_2 and NOx gases the auxiliary phases such as Na_2SO_4 by Kale et al. [51] and $AgNO_3$ or $NaNO_3$ by Miura et al. [52] are used respectively. Carbon dioxide sensors employing Na_2CO_3 suffer cross-sensitivity issues[20]. Binary carbonates have been proposed and employed and the results have been good. This will be discussed in more detail later in the chapter.

2.6 Reference Electrodes

The job of reference electrodes is to maintain a constant and stable chemical potential against which the activity of the unknown species are measured. It must also be completely stable, reversible, good electronic conductivity, compatible with sensing electrode and must not react with the cell components. It must also be independent of any chemical potential changes at sensing electrode[20, 53]. Reference electrodes can either be gaseous [54] liquid or solid materials. A gas reference system decreases the range of application of the sensor as well as sensitivity[49].

Elemental sodium has been used before as reference electrode in galvanic cells to sense NO_2[55] and CO_2[56] gases. The downside of its use is its low melting point, high vapour pressure and high reactivity and when the sealing is not good, leakages can occur hence making it hazardous and unsuitable for chemical sensor applications as reference electrode.

An alternative to the application of elemental sodium in the reference electrode is the use of a binary phase system such as binary sodium intermetallic compounds(alloys). This is because the sodium activity is constant, that is, it is independent of the overall composition, in view of the Gibbs phase rule[57]. Furthermore, its sodium activity is within the ionic conduction domain[2]

A number of these binary sodium alloys such as Na-Al, Na-Si, Na-B, Na-Sn and Na-Zn have been successfully applied as reference electrodes[58]. The major complication of using these binary compounds is their narrow temperature range over which they are solid and therefore, they can not be successfully used for sensors that are required to operate over a wide range of temperature.

[2]This is the region with respect to temperature and activity or partial pressure of the potential determining species of the electrolyte within which the electronic contribution to the total conductivity is less than 1%[40].

Success in the search of thermodynamically stable electrodes has seen the use of ternary systems of the group A_xMe_yO (A = Na, Li or K; Me = V, Cr, Ti, Mn, Co, Fe, Ta, La, W, etc)[59]. Sodium metal oxide ternary systems (Na-Ti-O) have been found to be the most probable materials for reference electrodes or other high temperature applications.

Therefore, recent progress has seen gaseous references being replaced by solid materials as they offer thermodynamically stable EMFs. For example, mixed reference materials such as $Na_2Ti_6O_{13}$/ TiO_2 and $Na_2Ti_6O_{13}$/$Na_2Ti_3O_7$ have been used for carbon dioxide sensors to fix Na_2O activity and rendering the sensor very stable within the operating temperature. Failure occurs when sodium carbonate may form because of the exposure of Na_2O from the electrolyte to the environment and particularly carbon dioxide.

There are two reference systems commonly used; the open reference system, where the reference electrode is exposed to the environment and the closed reference system where the reference is gas tight. A detailed discussion of different types of sensors using these two reference system is given in the upcoming sections.

2.7 Mechanism of Sensing with NASICON as Solid electrolyte

To elucidate how potentiometric sensor detection occurs we shall consider an open reference system involving $NaCO_3$ as the working electrode, NASICON as the solid electrolyte for Na^+ conduction and an open reference system. The section will conclude with the use of a mixed reference system consisting of $Na_2Ti_6O_{13}$/ TiO_2.

Considering the cell,

$$\mathrm{CO_2, O_2, Au|NaCO_3|NASICON|Au, O_2, CO_2}$$

The anode reaction at the sensing electrode will be

$$\mathrm{Na_2CO_3} \rightleftharpoons 2\,\mathrm{Na^+} + \mathrm{CO_2} + \frac{1}{2}\mathrm{O_2} + 2\,\mathrm{e} \tag{2.9}$$

and the cathodic reaction, at the reference electrode, involving the gas reference is

$$2\,\mathrm{Na^+(_{NASICON})} + 2\,\mathrm{e} + \frac{1}{2}\mathrm{O_2} \rightleftharpoons \mathrm{Na_2O_{NASICON}} \tag{2.10}$$

The overall reaction to the two redox half reaction is

$$\mathrm{Na_2CO_3} \rightleftharpoons \mathrm{Na_2O_{NASICON}} + \mathrm{CO_2} \tag{2.11}$$

It is important to recognise the fact that since both sides of the electrodes are exposed to the same type of gases, oxygen cancels out. This renders the sensor insensitive to $\mathrm{O_2}$ but sensitive to $\mathrm{CO_2}$ which is what it is supposed to do. The EMF detected follows a Nernstian law and since the Gibbs free energy change is $\Delta G = -nFE$, then

$$\begin{aligned} E &= E^\circ - \frac{RT}{nF}\ln\left(\frac{P_{\mathrm{CO_2}} a_{\mathrm{Na_2O}}}{a_{\mathrm{Na_2CO_3}}}\right) \\ &= -\frac{\Delta G^\circ}{nF} - \frac{RT}{nF}\ln\left(\frac{P_{\mathrm{CO_2}} a_{\mathrm{Na_2O}}}{a_{\mathrm{Na_2CO_3}}}\right) \end{aligned} \tag{2.12}$$

where the change in standard free energy of reaction, $\triangle G^{\circ}$ of Equation (2.11) is

$$\Delta G^{\circ} = \Delta G^{\circ}{}_{Na_2O} + \Delta G^{\circ}{}_{CO_2} - \Delta G^{\circ}{}_{Na_2CO_3} \tag{2.13}$$

From Equation 2.12, $n = 2$ is the number of electrons transferred in the external leads, F is the Faraday's constant, T is the absolute temperature, E^o is the standard electrode potential, $a_{Na_2O(\text{NASICON})}$ is the activity of Na_2O in NASICON and $a_{Na_2CO_3}$ is the activity of Na_2CO_3 in the auxiliary. The activity of Na_2CO_3 is unity since it is pure Na_2CO_3. The activity of Na_2O in NASICON is available in literature from Kale and Jacob [48], and therefore if the activity of Na_2O is constant in NASICON of fixed composition, the EMF will solely depend on the partial pressure of CO_2. If the Na_2O activity is not fixed then the EMF will depend not only on the CO_2 partial pressure but also on this activity.

Using the cell above, the CO_2 at the reference electrode may pose a deleterious threat to the NASICON and the sensor as a whole. Even when the Na_2O activity is fixed by the electrolyte alone, there is a risk that Na_2CO_3 can form at higher CO_2 partial pressures. This forms a symmetrical cell which then short circuits the sensor and results in zero or near zero EMF. Therefore to prevent this, the following is usually done

- The sensor can be designed such that CO_2 is isolated. This maybe be through a membrane which allows only O_2 but impermeable to CO_2. Achieving this is technologically challenging. The most common method is where the sensor is specially designed whereby the reference is just exposed to oxygen as demonstrated by Kale and Davison [10] as well as Maruyama et al. [9].

- The reference can be sealed completely. This is elegantly done when the sensor is fabricated on planar substrates. However, doing this will again

make the sensor oxygen dependent.

- The Na_2O can be prevented from reacting with CO_2 by fixing its activity. This is usually done using solid reference mixtures such as $Na_2Ti_6O_{13}/TiO_2$, $Na_2Ti_6O_{13}/Na_2Ti_3O_7$, Na_2SnO_3/SnO_2 and Na_2ZrO_3/ZrO_2 binary oxides[12, 14].

The most commonly used reference electrode mixture is $Na_2Ti_6O_{13}/TiO_2$. The mechanism of carbon dioxide sensing when using this reference electrode is illustrated below. Considering the cell

$$CO_2, O_2|Au, NaCO_3|NASICON|Na_2Ti_6O_{13}/TiO_2, Au|O_2, CO_2$$

the cathode half reaction becomes

$$6\,TiO_2 + 2\,Na^+ + 2e + \frac{1}{2}O_2 \rightleftharpoons Na_2Ti_6O_{13} \tag{2.14}$$

The overall reaction involving Equation 2.9 and 2.14 is

$$TiO_2 + Na_2CO_3 \rightleftharpoons Na_2Ti_6O_{13} + CO_2 \tag{2.15}$$

The two phase reference acts as a Na_2O activity buffer. The reference does not need encapsulation or sealing. The sensor can be exposed to the ambient atmosphere without any unnecessary reactions between Na_2O and CO_2. It is also notable that the EMF does not depend on oxygen partial pressure. This is the advantage of using an open reference electrode.

The EMF in this case becomes

$$\begin{aligned} EMF &= -\frac{\Delta G^{\circ}}{2F} - \frac{RT}{2F} \ln P_{\mathrm{CO_2}} \\ &= E^{\circ} - \frac{RT}{2F} \ln P_{\mathrm{CO_2}} \end{aligned} \tag{2.16}$$

where

$$\begin{aligned} \Delta G^{\circ} &= \Delta G^{\circ}{}_{\mathrm{Na_2Ti_6O_{13}}} + \Delta G^{\circ}{}_{\mathrm{CO_2}} - \Delta G^{\circ}{}_{\mathrm{Na_2CO_3}} - 6\Delta G^{\circ}{}_{\mathrm{TiO_2}} \\ &= \mu^{\circ}{}_{\mathrm{Na_2Ti_6O_{13}}} + \mu^{\circ}{}_{\mathrm{CO_2}} - \mu^{\circ}{}_{\mathrm{Na_2CO_3}} - 6\mu^{\circ}{}_{\mathrm{TiO_2}} \end{aligned} \tag{2.17}$$

and can be obtained from thermodynamic tables.

In order to ensure that the materials of the reference electrode do not react with the ambient CO_2 according to Equation 2.15 in the forward reaction, it has to be ensured that the thermodynamic condition

$$\Delta G = \Delta G^{\circ} + RT \ln \left(P_{\mathrm{CO_2}} \right) \leq 0 \tag{2.18}$$

is satisfied in a chosen temperature and partial pressure range [12]. This condition as well as phase stability and kinetic aspects makes the $Na_2O{-}TiO_2$ system a better choice, than most other systems such as $Na_2O{-}ZrO_2$ etc, which has a positive thermodynamic condition [9].

2.8 Carbon Dioxide Sensors

2.8.1 Types of CO_2 Sensors

CO_2 sensors are generally classified as electrochemical and optical sensors based on their sensing mechanisms. Quite a number of CO_2 sensing techniques have been proposed and developed for its routine measurements. The most common of them and commercially available are the Infra red absorption detectors called the Nondispersive infrared (NDIR) detector, gas chromatography (GC), mass spectrometers (MS) and the Severinghaus type potentiometric sensors.

The NDIR detector is one of the widely used and commercially available sensor[48, 60]. In the market now, the most available NDIR sensors are Model No. GMT220, GM20, GM70, GMM220 Carbocap, from Vaisala[61]; TGS4160 from FIGARO[62] and Model No. ARC-A1 and IRC-AT from Alphasense [63]. Despite their good selectivity, precision, sensitivity and easy to use NDIR sensors have disadvantages. They are bulky and expensive. They also cannot be used in harsh environments which limit their use to indoor and remote sensing applications. Additionally, the detection of CO_2 based on its strong absorption region encounters problems from water vapour and carbon monoxide interference [64, 65]. For this reason, there is a need for inexpensive, easy to use and portable sensors capable of working in hostile environments.

Apart from NDIR detectors, other optical sensors do exist such as the optodes also referred to as fibre optics sensors. They contain a chemical sensing layer at the tip of the fibre and upon exposure to CO_2 its optical properties change. Several researchers have fabricated optical based CO_2 sensors using materials exhibiting absorbance and reflective changes on exposure to CO_2[66, 67, 68]. Despite the fact that optodes are chemically inert and not cross-sensitive to the presence of

other gases in the background, their use of lenses results in the interference of light over time due to dust or soot coating. Hence the lenses need frequent cleaning. Expensive read-out equipment is also necessary for sensing at the tip of the fibre.

Table 2.1 – Carbon dioxide sensing materials for MOS.

Sensing material	**Range**	**T/ (°C)**	**Ref.**
$CuO/BaTiO_3$ and $NiO/BaTiO_3$	100-6000 ppm	800	[69]
$CrO/BaTiO_3/La_2O_3/CaCO_3$	0 - 7%	700	[70]
$LaCl_3.7\,H_2O/SnO_2$	0 - 2500 ppm	400	[71]
$LaCl_3/BaTiO_3$	0.1 -10 %	550	[72]
$LaOCl/SnO_2$	400 - 2000 ppm	350-550	[73]
Sm_2O_3	0.1-0.4%	400	[74]
Doped SnO_2	500ppm	250	[75]
$CuO/BaTiO_3$	0 -2000 ppm	400	[76]

Metal oxide sensors (MOS) have also been explored in the detection of carbon dioxide. The oxide sensor consists of a resistive metal oxide sensing material deposited over a substrate such as $BaTiO_3$ $-CuO$ [76] deposited on a substrate provided with electrodes for the measurements of electrical signals. With the sensor heated by its own on-board heater, upon exposure to CO_2, chemical reactions that take place at the surface of the sensing metal oxide cause change in its resistance, which is proportional to the concentration of carbon dioxide. Table 2.1 are some of the MOS CO_2 sensors. Furthermore, MOSs, one of the most commercially available sensors have advantages over the other competing sensor technologies such electrochemical sensors and polymer based sensors for their robustness and long term stability. Despite these advantages, their repeatability is poor.

Mutschall and Obermeier also investigated a capacitor-type carbon dioxide sensors using organically modified silicate as a sensitive layer. Changes in dielectric properties upon exposure to carbon dioxide were evident[77]. Most of these sensors had drawbacks as they experienced a large cross sensitivity to water vapour.

Nano-based sensors have also been explored. Anderson et al. [78] investigated the GaN and ZnO nanotube based CO_2 sensors. The sensor consisted of a AlGaN/GaN high electron mobility transistor (HEMT) coated with polyethyleneimine (PEI) and starch with PEI/starch being used as a CO_2 sensitive layer. The sensors were responsive but with relatively long response times of over 100 seconds.

Ong and Grimes [79] demonstrated another type of nano-based planar sensor based on PEI sensing layer and relying on the changes in permitivity of the nanotube coating due to exposure to CO_2. The response time was approximately 45 seconds.

A lot of work is also being done in the field of electrochemical sensors such as ones involving solid state ceramics and polymer based electrolytes. Polymer based sensors have been explored for low temperature measurements. They are some kind of a miniaturised version of Severinghaus CO_2 probe. They are capable of broadly detecting and identifying various gases in air. Tongol et al. [80] fabricated a CO_2 sensor based on pH indicating pyrrole membrane. This sensor detects change in gas concentration. It however displayed poor reproducibility. Oho et al. [81] also developed a sensor based on polyvinyl alcohol and poly aniline anthranalic acid film deposited on gold electrode. Sensing was based on the change of electrical conductivity upon exposure to CO_2. In follow-up research,

recently, Neethirajan et al. [82] developed a similar sensor using poly aniline boronic acid. The sensor measured gaseous CO_2 levels in the range of 380-2400 ppm and followed a curvilinear response.

Potentiometric CO_2 sensors based on solid electrolyte ceramics, which are the scope of this research have also been investigated extensively in the form of bulk(pellet type[12] or tube type[10]) and thick film (planar[83, 15, 14, 13] or stack type[16, 17]). They have numerous advantages such as compactness, high sensitivity in detecting very low CO_2 concentrations, technological simplicity and calibration free. They are also able to work under rugged conditions such as high temperatures. Lastly but certainly not the least, for the thick film sensors, their fabrication costs are low and have potential for large scale production through screen printing technology.

A standout advantage of electrochemical sensors (especially potentiometric sensors) is the ease for quantification (the Nernstian law) and hence predictability. Some sensors are just able to sense the changes to concentrations but not easily quantifiable (or based on empirical methods through trial and error) as the mathematical models are still being studied. This review and research is thus concentrating on the potentiometric sensors.

There has been a lot of research work on potentiometric sensors for the past 35 years now, with a lot of papers produced in the first two decades. From the first CO_2 sensor by Gauthier and Chamberland [8] where he used K_2CO_3 as an electrolyte to the most investigated sensors which use electrolytes such as NASICON and beta alumina, it has been demonstrated that potentiometric sensors have good sensing properties and repeatability.

More CO_2 sensors based on carbonate electrolytes have been investigated. As a follow-up to the 1977 work by Gauthier and Chamberland, Cote teamed up with them and investigated on the same electrolyte but using gold as a working electrode [29]. Several other studies have also used Na_2CO_3 as a solid electrolyte [84, 85]. The sensors all showed good sensing properties although the measured EMF was lower than the theoretical at higher temperatures. Another drawback is the fact that carbonates are difficult to sinter and have a lower conductivity [86].

CO_2 sensors based on Li^+ ion conducting electrolytes have also been explored [87, 88, 89] and have shown good sensing properties as well as suppressed interference to humidity. However, their response tended to deviate from Nernstian behaviour probably due to mixed conduction in the electrolyte [20]. NASICON and NBA based CO_2 sensors represent one of the most extensively investigated sensors.

Research work on sensors using NBA as an electrolyte have been carried out extensively by Maier, Sitte and Holzinger [12, 49, 90, 91]; with their first investigation by Warhus and Maier using the cell:

$$CO_2, Au, Na_2CO_3 | NBA | Au, Na_2ZrO_3, ZrO_2.$$

Biphasic mixtures of oxide materials were used as reference electrodes in most of these sensors and response time was found to be one second. Despite the good results reported by these researchers, NBA has a higher Na_2O activity than NASICON hence its CO_2 detection range is narrower and can not be used at lower temperatures than 427 °C. Another important finding by Holzinger et al. [12] while using the $Na_2Ti_6O_{13}/TiO_2$ reference electrode was that the sensor showed good Nernstian behaviour, and at temperatures above 500 °C the sensor signal was independent of oxygen partial pressure even after weeks of operation.

For its super ionic conductivity, NASICON has been widely used and studied in several gas sensing devices. A lot of papers have been published on its use including its doped form[31]. Because of the NASICON's super conductivity, the sensors investigated have shown great response and sensing properties.

Owing to the large number of papers already published on the NASICON based sensors, a summary of various researches [9, 92, 10, 93, 50, 94, 83, 86, 14] on the bulk (B) and planar (P) sensors is given along with their sensing properties in Table 2.2. Again almost all these sensors use metal carbonates as sensing electrodes.

Table 2.2 – Summary of NASICON based carbon dioxide sensors. Bulk = **B,** Planar = **P,** NASICON = **Na^+** , Rapid = **R.**

Cell	**Config.**	**B/P**	**T/°C**	t_{90}**/s**	**Ref.**
1	CO_2, O_2, Au $\|Na^+\|$ Au, O_2	B	327-727	R	Maruyama et al. [9]
2	CO_2, Air, Au, $Li_2CO_3\|Na^+\|$ Au, Air	P	450	123	Kaneyasu et al. [92]
3	CO_2, Pt, $Na_2CO_3\|Na^+\|$ Au-Pd,Pt, CO_2	B	377-447	-	Kale et al. [10]
4	CO_2,O_2, Au, $Na_2CO_3\|Na^+\|$Sealed reference electrode, Au, CO_2	B	500	-	Salam et al. [93]
5	CO_2,Air, Pt, Na_2CO_3-$BaCO_3\|Na^+\|$ Pt, Air	B	450-600	<8	Miura et al. [11]
6	CO_2,Air, Pt, Li_2CO_3-$BaCO_3\|Na^+\|$ Pt, Air	P	450-600	<20	Kida et al. [94]
7	CO_2,Air, Pt, Li_2CO_3-$BaCO_3\|Na^+\|$ Pt, Air	B	300-450	<10	Lee et al. [83]
8	CO_2,Air, Pt, Na_2CO_3-$BaCO_3\|Na^+\|$ Pt, Air	P	400-600	40-70	Wang and Kumar [86]
9	CO_2,O_2, Pt, Na_2CO_3-$BaCO_3\|Na^+\|$ NT6/TiO_2,Pt, Air	P	500-700	R	Sahner et al. [14]
10	CO_2,air, Pt, Li_2CO_3-$BaCO_3$(Li_2CO_3)$\|Na^+\|$ $Bi_8Nb_2O_{17}$,Pt, Air	B	500	-	Lorenc et al. [95]
11	CO_2,O_2, Pt, Li_2CO_3-$BaCO_3\|Na^+\|$ NT6/TiO_2,Pt, Air	P	525	-	Wiegartner et al. [15]

Whilst most sensors here were only tested in high CO_2 concentrations such as 500, 5000, 10000, and 50000 ppm or in decade scales, where the response is obvious and defined; few have tested the sensor for low concentrations of 500 ppm and below. Sometimes sensor requirements are that CO_2 concentrations be less than 500 ppm or even below the atmospheric CO_2 concentrations and so this research demonstrates low concentration detection also.

All these sensors either have an open reference (where all the electrodes are exposed to the same gas) like this cell by Wang and Kumar [86]

$$\mathrm{CO_2, O_2, Pt, Na_2CO_3 + BaCO_3}|NASICON|\mathrm{Pt, O_2, CO_2}$$

or closed reference (where it is completely sealed or only oxygen is allowed at the reference electrode but CO_2 is not allowed, through the use of filter membranes or other physical methods), like in this cell by Maruyama et al. [9]

$$\mathrm{CO_2, O_2, Au, Na_2CO_3}|NASICON|\mathrm{Au, O_2}.$$

As was seen in Equation 2.11, for an open reference sensor, the overall oxygen does not appear in the EMF total cell reaction because it is involved in both electrode reaction and thus it cancels out. In this way the device just senses gaseous carbon dioxide only. Open reference sensors can be in pellet (bulk) form or planar (thick film) form. Figure 2.5 shows an open reference planar sensor as used by Sahner et al. [14] in cell 9 of Table 2.2 and Belda et al. [13].

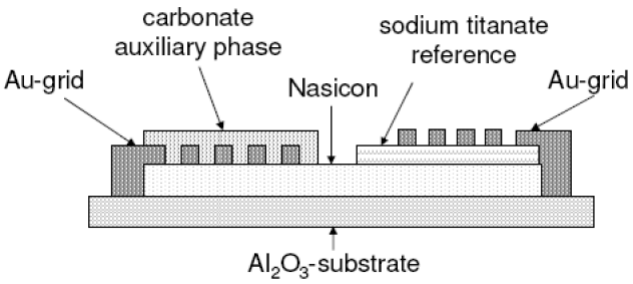

Figure 2.5 – Open reference planar sensor

Despite the usual advantages of open reference systems sensors, the fact that the reference electrode is exposed, there is a risk of carbonates being found at the reference electrode. Their deleterious effects have already been explained. Zosel et al. [96] found out that carbonates sublimate during high temperature operation and their gaseous phase can come into contact with the reference electrode. This could be confirmed after carbonate dendrites were observed in the colder part of the oven. In this setup, the gaseous carbonates getting to the reference is unavoidable.

Elegant ways of preventing carbonate contact with the reference electrodes is proposed in this research; (a) By shielding the reference. This may however render oxygen dependence on the sensor. By using buffer material this may redress the problem. (b)Employ a multilayered (stack) structure where the reference is printed on the alumina substrate followed by the electrolyte and then the sensing electrode on top. This would imply a complete coverage of the reference electrode. But then this would render the sensor oxygen dependent and so a need for a buffer maybe solve this too.

An attempt for a stack type sensor based on Li_3PO_4 as electrolyte, but without reference electrode material was recently produced by Choi et al. [16] and its performance tested in the temperature range 350-500 °C and CO_2 concentrations of 16-5000 ppm. The sensor showed good reproducibility and short response times of about 2-4 seconds. The Li_2O activity on the reference electrode side is assumed constant as no study is available on the alumina substrate/Li_3PO_4 interaction. However, as will be observed in this current research on the NASICON/alumina interaction, a stack sensor without reference would not guarantee a thermodynamically defined electrode with fixed Na_2O activity.

Shim et al. [17] also fabricated a stack sensor based on two materials only, NASICON and the sensing electrode, Na_2CO_3-$CaCO_3$ as shown in Figure 2.6. Despite the reported good sensing performance, such geometry is prone to EMF drifting because of the NASICON/alumina interactions and also the fact that the Pt counter electrode is at the interface. Furthermore the fact that NASICON is too exposed, the risk of degradation due to humidity is high[97].

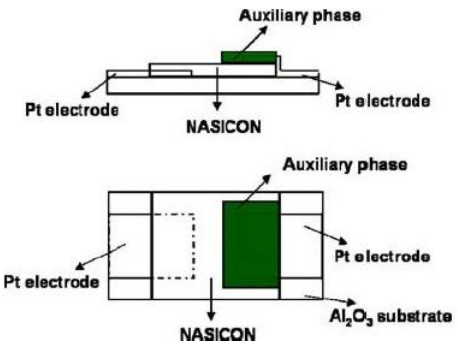

Figure 2.6 – Stack type sensor by Shim et al. [17]

Furthermore, the fact that the reference side was closed, the sensor could most likely suffer oxygen cross-sensitivity. In this research, to circumvent this problem, a layer of $CuAl_2O_4/CuAlO_2/Al_2O_3$ to fix the oxygen potential was used.

2.8.2 Quest for a Stable Sensor

2.8.2.1 Long Term Stability - Sensing Material

Long term stability of sensors is crucial to the commercializing of sensors and an important factor in the determination of practicability of the sensor device. It is in fact required that any gas sensing device should exhibit stable and reproducible signal for the period of at least 2–3 years (17 000–26 000 h) [98].

Long term stability of a carbon dioxide sensor does not only depend on the electrode composition but also on the sensor geometry (where thick carbonate sensing electrodes exhibit better stability than thin ones), thermal treatment history (stability of the sensor improved by thermal heating-up above the normal working temperature) and presence of water vapour.

In an attempt to improving sensor stability by modification of the sensing electrode material it was found that sensors based on binary carbonates $A_2CO_3{-}BCO_3$ (where A and B denote alkaline metal and alkaline-earth metal, respectively) or other oxides, exhibit much better long-term stability compared to sensors built on single carbonates[94].

$Bi_2Me_{0.1}V_{0.9}O_{5.35}$ has also been used successfully as counter electrode in a thick film sensor and showed good sensing capability in dry and humid air[99].

Carbonates such as Na_2CO_3 are usually employed as an auxiliary phase (AP) and this has been found to respond well to P_{CO_2}. The major drawback on the type of sensors which rely only on a carbonate auxiliary phase is its pronounced cross-sensitivity towards water vapour. This is because Na_2CO_3 is very deliquescent.

Efforts have been made at reducing cross interference at the sensing electrode through a careful choice of materials used at the working electrode.

Fuentes et al. [100] in their work, investigated the stability of NASICON in contact with water by impedance spectroscopy, structural and micro-structural analysis, using both dense and powder samples. Impedance spectroscopy data showed a significant decrease in ionic conductivity of dense pellets when exposed to water for more than 300 h. This is determinately one of the reasons why NASICON based sensors suffer drift after a long time.

Certain types of carbonates and filters have proved helpful. Zeolites have been used as filters at the sensing electrodes and been successful in reducing cross-sensitivity but under certain concentrations only and for limited durations. Xu et al. [101] gives a comprehensive review on the use of zeolites as filters.

Kaneyasu et al. [92] successfully demonstrated cross-sensitivity prevention using zeolites. Under continuous energizing, both the EMF and $\triangle$EMF were stable over a period of 2 years. However, after the sensor was exposed to a high humidity atmosphere in an unpowered state, the EMF decreased, but $\triangle$EMF stayed constant.

For sensors working without zeolites but using Na_2CO_3 as sensing electrode, replacing the carbonate with a binary metal carbonate system such as Na_2CO_3+ $BaCO_3$ or Li_2CO_3+ $BaCO_3$ solves the cross-sensitivity problem because they have low water solubility. Apart from eliminating water vapour cross-sensitivity, it also improves response time remarkably [48, 102, 50, 14, 103].

Miura et al. [11] describes the mechanism by which the eutectic mixture of Na_2CO_3 and $BaCO_3$ prevents cross-sensitivity of water vapour. One of the reasons is the lower solubility of $BaCO_3$ to water and that the more soluble Na_2CO_3 does not exist as a separate phase in the eutectic mixture but $BaCO_3$ is more pronounced. Furthermore, the sensor was able to work effectively (with no cross-sensitivity with water vapour nor oxygen) at temperatures greater than 450 °C .

The need for a stable sensor even below the operating temperature is also a necessity. There are reports that Na_2CO_3 in Na_2CO_3/ $BaCO_3$ mixture is too deliquescent at room temperature to survive in humid atmospheres. Once the sensor was kept switched off overnight, it lost its sensing properties almost completely [104]. It was found that the adsorbed water vapour was responsible for the dissolution of NASICON in the sensor. A sensor left for more than 3 days in humid atmosphere at room temperature was damaged irreversibly [97].

Yamazoe [104] and Kida et al. [97] also recommends that Na_2CO_3 be replaced by Li_2CO_3. This is because Li_2CO_3 is non deliquescent and that Li_2CO_3/$BaCO_3$ gave excellent CO_2 sensing properties at 450 °C as well as good stability at room temperature.

In the quest to improving the long term stability of the sensor, researchers have improved the stability of the sensor by either reducing humidity cross-sensitivity by using the binary mixtures of Na_2CO_3+ $BaCO_3$ or reducing chemical attacks of the NASICON by humidity when the sensor is not in operation mode by using Li_2CO_3+ $BaCO_3$ whereby Na_2CO_3 is replaced by Li_2CO_3. This is because Li_2CO_3 has the lowest affinity to water vapour than other alkaline metal carbonates [103]. They do not solve the two problems (prevention of chemical attack by water

vapour and cross-sensitivity) at the same time.

In the quest to producing a practical sensor, this research explores the possibility of not only preventing humidity cross-sensitivity but also long term stability by preventing water vapour chemical attacks on the sensor when the sensor is not in the operational mode. This will be through the use of eutectic phase of (Li−Ba−Na) carbonates where the carbonate of barium will be responsible for prevention of water sensitivity, lithium carbonate will be responsible for sensor stability at room temperature and sodium carbonate for sensing purposes.

2.8.2.2 Thermodynamically Stable Reference Electrode

In the case of a reference electrodes, platinum or gold are often used. However, despite their frequent use, such pure metal electrodes are not able to provide a thermodynamically well defined sodium chemical potential. For the sensors listed in Table 2.2, for both the bulk and planar sensors, in the absence of a reference electrode, fixing the activity of sodium/sodium oxide is not guaranteed and this leads to non-Nernstian behaviour or EMF drifting of sensor results. This problem may be more prominent in thick films. Use of a binary reference electrode is thus vital in the fixing of the sodium/sodium oxide potential by virtue of the Gibbs phase rule.[3] Particular reference is made to the NASICON based thick film sensor, cell 8 of Table 2.2 by Wang and Kumar [86] with no reference electrode. Without it , the sensor may not guarantee reproducibility and stability because of the need to fix Na_2O activity at the reference side. Furthermore, the fixing is dependent on the phase purity of NASICON and this is not possible in the present state. There is an incipient interfacial reaction between the substrate and NASICON

[3] **Gibbs phase rule :** $F = C - P + 2$, where F is the number of degrees of freedom of the system, C is the number of components and P is the number of phases. The constant 2 implies that both temperature and pressure/chemical potential are variables.

and this may continue at high temperature which may affect the thermodynamic stability. Even if most degradation occurs at the interface, progression up to the surface may eventually occur after prolonged high temperature use and so the thickness of the film also plays an important role. It could be observed actually that the stoichiometric make up of NASICON was far from the nominal($x = 2$) after sintering therefore the activity of sodium oxide would be different from the nominal one obtained by Kale and Jacob [48]. However, a thermodynamically well defined signal was obtained when $Na_2Ti_6O_{13}/Na_2Ti_3O_7$ or ($Na_2Ti_6O_{13}/TiO_2$) was used [12]. Sahner et al. [14] demonstrated that the sodium poor reference electrode $Na_2Ti_6O_{13}/TiO_2$ was a more promising candidate for thick films than the sodium rich reference $Na_2Ti_6O_{13}/Na_2Ti_3O_7$.

In terms of fabrication, NASICON in this device (cell 8) could only sinter at 1270 °C which is too high compared to the NASICON in this research which could sinter at 1100 °C. This offers a more economic way of sensor fabrication due to lower thermal input. Kida et al. [94] also developed a thick film sensor that contained $Li_2CO_3/BaCO_3$ as sensing electrode with no reference electrode. The sensor seems to rely on local equilibrium reactions since no chemical coupling is possible as long as the sensing electrode has no Na content. Good sensing properties have been reported but the negative side of reproducibility and drifts has not been reported. It is highly unlikely to maintain a stable equilibrium for long cycles at high temperature because of the usual NASICON/alumina interaction.

Although improvements of the thick film sensor have been reported by several research groups, mostly due to changes in material combinations, little is known on the influence of basic technological aspects in relation to the long term stability, issues to do with cross-sensitivity and drifting of EMF responses of the sensor. Modification of the planar sensor of the type of Figure 2.5, to reduce possible exposing of the reference to the sublimed Na_2CO_3 or its formation at high CO_2

concentrations is explored. Furthermore modification of stack sensor type of the form of Figure 2.6 is also made to enable fixing of the sodium/sodium oxide potential at the reference side.

Chapter 3

Experimental Methods

3.1 Introduction

This chapter will describe the synthesis procedures of the main materials used in this research as well as the experimental techniques that were used to characterise the materials. The experimental settings for all the instruments will be described.

The main aim of this research is to produce a low cost, stable and robust CO_2 sensor. Therefore, in the quest for a low cost CO_2 sensor that will be an alternative to the expensive NDIR sensor, the following was conducted.

1. Development of better and cheaper synthesis methods for material components such as NASICON and the buffer. The processes were energy efficient and considerably reduced reaction times.

2. Potential for mass production through screen printing technology opens up opportunities for miniaturisation resulting in less material usage.

This chapter will therefore describe the new synthesis method of the solid electrolyte, NASICON, and the buffer material which consists of $CuAlO_2/CuAl_2O_4/Al_2O_3$.

The sensor reference material used was the biphasic material of $Na_2Ti_6O_{13}$(NT6)/TiO_2 and $Na_2Ti_3O_7$(NT3)/$Na_2Ti_6O_{13}$. Its synthesis is also described. The techniques used to characterise the materials will described. The chapter will end with the description of the screen printing technology. Some details of techniques that are specific to a particular chapter, are provided in the relevant chapters.

3.2 Material Synthesis

This section comprises the synthesis procedures of the main materials (NASICON, $CuAlO_2$, $CuAl_2O_4$ and Sodium titanates) that were used in this research for the fabrication of the sensor. A detailed characterisation of the materials is presented in Chapter 5 and 6. Table 3.1 gives all the materials that were used in this research.

Table 3.1 – Chemicals used in the research. **TG** : Technical grade, **SLS**: Scientigic Laboratory Supplies, **SA**: Sigma aldrich, **FS**: Fisher Scientific, **AO**: Acros Organics, **FBR**: FisherBioreagents, **FB**: Fluka Biochemika, **O**: Organics

Chemical	**Source**	**Grade**	**Precursor for:**
2-Furic Acid	SA	TG	Screen Printing Paste
γ-Al_2O_3	SA	99.7	Buffer/Reference Elect.
Ammonium di hydrogen Phosphate	FB	$> 99.5\%$	NASICON
Barium Carbonate	AO	$> 99\%$	Sensing Electrode
Butyl carbitol acetate	SA	TG	Screen Printing Paste
Cu_2O	SLS	95%	Buffer
CuO	SLS	95%	Buffer
Ethyl Cellulose	SA	TG	Screen Printing Paste
Lithium Carbonate	FS	$> 98\%$	Sensing Electrode
Maltose Monohydrate	FBR	TG	NASICON
Pectin	O	TG	NASICON
Sodium Carbonate	AO	$> 99.6\%$	Sensing/Reference Elect.
Sodium Citrate	FS	$> 99\%$	NASICON
TEOS	SA	TG	NASICON
Titanium (IV) Oxide	SA	$> 99.5\%$	Reference Electrode
Zirconium (IV) Oxynitrate	SA	TG	NASICON

3.2.1 NASICON

The solid electrolyte (SE) used in this research for the sensor and thermodynamic measurements was NASICON ($x \backsimeq 2$), from the $Na_{1+x}Zr_2Si_xP_{3-x}O_{12}$ series for

which $0 \leq x \leq 3$. Sol-gel process developed in our lab was used in the synthesis of the NASICON with new precursors. A single phase was obtained in the powders at much lower calcination temperatures.

Single phase powders are important especially when there is a need for making NASICON inks for thick film applications. A single phase powder is always difficult to obtain because as the calcination temperature is increased in the quest to obtain a single phase powder, the powder starts coarsening and then sinters. There is also a problem of sodium oxide and phosphorus pentoxide sublimation at higher temperatures[43, 94] . This makes it difficult to obtain fine powders for ink making. Grinding the sintered powder is also a laborious effort. For single phase materials that are difficult to obtain in their powder form, a common practice is a sequence of pelletising the powder, sintering and grinding (and sometimes a series of sequences).

Most studies aimed at obtaining single phase NASICON have successfully done so only in sintered pellets at high temperatures and not in powder form[105, 106, 107, 35, 33]. This new procedure successfully obtained single phase NASICON powder at lower calcination temperature. Ammonium di-hydrogen phosphate ($NH_4H_2PO_4$), zirconium oxynitrate ($ZrO(NO_3)_2 \cdot H_2O$), Tri-sodium citrate ($Na_3C_6H_2O_5 \cdot 2\,H_2O$) and TetraEthyl OrthoSilicate (TEOS) were used as precursors for P, Zr, Na and Si respectively. Maltose and Pectin in the molar ratio of 20:1 were used as chelating and gelating agents respectively. For comparison, another batch was synthesised without the use of the maltose/pectin materials. This method was adapted from recent work by Wang et al[108, 109] for the synthesis of $Ce_{0.8}Gd_{0.2}O_{1.9}$ nanoparticles. Pectin is found in ripe fruits and is used by the food industry for making jelly and jam.

There is a general belief that the electronegative oxygen atom present per unit formula of maltose in each of the two glucose ring structure between C1 and C5 carbon atoms and in the C1–C4 a-glycosidic link per unit formula gains a partial negative charge. This subsequently enables chelation of the cations in the precursor solutions with the partially negatively charged oxygen atoms and are kept at a distance by the large pectin molecule consisting of 300 to 1000 monosaccharide units that forms a gelatinous matrix structure[109]. The chelating activity by maltose prevents agglomeration of crystals hence makes it possible to obtain very fine powders (nanopowders).

3.2.1.1 Synthesis

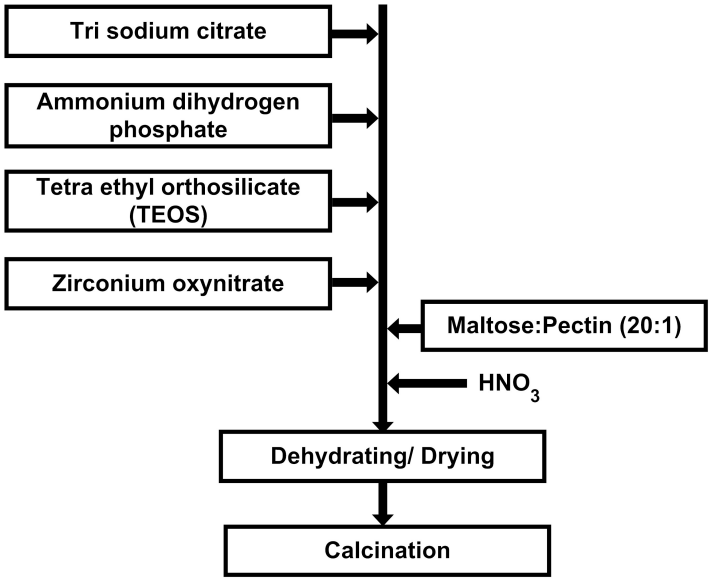

Figure 3.1 – Schematic of the NASICON synthesis

Appropriate amounts of precursor materials were weighed and dissolved in separate beakers. The volume of TEOS corresponding to the required weight was also measured. The precursors where then mixed according to the procedure schematic

shown in Figure 3.1. Nitric acid was used to control the pH at 2. After all the mixing, the mixture was stirred for an hour after which the hotplate was switched on for dehydration and drying at 100 °C for *ca* 12h.

For the batch without the use of maltose and pectin, the same procedure was followed but simply maltose and pectin were not added. In this thesis, the maltose /pectin assisted NASICON will be referred to as Malt-NASICON-T and that without, will be as-NASICON-T. The NASICON synthesised through Shimizu's procedure [107] will be denoted as simply Shimizu-NASICON.

The Malt-NASICON xerogel was brown in colour while the as-NASICON was yellowish. See Figure 3.2.

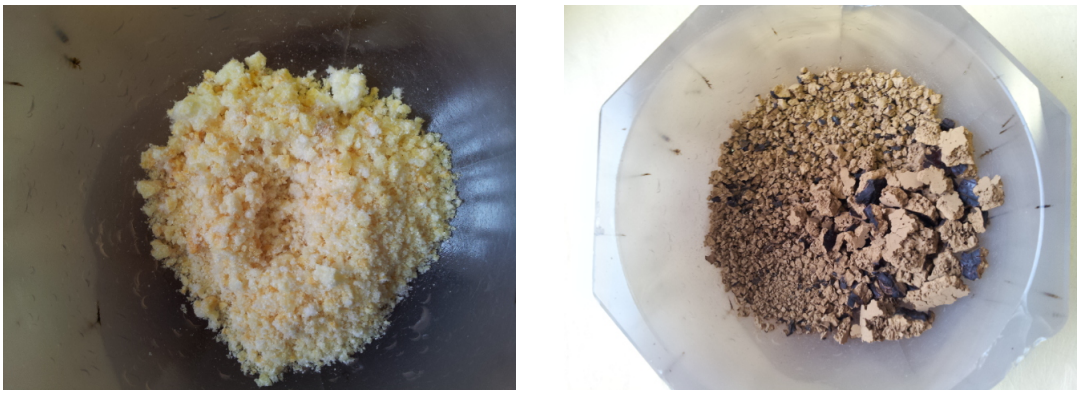

(a) as-NASICON-T **(b)** malt-NASICON-T

Figure 3.2 – Synthesized NASICON xerogels

The powder was then analysed for its weight losses and heat flow as a function of temperature using the TGA and DSC measurements and the calcination temperature determined thereof. The powder was then pressed into pellets uniaxially using a load of 5 kN and then isostatically pressed to a pressure of 300 MPa. The pellets where then sintered from 1000-1250 °C for 3-12h. Sintering of pellets was done on alumina tiles. Firstly, powder of the same material was placed on the tile to act as sacrificial material to prevent any potential reaction between

NASICON and alumina. The pellet was then placed on top of the sacrificial powder, then covered completely with the powder of same composition and finally the whole material (powder and pellet) were covered with an alumina lid. This was also to prevent any volatisation of Na_2O and P_2O_5 which easily occurs at high temperatures[43, 94].

XRD and HTXRD was conducted on both the powder and pellet to investigate the evolution of crystallinity and phase transition respectively using the X'Pert PANALYTICAL. SEM/EDS was conducted using the LEO 1530 FEGSEM and HITACHI SU8230 Cold FE - SEM while the conductivity measurements by AC Impedance spectroscopy was performed using the Solartron 1260. For dilatometric studies, sintered pellets using a 5 mm bore diameter steel die were used.

3.2.2 Cu-Al-O

For the fabrication of the multilayer sensor, a ternary phase of $CuAlO_2$, $CuAl_2O_4$ and γ/α-Al_2O_3 (denoted as Cu-Al-O in this research) was used as buffer to fix the oxygen potential at the reference electrode. The synthesis of copper aluminate has always been done after prolonged hours of calcinations and grinding, and sometimes repeated calcinations. However in this work we report a procedure where $CuAlO_2$ was obtained at a much lower temperature and in short reaction time using the conventional method of reacting Cu_2O and Al_2O_3 and calcining at high temperature. A phase pure powder was obtained as will be seen from the XRD patterns. The process involved milling precursor binary oxides, powder pelletising, isothermal firing under argon and quenching.

3.2.2.1 $CuAlO_2$

Thermodynamics considerations

From the Al_2O_3 - $\frac{1}{2}Cu_2O/CuO$ phase diagram by Jacob and Alcock [110], the upper temperature stability limit of the $CuAlO_2$ phase is 1160 °C at $P_{O_2} = 0.21$ atm. This means that the reactions (formation of CAO) can only be carried out at temperatures below 1160 °C. Considering the fact that the melting points of Cu_2O and Al_2O_3 are 1232 °C and 2072 °C respectively and, the absence of the eutectic below 1160 °C in the Al_2O_3- Cu_2O system, the formation of the $CuAlO_2$ phase is a solid state process. Since solid state reactions occur via diffusion of the cations, a higher temperature is required to enhance the diffusion. The calcination temperature of 1150 °C was therefore selected and gave the shortest reaction time.

Synthesis

Appropriate amounts of precursor oxides, Cu_2O and γ-Al_2O_3 , were weighed and mixed in a plastic milling jar. The mixture was according to the reaction in Equation (3.1)

$$Al_2O_3 + Cu_2O \rightarrow 2\,CuAlO_2 \tag{3.1}$$

Zirconia balls and isopropanol were used as milling media. The precursor powders were then milled overnight for convenience. After milling, the slurry was dried into homogeneously mixed powder. The powder was pressed into cylindrical pellets at loads of 1, 4 and 8 tonnes using a 13 mm diameter uni-axial steel die. This was meant to bring the reacting particles in intimate contact with each other

for easy reaction. The samples in the form of loose powder and pellets were isothermally[1] calcined at various temperatures of 1000, 1050, 1100, 1125 and 1150 °C for different durations ranging $10 \leq T \leq 180$ minutes under a flowing argon environment to prevent oxidation of Cu_2O. After firing the samples were removed from the furnace and cooled under the cover of a graphite crucible so as to prevent any possible oxidation of Cu^{+} to Cu^{2+} in the reacted products. The schematic of the process is shown in Figure 3.3

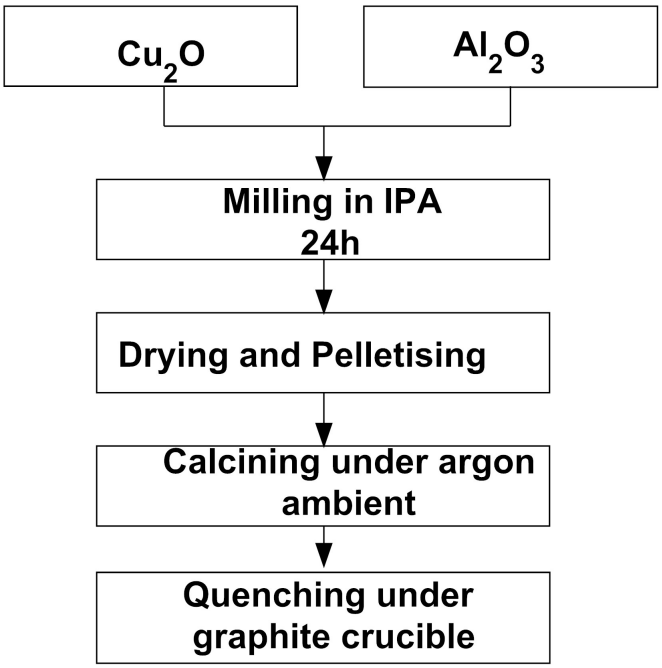

Figure 3.3 – Schematic of the synthesis process of the delaffosite cuprite $CuAlO_2$

Figure 3.4 is an image of the blue-greyish powder of $CuAlO_2$.

[1]**Isothermal** firing is when the sample is placed in the already hot furnace at that target temperature and then removed from the furnace at the same temperature.

Figure 3.4 – An optical image of the $CuAlO_2$ powder obtained during the synthesis.

For electrical characterisation, the sample that obtained pure phase pure powder was pelletized uniaxially by pressing under a load of 5 tonnes and sintered in air at 1150 C for 6 h.

Platinum ink was painted on the parallel sides of the pellet as electrode contacts and cured at 800 C for 30 minutes. The sample was spring loaded in a quartz assembly placed inside a Faraday cage within a horizontal tube furnace during the AC/DC electrical measurements. The DC conductivity measurements were conducted using a Hewlett Packard 34420A NanoVolt/Micro Ohm meter and AC conductivity measurements using a Solartron Instrument 1260. For phase analysis and reaction kinetics, XRD was used. This was first done by grinding the samples to fine powder and then analysing them using a P'Analytical X'Pert MPD ((using Cu - K_α) in a spinning mode. Morphological features and EDS scans (for chemical composition) were obtained using a LEO Gemini 1530 FEGSEM.

3.2.2.2 $CuAl_2O_4/CuAlO_2/Al_2O_3$

To prepare the multi-phase buffer system, delaffosite copper aluminate $CuAlO_2$ and γ-Al_2O_3 were weighed appropriately and mixed using a mortar and pestle until the powders were homogeneously mixed. It was then isothermally calcined

at 1150 °C for 3 h and quenched in air. XRD was then conducted on the powders to confirm the phases.

The resulting mixture was found to contain $CuAlO_2$, $CuAl_2O_4$ and the excess α-Al_2O_3 which is basically the system needed for buffering of the reference electrode according to the equilibrium reaction (7.5)

$$4\,CuAlO_2(\text{delafossite}) + 2\,Al_2O_3(\text{corundum}) + O_2(g) \rightarrow 4\,CuAl_2O_4(\text{spinel}). \quad (3.2)$$

3.2.3 Na-Ti-O

Biphasic mixtures of $Na_2Ti_6O_{13}/TiO_2$ (NT6-TiO_2) and $Na_2Ti_3O_7/Na_2Ti_6O_{13}$(NT3-NT6) were used as reference electrodes for the sensors in this research. Single phases of $Na_2Ti_3O_7$ and $Na_2Ti_6O_{13}$ were prepared by mixing appropriate molar amounts of TiO_2(Anatase) and Na_2CO_3 and, milling them in isopropanol using zirconia balls overnight. The slurry was then retrieved and dried. The dried powder mixtures were calcined in air at 950 °C for 6 h. The calcined powders were then appropriately mixed into biphasic powders, pelletised and sintered according to the details in Table 3.2. These pellets were then used for thermodynamics measurements as working electrodes. The remaining portion of powders was used to make pastes for thick film printing.

Table 3.2 – Sintering temperatures of pellets of NT6, NT3 and the biphasic mixtures

Sample	Ratio	Sintering (°C)
		Pellets
NT6-TiO_2	1:6	1050/2 h
	1:1	1050/2 h
NT6-NT3	1:2	1000/2 h
NT6	-	1050/2 h
NT3	-	1000/2 h

3.3 Experimental Techniques

3.3.1 X-Ray Diffraction (XRD)

XRD is a valuable characterisation technique commonly used for the analyses of solid materials, whose results enables the calculation of lattice parameters as well as identification of crystal phases[2] through comparing with known standards such as the JCPDS-ICDD standards. It uses X-rays as the probing source.

3.3.1.1 Operation

X-rays of a specific wavelength are produced from a target, in our case, a copper target and produces X-rays radiation (Cu - K_α) with a specific wavelength of 1.54178Å. A collimated beam of X-ray is directed on the sample of which some are reflected and some diffracted. To change the angle of incidence of X-rays on the sample, depending on what instrument is being used, the sample may be fixed

[2] **Phase** denotes atomic structure as well as chemical composition.

and the diffraction angle (2θ)is obtained by rotating the X-ray source and the detector at angle θ, in the opposite directions as shown in a schematic of Figure 3.5. In some instruments however, the sample may be fixed and the diffraction angle (2θ) is obtained by rotating the X-ray source and the detector at angle θ, in the opposite directions. In our lab its the former setup that was used.

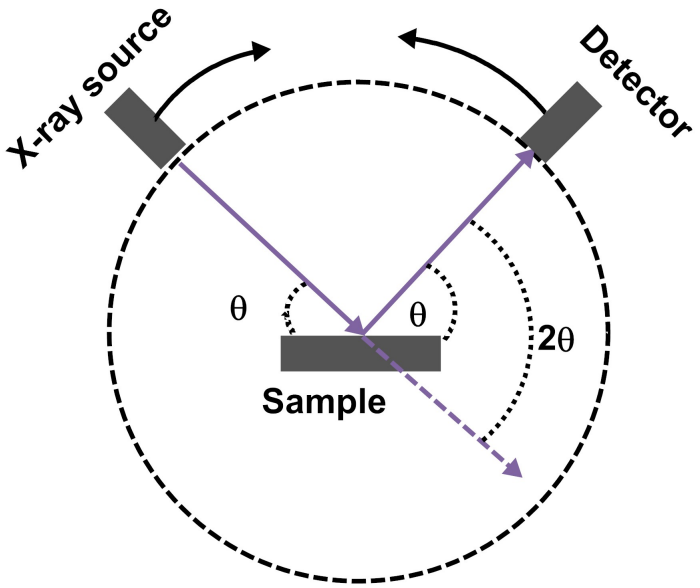

Figure 3.5 – XRD sample configuration.

A crystalline material will always have planes which will diffract the X-rays and the diffraction pattern depends on the crystal structure of the sample and the wavelength of the X-ray source. Each set of parallel planes has a definite spacing called the $d-$spacing. The diffraction is a constructive interference of the radiation from successive planes and occurs when the path difference is an integral number n of wavelengths ($n\lambda$). This diffraction happens at a unique angle and hence the angle and sometimes the intensity becomes the signature of that crystalline material. The Bragg condition is illustrated in Figure 3.6. Bragg's condition for

diffraction therefore is

$$n\lambda = \alpha + \beta = 2d\sin\theta \tag{3.3}$$

where θ is the angle of incidence, λ is the wavelength of the X-rays and n is a positive integer value of the wavelength that fulfils constructive interference.

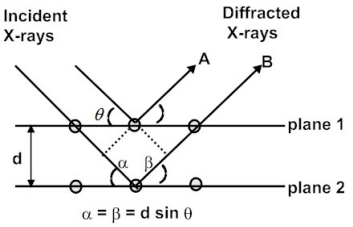

Figure 3.6 – Schematic representation for the Bragg condition on a crystal structure

For macro crystalline materials, because of the presence of numerous planes which are all diffracting the X-rays, a sharp and intense peak is recorded. Conversely for nanocrystalline materials, however, the intensity recorded is very low but broad.

This is because of the statistical nature of the counts, the area under the peak should always be constant therefore the peak in nanocrystalline material is always broad while in the macro crystalline materials it is sharp and intense.

3.3.1.2 Experimental Setup

The instrument used in this research was the MPD X'Pert PANALYTICAL with (Cu - $\mathbf{K}_\alpha$) X-Rays of wavelength of 1.54 Å produced from an acceleration voltage of 40 kV and current of 30 mA. This is capable of operating in both ambient and non ambient environments. Non ambient XRD was performed for high temperature XRD while ambient was for normal XRD at room temperature.

Different shapes such as pellets and screen printed materials could be loaded and analysed using a bracket sample holder. Powders on the other hand were analysed on a round steel sample holder. The powder was firstly compacted and leveled in the sample holder before it was put in the machine. The machine in this mode works under a spinning mode where the sample holder is rotating so that every crystal on the sample is accessed by the X-ray beam. The step size of $2\theta = 0.0334225°$ and time per step of 50 s. The results were stored in digital format and analysed using the HighScore Plus software loaded with the ICDD database.

3.3.2 Scanning Electron Microscopy (SEM) and Energy Dispersive X-Ray Spectroscopy (EDS)

Scanning electron microscopy is a powerful characterisation tool in the analysis of morphological features of materials. As the name suggests it operates by focusing a beam of electrons instead of light on a sample. The SEM uses electromagnetic lenses to form a focussed image of the electron source. This fine probe of energetic electrons is scanned over a small area across the sample and one of a number of possible signals arising from the electron-specimen interaction (i.e.; backscattered electrons, secondary electrons, photon emission, auger electrons, etc.) are detected and amplified[111]. Depending on what information is being sought for, an appropriate detector is used. In this research, secondary electrons (SE) for imaging, backscattered electrons (BSE) for elemental imaging/mapping, and photon emission for EDS and for chemical composition analysis will be used.

3.3.2.1 Experimental Setup

The imaging was conducted using either the LEO Gemini 1530 field emission scanning electron microscope(FESEM), Carl Zeiss Evo MA 15 SEM (Germany) and HITACHI SU8230 Cold FE- SEM (Japan). These are equipped with simultaneous SE/BSE and EDS imaging. Sample preparation involved polishing samples ([embedded in 3 parts epoxy resin + 1 part epoxy hardener] or not) sequentially on silicon carbide (SiC) paper of grits P600, P800, P1000, P1200 and P2500 on a rotary polishing machine with flowing water. For NASICON, water was not used because of a possible reaction with water. Before a sample was placed on the metal stub, an electrical conductive carbon sticker was placed on the stub after which the polished sample was stuck on the sticker. This was then e-beam deposited with a 5 nm Pt coating to prevent charging due to the high density electron beam. Aztec or INCA software (Oxford Instruments) was used to analyse the EDS results.

3.3.3 Electrical Characterisation

3.3.3.1 AC Impedance Spectroscopy

Two and four point probe direct current (DC) electrical measurements are the commonly employed techniques for studying electrical properties of materials. However, regarding the characterisation of electroceramics, these techniques are not able to resolve electrical processes from intergrain and intragrain contributions.

Despite attempts by several researchers[112, 113] to measure these contributions using miniature electrodes the technique is quite complex to implement experimentally.

An alternative method that is able to resolve the processes is AC impedance.

The measurements are made over a wide range of frequencies(several millihertz to several megahertz) and the different regions of the material are characterized according to their electrical relaxation times or time constants. In this way contributions from grains, grain boundaries and electrodes can be deduced[114, 115].

The interpretation of the resulting spectra is aided by analogy to equivalent circuits involving simple components such as resistors and capacitors. In general, such equivalent circuits are not unique, and indeed there exists an infinite set of circuits that can represent any given impedance but a common practice is to select a physically plausible circuit containing a minimal number of components and assign physical significance to the derived parameters[116].

This is achieved by applying an alternating potential across a sample resulting in a current that is out of phase. This is repeated stepwise with frequency. Dividing this voltage by current gives impedance. This is a complex vector quantity which is specified in imaginary and real components as given in Equation (3.4).

$$Z(\omega) = Z'(\omega) - jZ''(\omega) \tag{3.4}$$

where Z' is the resistive component of the sample while Z'' is the reactive component. The complex plane is shown in Figure 3.7 where it is presented in the form of imaginary, Z'' (capacitive) against real, Z' (resistive) impedance.

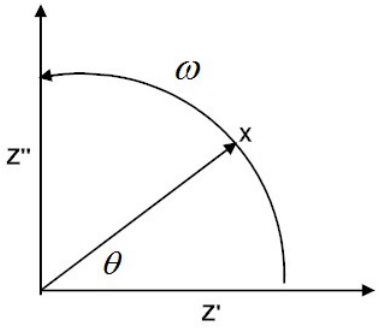

Figure 3.7 – Impedance in the complex plane.

As the frequency is swept from low to high, the locus X, which is a complex impedance sweeps a semicircle. Whenever a semicircle is observed in polycrystalline materials, the modeled circuit contains at least a resistor and a capacitor connected in parallel. When several semicircles appear, it is either contributions from intergrain , grain boundary, electrode effects or the material is multiphase. However, to distinguish if it is due to a second phase, a plot of modulus[3] against frequency is used to resolve the two contributions[115]. A schematic of the Nyquist plot showing possible contributions from the circles is given in Figure 3.8

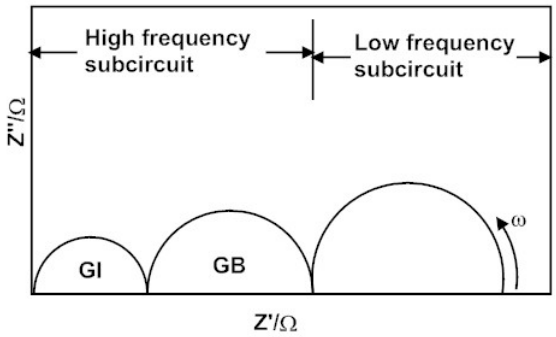

Figure 3.8 – Schematic of Nyquist plots of an ionic conductor

From Figure 3.8 the first high frequency semicircle is due to contribution from grain interior (GI), the second arc is the space charge contribution due to grain

[3]**Modulus** is a quantity that describes the dielectric relaxation of ions in the material

boundary(GB). If there is no space charge, the two arcs will combine into a single arc. The third arc may be due to electrode effects[116]. Each parallel RC element represents a semicircle (in an ideal case) from which the component R and C values may be extracted by curve fitting. R values are obtained from the intercepts on the Z' axis, while C values are obtained from; $\omega_{max}RC = 1$, where ω_{max} is the frequency at the maximum of each semicircle. Shapes of plots vary greatly with circuit elements. Sometimes, a quarter circle with a 45° can be observed instead of a semicircular arc. This represents a Warburg impedance which is an electrical analog of a diffusion process [41].

Since fast ion conductivity is a necessity for a sensor electrolyte, the determination of ionic conduction in a solid electrolyte is important before it can be applied in sensor fabrication. Normally when a sample is connected to the AC impedance analyser, it is connected with wires. Therefore the overall impedance is a sum of complex impedance contribution from the wires ($Z_{wire}(\omega) = R + i\omega L$), sample electrode interface ($Z_{SEI}(\omega)$) and complex impedance from the sample($Z_{sample}(\omega)$) so that $Z = Z_{sample}(\omega) + Z_{wire}(\omega) + Z_{SEI}(\omega)$ where R and L are the wire resistance and inductance respectively. To calculate the conductivity, the cross-sectional area S (may be in cm^2) of the pellet should be known as well as the thickness t (may be in (cm). The ionic conductivity is therefore given as $\sigma = t/(RS)$. The units are $1/\Omega$.cm or Siemens/cm (S/cm).

A detailed description of the theory behind impedance spectroscopy is found in various books and papers [117, 114, 115, 21].

Important for ionic conduction is the activation energy[4]. The lower the activation energy E_a the easier it is for the ion to migrate from one site to another. This is estimated from the Arrhenius equation showing the temperature dependent

[4] **Activation energy** is an energy barrier that the charge carrying ions must overcome to conduct through the material.

conductivity in Equation (3.5)

$$\sigma = \frac{\sigma_o}{T} \exp\left(-\frac{E_a}{kT}\right) \tag{3.5}$$

where σ is the ionic conductivity, T is the absolute temperature, k is the Boltzmann constant and σ_o is the pre-exponential factor. When $\log \sigma T$ is plotted against $\frac{1}{T}$, a linear graph is obtained with slope $-E_a/k$. From this the activation energy is obtained.

3.3.3.2 Experimental setup

Samples for impedance impedance measurements were prepared by lightly abrading the parallel surfaces of the sintered pellets sequentially with silicon carbide papers with grits P600, P800,P1200 and P2500. Platinum ink was painted on the parallel sides of the pellet as electrode contacts and cured at 800 °C for 30 minutes. The sample was spring loaded in a quartz assembly placed inside a Faraday cage within a horizontal Lenton LTF1200 tube furnace. A type-K thermocouple was inserted at the point of measurement to monitor the precise temperature of the sample. The platinum leads were then connected to the Solartron 1260 impedance analyser which was connected to the computer and controlled by the Scribner Zplot software. A schematic representation of the quartz assembly is shown in Figure 3.9;

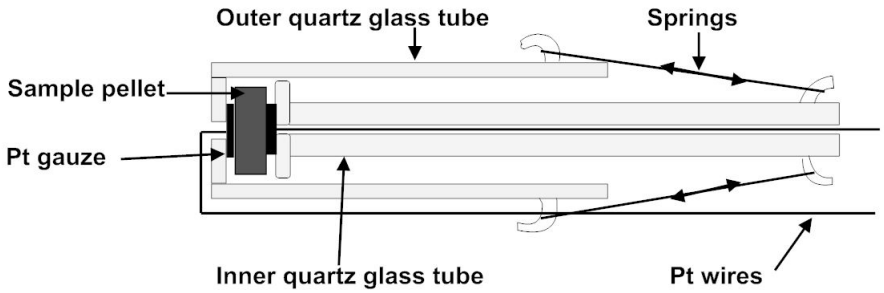

Figure 3.9 – Rig assembly for impedance measurements.

The measurements were performed in an air ambient and over a range of temperatures. To check the reproducibility of the results, the measurements were taken on both decreasing and increasing temperature runs. Measurements were only performed after the temperature had stabilized.

The rig for the electrical measurements of thick films was simple. Lead platinum wires were inserted into a two bore alumina tube, and then connected to the sample on the other end. Tube was then tied parallel to the outer tube of Figure 3.9 for support. On the other end, the two wires were connected to the impedance analyser for measurements. The measurement parameters are in Table 3.3;

Table 3.3 – Measurement parameters for the Solartron 1260

DC Potential	0.1 V
AC amplitude	50, 100 mV
Frequency range	$0.1 \leq f \leq 32 \times 10^6$ Hz

3.3.3.3 EMF Measurement - Thermodynamic and Sensor Measurements

The study of thermodynamics of materials in terms of chemical stability through the determination of chemical activities of oxides used in this research was conducted through the measurement of EMFs generated in the constructed galvanic cells. Sensor signals were also measured as EMFs therefore a reliable EMF data acquisition system was needed. LabVIEW[5] programming language was used to develop an inhouse acquisition program (application) that interfaced with the Keithley 6517A to acquire the data. The cell electrodes were connected to Keithley electrometer which digitized the data and LabVIEW which sat on the computer ensured real time data reading and display.

3.3.4 Thermogravimetric Analysis/ Differential Scanning Calorimetry (TGA/DSC)

TGA and DSC are techniques used for thermal characteristics of materials. TGA measures weight loss or gain of a sample as a function of temperature. With is technique(TGA), a sample is heated under a flowing gas or synthetic air with constant heat rate while the relative difference of the mass during this process is measured. The TGA trace will then appear as steps and a mass loss will indicate a degradation of the measured substance taking place. Sometimes a mass gain is observed when there is a reaction of the sample with oxygen from the synthetic air. To clearly identify the temperature of mass change the derivative of TGA curve with respect to temperature to obtain peaks is usually used.

DSC measures heat flow difference between the sample and a reference. Normally,

[5] **LabVIEW** (**L**aboratory **V**irtual **I**nstrument **E**ngineering **W**orkbench) is a system-design platform and development environment for a visual or graphical programming for the purpose of creating custom applications that interact with real-world data or signals.

temperatures of the sample T_s and reference pan T_r are measured. Depending on the temperature difference between T_r and T_s heat is supplied to either pan in order to balance the temperatures. This additional heat is supplied by the filament of resistance R close to the sample pan or reference pan, by joule heating. The additional power $P(t)$, also equal to the heat flux is given as $P = i^2R = \frac{dQ}{dt}$ where $i(t)$ is the filament electric current[118]. The heat flux is also equal to the enthalpy flux, which gives the typical DSC measurement curve.

By measuring the difference in heat flow rate (mW = mJ/sec) between a sample and inert reference as a function of time and temperature thermal critical points like, enthalpy specific heat, melting points or glass transition temperature of substances can be determined. Depending on whether the process is endothermic or exothermic, a peak will be observed. Endothermic peaks are heat flow into the sample from processes such as heat capacity (heating), glass transition, melting, evaporation while exothermic peaks are due to processes that allow heat to flow out of the sample such as heat capacity (cooling) or crystallization, cure, oxidation, etc [119].

3.3.4.1 Experimental Setup

About 3-5 mg of powder sample was placed into an alumina crucible for TGA/DSC measurements. The measurements were performed using the Mettler Toledo STAR system (Mettler-Toledo LTD, Leicester, UK). The machine did simultaneous measurements of TGA and DSC under a flow rate of 50 mL/min of air and a heating rate of 3 °C/min. The scan range was from 30 to 850 °C.

The simultaneous measurement of TGA and DSC ensures that the test conditions are perfectly identical for both signals from TGA and DSC that is, same atmosphere, gas flow rate, vapor pressure on the sample, heating rate, thermal contact

to the sample crucible and sensor.

3.3.5 Dilatometry

This is a thermo-analytical method for measuring the shrinkage or expansion of materials over a controlled temperature regime to monitor the progress of chemical reactions, particularly those displaying a substantial molar volume change or structural change. With dilatometry processes such as phase transition and sintering temperature and shrinkage steps can be measured. It can also be used to measure thermal expansion and the coefficient of thermal expansion.

3.3.5.1 Experimental Setup

To prepare samples for dilatometry measurements pellets of diameter 5 mm were pressed, sintered and coated with Pt paint. The pellets were then fired at 850 for 30 min to platinize the paint on the pellets. It was then placed between the electrodes of the Horizontal Linseis Dilatometer L76/L75H.

3.4 Thick Film Technology

3.4.1 Introduction

The electromotive force of an electrochemical cell has a special property called an intensive property which, like temperature and pressure is independent of the geometry and size of the cell[120, 121]. Because of this, it opens up potentialities for miniaturization to bring down the cost of production of the sensor. This is achieved by screen printing[6] technology whose process can not only guarantee

[6] **Screen printing** is a stenciling technology used to print inks onto flat substrates.

mass production but also massive material savings. This is because the amount of material that is used for the sensor is extremely low, whereby a sensor can be only 50 microns or less in thickness. Extra details of the art of screen printing is found elsewhere [120, 122].

3.4.2 Essential features of screen printing

There are three essential features of a screen printer that makes the screen printing of inks on substrates successful. These are: the screen, squeegee and substrate. It uses squeegees to force the paste/ink through an mesh artwork prepared on the screen. When a squeegee makes a stroke the ink is deposited on the flat substrate underneath.

3.4.2.1 Screen

This basically comprises three components; a stencil which defines the artwork to be printed, a mesh which supports the stencil, and then a frame which supports the mesh. These are described below.

Stencil

This is the artwork which defines what is to be printed on the substrate. Furthermore, apart from defining the artwork of the print, the stencil also has a major influence on the thickness of the film, that is, the thicker the stencil the thicker the print to be.

Frame

Screen frames that are always used for thick film printing are made of metal and usually of aluminium alloy. Plastic frames as well as wood frames may be common in industrial and fine art screen printing but they have cons of not being sufficiently stable for thick film applications.

Mesh

The mesh supports the artwork. The thread in the mesh are normally aligned at 45°. The mesh is usually made of nylon, stainless steel or polyester. The choice of which one to use depends on the pros and cons of the material and if it will be heavy duty printing or not.

Mesh that is made of nylon is strong and resilient but it has disadvantages of being unstable in humidity and temperature changes.

Polyester mesh on the other hand is more flexible and stable than nylon. This is the commonly used mesh for industrial printing as well as thick film printing.

Lastly but not the least, stainless steel mesh is more stable and much stronger. Despite being less susceptible to wear and being elastic, its elastic limit is low hence it is easily damaged subsequently lowering its lifespan because it is usually accidentally damaged long before it is worn out.

3.4.2.2 Squeegees

These are part of the screen printer that press the screen into contact with the substrate thereby by pushing down the paste into the stencil and onto the substrate that is placed underneath. Squeegees are flexible in nature to compensate for possible printing on irregular substrates. The squeegee should be immune to

chemical attacks from the pastes therefore the universal material used for making squeegees is polyurethane[120, 122].

Squeegees come in two design forms; the diamond squeegee (which was used in this research) and the trailing edge squeegee. Figure 3.10 is a schematic of the two types of available squeegees.

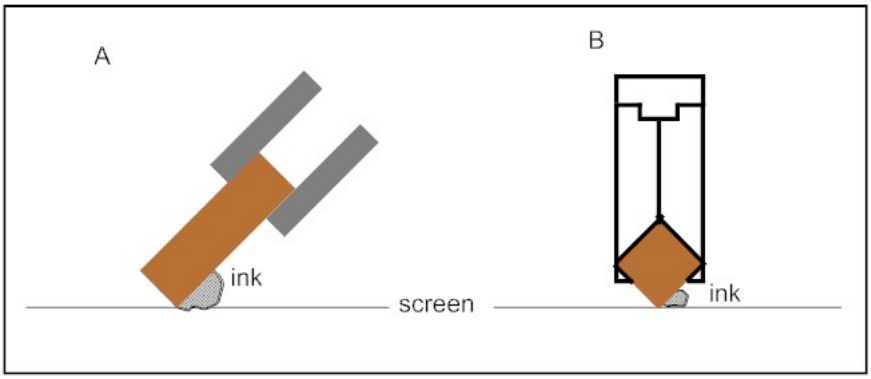

Figure 3.10 – Types of squeegees. (A) Trailing edge squeegee, (B) Fixed angle diamond squeegee.

Both of these present an angle of attack[7] of 45° to the screen, and this has been found to be optimum angle for a successful shearing of a paste on the screen: too vertical a squeegee ($> 45°$) will fill the aperture very inefficiently, too shallow an angle (< 45 °) will not perform the shearing action completely and leads to poor thickness control. An advantage over the use of a diamond squeegee is that once one edge is worn out, it can be recycled by using the other three edges by just flipping the squeegee by 90°.

3.4.2.3 Substrate

Substrates provide a base onto which all thick film devices/layers are fabricated. Substrates can be ceramics such as Al_2O_3, AlN and BeO and metal substrates

[7] **Angle of attack** is the angle between the substrate surface and the leading edge of the squeegee that controls the transfer of material to the substrate.

covered with an insulator layer [122].

However, the commonly used substrates which are best suited for thick film substrates are alumina ceramics consisting of $94 - 96\%$ Al_2O_3 because of their good adhesive properties to fired thick films.

3.4.3 Operation

The process of thick film layer preparation involves screen printing, film settling, drying and firing. The whole purpose is to have a uniform print in terms of thickness and position. The film thickness must be controlled for reproducible results in electrical properties while the print position must be precise in order to align the prints in desirable positions. This is especially very important when multilayers are desired.

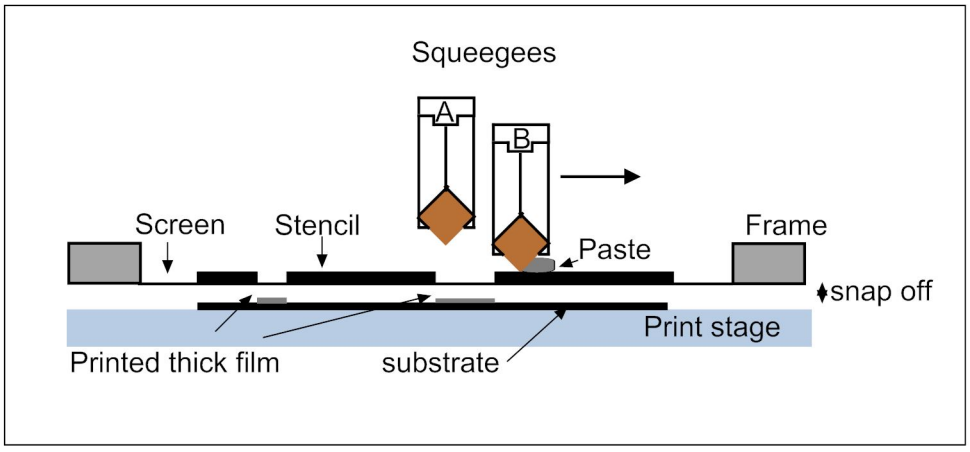

Figure 3.11 – Art of screen printing.

Table 3.4 is a table of parameters which affect print thickness but some may not be a means of controlling the thickness during printing. However, the viscosity and the snap off can be adjusted.

Table 3.4 – Thickness control. For a thinner print these parameters apply.

Parameters		Level
Snap off		low
Viscosity		low
Squeegee	pressure	high
	speed	low
	angle	high
	wear	low
	hardness	high
	room temperature	low

The screen printing process starts by fixing the screen on the printer and the substrate fixed firmly on the print stage by means of an adhesive tape or a vacuum suction. When print button is pressed, the sharp edge of squeegee pushes the screen to the substrate. As the squeegee travels across the screen, it forces the paste through windows of the artwork onto the substrate. Besides rheological characteristics of the ink, with viscosity topping the list, the following technological operating parameters have an influence on the production:

- Snap off distance (the screen-to-substrate distance) usually $0.35 - 1$mm
- attack angle usually $45°$
- squeegee velocity - printing speed of about $5 - 20$ cm/s
- elasticity of the screen which depends on the type, sizes and tension. Stainless steel mesh was used in this research.

- The above technological parameters can be adjustable to achieve reproducible results because the process applies semi-automatic or automatic equipment. In this research the MOD C380 semi automatic screen printer was used.

Apart from using squeegee parameters laid out in Table 3.4 to control the thickness, an alternative way of controlling thickness was employed by controlling the snap off distance. A pattern is first printed, dried and then the stage is lowered to increase the snap off distance. A second printing cycle on the same print is performed. Depending on the range of thickness required, multiple printing cycles can be used. The limitation to this is the difficulty in printing a precise thickness. Caution is taken against snap off distance being too low as the screen may get stuck to the paste/substrate.

The second step after printing is the settling period. The printed substrate is retrieved from the printer and placed on a flat surface for settling. This will also allow some mesh marks to close up leaving a smooth and shinny print. Various periods of settling are necessary before the actual drying is induced. Depending on the viscosity of the pastes at room temperature, this period can be $10 - 30$ minutes long. The settling time for the prints in this research was 10 minutes.

The next step is the drying process to fix the print on the substrate and to remove volatile solvents from the deposit before furnace sintering. After the drying process, it is sintered to permanently fix it on the substrate as well as ensure a densified film. This is usually done at $75 - 150$ °C for $15 - 60$ minutes.

Finally the drying step is followed by the key process of the thick film technology that is the furnace firing. Firing is to ensure densification of the powder and mechanical lock between the film and the substrate.

Sometimes additional layers can be printed on the dried substrates before firing is done. This is done provided the layers are stable at the firing temperature

of the subsequent layers that are of different chemical make up. However the rule of thumb is that if more different layers are to be printed on top, after each printed layer the firing temperature is reduced as you go up the layer, i.e $T_{\text{top layer}} \leq T_{\text{bottom layer}}$ where $T_{\text{top layer}}$ and $T_{\text{bottom layer}}$ are firing temperatures for the top and bottom layers respectively. This is to ensure no inadvertent interface reaction or melting takes place in the bottom layers.

3.4.4 Ink/paste Making

Thick film pastes used in thick film printing technology are colloidal systems. They comprise three main componets; the functional phase (powder of material to be deposited), the carrier (organic solvent systems and plasticizers) which gives dispersion characteristics and the binder which gives the desired printing characteristics such as wetting and adhesive properties.

In this research, the following were the precursors of the formulation; Butyl carbitol acetate (BCA) chemically known as Diethylene glycol n-butyl ether acetate (boiling point: 245 °C) which acted as the carrier and dispersant, Ethyl cellulose + Furoic acid which acted as binder while Aceteone was used as a diluent.

Use of BCA was chosen because it has superior dispersion stability, good balance of volatility and solvency, excellent film formation, good coalescing efficiency and slow evaporation rate. Sometimes glass frits are added as binder in some formulations, which melts upon firing for adhesive properties, however, in this formulation, ethylcellulose does give the binding properties well right up to the firing stage.

Procedure

To prepare screen printing pastes meant for the screens, each functional powder was first milled in isopropanol alcohol (IPA) overnight to obtain fine powder. The slurries were dried to form the powder and the powder was further sieved under a 7 micron sieve. The respective powders of NASICON, reference electrode (NT6 + TiO_2 and NT6 + NT3), oxygen buffer (Cu-Al-O), and sensing electrode slurries involved a mixing of the respective active powders with the organic solvents and vigorously mixing them using a metal spatula in plastic mixing bowl or beaker. This formulation is adapted from Wang and Kumar [86]

Firstly the functional powder was mixed with the BCA in the appropriate ratio followed by mixing vigorously. When a homogenous mix is obtained, furoic acid (FA) and ethyl cellulose (EtC) were added to the homogenous mixture and mixed slowly to ensure complete dispersion. The mixing was continued until all ethyl cellulose particles were disolved and the slurry was smooth. The slurry was diluted with acetone when necessary to control the viscosity.

The solid loading of the functional phase powder was 55.8%. Table 3.5 shows the mixing mass ratios of precursors.

Table 3.5 – Mass ratios of paste precursors.

	Functional powder	**BCA**	**FA**	**EtC**
Mass ratio (g)	1.501	1.00	0.058	0.132

Obtaining the correct rheology in inks is vital in order to have a homogeneous print. Viscous pastes do not settle the deposited prints sufficiently and this leaves mesh marks of the screen which is a source of film inhomogeneity. In this research, the paste viscosity was controlled by adding extra required amounts of acetone.

3.4.5 Printing

The artwork for the stencil was produced using the SolidWorks2012 software. This was then sent to the screen manufacturers for fabrication. The printing was performed at the ambient temperature of about 20 °C. An Aurel Model C890 semi automatic screen printer was used with a double diamond squeegee for back and forward double stroke printing. Figure 3.12 is the screen printer.

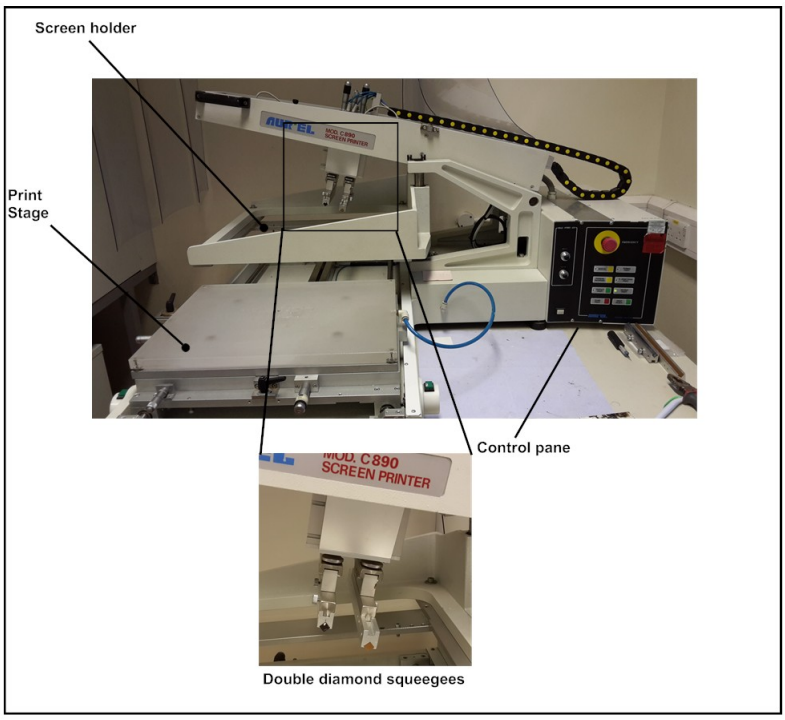

Figure 3.12 – Aurel MOD C890 screen printer that was used to print the films. The essesntial parts can be clearly seen.

Before the printing, the substrates were cut into desired square pieces of dimensions of 1.5 cm x 1.20 cm using a diamond scribe. They were then sequentially sonicated in distilled water, acetone and distilled water again to remove all the dirt and oils. The whole printing process and parameters are shown in Figure 3.13.

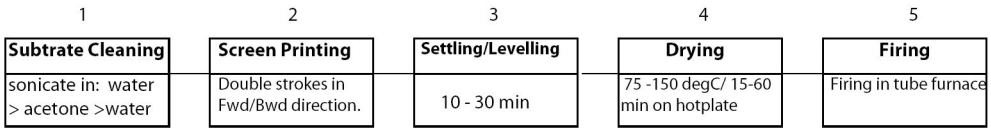

Figure 3.13 – Screen printing process.

Details of the pastes, printing and sintering conditions are given in respective sections of the upcoming chapters.

3.5 Summary

This chapter was about the synthesis of the main materials used in this research. New synthesis procedures were developed for NASICON and the buffer (Cu-Al-O). The techniques used to characterise these materials were also described. Lastly, thick film screen printing technology was described as well as how the inks/pastes were made and printed. The results from the characterisation of the materials are described in chapters 4, 5 and 6.

Chapter 4

Materials Characterisation I - NASICON

4.1 Background

The previous chapter presented the synthesis procedures of materials used in this research as well as the characterisation techniques used to characterise these materials. This chapter will report on the characterisation of NASICON while the next chapter will report on the characterisation of reference systems (Na-Ti-O) and the buffer components(Cu-Al-O).

In this characterisation, powders and bulk samples in the form of pellets of NASICON were analysed. Finally, since the ultimate device is a planar sensor, characterisation of screen printed thick films on alumina substrates were conducted. Possible interfacial reactions are revealed.

NASICON is a well known family of fast sodium ion conductors, with a wide range of allowed stoichiometries, $Na_{1+x}Zr_2Si_xP_{3-x}O_{12}$ for $0 \leq x \leq 3$. Unlike sodium beta alumina (NBA) which conducts Na^+ ions in two dimensional plane,

NASICON has 3D channels. This results in far better ionic conductivity than in NBA [33, 45]. The conductivity is often high and is comparable to liquids at high temperatures[34]. The highest ionic conductivity is usually obtained for $x = 2$ [45, 32]. This is because at $x = 2$, the relative partial molar enthalpy of Na_2O is maximum while the relative partial molar entropy of Na_2O exhibits maximum deviation from the linear[1] plot, hence Na^+ ions are more mobile in this composition [48]. Because of this, NASICON finds extensive use in devices such as separation membranes, fuel cells and gas sensors[123, 86, 10, 103, 14].

In terms of thermal properties, NASICON shows low thermal expansion behaviour whose thermal expansion depends on the composition and the lowest value occurring at $x = 0.33$ [124]. There is no information about crack formation in NASICON upon heating and cooling or due to thermal shock reported in the literature and the properties such as these have led to NASICON being used as solid electrolyte in planar gas sensors in form of thick films[34, 14, 86, 123, 125, 99].

Ionic conductivities and related characteristics are determined by using AC impedance measurements to avoid the requirement for non-blocking electrodes needed for DC measurements[126]. Using AC impedance measurements, conductivity as a function of frequency, hopping rates and ion dynamics of superionic materials can be obtained. This spectral analysis has been applied to Na-β"-alumina, $LiGaO_2$ and Ag/Na-mixed alkali β-alumina [127, 128], NASICON type materials such as $NaNi_2ZrP_3O_{12}$, $Na_2(La,Co)TiP_3O_{12}$ and $Na_2(La,Al)TiP_3O_{12}$[126] and NASICON bulk material[129].

The need for miniaturising devices including sensors has seen the emergence of planar devices printed by screen printing technology for mass production [130, 131]. For the fabrication of solid state gas sensors for example, NASICON is a suitable

[1] Linear plot gives the entropy of the solid solution as the sum of the end member contributions.

option as a solid electrolyte since it can be easily coupled with commonly available auxiliary electrodes for indirectly sensing gases such as CO_2, NO_x, SO_x and H_2S that could not be otherwise realised using any other solid electrolytes. Just as it is well known that the bulk conductivity is greater than thick film conductivity[86], knowledge of the electrical properties of thick films to be used as electrolyte for planar sensors is vital.

Although the conductivity measurements of bulk NASICON is well explored, the spectral studies are limited. In this chapter, both the conductivity and spectral measurements of NASICON thick films from AC impedance measurements are investigated and reported.

The effect of film thickness on conductivity is also investigated. Also, the electrode configuration are in such a way that they resemble the configuration of commonly used planar NASICON based sensors[86, 14, 131] as well as the multilayered sensor so that it can reflect real time electrical properties during sensing. In spite of the fact that NASICON is one of the most investigated superionic conductor the effect of thickness and electrode configuration on the ionic conductivity and ionic dynamics of NASICON as thick films has never been studied and this is the first reported.

Furthermore, to isolate the intrinsic effects of thickness on conductivity from other phenomena that may influence surface conductivity, the skin effect is investigated. Skin effect is the tendency of an alternating electric current (AC) to become distributed within a conductor such that the current density is largest near the surface of the conductor, and decreases exponentially with depths in the conductor [132]. Since this study also investigates the effect of film thickness on conductivity, it is important to establish also if NASICON thick films are prone to skin effect.

4.2 Powders and Pellets

As a way of comparing the robustness of our newly developed sol-gel procedure in our lab, the process is compared with the sol-gel process reported in literature by Shimizu et al. [107], Shimizu and Ushijima [106].

4.2.1 TGA/DSC

The xerogel of the three different powders, two of them from our newly developed procedure and one synthesised according to literature were run in TGA and DSC to study the weight loss and heat flow in order to estimate the calcining conditions.

Calcined powder was also run in the TGA and DSC to confirm any phase transformation. This is shown in Figure 4.1. From the Figure it is clear that the new procedure depicted in Figure 4.1a and Figure 4.1b obtains NASICON faster than the Shimizu process. In our process, TEOS acts as a Si precursor, chelating agent and a source of hydrocarbons which later act as extra fuel for phase formation. The hydrocarbons from the sodium citrate as well as the TEOS is thus believed to contribute to rapid reaction and crystallisation of the NASICON phase.

The decomposition of NASICON incorporated maltose and pectin mixed gel (Malt-NASICON-T) was found to be a three step process as shown in Figure 4.1b These three decomposition processes were observed in the temperature range of $150 - 192$, $230 - 334$ and $334 - 400$ °C. The first peak which occurs at 180 °C is the decomposition peak of the hydrocarbons. This was also reported by Wang et al. [108].

In contrast to the Malt-NASICON, the first decomposition peak that burns the hydrocarbons for the as-NASICON-T occurs at 269 °C as shown in Figure 4.1a which is much later than in the Malt-NASICON and this sets the pace as to which process will complete the reaction first.

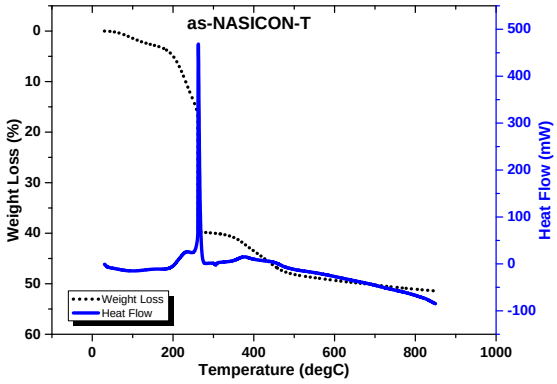

(a) As- NASICON xerogel

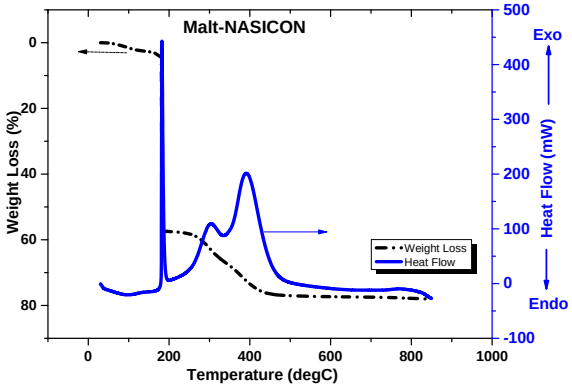

(b) Malt-NASICON xerogel

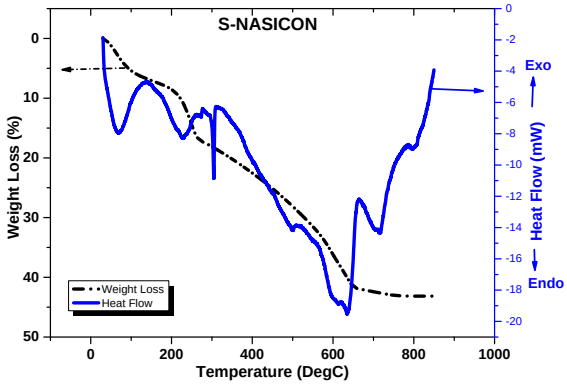

(c) S-NASICON xerogel

Figure 4.1 – TGA/DSC traces of the three powder xerogels.

Unlike the sharp endothermic peak that represented the melting of sodium nitrate (reaction byproduct of the co-precipitation method of the Shimizu process) at 308 °C in Figure 4.1c, in this Malt-NASICON xerogel the sodium nitrate does not melt but quickly oxidises the hydrocarbons and results in the second highly exothermic peak at 269 °C. This reaction generates a lot of heat and is mildly explosive.

This highly exothermic peak is majorly desirable as the onset of NASICON phase formation happens earlier than in the S-NASICON. After all the hydrocarbons have been burnt, the remaining nitrates decompose at 380 °C as shown in the third exothermic peak. Because of the second highly exothermic peak, the mass loss is complete as early as 400-500 °C to set up the NASICON phase formation.

Onset of crystallization starts earlier in the Malt-NASICON than in the co-precipitated (S-NASICON) with the crystallization exothermic peak appearing at *ca.* 400 °C for the Malt-NASICON. After the crystallization process, it can be seen that there is no appreciable physical/chemical transformation except crystal growth as the DSC curve is flat exhibiting negligible heat changes. The weight loss is in fact complete as early as 500 °C.

For the S-NASICON, crystallisation and solid-solid reactions continue even after 700 °C. Weight loss is only complete after 750 °C. From these results, it can be concluded that the new procedure developed in this study for the synthesis of NASICON has lower calcination temperatures than the conventional Shimizu procedure. In fact to obtain a phase pure powder, a cycle of re-calcining and grinding is necessary for the conventional procedure while, in our new procedure, only one cycle of calcination will produce a phase powder powder. This effectively lowers the cost of NASICON synthesis and in effect lowers the cost of the ultimate sensor or any device that applies NASICON.

DSC measurements were performed on the phase pure calcined powders to check any phase transformation. This is shown in Figure 4.2.

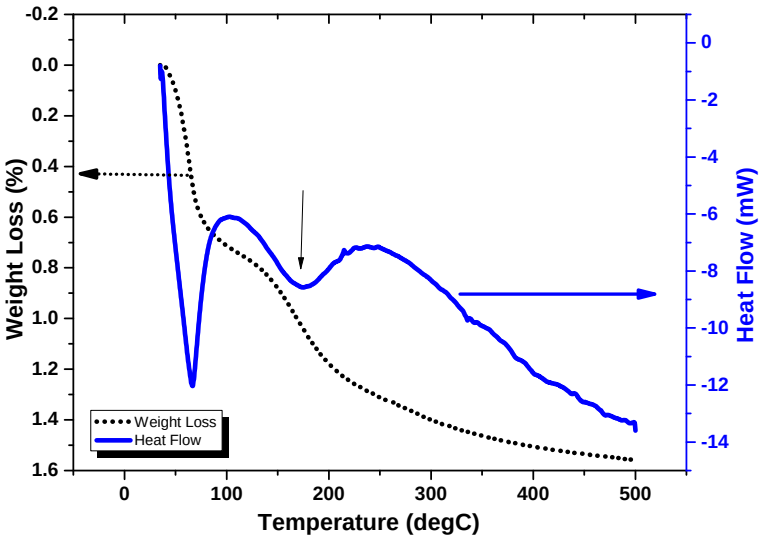

Figure 4.2 – DSC/TGA of NASICON powder calcined at 1000 °C. No phase transformation is of NASICON is observed.

No phase monoclinic to rhombohedral transformation is observed. The first endothermic peak is attributed to moisture loss while the source for the second peak (at $\sim$ 172 °C) is not clear. In spite of the fact that is within the transition range it still cannot not be attributed to the transition temperature because there is a weight loss that accompanies it. The phase transition is just a structural change.

This result demonstrates that as long as the powder is heat treated at temperatures below 1100 °C no transition is expected as NASICON is in a disordered state, with an average rhombohedral structure[35, 43]. This confirms earlier studies by Perthius and Colomban [35].

4.2.2 XRD

Both ambient temperature (using the Bruker D8 diffractometer, using **(**Cu **-** $\mathbf{K}_\alpha$ X-rays) and non ambient (high temperature) XRD analysis (using the X'pert

difractometer) was conducted on the powders and pellets. Because TGA measurements showed a complete shrinkage at 760 °C and beyond, the results gave us an indication of what temperatures to calcine the xerogel powders. Non ambient XRD was performed on the xerogels from room temperature to 925 °C to compliment the TGA results. The development of patterns is as shown in Figures 4.3 and 4.4.

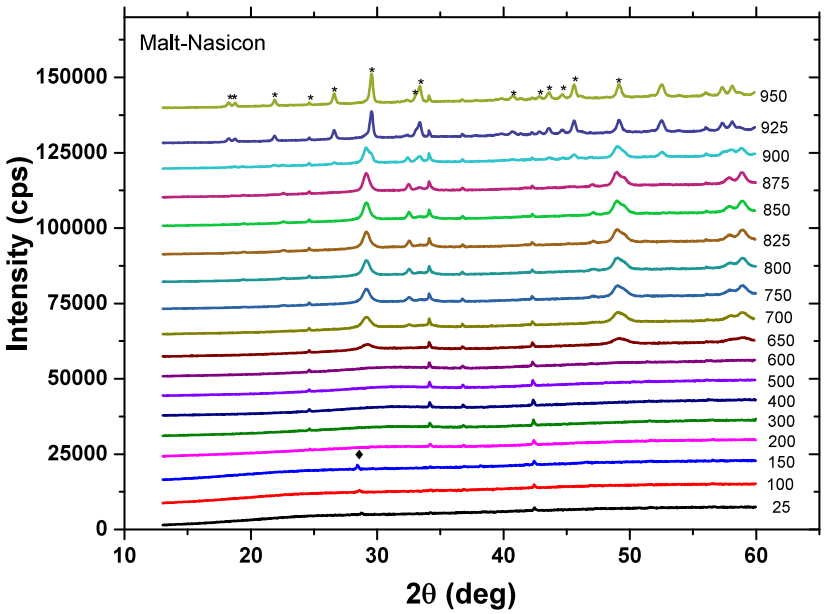

Figure 4.3 – High temperature XRD for Malt-NASICON. A well crystallised single phase is observed at 925 °C. *NASICON peaks, ◆ $NaNO_3$..

In both the xerogel it can be observed that the formation of NASICON involved intermediate reactions. The xerogels contained a mixture of an amorphous phase and sodium nitrate which oxidised the explosive combustion of organics as has been pointed out in Figure 4.1b and 4.1a. The presence of sodium nitrate(ICDD 04-7-5274) in the XRD patterns and the highly exothermic peak at 180 and 269 °C for the Malt-NASICON and as-NASICON-T patterns respectively agrees well with the TGA/DSC results before which combustion takes place. This is because sodium nitrate(clearly visible peaks at $T \leq 200$ °C) is a powerful oxidizing

agent and in the presence of combustible materials such as maltose and pectin an explosion may occur. It can also ignite hydrocarbons or mixtures of nitrate with phosphorous [133].

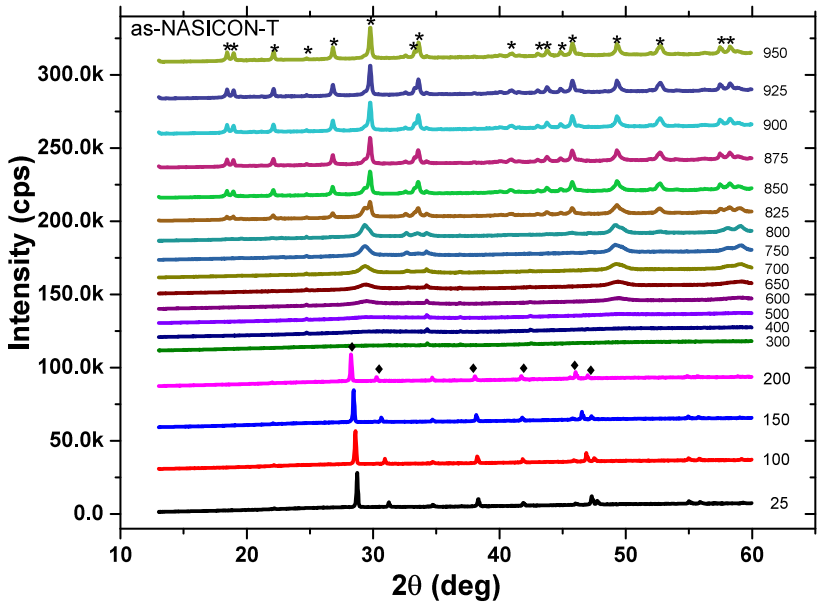

Figure 4.4 – High temperature XRD for the as-NASICON-T. The NASICON phase starts forming at 825 °C and the reaction is complete at > 925°C. * NASICON peaks, ◆ $NaNO_3$.

From Figure 4.3 it can be seen that highly crystalline and single phase NASICON is formed at 925 °C and that the transition between the intermediate phases and the final NASICON phase was fast. However, for the as-NASICON-T, the NASICON phase starts to form at 825 °C and the reactions are only complete at > 925 °C.

Since a significant proportion of powder is lost(about 80% of the xerogel is lost) during the calcination due to the explosive nature of the Malt-NASICON process, the as-NASICON-T procedure was adapted for all characterisations such as electrolyte for galvanic cells in EMF thermodynamic measurements and for making NASICON paste for sensors.

In the new synthesis procedure calcination at temperatures from $925 - 1000$ °C yields a single phase, highly crystalline fine powder that is suitable for ink making. This is a success because in contrast to many other process which require pelletising, grinding, re-calcining and regrinding just to obtain a single phase powder[107, 106, 38, 48, 35], this process yields it in one attempt.

In these two procedures, the homogeneous distribution of precursor ions and slow collapse of the carbohydrate structure (in the case of Malt-NASICON) and organic complexation(due to the organics from sodium citrate and TEOS in the case of as-NASICON-T), during calcination seems to prevent the rapid agglomeration of precursor ions, which ensures small particle size of the product and therefore yields high purity single phase NASICON at much lower temperatures.

Figure 4.5 is a comparison of XRD patterns for the as-NASICON-T and Malt-NASICON powders calcined at 1000 °C for 1h. A highly crystalline phase of NASICON is observed in both NASICONs except for the traces of intermediate phases in the as-NASICON-T. However these readily disappear with a slight increase in temperature during sintering and so this can not be problem when sintering thick films or pellets. The phase conforms with the NASICON standard from the ICDD 04-008-8548 card.

Furthermore, the evidence of a complete reaction in Malt-NASICON underlines the synergistic contribution of maltose and pectin in the complexation and chelation of precursor ions resulting in small particle size and highly reactive mixture of particles. In addition, the highly exothermic reaction arising from the oxidative decomposition of the organics as was observed in the TGA/DSC measurements provides extra energy for the reaction.

NASICON powders obtained in these two procedures are very fine and suitable for making pellets or thick film pastes without the need for grinding or re-calcining.

In fact re-calcining usually promotes zirconia precipitation due to rapid loss of sodium and phosphorous oxides[43]. Many processes fail to obtain a single phase at calcination stage and are only able to do so after sintering and sometimes regrinding, pelletising and re-sintering again at higher temperatures in excess of 1000 °C for prolonged sintering times [134, 38, 107, 135]. This underlines the success of the present procedure as it is cost efficient as the energy saving may trickle down to the the final device.

The intermediate phases in the as-NASICON-T powder observed in Figure 4.5 often reacted at higher temperatures as is shown Figure 4.6 of XRD pattern of the pellet sintered at 1150 °C for 6 h. However, high temperature sintering introduces traces of zirconia phase due to a loss of Na_2O.

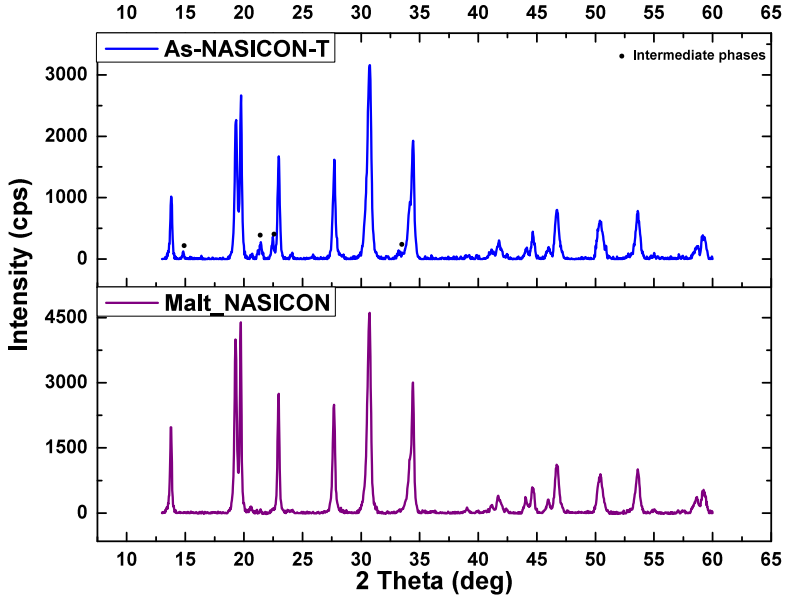

Figure 4.5 – as-NASICON-T vs Malt-NASICON calcined at 1000 °C for 1 h. All peaks are attributed to NASICON(ICDD 04-008-8548) phase except for the indicated.

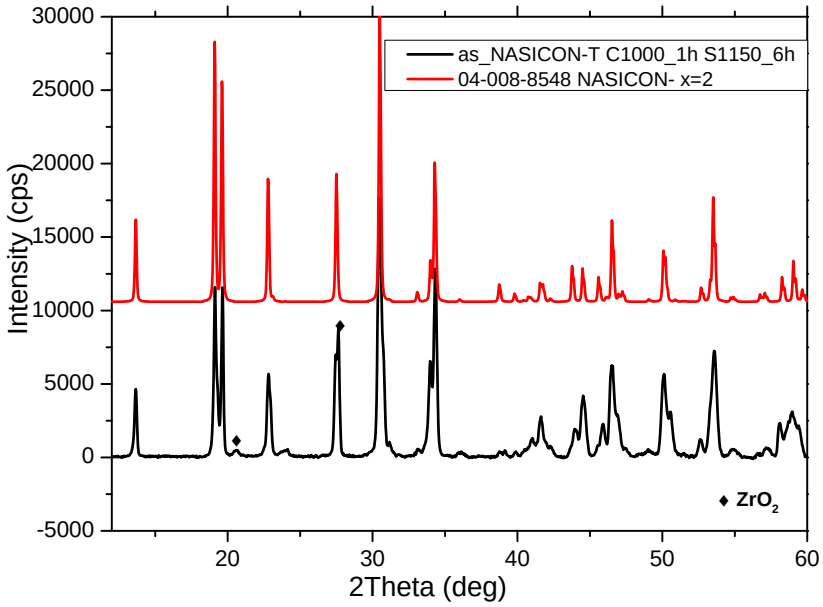

Figure 4.6 – XRD pattern of Pellet of as-NASICON-T sintered at 1150 °C for 6 h compared with the standard NASICON pattern of $x = 2$ composition, ICDD 04-008-8545. Traces of ZrO_2 are also present.

4.2.3 Density

Obtaining a high density, phase pure pellet of NASICON is quite a challenging activity. This is because, a balance between sintering temperature and NASICON purity has to be reached. In the quest for a highly densified pellet, a higher sintering temperature is normally used but this has negative effects towards the purity of NASICON because of its volatility through the loss of Na_2O and P_2O_5 leaving zirconia precipitates and other NASICON phases deviant from the original phase.

A common practice to redress this problem is

- to use excess Na and P precursor to compensate for the loss. This is still not exact as it is difficult to predict how much loss will take place as it depends on the sintering conditions such as temperature, sample preparation and

sintering crucible,

- to use a much lower sintering temperature. A much lower sintering may obtain a fairly dense pellet but with compromised conductivity as expected. However, since NASICON is a superionic conductor, the conductivity is quite appreciable and can actually be applied in sensing measurements as will be demonstrated later in thick film sensors.

Determination of the density of a pellet involves the accurate measurement of the volume using the density bottle as well as its mass. However, for NASICON pellets it was not used because of NASICON's inadvertent reaction with water[100], which is usually used in density bottle measurements. In this research, the volume was calculated from the disc (pellet) dimensions. This had an element of error associated with it because the pellets were not perfect discs.

Figure 4.7 is a histogram showing densities of pellets with different thermal pre-treatment. Sintering for 6 h achieved an 88% densification close to the most dense pellets that were sintered for 15 h or more. For the sake of NASICON purity sintering for 6 hours was chosen.

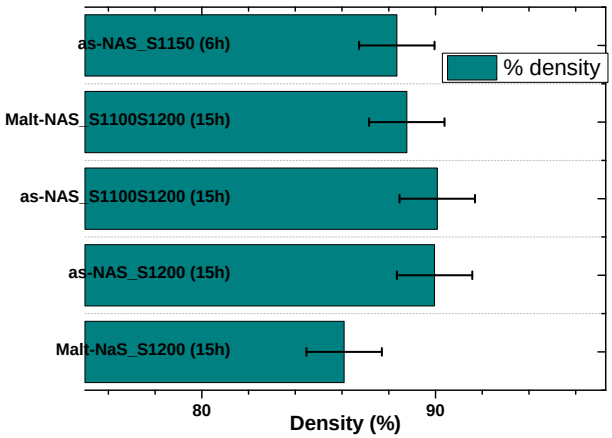

Figure 4.7 – Densities of pellets from the two procedures. Double sintering slightly improved the density.

In terms of sintering, the pellets from the new procedure sintered well at 1150 °C for 6 h into a dense pellet while the S-NASICON could not sinter at this temperature and this is shown in Figure 4.8. The S-NASICON could only sinter into a dense pellet at temperatures $T > 1200$ °C. Furthermore, the diameter of the shape forming dies used in the pelletising were different. The initial green diameter of the S-NASICON pellet was 10 mm while that of as-NASICON-T was 12 mm. After sintering, the as-NASICON looked smaller than the S-NASICON and very compacted, a reason already elaborated, which is small particle size of the powder leading to better compaction.

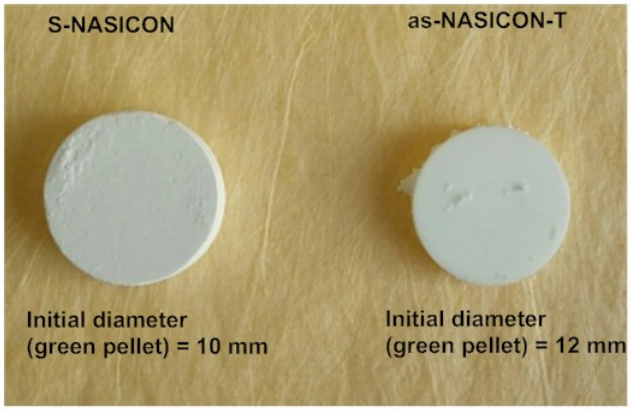

Figure 4.8 – Comparison between the S-NASICON and as-NASICON-T fired pellets. The pellet from the new procedure was well sintered after firing at 1150 °C while the S-NASICON was not sintered.

As for the S-NASICON, the agglomerated particles leads to higher sintering temperature which subsequently leads to Na_2O and P_2O_5 loss and ZrO_2 precipitation. The presence of zirconia gives the powder some refractory behavior which drives the sintering temperature even higher. Furthermore zirconia is also deleterious to electrical properties of NASICON, therefore the new procedure is highly economical and superior.

4.2.4 Dilatometry

Figure 4.9 show the dilatometric measurements of a sintered pellet of as-NASICON at 1200 °C well above the boundary temperature of the mono-phase disordered state in order to reveal any phase transition temperature. The figure reveals a structural transition at 162 °C. This is likely to be the transition from monoclinic to rhombohedral structure which is reported in literature. The transition temperature lies between $147 < T < 300$ °C[35, 43, 33, 36, 37]. Therefore this value agrees well with literature. Furthermore this results proves the fact that NASICON fired at $T \leq 1100$ °C is rhombohedral from room temperature up to the boundary temperature, $T = 1100$ °C and therefore no monoclinic to rhombohedral transition takes place. This was confirmed in DSC/TGA results. Incorporating the results in Figure 4.2 and Figure 4.9 confirms that unless the powder is heat treated at $T > 1100$ °C it wont change structure.

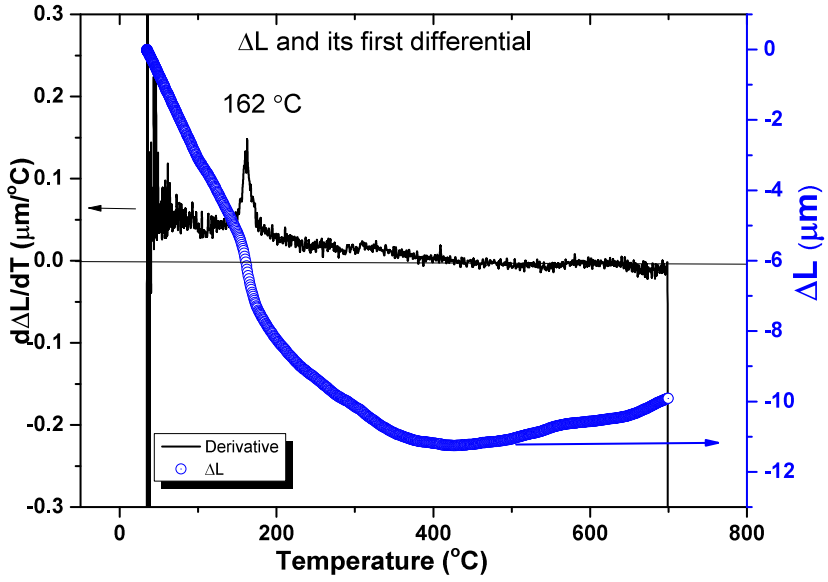

Figure 4.9 – Dilatometric measurements of the as-NASICON pellet calcined at 750 and sintered at 1200 °C. A first derivative reveals the transition from monoclinic to rhombohedral structure at 162 °C.

4.2.5 SEM/EDS

SEM imaging was performed on the as-NASICON-T and Malt-NASICON powders calcined at 1000 °C. As can be seen in Figure 4.10 for the as-NASICON the hydrolysis and condensation reactions that are synonymous with silicon alkoxide of TEOS[35] results in growth of spherical particles and these particles which are about 2 μm are loosely bound to each other. Each spherical particle further contains aggregates of crystallites, much smaller than 1 μm, loosely bound and still in a polymeric gel like structure which could be due to the organics from the citrate.

These small particles and loosely bound ensures a fine powder product such that grinding and milling is not necessary for further processing of these powders into printing inks.

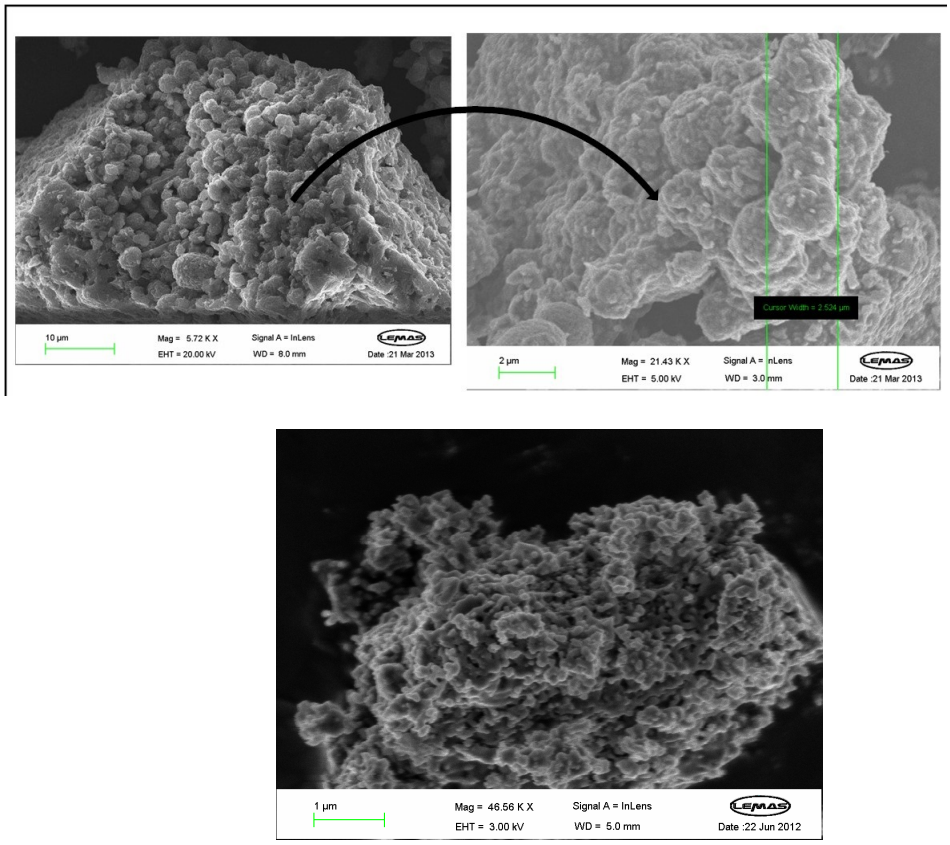

Figure 4.10 – SEM images of as-NASICON calcined at 1000 °C. Spherical agglomerates of crystal aggregates are evident containing. The loosely bound particles are of the order of $\ll 1\mu$m.

Figure 4.11 is an image of the maltose/pectin assisted NASICON, Malt-NASICON powder. Noticeable is a porous structure that looks like a woven mesh. This structure could have formed after the chelating hydrocarbons were driven off during the calcination stage leaving the interwoven strands of NASICON akin to a polymeric structure.This structure is easily crumbled because of the loose crystallites that form the structure. This produced a very fine powder that needs no milling for thick film paste making.

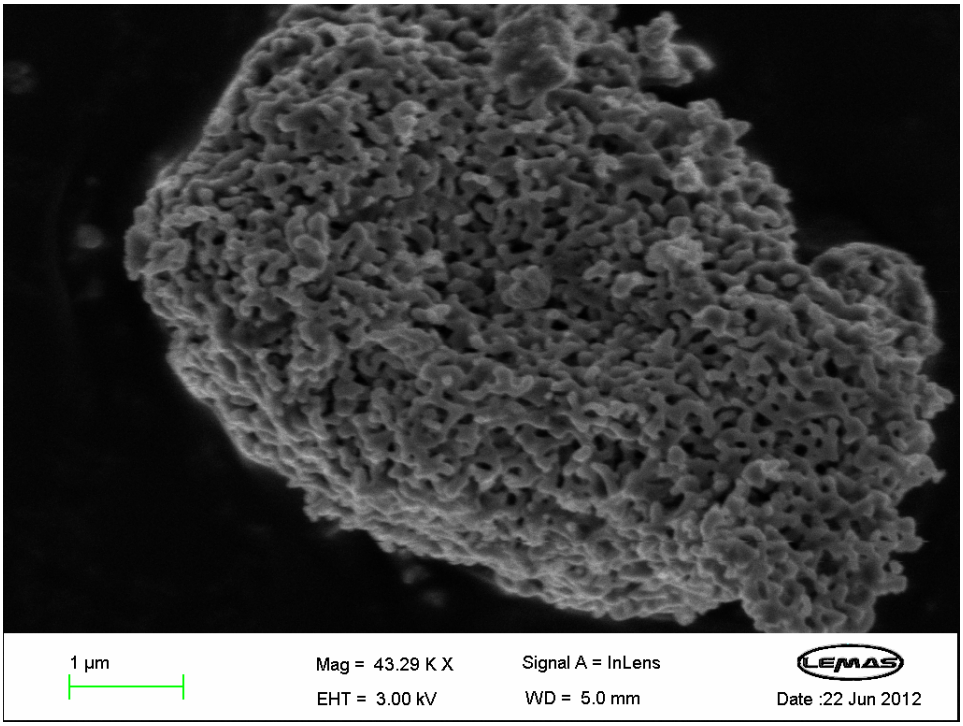

Figure 4.11 – Malt-NASICON powder calcined at 1000 °C. A polymeric-like structure of interconnected particles is evident.

EDS mapping as well as EDS (point and square) measurements from a number of sites showed that the powder was homogenously mixed and the elemental composition which was averaged from all the spectra from different sites showed that the NASICON was close to $x = 2$. This confirmed the results from XRD which was in conformity with the standard, $x = 2$, of ICDD 04-008-8548. The EDS data and how it compares with the theoretical values of $x = 2$ is shown in Table 4.1.

Table 4.1 – Averaged elemental composition of EDS data from as-NASICON powder.

Element	**Na**	**Zr**	**Si**	**P**	**O**
Atomic %	14.41	9.67	9.59	4.88	61.45
Theoretical ($x = 2$)	15	10	10	5	60

4.2.6 Electrochemical Impedance Spectroscopy

Figure 4.12 is a Cole-Cole plot from measurements on the Malt-NASICON pellet fired at 1150 °C. Semi circles(corresponding to a lumped RC combination) are observed which enables impedance determination. The lower frequency of the semi circles show a high capacitative effect as deduced from the vertical line[41]. This could be due to the electrode effect. A zoomed image on the right shows that at high temperature this capacitative effect increases and the semicircles diminish.

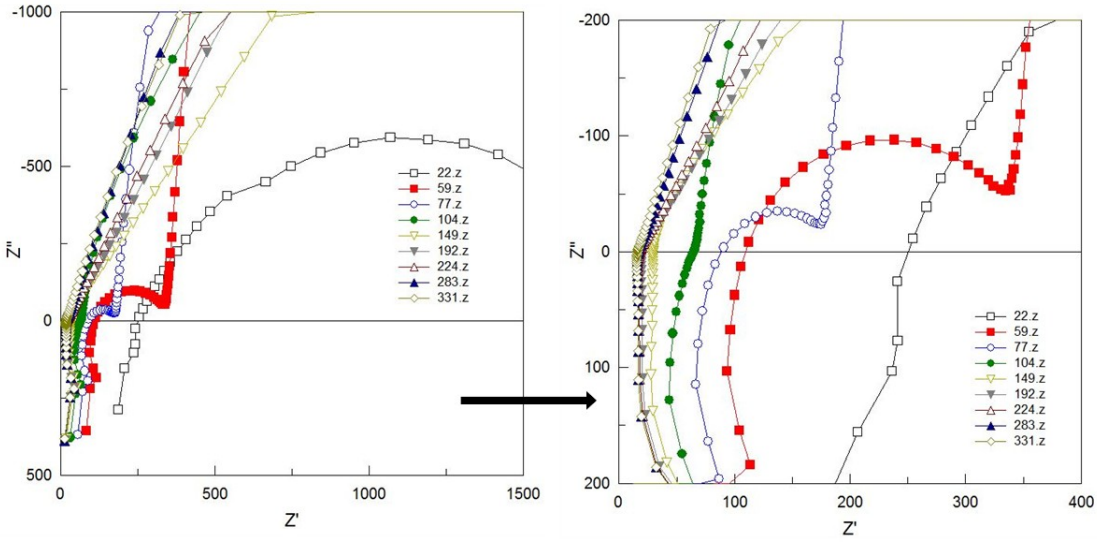

Figure 4.12 – Nyquist plot from a malt-NASICON pellet fired at 1150 °C. The legend are temperatures in °C.

For a pellet of cross-sectional area A in and thickness t, the conductivity was calculated from $\sigma = \frac{t}{ZA}$ where Z is the impedance obtained from the AC impedance measurement after fitting appropriate equivalent circuits to the data.

A comparison of conductivity of as-NASICON and Malt-NASICON pellets fired 1200 °C show no difference in the conductivity values. This is shown in Figure 4.13. This shows that pure NASICON was formed whether maltose/pectin was used as a precursor or not.

As was pointed out earlier, since the Malt-NASICON synthesis route results in a loss of significant amount of powder during calcination due to its explosive nature, as-NASICON was adapted as precursor for the NASICON paste for the fabrication of planar sensors.

In a thermally activated process, the temperature dependence of conductivity is represented by the Arrhenius relation in Equation (4.1);

$$\sigma T = \sigma_0(T) \exp\left(-\frac{E_a}{kT}\right) \tag{4.1}$$

where $\sigma_0(T)$ is a pre-exponential factor which is a function of charge carrier concentration, temperature and material structural parameters, k is the Boltzmann constant and E_a is the activation energy of conduction. It can therefore be seen that the conductivity profile follows the exponential relation $\sigma \propto \exp(-\frac{1}{T})$ derived from the Arrhenius Equation (4.1).

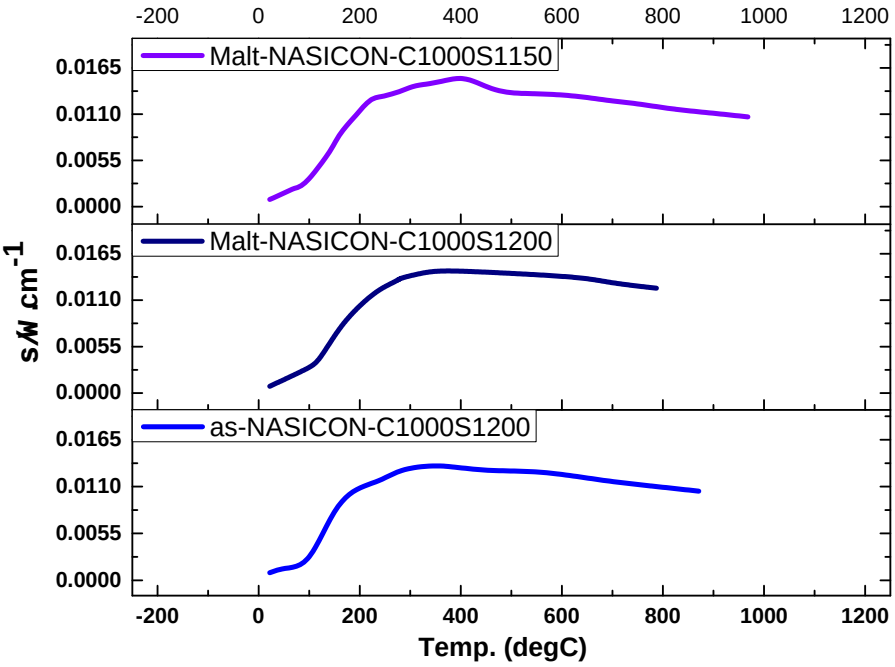

Figure 4.13 – Conductivity as a function of temperature. Conduction seem to possess a maxima between 300 and 400 °C.

Figure 4.14 is first derivative of conductivity with respect to temperature. This was to reveal the sharp change in conductivity that would not be otherwise resolved by Figure 4.13. It clearly shows a peak almost at the same temperature in all the samples which may be attributed to the monoclinic-rhombohedral phase transition that occurs in NASICON. This also compliments the dilatometric data in Figure 4.9.

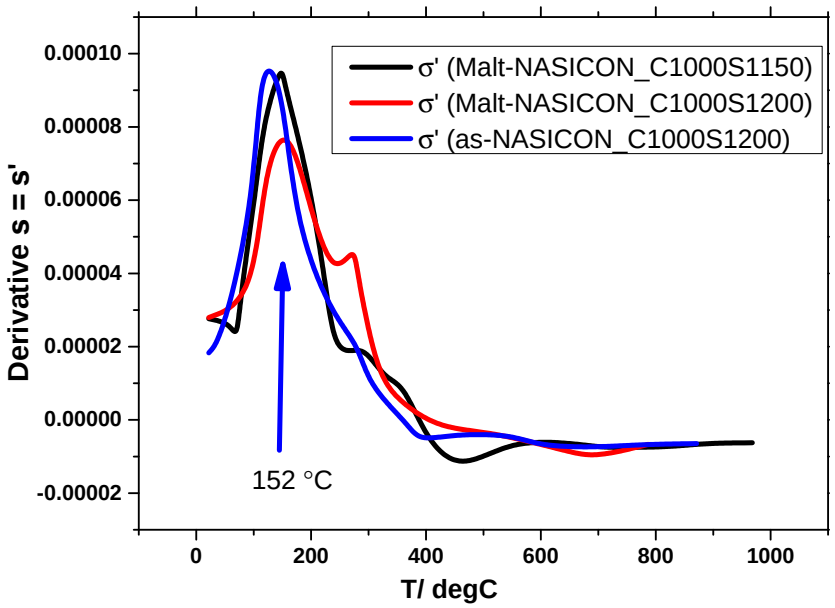

Figure 4.14 – First derivative of conductivity as a function of temperature. Possible phase transition is revealed.

The fact that the transition can be observed in the pellets, that was not observed in the powders is because of the thermal history which has now exceeded 1100 °C, during sintering. As Perthius and Colomban [35] observed, when NASICON is sintered below 1100 °C it exhibits a high degree of disordered form, with an average rhombohedral symmetry hence no rhombohedral to monoclinic switch is observed. However when the temperature is increased, the tetrahedra disorder is lowered leading to a monoclinic average symmetry consequently phase transition is observed as is the case here.

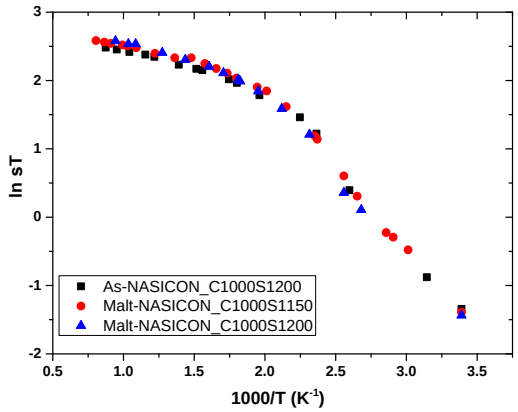

(a) Arrhenius plots of all the pellets compared.

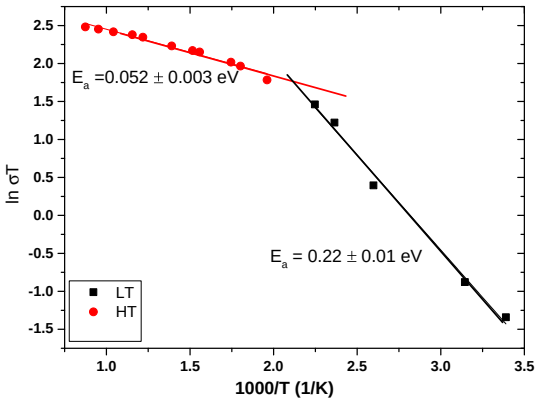

(b) Arrhenius plot of as-NASICON fired at 1200 °C.

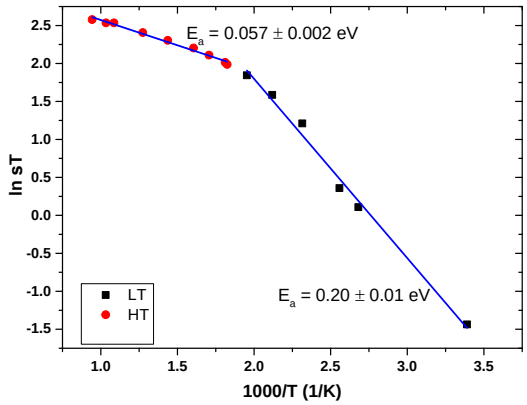

(c) Arrhenius plot of malt-NASICON pellet fired at 1200 °C.

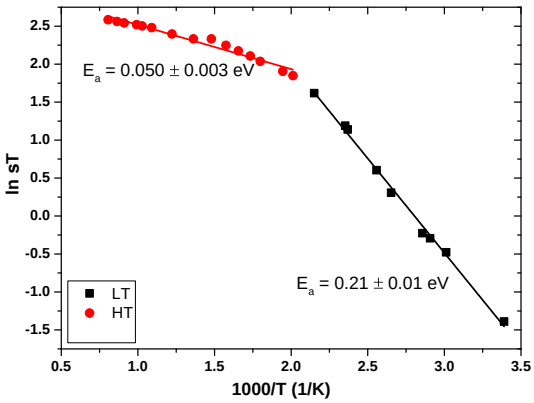

(d) Arrhenius plot of malt-NASICON fired at 1150 °C.

Figure 4.15 – Arrhenius plot of ion conductivity of NASICON pellets.

Figure 4.15 are Arrhenius plots of NASICON pellets obtained from the data in Figure 4.13. The plots are linear and follow the Arrhenius equation in Equation (3.5), $\ln \sigma T = \ln \sigma_o - E_a/T$.

Linear regression analysis using Origin software yields the slopes which corresponds to

$$\text{slope} = -E_a/1000k \tag{4.2}$$

where $k = 8.617 \times 10^{-5}$(eV/K) is the Boltzmann constant and E_a(eV) is the activation energy which is a measure of energy barrier to ion transport. The average LT activation energy from the pellets was $E_a = 0.21 \pm 0.01$ eV. The lower the activation energy the more conductive a material is. Figure 4.15a shows that, not much difference is observed in the NASICONs from the two process as well as from different sintering temperature of 1150 and 1200 °C. Again this confirms the internal consistency of the two processes in making NASICON.

The activation energies in Figures 4.15b, 4.15c and 4.15d are within the range as obtained by Perthius and Colomban [35] as shown in Table 4.2.

Table 4.2 – Activation energies (eV) of NASICON, $x = 2$ as a function of disorder from Perthius and Colomban [35].

	Glassy	Highly disordered			Low disordered	
Sintering Temp. °C	600	900	950	1050	1200	1250
E_{HT}:T>157 °C		0.26	0.23	0.24	0.15	0.13
E_{LT}:T<157 °C	0.65	0.30	0.42	0.38	0.37	0.32

At high temperature, the activation energy is very low and is comparable to that of metals. This is because the Nyquist plots at high temperatures could not produce semicircles and so the determination of impedance from the plots was inaccurate and therefore the impedance obtained at high temperature can not be relied upon. This is shown in Figure 4.12.

The next section is the characterisation of thick films derived from the NASICON powder.

4.3 Thick Films

Printed and dried thick films were fired at different temperatures and duration in order to obtain an optimised sintering schedule aimed at obtaining an optimised film, that is, a film that is fairly phase pure and well densified.

The effect of thickness on electrical properties and phase purity after firing was also investigated. Furthermore the effect of electrode configuration on surface conductivity is also considered.

To vary the NASICON film thickness on the alumina substrate, different printing cycles were used where the least number of printing strokes represent the thinnest layer. The screen stage was also raised after each cycle to accommodate the additional layer. Three substrates were printed, the first sample printed with only one double stroke (DS)[2] cycle denoted as 1DS, the second, with two cycles (2DS) and the third with three cycles (3DS) respectively. After printing, the NASICON thick film samples were left for 10 minutes in air for the film to settle until they were smooth.

4.3.1 XRD

Figure 4.16 are plots showing the effect of firing temperature and duration on the sinterability and phase purity of NASICON film on alumina substrate. The results in Figure 4.16a reveal that at lower sintering temperatures, $T \leq 1000$ °C, the film does not sinter even when fired for longer duration. This of course directly translates to low ionic conductivity of films. However, being a superionic conductor, NASICON can still conduct and can actually be used as solid electrolyte in sensors albeit having low conductivity as will be seen in Chapter 7.

[2] A **double stroke (DS)** is the printing where the squeegee prints in a forward and backward direction.

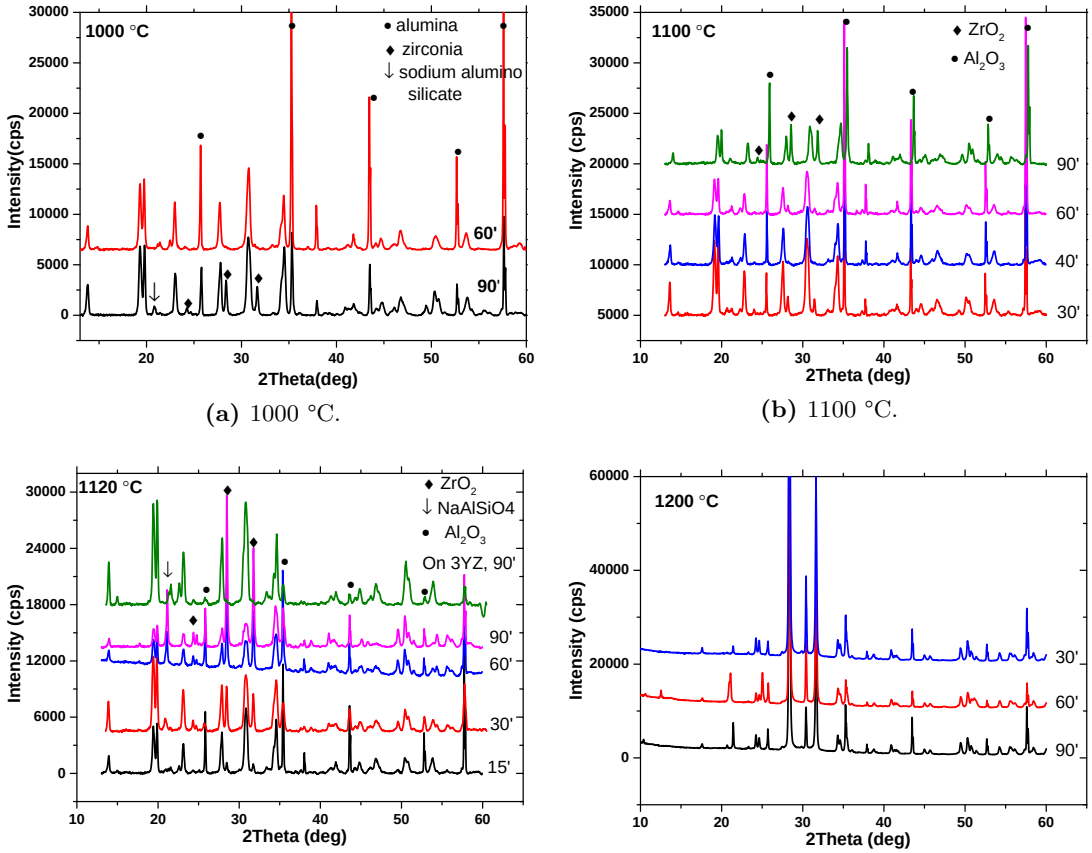

(a) 1000 °C. **(b)** 1100 °C. **(c)** 1120 °C. **(d)** 1200 °C.

Figure 4.16 – Effect of firing temperature and duration on the NASICON thick film phase purity and sinterability. No presence of NASICON is observed for the 1200 °C fired sample.

For the films fired at 1120 and 1200 °C in Figures 4.16c and 4.16d, it can be seen that these temperatures were too high for the films as the NASICON deteriorated significantly despite being well sintered. The phase deterioration of NASICON was found to be due to competing reactions:

- The volatisation of Na_2O and P_2O_5 which preferentially occurs on the surface[94, 136] may have taken place leading to intergranular precipitation of monoclinic zirconia and to a slight shift in composition of NASICON. This process is common in $x = 2$ NASICON[43].

- Inadvertent interfacial reaction between alumina substrate and NASICON leading to extensive zirconia precipitation at the interface. This process, occurring in all the fired films was more dominant than the alkali and phosphorous loss and was found in all the fired films and more pronounced at high temperature.

  Previous studies have showed that doping Al into NASICON improved the sintering[35] therefore the diffusion into the NASICON matrix may have contributed to the sintering of the films albeit with negative effects because this disturbed the chemical stoichiometry which drove the zirconia precipitation. This is elucidated in the SEM/EDS Section 4.3.2. Furthermore there was an increase in the sodium alumino silicate peak as sintering temperature and duration increased. This was due to the upward diffusion of aluminium which reacted with the Na_2O in NASICON.

In the quest to avoid the interfacial reactions between NASICON and the underlying alumina substrate, 3% stabilised zirconia (3YZ) was firstly printed on the alumina substrate and then fired at 1400 °C. 3YSZ was found not to sinter at this temperature. NASICON was then printed and fired at 1120 °C for 90′. The NASICON did not sinter at this temperature. However, due to the duration of firing and the temperature it could not prevent the surface volatization that leads to zirconia precipitation. Therefore the 3YSZ route was not followed. This finding implies that the interfacial reactions of NASICON and alumina substrate actually aid in the NASICON sintering because when 3YSZ was used, it couldn't sinter even at 1120 °C,

The challenge now was that, low firing temperatures did not sinter the films and while longer firing temperatures and longer durations promoted zirconia and sodium alumina silicate precipitation. A balance had to be reached where an

optimised schedule was reached, at which the temperature promoted a fairly densified film as well as an allowance of only traces of zirconia.

The optimal firing schedule was 1100 °C for 60 minutes. This is shown in Figure 4.16b. Firing for 30 minutes never sintered the film while firing for $t > 60$ minutes was deleterious to the NASICON purity due to the process that occurs in higher temperature firing.

Firing at 1100 °C for 60 minutes was the optimal schedule because the film was fairly well sintered, preserved the NASICON phase with only traces of ZrO_2.

Sintering NASICON at $T = 1100$ °C obtained a dense film and at this temperature structural anomaly effects that occur between 147 - 300 °C are strongly attenuated because the the NASICON is rhombohedral[43, 35]. This is especially important because microcracks that would otherwise form on a sintered thick film due to the structural readjustment won't develop on the thick films. Therefore the sintering temperature is just right, in terms of conductivity, phase purity and structure; parameters desirable for a solid electrolyte in thick film gas sensors.

Longer durations of firing had an effect on the phase purity of NASICON regardless of the sintering temperature used. Firing durations of $t > 60$ minutes promoted ZrO_2 precipitation. Figure 4.17 is a comparison of the zirconia fraction present in the NASICON films fired at 1100 and 1120 for different durations, data extracted from the XRD patterns of Figure 4.16. The fraction of zirconia contained in the film was calculated by noting its peak intensity at I_{ZrO_2} at 28.4° and the NASICON intensity at I_{NAS} at 19.4° and substituted into the formula $\frac{I_{ZrO_2}}{\left(I_{ZrO_2}+I_{\mathrm{NAS}}\right)}$. It can been seen that the fired film at 1120 °C has a higher zirconia content than in the 1100 °C fired film. Further, the zirconia evolution was also a function of sintering duration and that at longer durations, the presence of zirconia does not depend on the sintering temperature.

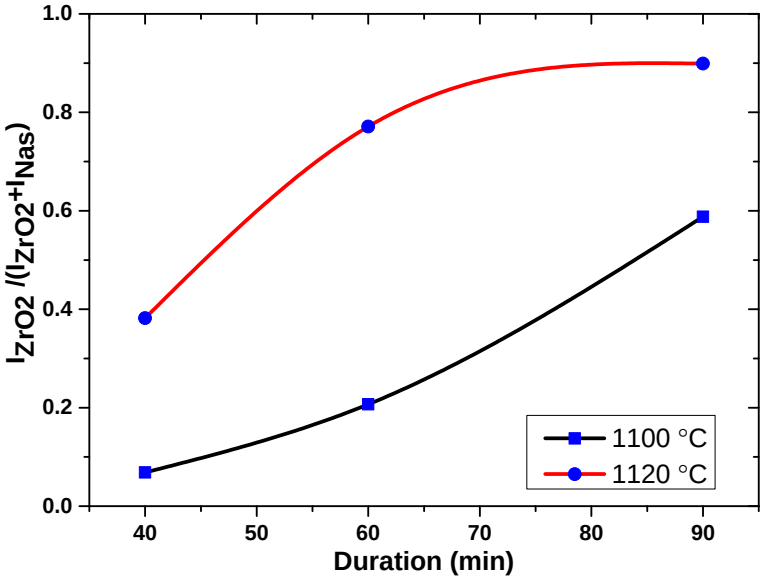

Figure 4.17 – Fraction of Zirconia present in NASICON film as a function of firing temperature and duration.

Table 4.3 is a summary of the process of optimising of the firing schedule. A red cell implies that the film is unusable, zirconia dominates in the NASICON sintered or not. Amber means even if the film is not sintered at least the NASICON phase is $> 75\%$ and therefore can be used. The green cell means the film ticks all the boxes in terms of sintering and NASICON content.

Table 4.3 – Summary of the sintering schedule of the NASICON thick films. The thick film fired at 1100 °C for 60 minutes sintered well and had only traces of zirconia. This is shown in the green cell. Green=ideal film, amber = usable but not well sintered, red = unusable film.

Sintering temperature↷	Sintering time→	15′	30′	40′	60′	90′
1000 °C	Sintered				✗	✗
	>75 % Nasicon phase				✓	✗
1100 °C	Sintered			✗	✓	✓
	>75 % Nasicon phase			✓	✓	✗
1120 °C	Sintered	✗	✗	✓	✓	✓
	>75 % Nasicon phase	✓	✓	✗	✗	✗
1200 °C	Sintered			✓	✓	✓
	>75 % Nasicon phase			✗	✗	✗

4.3.2 SEM/EDS

Figure 4.18 are thick films fired at different temperatures and durations in backscattered mode. Clearly seen is the precipitated zirconia at the interface and traces of it on the surface. Contrary to the claim by [86, 94] that the presence of zirconia is solely due to the Na_2O and P_2O_5 loss on the surface, zirconia precipitation is actually dominated at the interface between NASICON and alumina. Therefore the zirconia precipitation occurs both on the surface of the film and at the interface.

Furthermore, as can been seen from the figure the optimised film has a considerable amount of NASICON phase on top of the underlying zirconia crystals. The phase is not as mixed with zirconia as it is in the films fired at 1200 °C or films fired longer than 60 minutes. These observations are in agreement with the XRD results of Figure 4.16.

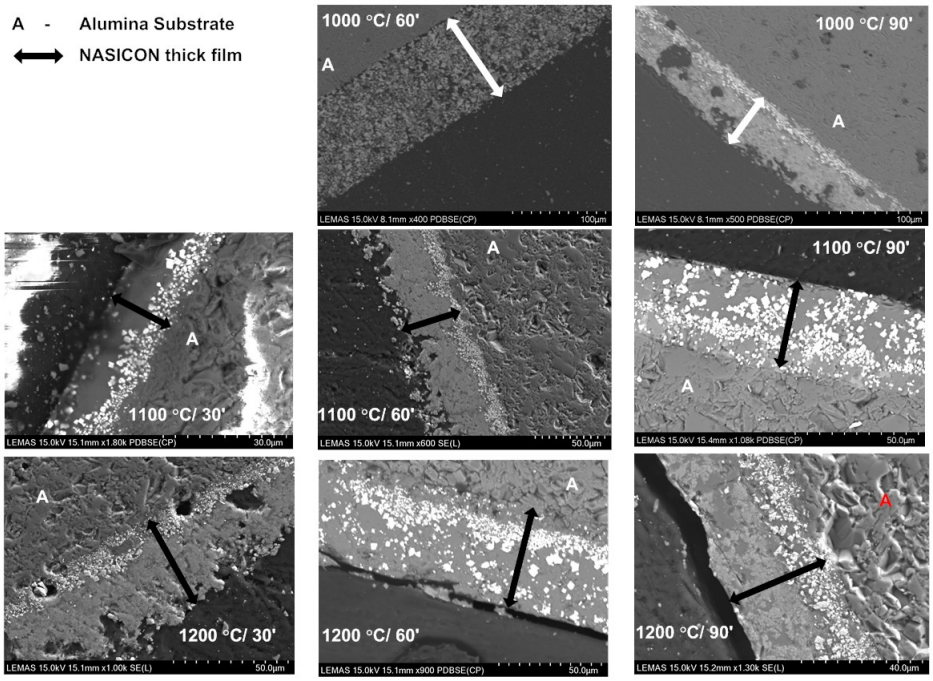

Figure 4.18 – Backscattered images of thick film NASICON fired at different temperatures and durations.

Figure 4.19 is the mapping data for the 1200 °C fired for 90 minutes to elucidate the interface reactions. From the figure it shows that considerable amounts of aluminium diffused into the NASICON matrix. Its fate was either to react with the sodium oxide and silica in the NASICON to form a glassy sodium alumino silicate or partially substitute zirconium in the NASICON to form a doped NASICON which is believed to sinter well[35, 86]. The sodium alumino silicate ($NaAlSiO_4$) as was detected in XRD and the amount increased with increasing firing temperature and duration. The region which had a phase content of zirconia had traces of Na detected. Despite being dominated by ZrO_2 there could be traces of Na_2ZrO_3 also or Na may only be there to stabilize the ZrO_2.

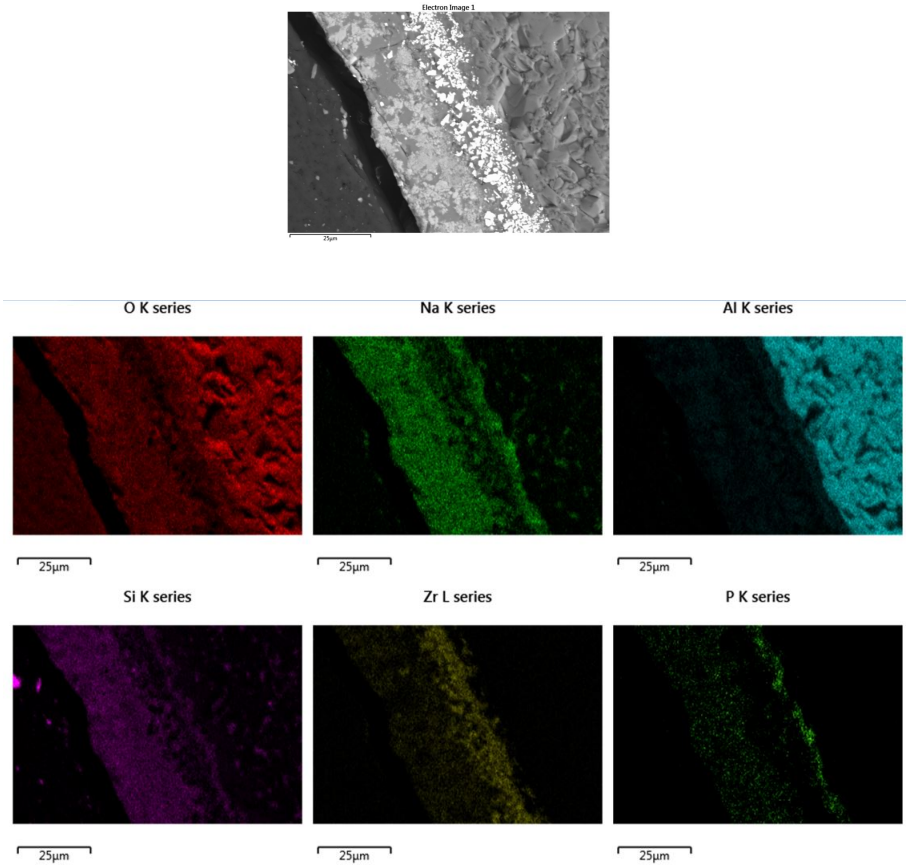

Figure 4.19 – EDS Mapping across the NASICON thick film fired at 1200 °C for 90′.

Furthermore at the interface immediately after the precipitated zirconia, into the alumina substrate, there was phosphorous and sodium diffusion. This diffusion could be the one responsible for the zirconia precipitation at the interface. The new layer, sandwiched between zirconia crystals and alumina comprises Na and P as shown in the EDS line scan of Figure 4.20. This interface reaction in fact is advantageous in that it improves the integrity of thick film adhesion to the alumina substrate because of the atomic mixing at the interface. Also it can clearly be seen that the light crystals in the image is zirconia.

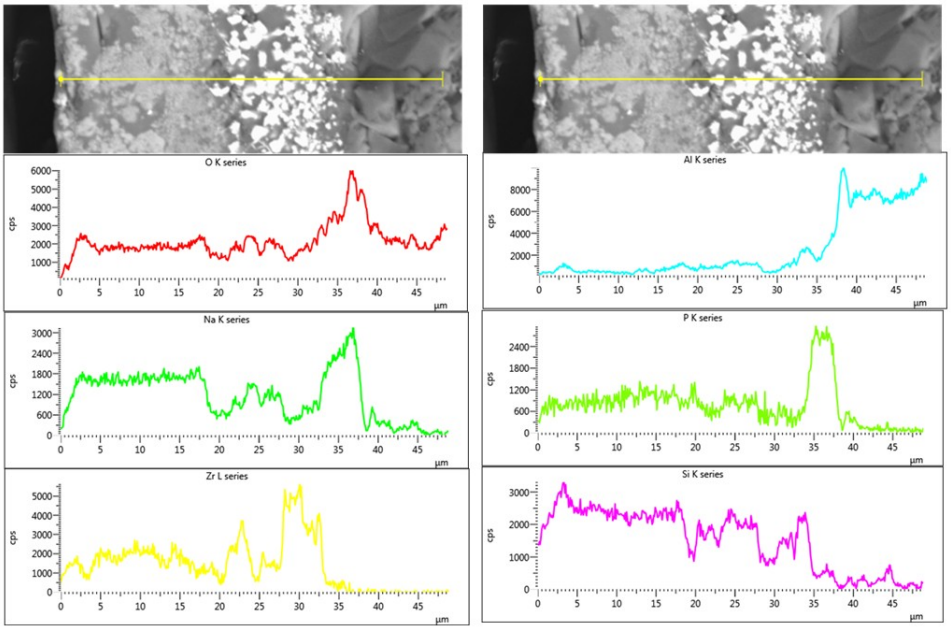

Figure 4.20 – EDS Line scan across the film to reveal elemental distribution.

The revelation by SEM/EDS of the interface reaction between NASICON and alumina emphasizes the need for reference electrodes in the planar sensors to fix the sodium oxide activity because, without it, the NASICON composition will continuously be changing, consequently altering the Na_2O activity and this may give inaccurate sensor results or difficulty in achieving equilibrium. Such a sensor that doesn't employ a reference electrode was reported by Wang and Kumar [86]. With such reactions taking place at the interface, long term stability is not guaranteed.

However, the presence of zirconia at the interface of NASICON/alumina substrate offers an advantage. It helps strengthen the integrity of adhesion between the alumina substrate and the NASICON film.

4.3.3 Effect of Electrode Configuration on the Electrical Properties - EIS

Despite the fact that the conductivity of bulk NASICON is well explored, the spectral studies are scanty and not well understood in light of thick films configurations. In this section the conductivity and spectral measurements of NASICON thick films employing AC impedance spectroscopy as a function of film thickness is reported. Furthermore, different electrode configurations that resemble the commonly used configurations in planar gas sensors so that it can reflect closely the electrical behavior of NASICON during sensing will be presented.

Electrode configuration on the thick film was varied in order to investigate the effect on the electrical properties. These were:

- in plane configuration (IP) - where the Pt electrodes were printed on top of the film
- across the plane (AP) - where the electrodes were printed across the film, i.e on either side of the film
- in plane bottom (IPB)- where the electrodes were printed on the substrate and then the film on top of the electrodes.

This is shown in Figure 4.21.

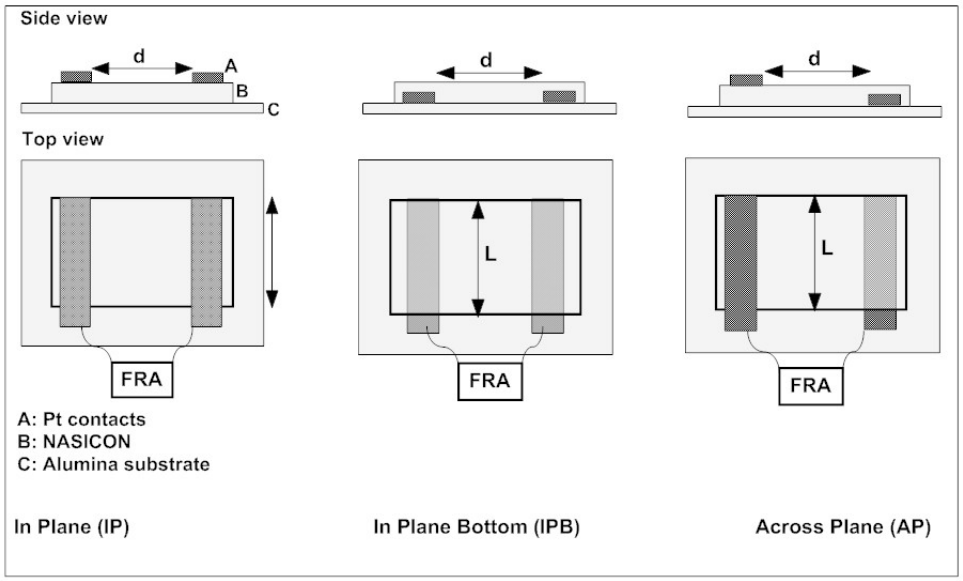

Figure 4.21 – Thick film electrode configuration. In plane (IP), In plane (IPB) and Across plane (AP).

The IP configuration printing was conducted by printing NASICON on the substrate, drying and firing. Platinum strips were then printed as electrodes. Finally wire bonding was conducted by attaching Pt wires on the strips using Pt ink. After drying the device was fired at 850 °C for 30 minutes. This is the commonly used configuration in planar sensor such as those used by Sahner et al. [14], Wang and Kumar [86], Miyachi et al. [99].

For the IPB configuration, platinum was firstly printed, dried and fired at 850 °C. NASICON was then printed on top, dried and fired at 1100 °C. The last step was wire bonding.

Finally for the AP electrode configuration, one electrode was printed on the substrate, dried and fired. NASICON was then printed on top, dried and fired. Another strip of Pt electrode was printed on the opposite side. Pt wire was then attached to the strips and wire bonded in the furnace. This configuration is was used by Kida et al. [94], Shim et al. [17].

The measurements obtained here are related to the surface conductivity measurements. There is limited or no information in the literature on the AC impedance measurements of NASICON thick films with the present electrode configuration. Based on the sample dimensions and electrode arrangement shown of configuration IP, the surface resistivity (ρ_s) is determined from surface resistance (R_s). R_s or $Z_s(\omega)$ is the ratio of voltage V to the current I_s flowing between the two electrodes. Thus

$$R_s = \frac{V}{I_s} = Z_s(\omega) \tag{4.3}$$

Surface resistivity, (ρ_s) on the other hand is the ratio of voltage drop per unit length d to the surface current I_s per unit length L [24, 137]. Using this ratio and Equation (4.3) we obtain

$$\rho_s = \frac{V/d}{I_s/L} = \frac{V}{I_s} \cdot \frac{L}{d} = Z_s \cdot \frac{L}{d} \tag{4.4}$$

The units are ohm/square or ($\Omega/\square$). From the measured impedance, conductivity is deduced using the reciprocal of Equation (4.4).

Figure 4.22 is a Cole-Cole plot for the IP configurations of the 1DS film. Only single semi-circles can be observed representing a contribution from only grain interiors ($Z_{\text{sample}}(\omega)$) suggesting a single relaxation process. It also can be seen that ionic conductivity is temperature activated and that the existence of these perfect semi circles implies that not only do ions conduct in bulk materials but on the surfaces too.

The perfect semi circular plots are modeled as single RC circuit elements each that represent a combined grain interior and grain boundary resistance. At the lower

frequency side of the semi circle is an arc at 45^{o} angle that can be attributed to the Warburg's impedance and this in real situation is the electrical contribution due to diffusion of species[117, 41]. Indeed as will be seen later, there was some amount of Na that diffused into the platinum and such phenomenon is not uncommon to form alloys.

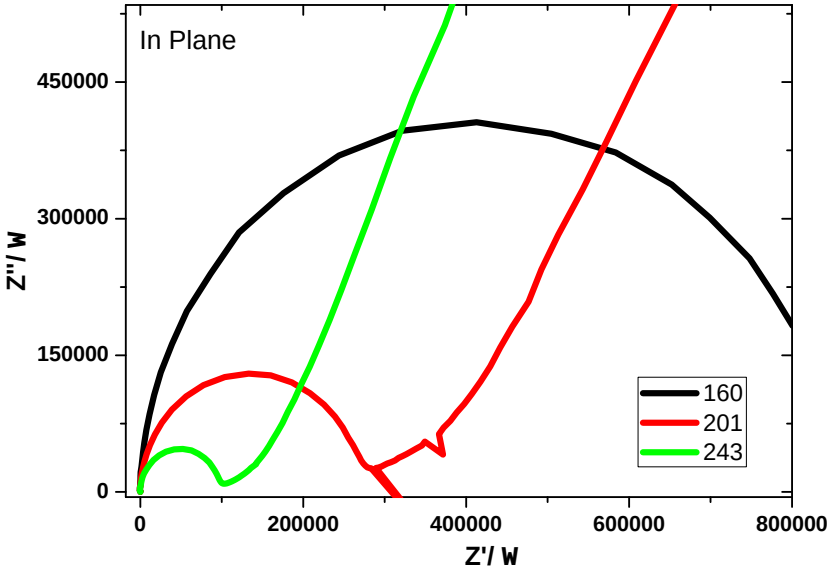

Figure 4.22 – Cole-Cole plot for the IP configuration of the 1DS film and showing the variation of impedance with temperature from frequency range of 32 MHz to 0.1 Hz. Only single semi-circles are evident corresponding to grain interior.

Capacitance values for each RC elements are obtained by determining R from the the intercepts on the Z' axis, and then employing the $\omega_{max}RC = 1$, where ω_{max} is the frequency at the maximum of each semicircle. The values are all in the pico Farad range(10^{-12} Farads) indicating superionic grain conduction [115] also implying that grain boundary contribution is negligible.

The product $\omega_{max}RC$ is also close to unity at every temperature showing consistency of the results and in conformity with theory. This is shown in Figure 4.23.

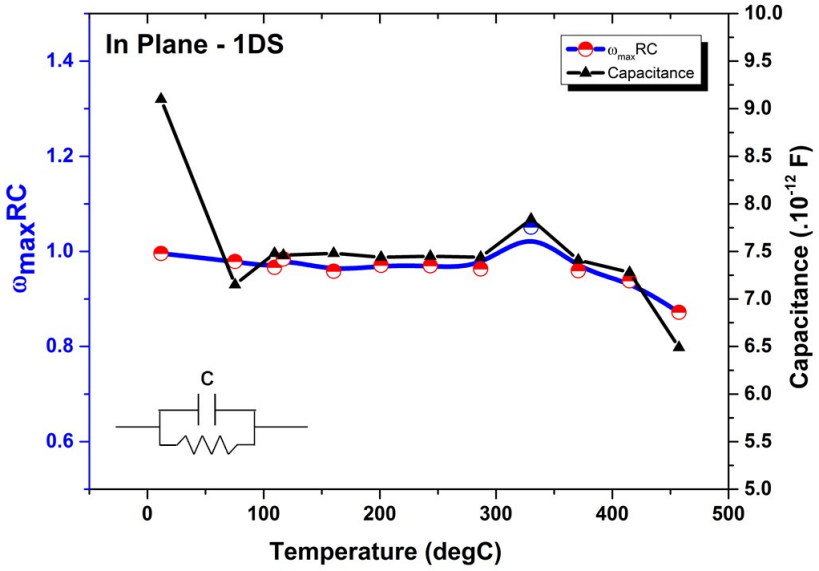

Figure 4.23 – Capacitance values and $\omega_{max}RC$ as a function of temperature on the IP 1DS sample. They are all in pico Farad range indication interior grain conduction. $\omega_{max}RC \backsimeq 1$ and conforms to theory.

Figure 4.24 shows Arrhenius plots of the effect of electrode configuration to electrical properties. Each film thickness against each configuration was compared.

From the figures, it is observed that no significant difference exists in conductivity of the samples whose electrodes are planar configuration, be it on top(IP) or bottom (IPB) while in the sample with the across the plane (AP) configuration had lower conductivity than the planar configurations for all the thicknesses.

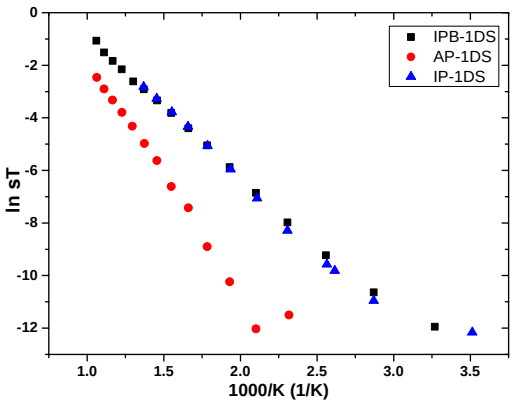

(a) Effect of configuration on electrical properties - 1DS

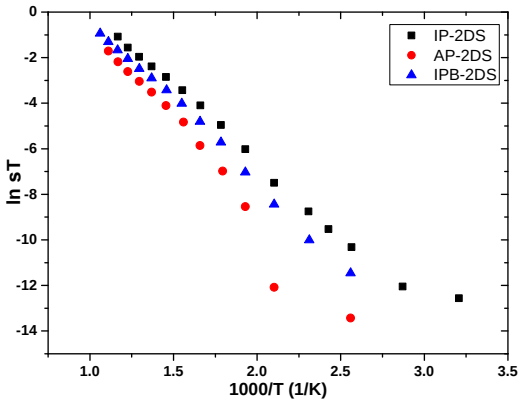

(b) Effect of configuration on electrical properties - 2DS

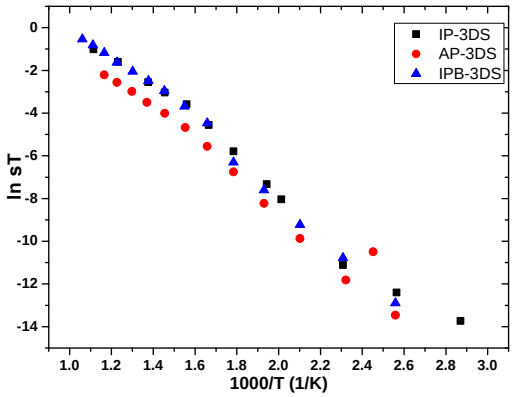

(c) Effect of configuration on electrical properties - 3DS

Figure 4.24 – Arrhenius plots showing the effect of configuration on ionic conductivity.

Table 4.4 is a table of activation energies derived from Figure 4.24. The conductivity exhibited both intrinsic and extrinsic behaviour divided into high and low temperature regions respectively and this is common in ionic electrolytes[41, 138]. All electrode configurations show no significant difference in the conduction as the activation energies at high temperatures are all close to 0.54 eV (or lie in the range $0.51 \leqslant E_a(HT) \leqslant 0.57$ eV). All these exhibit intrinsic behaviour with this similar activation energy.

As has been observed in the Arrhenius plots, conductivity in the the planar

configurations(IP and IPB) is perfectly matched for thinner films (1DS) and is much higher than in the thicker films (2DS and 3DS) probably because thinner films densified much better than the thicker films.

Lastly, across the plane (AP) conduction was less than the basal conduction (IP and IPB) owing to the presence of the resistive zirconia within the interface area and so the conducting species (Na^+) have to encounter this resistance when migrating across the film.

Table 4.4 – Table showing the activation energies of the films of different electrode configurations and thicknesses.

Config. $\curvearrowright \backslash E_a \rightarrow$		E_a(LT)/eV	E_a(HT)/eV
AP	1DS	0.89 ± 0.03	0.72 ± 0.01
	2DS	0.77 ± 0.03	0.55 ± 0.01
	3DS		
IPB	1DS	0.46 ± 0.01	
	2DS	0.65 ± 0.02	0.53 ± 0.01
	3DS	0.78 ± 0.04	0.55 ± 0.01
IP	1DS	0.46 ± 0.01	
	2DS	0.57 ± 0.01	
	3DS	0.51 ± 0.01	

4.3.4 Effect of Film Thickness on the Electrical Properties - EIS

Does the thickness of the film have an effect on the electrical properties of NASICON thick film? Firstly, XRD was performed on the sintered films of different thickness. Also using SEM the thicknesses of samples 1DS, 2DS and 3DS were found to be 20 μm, 31 μm and 32 μm respectively for the IP configuration.

Figure 4.25 shows the XRD reflections of the three NASICON thick films of the IP configuration.

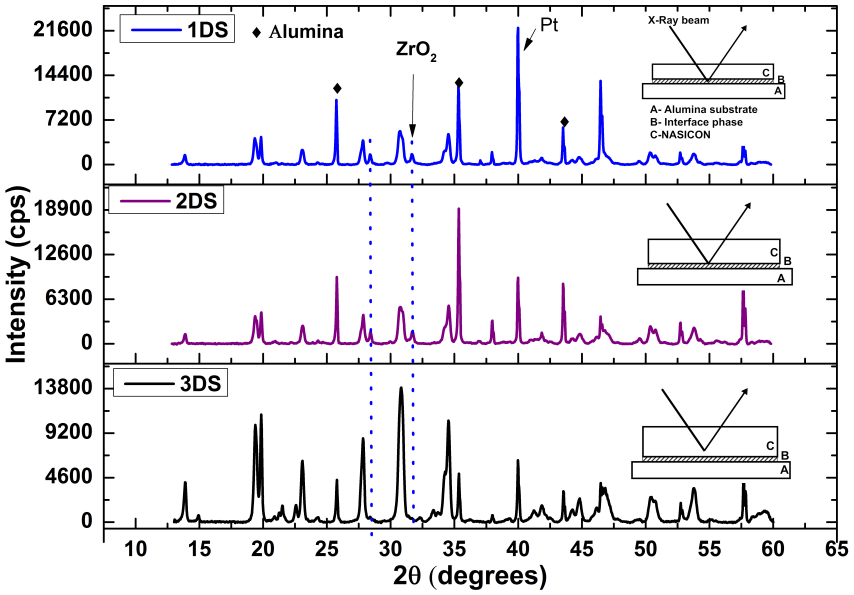

Figure 4.25 – XRD reflections for the thick film NASICON sintered at 1100 °C for 60 minutes. The insets are a sketch of the proposed reason why a zirconia phase is observed in thinner films, 1DS, 2DS and not in the thicker film, 3DS.

The thinner films, 1DS and 2DS had some observed traces of zirconia due to the reasons stated earlier in Section 4.3.2. The fact that the thicker film, 3DS, does not show the zirconia phase implies that the presence of zirconia in 1DS and 2DS thick films is not to a large extent due to the volatisation as reported by other workers[86, 94] but due to zirconia precipitation at the interface and this is not accessed by the X-rays since it is thicker than the 1DS and 2DS films. On the other hand, in terms of densification, the thinner films were more smooth and shinny showing better densification and this positively impacted on the electrical conductivity.

Figure 4.26 shows a backscattered image of a cross-section of NASICON thick film sample after AC impedance measurements. It can be seen that NASICON

underwent a compositional change at the interface that was in contact with the alumina substrate. The thickness of the interface layer was found to be constant in all the samples, that is, it was independent of the NASICON film thickness and was found to be approximately 7 ± 1 μm.

This implies that there is a minimum thickness of NASICON that can be printed and used in high temperature applications, should be $>> 7$ μm in order to retain the original intrinsic properties of NASICON.

From the XRD patterns and the inset sketches in Figure 4.25, since the thickness of the interface layer is constant, X-rays were able to penetrate through the entire thickness of NASICON film up to the interface except in the thickest film, 3DS examined in this study. This could have been the probable reason for observing zirconia traces in the thinner films and not in the thickest film, 3DS in XRD patterns shown in Figure 4.25. In terms of electrical conductivity therefore, the presence of zirconia at the interface would not seem to affect the surface ionic conductivity unless the film is less than 7 ± 1 μm thick.

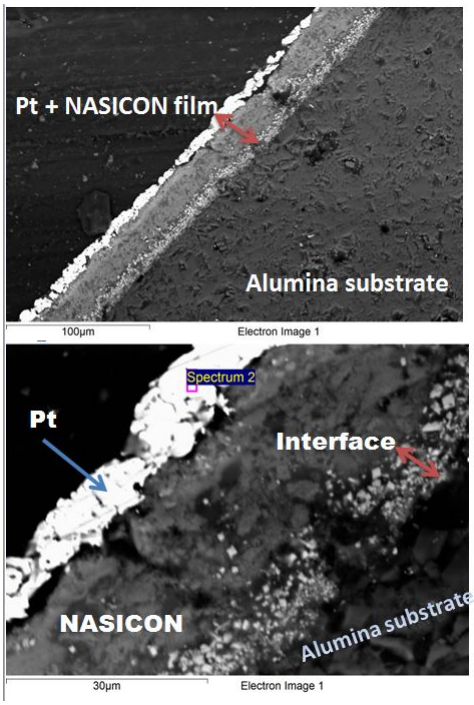

Figure 4.26 – Backscattered SEM image of NASICON thick film (2DS) on alumina substrate coated with Pt (IP configuration). A zirconia rich phase is observed at the interface.

Figure 4.27 show the dependencies of the three thicknesses to conductivity. Comparison of conductivity as a function of temperature reveals that there is no systematic dependence of conductivity with thickness above 600 K in planar configurations of Figures 4.27b and 4.27c indicating that conduction is indeed a surface phenomenon in NASICON thick films and not thickness related. There is however the expected extrinsic behaviour at lower temperatures due to the different amounts of impurities in films having three different thicknesses.

There is however different behaviour on conductivity across the film in the AP configuration. It can be seen in Figure 4.27a that thicker films (2DS and 3DS) are more conductive than the thinner films(1DS).

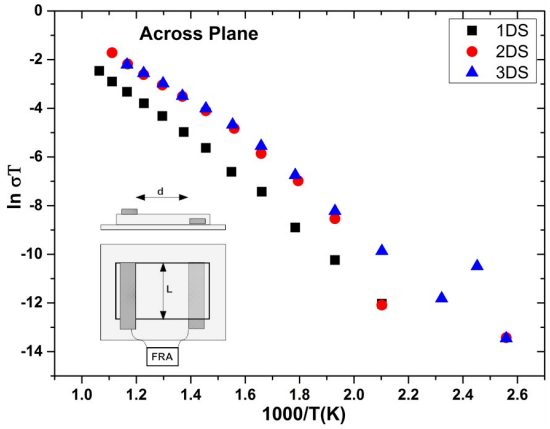

(a) AP (vertical) configuration versus thickness.

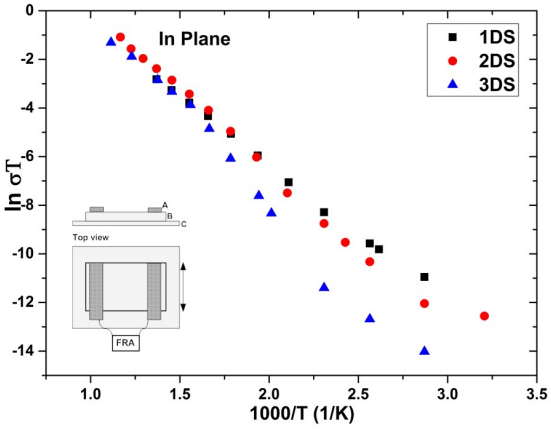

(b) IP(basal) configuration versus thickness.

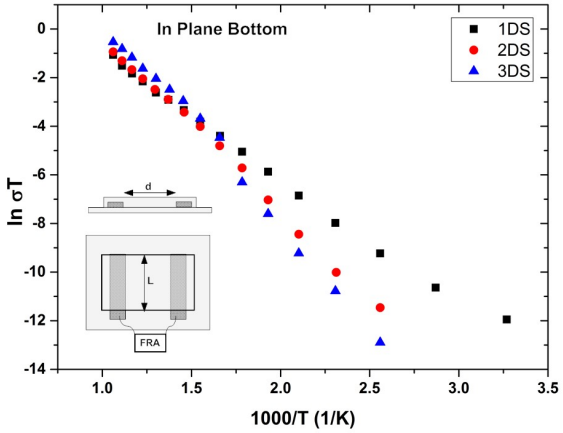

(c) IPB(basal bottom)configuration versus thickness.

Figure 4.27 – Arrhenius plots on the effect thick film thickness on the electrical properties.

Since the thickness of the zirconia film at the interface is constant for all the thicknesses with the same thermal pre-treatment history, the thicker the film, the more pure the bulk of the film is therefore thicker films are more conductive. This is the reason why as the thickness increased more, the corresponding increase in conductivity eventually saturates as is shown in the 2DS and 3DS. This is because conductivity is an intensive property therefore, the conductivity eventually ceases to respond to increase in thickness after a critical film thickness is attained.

Furthermore, values of activation energies are higher than that reported in literature for bulk NASICON as well as the measured value (of pellets) in this research but it is in perfect agreement with 0.57 eV obtained by Wang and Kumar [86] for alumina containing NASICON film. The values of activation energy obtained in this study are close to the values reported by Fuentes et al. [139, 140], Funke [127] on pellets. From this finding it is apparent that the ions encounter a higher energy barrier in surface conduction than in bulk.

4.3.4.1 Skin effect

To ascertain whether the non-dependence of surface conductivity to film thickness especially at higher temperatures is due to skin effect[3], the skin depth (δ_s) was calculated as a function of frequency and conductivity. This is given by

$$\delta_s = \sqrt{\frac{2}{\sigma\omega\mu}} \tag{4.5}$$

where σ is the material conductivity, $\mu = \mu_r\mu_o = 4\pi\times10^{-7}$ H/m is the conductivity magnetic permeability and ω is the radian frequency[132]. The value of μ_r is taken as unity for a non magnetic material such as NASICON. This implies that the electrical conduction will only be limited to the skin of the surface regardless of the thickness thereby masking the intrinsic effects of thickness or interfacial reaction between substrate material and NASICON, on surface conductivity.

A plot of skin depth vs frequency at each temperature is given in Figure 4.28. It can be seen that due to lower magnitude of the surface conductivities in NASICON,

[3]**Skin effect** is the tendency of an alternating electric current (AC) to become distributed within a conductor such that the current density is largest near the surface of the conductor, and decreases exponentially with depths in the conductor [132].

skin effect does not have significant influence on the overall conductivity of NASICON in the experimental condition as the calculated values of skin depth are, $\delta_s \gg t$ where t is the film thickness.

The insert of Figure 4.28 is skin depth as a function of temperature at a frequency of 32 MHz, representing the smallest skin depth at each temperature in the present experimental setup. The smallest skin depth is ~ 9.85 m and occurred at a temperature of 457 °C indicating immunity of thick film NASICON to skin effect.

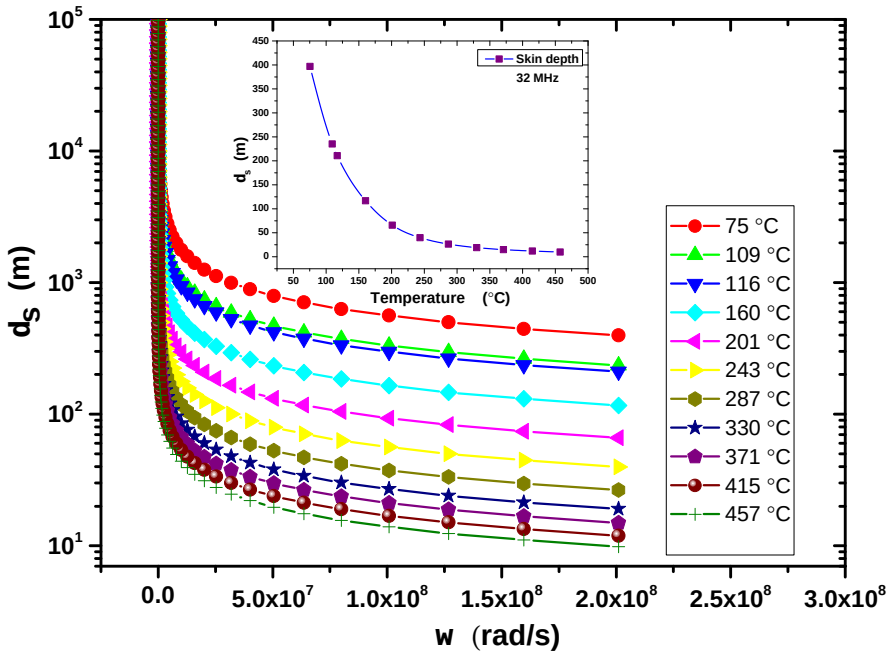

Figure 4.28 – Skin depth as a function of radian frequency. The inset is a plot of skin depth as a function of temperature.

4.3.5 Spectral Analysis

The study of ion dynamics is conducted through the spectral analysis of the electrochemical impedance spectroscopy (EIS) data. The spectral analysis of the thick film here in was based on the in plane (IP) electrode configuration.

Measurement of AC conductivity, ($\sigma(\omega) = \sigma'(\omega) + j\sigma''(\omega)$), generally shows a frequency dispersion where, the real part of AC conductivity ($\sigma'(\omega)$) is frequency (ω) dependent. Each curve may be characterized by a low-frequency plateau, which corresponds to the DC conductivity of the material, and a dispersive region at high frequency, which corresponds to the ionic or AC conductivity. The behavior obeys the Jonscher's power law [141] called the universal dielectric response (UDR) and it is found to vary with angular frequency according to Equation (4.6);

$$\sigma = \sigma_{DC} + A\omega^n \tag{4.6}$$

where σ_{DC} is the DC conductivity, A and n are temperature-dependent parameters.

Frequency dependence of conductivity of the thinnest sample (1DS) of NASICON examined in this study at various temperatures is shown in Figure 4.29. Three regions are observed here. Low frequency dispersive region, plateau and high frequency dispersive region. The first low frequency dispersive region may be due to polarization effects (sample electrode interface phenomena (SEI)). This is because as frequency decreases, more and more charge accumulation takes place at the interface leading to a decrease in the number of mobile ions subsequently lowering the conductivity. This was also observed by other workers [142, 143].

Furthermore, the relaxation time could be as long as 10s hence giving enough time for ion polarization to take place. Since electrode effect is more pronounced at high temperatures this could be the reason for the spectra curving in to almost zero in higher temperature plots of Figure 4.29.

The plateau represents the DC conductivity and is independent of frequency. The dispersive region at high frequency ($(10^4 - 10^8)$Hz) represents the AC ion conductivity. In this region the mobility is high hence conductivity increases with

increasing frequency. This dispersive-plateau pair is distinctive of a non-random hopping mechanism[4][142, 144].

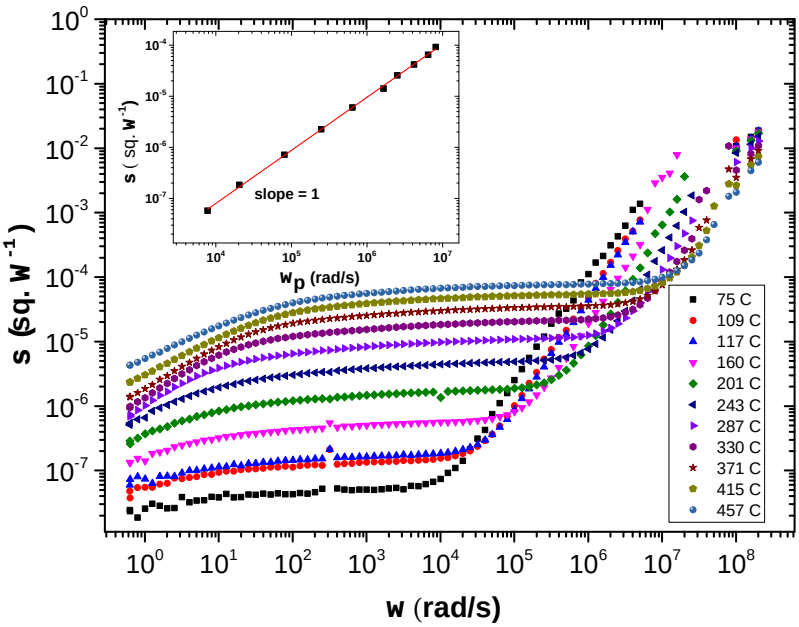

Figure 4.29 – Conductivity dispersion of NASICON for the 1DS sample. The inset is a plot of log σ vs log ω_p.

Furthermore it can be clearly seen that the crossover frequencies[5] ω_p increases with temperature or shifts towards high frequency with increase in temperature. The logarithmic plot between DC conductivity and cross over frequency (ω_p) shown as a solid line in the inset of Figure 4.29 gives a unity slope, which perfectly agrees with the AC conductivity formalism [127] implying that the DC and AC conductions are closely correlated to each other and that they are of the same mechanism[145] or that the characteristic angular frequency ω_p is activated with same thermal activation energy as the dc conductivity, as expected[144, 143].

[4]In a case where each conducting ion is normally surrounded by vacant neighbouring sites, the non-random hopping (correlated hoping) is where the backward jumps cannot happen until the intial forward hop occurs[127].

[5]**Crossover frequency** is a frequency at which transition from DC conductivity to AC dispersion occurs.

Non-linear fitting (with a goodness of fit ≥ 0.98) of data in Figure 4.29 using Equation (4.6) of the dispersion-plateau pair gave $n < 1$ implying that the hopping motion of Na^+ in NASICON is a big hop translational motion. This is because the value of n might have a physical meaning according to [127] and [146]. For instance, value of $n < 1$ would mean that the hopping motion involved is a translational motion with a big hop [146]. On the other hand, value of $n \geq 1$ would mean that the motion involved is a localized hopping of the species with a small hop without leaving the neighborhood. In this case, for NASICON, the transport phenomena is a long range hopping from one vacancy site to another.

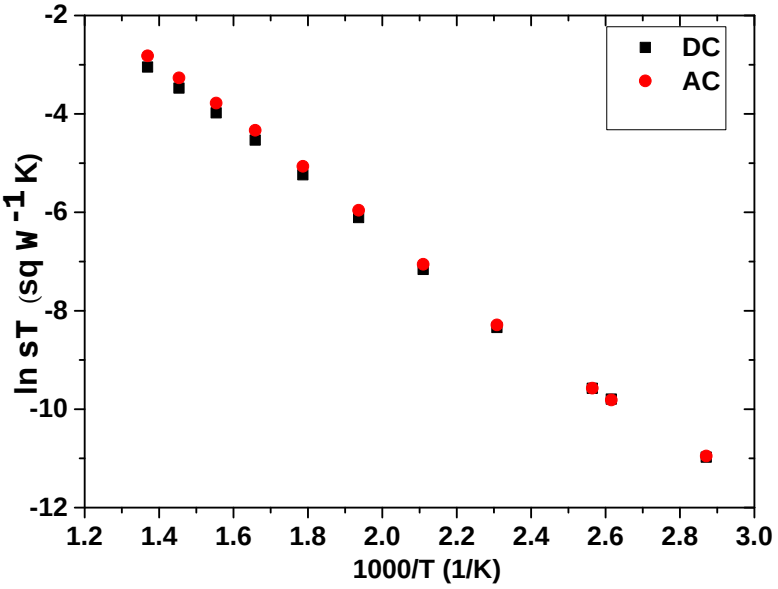

Figure 4.30 – Comparison of DC conductivity obtained from the low frequency plateau with AC conductivity.

Comparison of DC conductivity obtained from the low frequency plateau with AC conductivity using the Arrhenius relation is shown in Figure 4.30. The close correlation in the values implies that the conduction is from the same majority charge carrier, the Na^+, in this case. This also suggests a high transference

number of Na^+ in NASICON.

To study the dynamics of relaxing species, electric modulus formalism is employed. Electric complex modulus is related to complex impedance by [115]

$$M^* = j\omega C_o Z^* = M' + jM''. \tag{4.7}$$

so that substituting $Z^* = Z' - jZ''$ into Equation (4.7) yields $M'' = \omega C_0 Z'$, where C_0 is the vacuum capacitance from the two parallel plate electrodes. For two parallel plates of area A and separation L, $C_0 = \epsilon_0 \frac{A}{L}$.

The exact values of M'' in this work were not determined owing to the complex nature of the vacuum capacitance C_0 between the two electrodes of the sample configuration in thick films shown Figure 4.31. This is because the electrodes that are in contact with the NASICON are not parallel plates anymore but can be modeled as two parallel wires of capacitance,
$C_0 = \frac{\pi\epsilon_0}{ln(d/a)}$, where a is the radius of each electrode wire and this is difficult to determine in the current setting[147]. However, since M'' is dependent of Z' and ω, the relaxation processes and ion dynamics can be studied without the need to know the constant C_0.

Therefore the plot of M''/C_0 vs frequency will still reserve the shapes of the peaks to yield the much needed data of crossover frequencies.

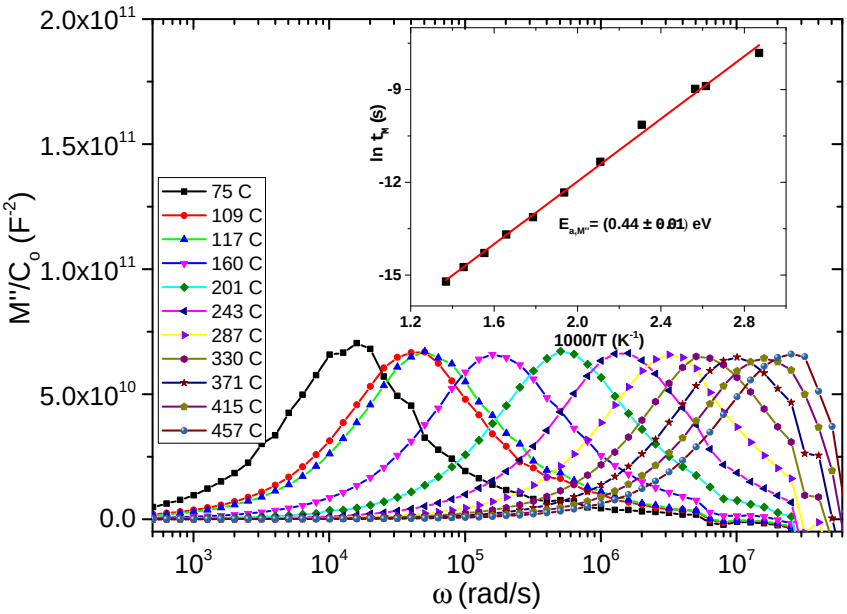

Figure 4.31 – Electric Modulus of NASICON thick film (1DS). Peak frequency decreases with temperature showing a thermal activated process. The inset is the Arrhenius plot of relaxation times.

In Figure 4.31 the variations of imaginary component of (M''/C_0) as a function of frequency (ω) at different temperatures show clearly resolved peaks at unique peak frequencies, with the peaks showing a tendency to shift towards higher frequency end with increase in temperature. This behaviour suggests a conduction mechanism which is a thermally activated type of correlated hopping of Na^+ ions. The crossover frequency (ω_p) is the frequency of transition from long range to short range hopping of ions from the low frequency to high frequency regions respectively.

The high frequency side of M''/C_0 represents the range of frequencies in which charge carriers can only make localized motions within their spatial confinement of potential wells[148, 142]. The inverse of the crossover frequency gives the characteristic relaxation time and follows the relation in Equation (4.8)

$$\tau_M = \tau_{o,M} \exp \frac{E_{a,M}}{kT} \tag{4.8}$$

where τ_o is a pre-exponential factor of relaxation time and T is the absolute temperature. This relation is shown in the inset of Figure 4.31.

The activation energy of relaxation is $E_{a,M} = 0.44 \pm 0.01$ eV which is comparable with the conduction activation energy value of 0.46 eV obtained in this study. This result implies that ions have to overcome same energy barrier whilst conducting as well as relaxing [142].

The main advantage of using modulus spectroscopy is that, in this formalism the information about the electrode effect is suppressed and one can easily study the intrinsic effect of the sample that originates from electro-active region (i.e., grain) in the sample. This formalism is also helpful in the study of conductivity relaxation time.

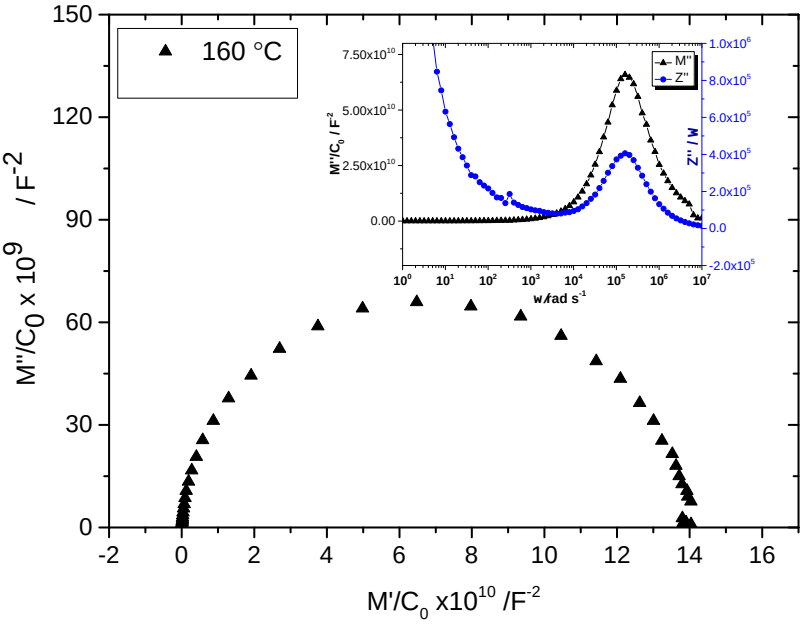

Figure 4.32 – Cole-Cole plot of M''/C_0 against M'/C_0 to exclude electrode effects. The inset is the frequency dependence of Z" and M''/C_0 at 160 °C.

Figure 4.32 is a plot manifesting the suppression of electrode effects when M'/C_0 is plotted against M''/C_0. A perfect semi circle is obtained. The inset shows how electrode effects seen in the low frequency tail of Z'' are suppressed in the modulus formalism plot. In the inset it can be observed that Z'' and M'' peaks occur at the same frequency implying grain contribution to impedance relaxation.

4.3.6 Scaling

Scaling is a vital feature in any data evaluation program to normalize data for better comparison of different data sets. The study of the conductivity spectra and relaxation of conducting samples at different temperatures leads to scaling laws, $\sigma(\omega)/\sigma_{DC} = \sigma'/\sigma_o = F(\omega/\omega_c)$ and $M''/M''_{max} = F(\omega/\omega_c)$ respectively, known as the time-temperature superposition principle (TTSP) where ω_c is an arbitrarily determined characteristic frequency[149, 143].

Here, $\omega_c = \omega_p$ and $M''_{max} = M''(\omega_p)$. This scaling which collapses all data sets into one common curve indicates that the process can be resolved into a common physical mechanism modified only by thermodynamic scales[149].

Figure 4.33 shows the TTSP of conductivity and relaxation. In Figure 4.33a the conductivity spectra at different temperatures collapsed into a single curve at higher frequencies on appropriate scaling. However, the low frequency part of the plot does not collapse into a single plot due to varying contribution from electrode.

Furthermore, similar scaling of modulus as shown in Figure 4.33b reveals a perfect overlapping of different temperature data into a single master curve indicating a single relaxation process occurring within the sample. There is a perfect overlap even at low frequencies since modulus suppresses electrode effects. This is also observed in the inset plot of Figure 4.32.

From these findings, it is clear that the TTSP is observed implying that relaxation mechanism at the higher frequency is independent of temperature. Also observed in the Figure is the single boundary/knee at which crossover frequency occurs implying that the material has only single ionic species whose conduction mechanism is independent of temperature.

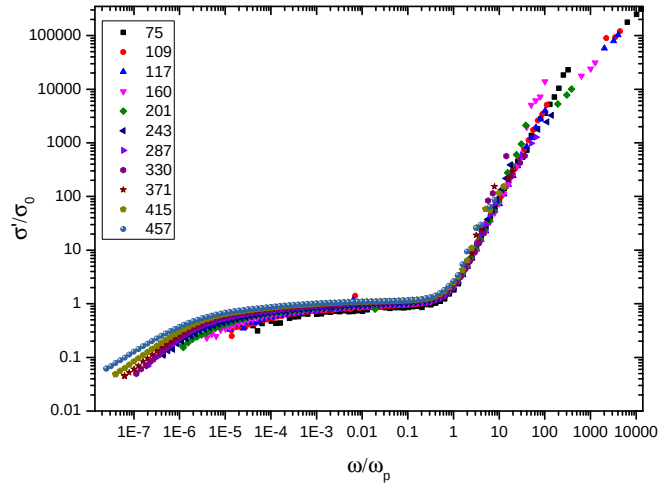

(a) Conductivity Scaling. The conductivity collapsed to a single curve indicating temperature independence of relaxation at higher frequency

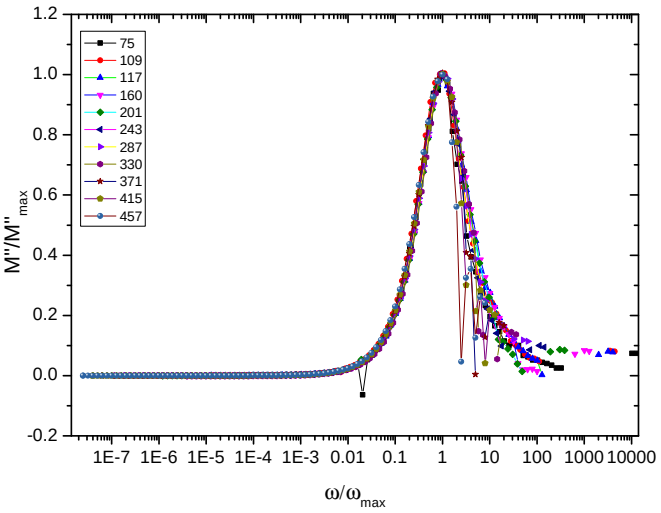

(b) Modulus Scaling. The modulus collapsed into a single curve and no electrode effect is observed at lower frequencies.

Figure 4.33 – Scaling formalism in conductivity and modulus.

Finally modulus and conductivity scaling is compared with thickness of the film. Figure 4.34 shows the effect of thickness on the relaxation process as well as conductivity. It can be seen that all the plots for different thicknesses overlapped into single master plot both for conductivity and relaxation implying that the

relaxation (Figure 4.34) and conduction mechanism(inset) are not dependent on thickness at least for films less than 32 μm investigated in this study.

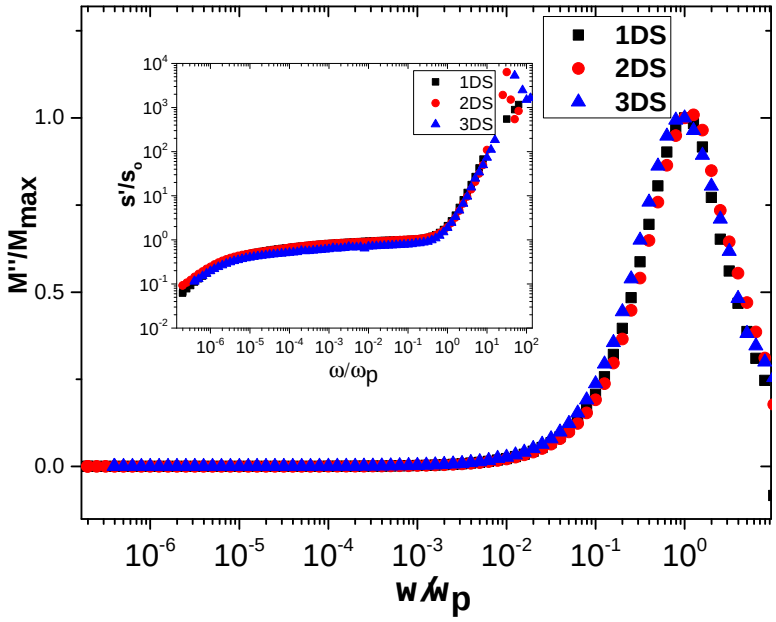

Figure 4.34 – Scaling vs Thickness

4.4 Conclusions

- The new procedure of NASICON synthesis has produced fine, single phase NASICON powders which need no further cycles of re-calcination, milling and grinding. A single phase is obtained in just one attempt of calcination at 1000 °C for 1h and the powder is ready for thick film slurry making.
- The maltose-pectin incorporated NASICON procedure was able to obtain very fine powders but the explosive nature of the calcination process limited its use because a lot of powder was lost during calcination.
- NASICON paste/slurry was successfully made from the resulting powders.
- Optimisation of sintering schedules of NASICON thick film on alumina

substrate revealed a narrow window in which a well densified, sintered film and an almost phase pure NASICON is obtained. On either side of the window, the film won't sinter or, the film will sinter but the NASICON phase would be denuded leaving a precipitation of zirconia and traces of other phases. Therefore a sintering schedule of 1100 °C for 60 minutes was found appropriate.

- Effect of electrode configuration on electrical conductivity showed no significant difference in conductivity when the electrodes were in a basal/planar configuration(IP and IPB) but a much lower values than in the planar when the electrodes are placed across the thickness of the film(AP).

- Effect of film thickness on electrical conductivity: Varying film thickness as well showed no difference in surface conductivity in the intrinsic regions (high temperature region) while at lower temperatures thinner films possessed higher conductivity than thicker films(because thinner films sintered better than thicker films).

- Spectral conductivity studies showed that Na^+ conduction was of long range hopping while scaling studies showed that surface ion conductivity and relaxation were independent of temperature and thickness. Skin effect due to high frequency alternating electric-field also had no effect on surface conductivity because of the low magnitudes of the conductivity values involved.

- Thick film surface conduction activation energy ($E_a = 0.46$ eV) is much higher than the bulk activation energy ($E_a = 0.21$ eV) reported in literature [150]. The values of conductivity and relaxation activation energies suggest that ions whilst conducting and relaxing overcome the same energy barrier.

- SEM investigation showed that the film thickness for which NASICON can be printed on alumina substrate and used in high temperature applications (up to 1100 °C) successfully should be significantly greater than 7 μm and less than that, the entire film may undergo phase change, zirconia being the dominant secondary phase.

Chapter 5

Materials Characterisation II - Cu-Al-O and Na-Ti-O

5.1 Introduction

Establishing a known sodium oxide potential at the reference electrode is key to the proper operation of a Nernstian solid electrolyte sensor, in this case a cell that is represented as : **Sensing electrode | NASICON | Reference electrode**. Therefore the importance of a reference electrode (RE) can never be underestimated.

In a sensor that has NASICON as solid electrolyte especially in the form of thick film the progressive precipitation of zirconia and other reactions between the alumina substrate and NASICON may slightly change the NASICON composition hence the Na_2O potential may not be uniquely fixed if no RE is used in a sensor.

In this chapter, characterisation of the inter-oxides in Na-Ti-O and Cu-Al-O systems synthesised as described in Chapter 3 is given. Biphasic mixtures of NT6-TiO_2 and NT6-NT3 were proposed to be used as sodium reference while the

$CuAlO_2$-$CuAl_2O_4$-Al_2O_3 mixture was proposed to be used as an oxygen buffer in the final sensor.

5.2 Cu-Al-O System

Detailed synthesis characterisation of $CuAlO_2$ as well as its electrical properties is reported. The $CuAlO_2$ in this case is the main material of interest as it was also used to obtain the three phase material of $CuAlO_2$-$CuAl_2O_4$-Al_2O_3.

5.2.1 $CuAlO_2$

$CuAlO_2$ (CAO) is a delaffosite p-type semiconductor with a band gap of ≥ 3.0 eV [151, 152]. The visible transmittance of the CAO can be as high as 80%, suggesting that CAO can be considered as an ideal candidate for p-type transparent conductive oxides (TCOs)[153].

TCOs find applications in a wide range of optoelectronics devices such as solar cells, flat panel displays and touch panel controls as transparent electrodes. Most of the transparent films are made up of n-type semiconductors from oxides and their doped versions of SnO_2, In_2O_3, ZnO[154, 155]. These are readily available. However in the formulation of p-n junctions meant for transparent elements such as transistors and diodes, transparent p-type semiconductors are required. Their development has been a challenge as observed by Scanlon and Smith [156].

It was not until 1997 when Kawazoe et al. [152] first reported a simultaneous p-type conductivity and optical transparency of the $CuAlO_2$ thin films that spurred extensive research for these type of materials and led to a discovery of many other delaffosite-type compounds such as $CuMO_2$: (M= B, Cr, Sc, Y, Eu, Ga)[157] and $SrCu_2O_2$[158].

More importantly, in the scope of this research, $CuAlO_2$ also find use in gas sensing applications such as in ozone gas sensing[159, 160] and will be used as precursor for a buffer in the sensor in this research.

In terms of synthesis, a number of methods have been employed for the synthesis of bulk CAO, such as wet chemical synthesis (Sol-gel, hydrothermal)[155, 153, 161, 162, 163], and the conventional method involving a prolonged solid state reaction of Cu_2O and Al_2O_3[152, 164, 165, 166]. Other solid state reactions involving boehmite(AlOOH) and Cu_2O have also been reported recently[167, 168]. The synthesis temperatures involved here are always in the excess of 1100 °C and for prolonged reaction times, ranging from 3 to 96 hours as shown in Table 5.1. Despite all this, obtaining single phases and well crystallined material has been a problem as observed from their XRD patterns. Recently, Jarman et al. [169] synthesized CAO using the Pechini method and obtained a pure phase at the reaction time of 3 h and calcination temperature of 1100 °C. Despite the success, the number of stages and reagents involved for the preparation for the CAO still make the conventional process economical and less involving. Amrute et al. [166] also synthesised CAO using solid state reaction, one in air and the other one in nitrogen. After 30 h of reaction at 1100 °C CAO reacted in air was 100 % pure while the nitrogen environment obtained only 70 % pure CAO.

In the new procedure of this research, it has been shown that an argon environment and quenching under graphite effectively produces a 100 % pure CAO in just 1.5h. There is therefore significant energy saving with respect to reaction temperature and durations in the new procedure than in the processes shown in Table 5.1 by various researchers.

Table 5.1 – Calcination temperatures and durations for the synthesis of CAO. **WC: Wet Chemical, SS: Solid State**

Method	T (°C)	Dur. (h)	Environ.	Refs
SS	1100	10/2.	N_2/air	[168]
SS	1150	2 resp.	Ar	[167]
SS	1100	>30/30	N_2/ air	[166]
WC	1100/800	24/48	Air/N_2	[163]
WC	320/400	12/4	-	[162]
SS	1050 /1200	96/5 .	Air	[170]
WC	1100	11	Air	[153]
WC	1100	3	Air	[169]
SS	1102	24	Air	[164]
WC/SS	1100	6/15	Air	[171]
SS	1100	24/36	Air	[165]
SS	1100	10	-	[172]
SS	1100	20	Air	[173]
SS	1200	12	Air	[174]
WC	1200	4	Air	[161]
SS	1100	72	Vacuum	[110]

5.2.2 XRD

Fig. 5.1 shows XRD patterns of the CAO powder and pellets annealed at 1150 °C for 1.5 h under argon atmosphere. To study the effect of pelletising, unpelletised samples were also characterised as a control.

It can clearly be seen from the XRD patterns in Fig. 5.1, especially of the pellets,

that a pure phase devoid of any detectable impurity phase or unreacted precursors was formed. This exactly matches with the standard, ICDD 04-010-0381 pattern. However, for the unpelletised sample, very low intensity XRD peaks for CuO at $2\theta = 36°, 38°$ can be seen. The presence of CuO clearly indicates that the unpelletised sample did not fully react during the 1.5 h isothermal heating. As a result, the unreacted Cu_2O might have oxidised when removing the sample from the furnace after isothermal heat treatment. The CAO peaks are also very intense showing a high degree of crystallinity.

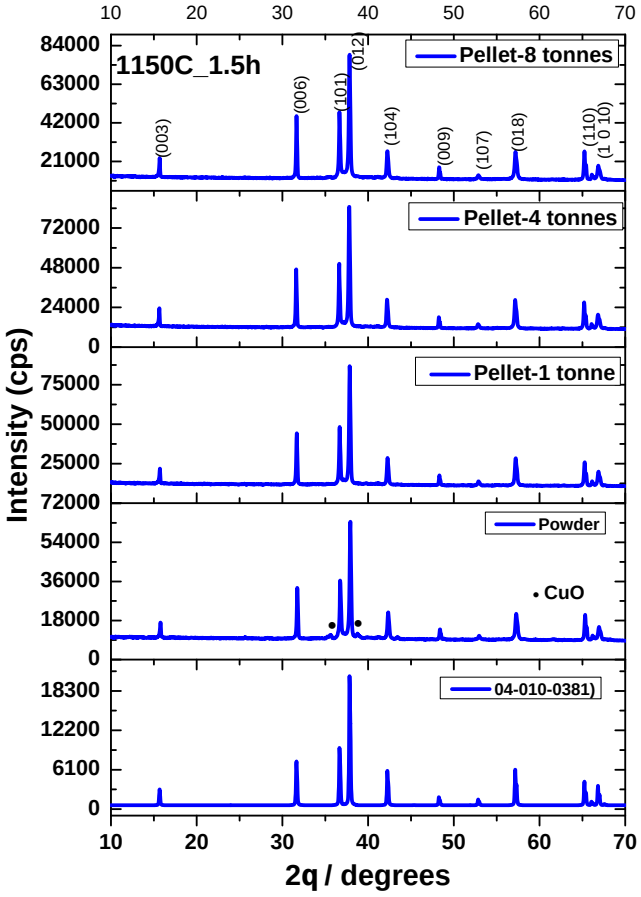

Figure 5.1 – XRD pattern of $CuAlO_2$ powder, and pellets pressed at different loads and calcined at 1150 °C for 1.5 h. At the bottom the standard (ICDD 04-010-0381) is shown as well.

It was also observed that the pelletising load had no observable effect on the kinetics of the reaction, since all pelletised samples gave pure $CuAlO_2$. From this observation, it can therefore be concluded that it is important to pelletise the samples regardless of the amount of load. Figure 5.2 showed that increasing the reaction time above 1.5 h, all samples (powders and pellets) produced a pure $CuAlO_2$ phase. Hence it seems that 1.5 h duration is the lower limit for obtaining a pure phase in pellets at 1150 °C.

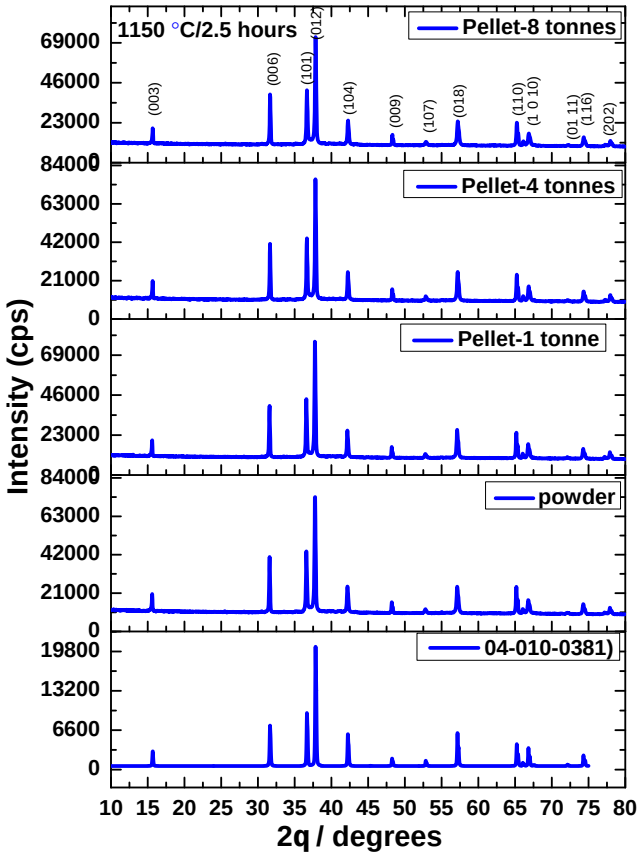

Figure 5.2 – XRD pattern of $CuAlO_2$ powder, and pellets pressed at different loads and calcined at 1150 °C for 2.5 h. For this duration, the phase is fully formed.

The success of the procedure that has ensured a phase pure $CuAlO_2$ within 1.5 h of reaction may be because of

(a) the inert environment which inhibits the oxidation of $Cu^{+} \rightarrow Cu^{2+}$. This is

because the oxide of Cu(I) is more reactive than the oxide of Cu(II) in ambient atmosphere at elevated temperatures [166, 168, 162]. Passing argon having low P_{O_2} helps preserve the reactive precursor for subsequent reaction.

(b) pelletising brings reactive species in intimate contact for easy reaction. In addition, pelletising guarantees that any trace of oxygen in the reaction furnace does not have access to the bulk of the material except for the surface of the pellet.

(c) isothermal firing ensures that only the intended reaction takes place at a particular target temperature, instead of many side reactions which may inhibit or retard the intended formation of CAO due to the formation of CuO which is less reactive.

(d) Quenching the sample under a graphite crucible preserves the CAO phase by preventing the slow formation of $CuAl_2O_4$. This process is oxygen dependent, therefore quenching under the graphite crucible prevents CAO oxidation because graphite acts as an oxygen scavenger. Therefore, to obtain a pure and high quality CAO powder, the powder prepared by conventional method above and annealed at 1150 for 1.5 h would yield the much desired quality of CAO.

Figure 5.3 is an XRD pattern of the three phase material consisting of $CuAlO_2$-$CuAl_2O_4$-Al_2O_3 synthesised by stoichiometricmixing of $CuAlO_2$ with Al_2O_3 and calcining in air at 1150 °C for 3 h. This was formed from the reaction of $4\,CuAlO_2 + 2\,Al_2O_3 + O_2 \rightarrow 4\,CuAl_2O_4$ which is just the required multi-phase system to fix the oxygen potential in the sensor. By calcining in air at 1150 °C for 3 h, the reaction is not complete and this gives rise to the three phases.

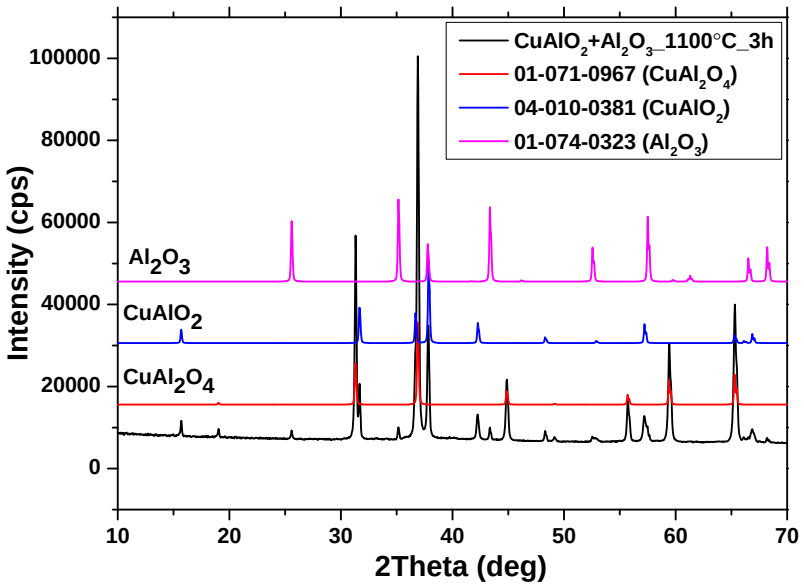

Figure 5.3 – XRD pattern for the calcined product of the reaction; $CuAlO_2 + Al_2O_3$, calcined at 1150 for 3 h. A multiphase product, $CuAlO_2 + Al_2O_3 + CuAl_2O_4$ is observed based on the ICDD standards.

5.2.3 SEM/EDS

Figure 5.4 shows an SEM image and results of EDS scan of the CAO powder annealed at 1150 °C. The top figure indicates that elongated grains are formed during calcination. The crystal growth seems to be more pronounced in one preferred direction. However, the grains are randomly oriented. This has negative effects on the electrical conductivity due to the anisotropic behaviour of the CAO [175, 176]. The microstructure shows that the powder looks sintered at this temperature.

To confirm chemical composition, EDS measurements were performed over the sintered grain. The bottom image shows the scan area. On the right side is the table of elemental composition.

From the table, the ratio, Cu/Al = $\frac{24.14}{22.15} = 1.08$, suggesting that $CuAlO_2$ may be slightly non-stoichiometric having an excess of Cu^+.

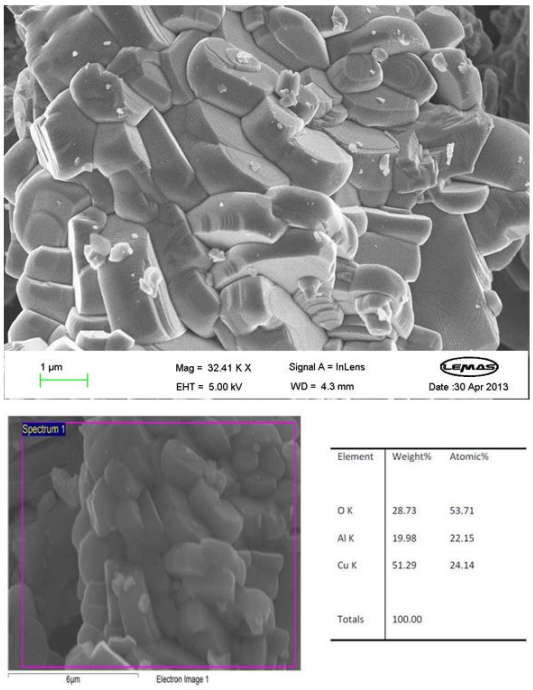

Figure 5.4 – EDS/SEM measurements on sintered CAO. The bottom image is the EDS.

5.2.4 Electrical Properties of $CuAlO_2$

5.2.4.1 AC Impedance Analysis

The temperature dependence of conductivity of CAO has been studied before but mostly below room temperature (RT) by previous researchers [153, 176, 152]. These measurements were on thin films and employing DC measurements technique. Less work has been done on high temperature measurements, although some researchers [164, 177, 145] attempted to measure in the temperature range (in °C) of $302 \geq T \geq RT$. These were thin films too and used DC measurements. [145] used bulk samples and studied AC conductivity from 60 to 200 °C. In this study, high temperature DC and AC measurements were performed over a temperature range of $711 \geq T \geq RT$ °C.

Figure 5.5 shows the Cole-Cole plots from the AC measurements of the sample. As can clearly be seen from the semi-circular Cole-Cole plots, the material conducts ions too. The conduction is a polaronic thermally activated process. This can be seen from the semi circles' diameters decreasing with temperature. The conductivity continues to increase with temperature until a breakdown in ionic conductivity occurs at a temperature of 375 °C. At temperatures higher than 375 °C, no ionic conductivity is observed except for the inductive effects. This can be clearly seen in the inset of Figure 5.5.

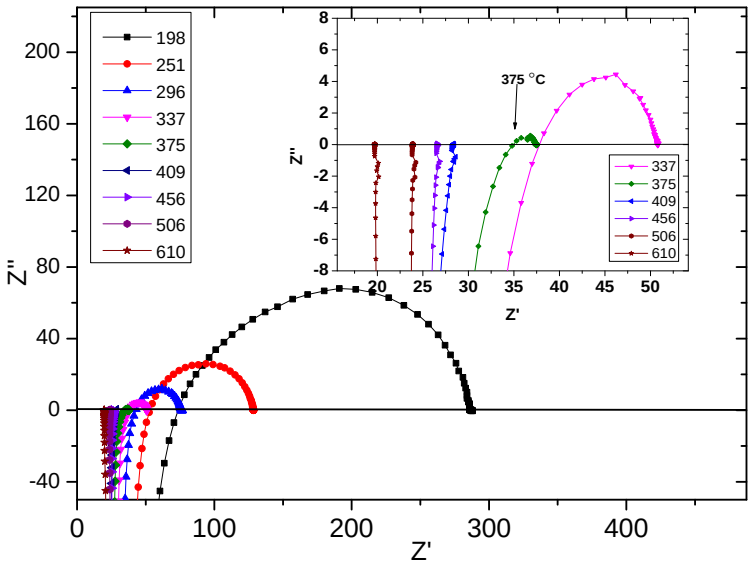

Figure 5.5 – AC Impedance measurements of CAO. The inset shows the temperatures at which there is a breakdown of ionic conductivity. After 375 °C ionic conductivity diminishes.

A comparison of *p*-type (hole) conductivity (from DC measurements) and ionic conductivity (from AC impedance measurements) is shown in the Arrhenius plot in Figure 5.6. The plot conforms to a polaronic thermally activated process. As can be seen from these two measurements, it is clear that the material is a mixed conductor (holes and ions) since both hole and ionic phenomena could be

measured through DC and AC measurements respectively over a selected range of temperatures.

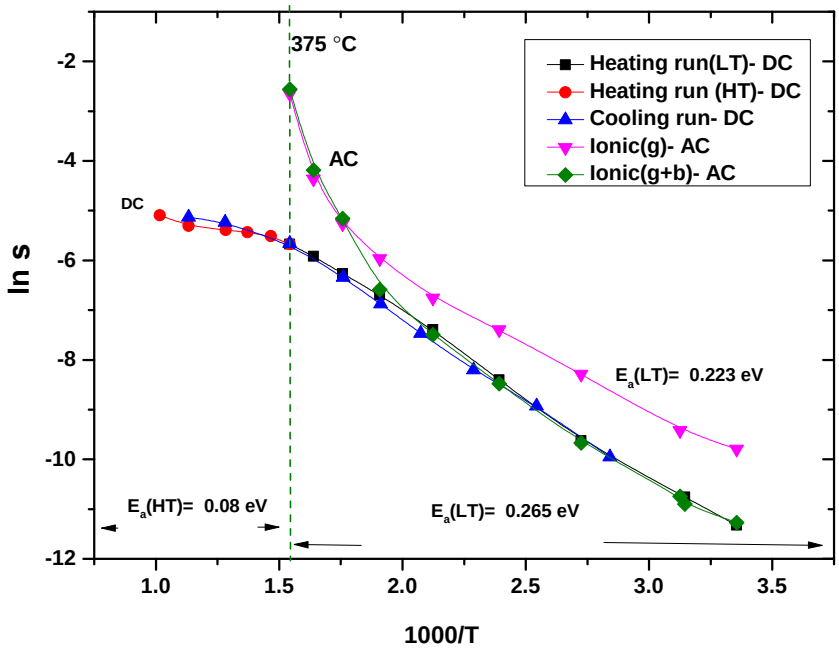

Figure 5.6 – Arrhenius for DC and AC Conductivities. Ionic(g) and ionic(g+b) are contributions from grains and grain+grain boundary respectively.

The plot attributed to the hole conductivity in the Arrhenius plot shows that DC conduction was reproducible as can be seen from the Figure 5.6.

It can also be seen that conductivity exhibits two segments, high temperature (HT) and low temperature (LT). The slopes of the two segments yield the value of activation energy (E_a), which corresponds to the minimum energy required to transfer carriers from acceptor level to the valence band. The LT activation energy for DC conduction and AC grain conduction were $E_a(LT) = 0.27$ eV and $E_a(LT) = 0.22$ eV respectively. The values obtained in this study are in excellent agreement with each other and are within the range of activation energies reported in literature for both bulk and thin films in the temperature regimes of $T \geq RT$. Table 5.2 shows the activation energy as obtained by various research workers in

comparison with the data obtained in this study.

Table 5.2 – Activation energies and how they compare to this work. Bulk (**B**), thin film (**TF**), lamina crystal (**LC**).

Meas.Type	Sample	T. range/°C	E_a/ (eV)	Refs
DC	LC	-117 - 30	0.20 (c axis) 0.13 (ab plane)	[176]
DC	TF	-196 - 25	0.20	[152]
DC	B	-99 - 35	0.175	[153]
DC	TF	-214 - 25	0.22	[172]
DC	B	-143 - 377	0.26, 0.295	[178]
DC	TF	25 - 127	0.26	[164]
DC	TF	25 - 227	0.25	[177]
DC	TF	679 - 742	0.14	[179]
DC	TF	25 - 467	0.26, 0.23, 0.11	[180]
DC	B	25 - 711	0.265 (LT) 0.08 (HT)	This study
AC	B	25 - 375	0.223	This study

In the present work, it has been shown for the first time that there is a HT regime which begins at 375 °C with an activation energy of $E_a(HT) = 0.08$ eV. This corresponds to the regime where hole conductivity completely dominates and the ionic conductivity ceases to exist. This result suggests a change in conduction mechanism from mixed conductivity (ionic + p-type) in the temperature range of $375 \geq T \geq 25$ °C to intrinsic type behavior above 375 °C. This is because at high temperatures carriers from acceptors become insignificant compared to the thermally generated carriers because of the complete ionization that takes place [181, 182]. This behavior is a hallmark of most semiconductors. The transition

temperature T_{trans} is related by

$$T_{trans} = E_g/k_B(N_C(T_{trans})N_V(T_{trans})). \tag{5.1}$$

where $N_C(T_{trans})$ and $N_V(T_{trans})$ are the effective number of states in the conduction and valence band respectively, at a temperature close to the T_{trans}. The transition temperatures of different ternary adamantine semiconductors similar to delafossites are reported elsewhere[181] and this work reports for the first time the T_{trans} for the delaffosite CAO, being $T_{trans} \simeq 375$ °C which has been reported in [183].

The resistivity values obtained in this study are higher than those reported in the literature probably because of two possible reasons: Firstly, the electrical conductivity in CAO appears to be anisotropic, $\sigma_{ab} = 25\sigma_c$ [176], where σ_{ab} is the conductivity in the a-b plane and σ_c the conductivity in the c-axis, whereas the random arrangement of grains in the bulk sample of the CAO as shown in the SEM images in Figure 5.4 may have played a part in giving rise to a lower conductivity of samples investigated in this study.

Secondly, the presence of an orange brown phase later identified as $CuAl_2O_4$ under the Pt electrical contact coating may have perhaps hindered charge transport. This was also observed by Lee. et al. [176]. After sample retrieval, it was also observed that part of the Pt coating on the sample surface of the pellet had delaminated as a result of the formation of $CuAl_2O_4$ phase at the interface between Pt and $CuAlO_2$, however, on the exposed circumference of the pellet that was uncoated, no signature of $CuAl_2O_4$ was seen. This is believed to be due to the catalytic behaviour of Pt which promotes the formation of $CuAl_2O_4$ at the interface by virtue of the reaction : $Pt + 2CuAlO_2 \rightarrow CuAl_2O_4 + \underline{Pt}_{Cu}$.

Under normal circumstances, the formation of $CuAl_2O_4$ from CAO according to

$4\,CuAlO_2+O_2 \rightarrow 2\,CuAl_2O_4 + 2\,CuO$ reaction which is P_{O_2} dependent is very slow especially at lower temperatures, below 1003 °C at 0.21 atm [184]. This implies that it is important to carefully select the contact electrode metal however noble that may be when it is to be placed in contact with another material containing copper. Supplementary data on this topic is in appendix A.

5.2.4.2 Conductivity Spectral Analysis.

The AC conductivity, $\sigma(\omega)$; obeys the Jonscher's power law called the universal dielectric response (UDR) [141] and it is found to vary with angular frequency according to Equation (4.6). Frequency dependency of conductivity at various temperatures is shown in Figure 5.7.

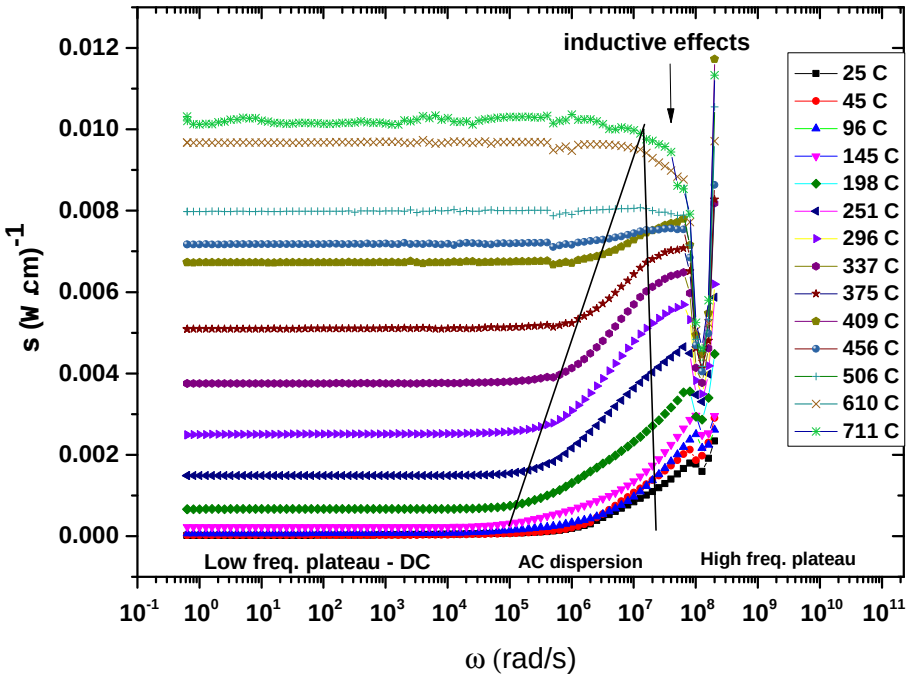

Figure 5.7 – Frequency dispersion of the real part of the conductivity of CAO at different temperatures.

It can be observed that at low frequencies, the real part of conductivity, $\sigma'(\omega)$

is indeed independent of frequency giving rise to DC conductivity while at high frequencies, AC conductivity is dominant.

The existence of such a dispersive regime in the conductivity at higher frequencies rules out the possibility of random hopping of mobile ions and suggests that ionic motion is somehow correlated. The crossover frequency, the frequency at which AC conductivity sets in is dependent on temperature. Just as has been shown in the Figure 5.6, the existence of both the DC and high frequency dispersion in Figure 5.7 confirms that CAO is indeed a mixed conductor. In addition, the figure also confirms the disappearance of ionic conductivity and dominance of DC conductivity at high temperatures which sets in at $T > 375$ °C, the result also observed in Figs. 5.5 and 5.6.

At high temperatures, and at much higher frequencies, there is a second plateau also observed by other workers [127] believed to be due to excitation of Einstein oscillators and transverse optical phonons. Furthermore, at high temperature and frequency, inductive effects are also observed which may indicate ion adsorption. It may explain why copper was observed in the Pt electrode after the measurements leaving an interface rich with copper-deficient aluminate, $CuAl_2O_4$ as explained previously.

Non linear curve fitting employing the allometric power function in origin software was used to fit every single curve of Figure 5.7 to obtain the values of n, A and σ_{DC}. The goodness of the fit were greater than 98%. The DC conductivity obtained was in perfect agreement with the actual DC measurements obtained using a two point probe, except for the slight deviation of about 10% at temperatures above 375 °C when the material is purely non ionic conducting. This is shown in Figure 5.8. The deviation at high temperatures is because of contribution from DC conductivity of the material and electrode contribution since at high temperature

electrode contribution dominates impedance data [148].

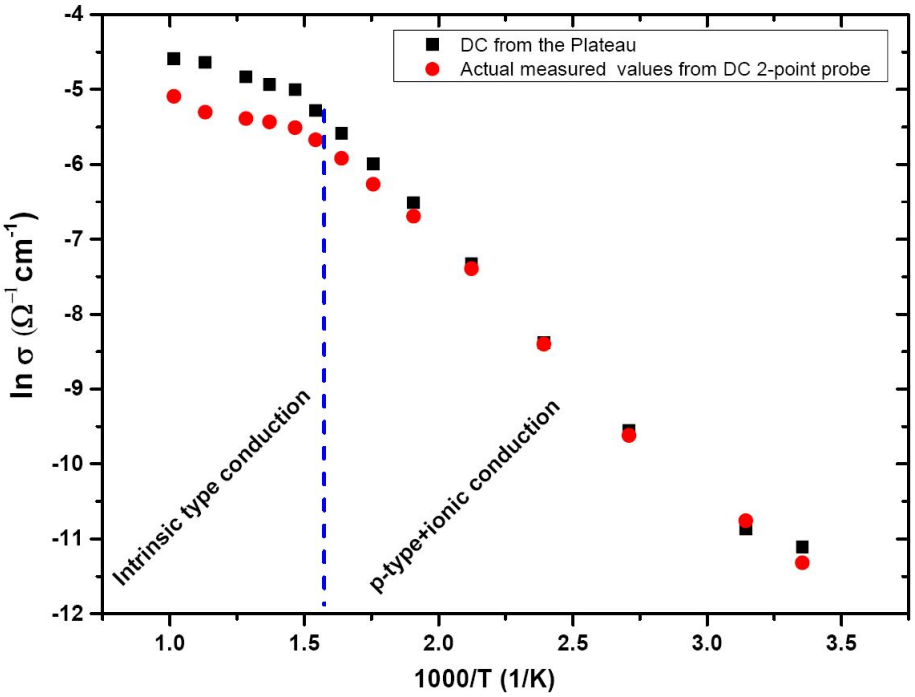

Figure 5.8 – An Arrhenius plot to compare the DC conductivity of the actual measured values against the low frequency values.

The values of n in Equation (4.6) were found to range from 0.5-0.85, and showed no systematic temperature dependence. The values of n in this case implies that for CAO, the transport phenomena is a long range hopping from one vacant site to another.

To determine the hopping frequency, ω_H, the Almond and West formalism [185] was used. This is expressed as

$$\omega_H = \left(\frac{\sigma_{DC}}{A}\right)^{1/n} \tag{5.2}$$

with A and n being temperature dependent parameters obtained from the nonlinear function fitting of the conductivity spectra of Figure 5.7 at different temperatures.

The hopping frequency which is a function of temperature was then fitted to Equation (5.3)

$$\omega_H = \omega_o \exp\left(-E_\omega / kT\right) \tag{5.3}$$

where ω_o is the pre-exponential factor of the hopping rate and E_ω is hopping activation energy.

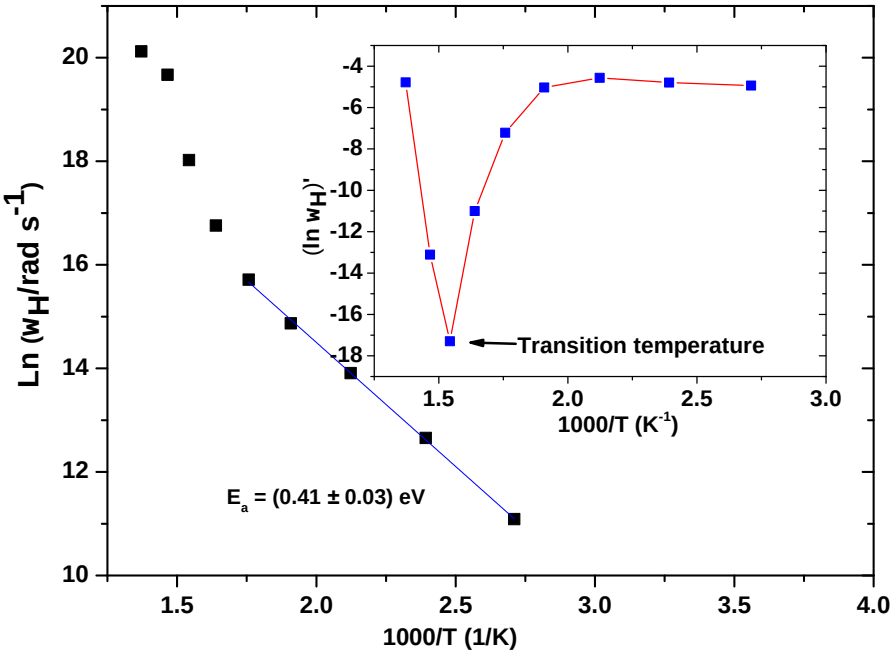

Figure 5.9 – Temperature dependence of hopping rate for CAO. There is a change of slope at temperatures greater than 375 °C. The inset is a first derivative of $\ln \omega_H$ denoted as $(\ln \omega_H)'$ with respect to $1000/T$. The transition point is evident.

The activation energy for hopping is obtained from Figure 5.9 and Equation (5.3). The inset of Fig. 5.9 shows the transition temperature when the first derivative of $\ln \omega_H$ denoted as $(\ln \omega_H)'$ with respect to $1000/T$ is plotted.

The activation energy of hopping, ($E_\omega = 0.41$ eV was higher than the DC activation energy obtained from the Arrhenius equation ($E_a = 0.27$ eV) in Equation (4.1).

This value is however close to the value (0.40 eV) obtained by other workers [173]. This implies that the charge carriers have to overcome a lower energy barrier while conducting than relaxing.

5.3 Na-Ti-O System

Characterisation is performed on the single phase materials of NT3 and NT6 as well as biphasic mixtures of NT6-TiO_2 and NT6-NT3.

5.3.1 SEM/EDS

Figure 5.10 shows an SEM image and EDS data of the NT3 powder. Hexagonal rods can be observed of the NT3 and EDS point analysis confirms that the phase was formed and has close to the theoretical composition.

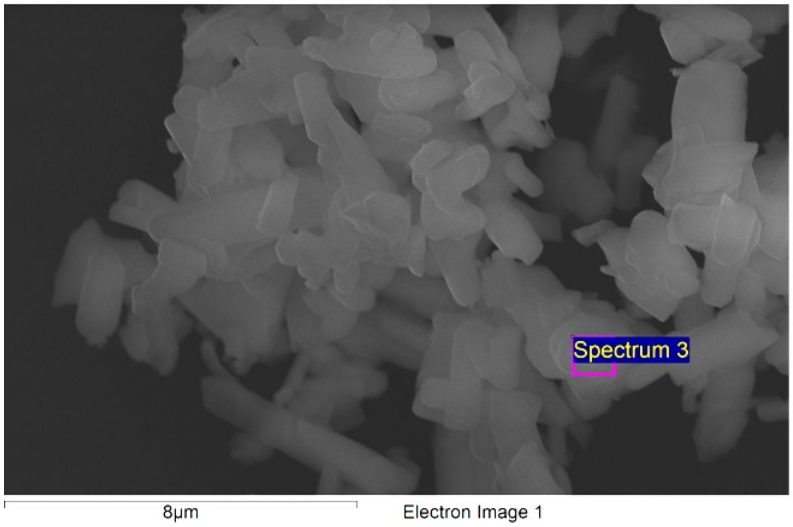

Element	Weight %	Atomic %	Theo. atomic %
Na	24.92	40.88	40
Ti	75.08	59.12	60

Figure 5.10 – SEM and EDS measurement of NT3 powder.

Similarly, Figure 5.11 shows perfectly hexagonal rods of NT6 composition, EDS data is also close to the theoretical value. The arrow in the diagram points to the perfectly visible hexagonal rod.

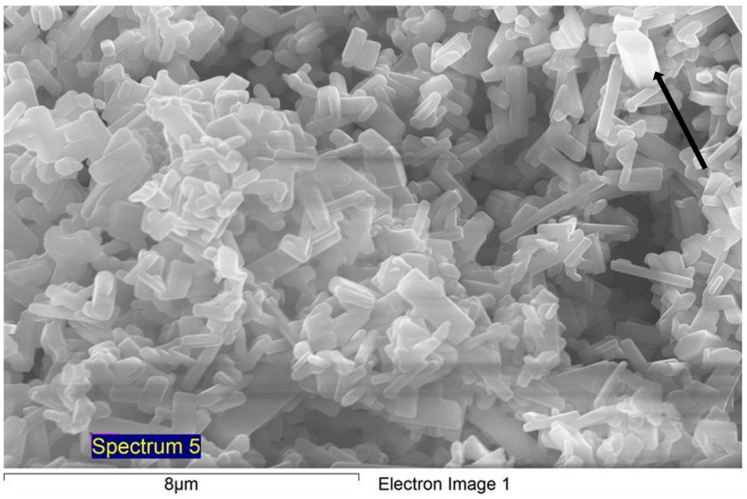

Element	Weight %	Atomic %	Theo. atomic %
Na	12.87	23.53	25
Ti	87.13	76.47	75

Figure 5.11 – SEM and EDS measurement of NT6 powder.

5.3.2 XRD

XRD was performed on the NT6 and NT3 powders to confirm the phase formation during calcination. Figure 5.12 shows the XRD patterns and how they compare with the standard, ICDD patterns. This is in agreement with the EDS data as well as ICDD data. Powders were thus used for thick film slurries and pellets for thermodynamic measurements.

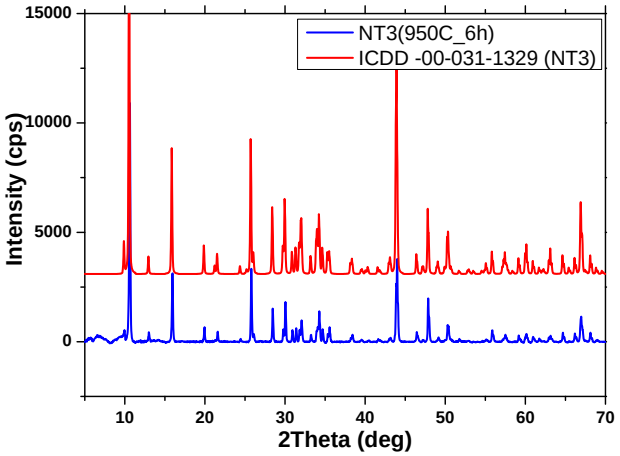

(a) NT3 calcined at 950 for 6 h.

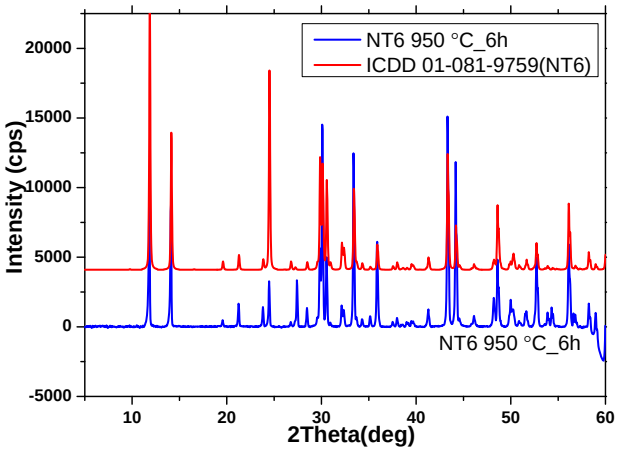

(b) NT6 calcined at 950 for 6 h.

Figure 5.12 – XRD reflections for the NT3 and NT6 powders calcined at 950 °C for 6 h.

Pellets of the biphasic mixtures after sintering at 1050 °C for 2 h, meant for thermodynamic cells, were also characterised using XRD. Figure 5.13 shows that after successful sintering at 1050 °C for 2 h, the phases are still preserved.

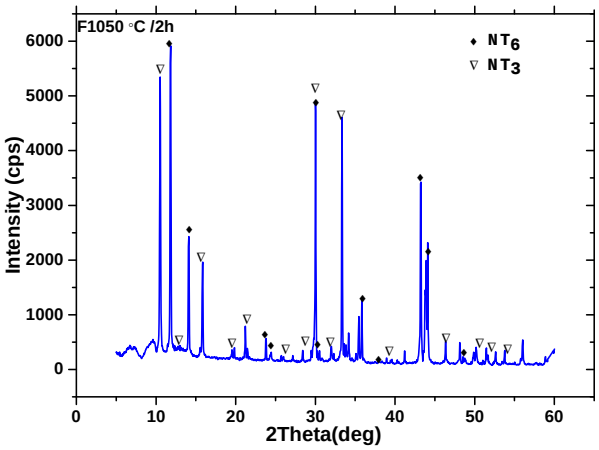

(a) NT6-NT3

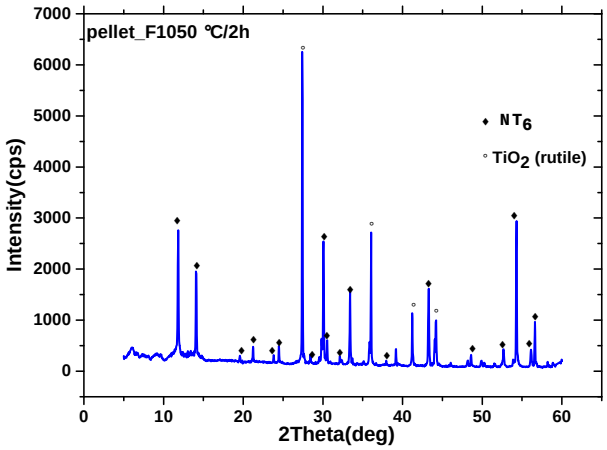

(b) NT6-TiO_2

Figure 5.13 – XRD reflections of the NT6-NT3 and NT6-TiO_2 biphasic mixtures of pellets sintered at 1050 °C for 2 h.

5.4 Conclusions

- Synthesis of a phase pure delaffosite $CuAlO_2$ through the conventional high temperature processing of mixed component oxides, Cu_2O and Al_2O_3 has always been obtained after prolonged reaction time some as long as 4 days. In this research a process of pelletising component oxides followed by

isothermal calcination in argon environment and quenching under graphite crucible has been successfully employed to reduce the reaction time down to 1.5 h. A single phase $CuAlO_2$ can be easily synthesized from mixed component oxides as long as the powder has been pelletised regardless of the amount of load applied.

- By calcining $CuAlO_2$ with Al_2O_3 at 1150°C for 3 h, results in the formation of a multi-phase of $CuAlO_2$-$CuAl_2O_4$-Al_2O_3 to be used as an oxygen buffer in the CO_2 sensor as discussed later in Chapter 7.

- High temperature electrical measurements show that the $CuAlO_2$ is a mixed conductor (holes and ions) up to about 375 °C beyond which the intrinsic type behavior completely dominates, the result is also confirmed by the spectral analysis. Spectral analysis also revealed that conduction is of long range hopping. The LT activation energy from DC measurements was, $E_a(LT) = 0.27$ eV and high temperature value, $E_a(HT) = 0.08$ eV while the LT activation energy for ionic conductivity was $E_a(LT) = 0.22$ eV. The transition from p-type to intrinsic type conduction occurs at around 375 °C in $CuAlO_2$.

- Electrical characterisation has revealed the transition to intrinsic type conduction (T_{trans}) of $CuAlO_2$ and this work reports for the first time the T_{trans} for the delaffosite, being $T_{trans} \simeq 375$ °C which has been reported in [183].

- It has also been shown for the first time that Pt can catalyse the inadvertent formation of $CuAl_2O_4$ spinel from $CuAlO_2$, the former being an insulator whereas the latter is a good p-type conductor. This is in complete agreement with the current understanding of the thermodynamic principles of Cu-Al-O, $Cu-Cr-O$ and $Cu-Y-O$ ternary systems [110, 186, 187, 188].

Chapter 6

Thermodynamics Studies of Na-Ti-O Systems Using Electrochemical Method

6.1 Background

The electrochemical method is considered the most accurate method for the determination of partial Gibbs energy[189, 190]. The electrolyte being used should have a transference number of 0.99 or better. When this is the case the cell would only conduct migrating ions whilst the electrons move through the external circuit. However this flow has to be stopped to create an open circuit voltage between the two electrodes of the cell and this corresponds to the state of thermodynamic equilibrium potential. To achieve this, a high internal resistance measuring device is required where in the scope of this research the Keithley instrument 6517A has been used having an internal impedance $> 10^{14}$ Ω.

Thermodynamic measurements offer an important tool for the determination of

compatibility and chemical stability among materials at high temperatures. There is therefore a continuous need for accurate thermodynamic data for existing and future ceramic materials.

For instance, Sahner et al. [14] in his investigation on thick films sensors investigated the stability of the fired mixtures of NT6/NASICON and NT3/NASICON. Observed was a parasitic reaction in the NT3/NASICON mixtures which converted NT3 to NT6 and no change was observed in the NT6/NASICON mixture. Thermodynamics using the electrochemical method is the robust and quantitative way to prove this.

For high temperature applications, sodium metal oxide (Na-Ti-O) ternary systems are most probable materials for reference electrodes in potentiometric gas sensors[105, 12, 49, 94]. To ascertain for phase composition constancy in a binary mixture, electrode characterization of the thermodynamic stability of the heterogeneous phase equilibria is often compulsory. Whilst calorimetric measurements can accurately give information on enthalpies, the electrochemical method is considered the most accurate method as far as the determination of partial Gibbs energy is concerned[189, 190, 191, 192, 193]. Measurement of surface energy and entropy of nano sized anatase using EMF method has also been reported[192].

Figure 6.1 depicts the the equilibrium phase diagram of the Na-Ti-O system. In this research attention will be focused on NT6-NT3 and NT6-TiO_2 phase mixtures due to their wide application as electrode materials.

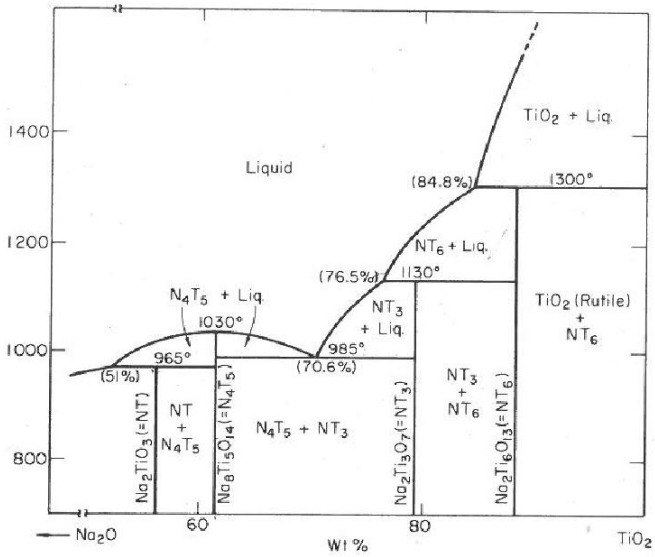

Figure 6.1 – Phase diagram of the Na-Ti-O system[194].

Thermodynamic data on NT6- TiO_2 and NT6-NT3, that is, the activity of sodium oxide (a_{Na_2O}) in NT6-TiO_2 or in NT6-NT3 respectively is vital for assessing its compatibility and stability against a variety of solid electrolytes in cells working at high temperatures.

The electrochemical characterization of the thermodynamic stability of the heterogeneous phase equilibria comprising sodium containing compounds usually comes down to the determination of the sodium (or sodium oxide) activity of these phase mixtures[40] and is usually accomplished by means of potentiometric measurements on galvanic cells using a sodium ion conductor such as sodium beta alumina (NBA) or NASICON.

Although there are few investigations already reported in the literature employing calorimetry[195, 196] and the EMF method[196, 40] the magnitude of scatter of the thermodynamic data makes another independent investigation necessary. Furthermore, during these measurements new information has been obtained which was never picked up from the previous investigations such as a probable

reversible phase transition in the temperature range of $705 < T \leq 800$ (K) . In addition, although the Gibbs energies have been reported[197], activities of a_{Na_2O} in biphasic mixtures which are needed for accurate characterisation of potentiometric gas sensor operations, are not reported.

Furthermore, there still exists conflicting data from previous researchers [40, 14] on the stability of NT6-TiO_2 and NT6-NT3. For instance, Amin [40] in the investigation of Na-Me-O systems where Me = Nb, Mo, Ti, found NT6-NT3 to be more stable than NT6-TiO_2 at high temperatures. The proposed reason was the possible formation of another sodium titanate phase NT7 at the NT6-TiO_2/ NASICON interface. On the other hand, Sahner et al. [14] found NT6-TiO_2 to be more stable than NT6-NT3 when powders were heat treated with NASICON at 950 °C. NT3 was found to have converted to NT6 due to a parasitic reaction with NASICON. On this premise, an independent investigation on the chemical stability of the two biphasic oxides is sufficed.

The purpose of this study therefore is to measure the chemical stability of the biphasic mixtures of NT6-TiO_2 and NT6-NT3 as well as activity of Na_2O in the systems as a function of temperature, using a solid-state EMF technique with NASICON as the solid electrolyte. Thse data are desirable for the calculation of the theoretical EMF and interpretation of the measured EMF of CO_2 sensors employing NT6-TiO_2 and NT6-NT3 as reference electrodes. Also, knowledge of the thermodynamic stability will be a guide as to what temperature the sensor should operate at before chemical reactions start taking place at the interface or before there is a domination of only one phase in the electrode[40].

6.2 Procedure

In this investigation, NASICON ($x = 2$) was used as a solid electrolyte for the cells. The reference electrode was a biphasic mixture of α - Al_2O_3(Sigma Aldrich, 99.7 %) and Na - β - Al_2O_3 denoted in this research as ($\alpha + \beta$ - Al_2O_3).It was used because the sodium oxide activity in it is well known [193, 48]. The materials to be characterised, that is, $Na_2Ti_6O_{13} + TiO_2$ and $Na_2Ti_6O_{13} + Na_2Ti_3O_7$ to be denoted as NT6-TiO_2 and NT6 - NT3 respectively, in this study, were used as working electrodes. Their synthesis and sintering is described in Chapter 3.

The biphasic sodium beta alumina (NBA) and alpha alumina, was synthesised by mechanical mixing through a 12 h ball milling of γ-Al_2O_3 and Na_2CO_3(Acros Organics, >99.6 %). Firstly, Na_2CO_3 was dried in a convectional oven at 150 °C to remove any moisture. It was then weighed and stoichiometric amounts of the two precursors were mixed. The amounts mixed was corresponding to Na_2O : xAl_2O_3 where $x = 9.5$ with extra amounts of Al_2O_3.The mixture was then calcined at 1270 °C for 5 h. A biphasic sodium beta alumina and alpha alumina (($\alpha + \beta$) - Al_2O_3) was formed as was confirmed by XRD analysis of Figure 6.2. A 5 tonne load was used to press pellets after which they were sintered at 1600 °C for 15 h. The pellets were not very well sintered but could be used as electrodes anyway as long as the electrolyte was well sintered.

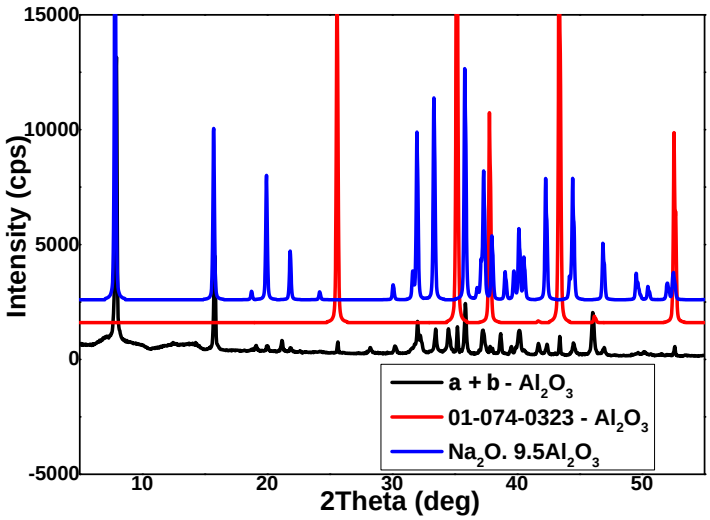

Figure 6.2 – XRD pattern of α - Al_2O_3 and Na - β - Al_2O_3 powder whose precursors were calcined at 1270 °C for 5 h. The ICDD standard references match with the sample peaks.

Electroding was done using platinum ink. After the ink was painted as illustrated in Figure 6.3, it was dried at 70 °C for 30 minutes. It was then fired for a further 30 minutes at 850 °C.

Furthermore, to check for any phase transition of NT6 and NT3 at different temperatures three samples were equilibriated at 180, 383 and 733 °C for 23 h respectively. They were then quenched in subzero liquid nitrogen to arrest the phases at those temperatures. XRD was performed before and after the equilibration.

6.2.1 Measurement cell set-up

The cells based on the pellets were connected according to the notations in cell I and cell II. The sign of the electrodes is indicated in the parentheses

$$\text{(-)Pt, NT6-}TiO_2 \mid \text{NASICON} \mid (\alpha+\beta)\text{ - }Al_2O_3\text{, Pt(+)} \quad \text{.....I}$$

$$\text{(-)Pt, NT6 - NT3} \mid \text{NASICON} \mid (\alpha+\beta)\text{ - }Al_2O_3\text{, Pt(+)} \quad \text{.....II}$$

To check the internal consistence of the results, cell III was constructed.

$$\text{(-)Pt, NT6 - NT3 | NASICON | NT6-TiO}_2\text{, Pt(+) .....III}$$

Figure 6.3 shows the cell arrangement. Platinum was used both as contact and leads. On one side of the pellet, platinum was fully painted while on the other side which would interface with the electrolyte pellet, thin strips of platinum were painted and then connected to the outer coated side. This was to ensure that the leads were directly connected to where the reactions were actually taking place, at the interface between the electrode and the solid electrolyte. The measurement rig was inserted into the Faraday cage within a horizontal tube furnace. This was to shield from any induced Faraday EMFs.

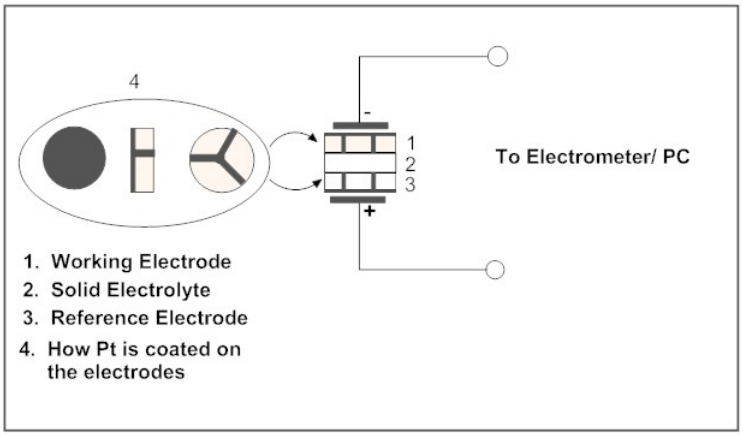

Figure 6.3 – Cell assembly. For the electrode pellets, one of the parallel sides was coated while the other side in contact with the electrolyte was just partially coated with strips of platinum.

6.2.2 Measurements

The EMF of the solid cell was measured as a function in the temperature range of $250 \leq T \leq 800$ °C using a high impedance Keithley 6517A electrometer. The cell electrodes were connected to the Keithley electrometer which digitized the

data and LabVIEW which sat on the computer ensured real time data reading and display. A type-K thermocouple was placed close to the sample to ensure real time temperature measurement.

Apart from the use of the third cell, cell III, EMF reproducibility and internal consistency was checked by approaching the target temperature from higher and lower values. The first measurement point was at 800 °C and then decreased with a step of *ca.* 50 °C . The equilibration time during the cooling run was 12 h while in the second cycle of measurement in the heating run, the equilibration time was 6 h. Starting measurements from the higher values is in fact advantageous as it rules out any irreversible reaction which would affect the EMF during the heating.

6.3 Cell: (-)NT6-TiO_2 | NASICON | $\alpha + \beta$

6.3.1 Theoretical Considerations

The anodic reaction at the NASICON/NT6-TiO_2 in the galvanic cell shown in cell I is given by

$$Na_2O(NT6 - TiO_2) \rightarrow 2\,Na^+ + 2e + \frac{1}{2}O_2. \tag{6.1}$$

The Na^+ ions migrate through the NASICON/$\alpha + \beta - Al_2O_3$ interface where they react with oxygen in the cathodic reaction as

$$2\,Na^+ + 2e + \frac{1}{2}O_2 \rightarrow Na_2O(\alpha + \beta). \tag{6.2}$$

Because the oxygen gas (P_{O_2}) atmosphere is common to both electrodes of the

cell, the net cell reaction from (6.12) and (6.13) is

$$\mathrm{Na_2O(NT6 - TiO_2)} \rightarrow \mathrm{Na_2O}(\alpha + \beta). \tag{6.3}$$

and is also equivalent to the overall virtual cell reaction

$$\mathrm{Na_2Ti_6O_{13}} + 9.5\,\mathrm{Al_2O_3} \rightarrow 6\,\mathrm{TiO_2} + 2\,\mathrm{NaAl_{9.5}O_{17}}. \tag{6.4}$$

The EMF generated due to the electrode reactions in (6.3) is related to the difference in chemical potential of $\mathrm{Na_2O}$ between the reference and working electode through the relationship

$$E = -RT \ln \frac{a_{\mathrm{Na_2O}}(RE)}{a_{\mathrm{Na_2O}}(WE)} \tag{6.5}$$

at constant temperature, where z and F are the electrons transferred, Faraday's number (96485 C/mol) respectively.

6.3.2 Results

The variation in EMF of the cell with temperature is shown in Figure 6.4b. The EMF varies non-linearly in the temperature range of $705 < T \leq 800$ (K) indicating a possible phase or electronic transition in one of the oxide phases present in the electrode.

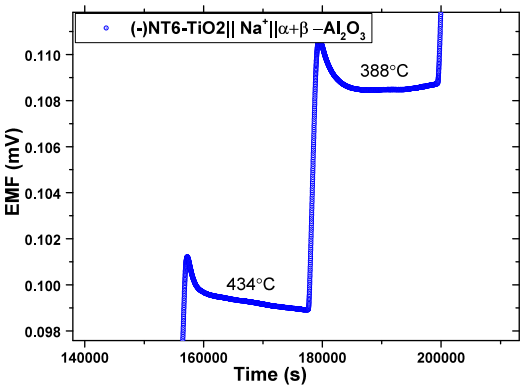

(a) Typical equilibration of the cell during EMF measurements.

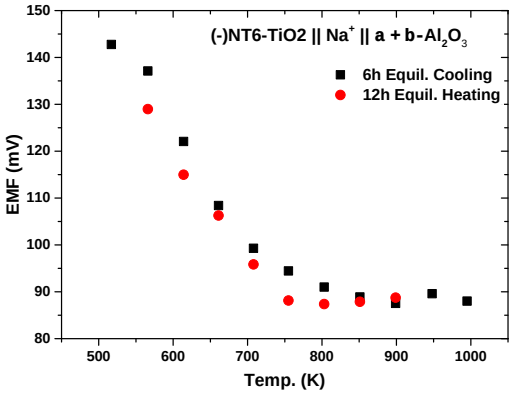

(b) EMF measurements on heating and cooling runs for 12 h and 6 h equilibration times respectively.

Figure 6.4 – EMF measurements of the cell: NT6-TiO_2 || NASICON || $\alpha + \beta$ which includes heating and cooling runs.

The heating and cooling run data were then combined and averaged to get a normalised representation of the data. This is given in Figure 6.5.

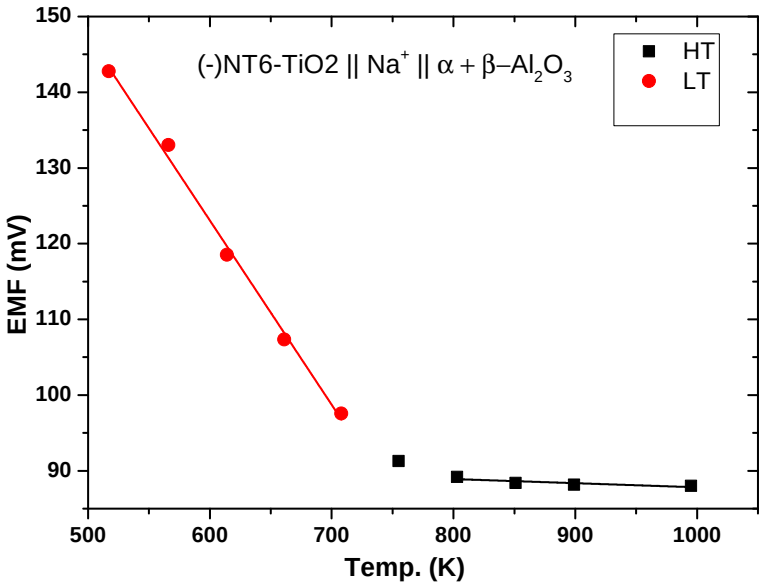

Figure 6.5 – Normalised data for the EMF cell, NT6-TiO_2 || NASICON || $\alpha + \beta$ including the linear fits. A nonlinear dependence is observed in the temperature range $705 < T \leq 800$ (K) while two linear dependences are observed at high temperature(HT) and low temperature (LT) regions.

Let EMF be denoted as E in this study. From Figure 6.5, the EMF is linear in two temperature regions, $523 \leq T < 705$ (K) and $800 < T \leq 1073$ (K) referred to as LT (low temperature) and HT (high temperature) respectively. From linear regression analysis, the EMF obtained is as in Equation (6.6)

$$E_I(\text{mV}) = \begin{cases} (269.08 \pm 5.72) - (0.02434 \pm 0.0093)T & \text{for} \quad 523 \leq T(K) < 705 \\ (93.27 \pm 2.12) - (0.00545 \pm 0.00239)T & \text{for} \quad 800 \leq T(K) < 1073 \end{cases} \tag{6.6}$$

To obtain the sodium oxide activity in the two phase mixture of NT6 and TiO_2, Equation (6.5) is employed and rearranging it gives the relationship

$$\ln a_{Na_2O(NT6-TiO_2)} = \frac{2E_IF}{RT} + \ln a_{Na_2O(\alpha+\beta)} \tag{6.7}$$

The only unknown in Equation (6.7) is the sodium oxide activity in the biphasic mixture NT6 - TiO_2 because the sodium oxide activity in the reference electrode α-Al_2O_3 + Na-β-Al_2O_3 denoted as $Na_2O(\alpha+\beta)$ is known from earlier measurements by Kale [193] in the temperature range of $700 \geq T/K \geq 1100$, and is given by

$$\log a_{Na_2O(\alpha+\beta)} = 1.85 - \frac{14750}{T}(\pm 0.3) \tag{6.8}$$

Combining (6.6) and (6.8) gives

$$\log a_{Na_2O(NT6-TiO_2)} = \begin{cases} -0.76 - \frac{12031}{T} & \text{for} \quad 523 \leq T(K) < 705 \\ 1.80 - \frac{13810}{T} & \text{for} \quad 800 \leq T(K) < 1073 \end{cases} \tag{6.9}$$

Figure 6.6a is the sodium oxide activity in NT6-TiO_2 according to the relation in

Equation (6.11) while Figure 6.6b compares the variation of sodium oxide activity in NT6-TiO_2, NASICON[48] and $\alpha + \beta$[193] as a function of temperature.

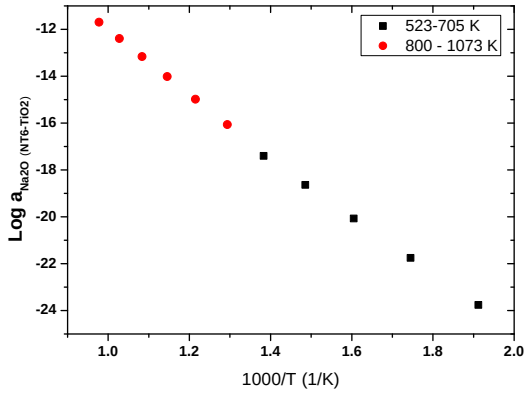

(a) Activity of Na_2O in NT6-TiO_2 vs temperature

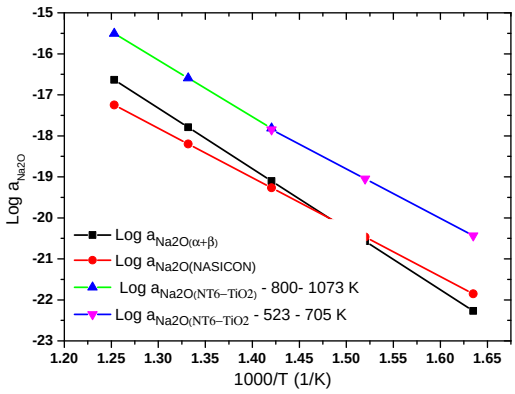

(b) Comparison of sodium oxide in NT6-TiO_2 with that in NASICON and $\alpha + \beta$

Figure 6.6 – Variation of activity of sodium oxide in NT6-TiO_2 as a function of temperature. It is higher than that in NASICON and $\alpha + \beta$ confirming its stability.

It can be seen that $\log a_{\mathrm{NT6-TiO_2}}$ as a function of temperature is higher than that of NASICON and the biphasic mixture of α-alumina and sodium beta alumina. This implies that the solid electrolyte is more thermodynamically stable than the working electrode, NT6 - TiO_2, which is essential in obtaining reliable thermodynamic equilibrium data.

Furthermore, it also implies that at any fixed temperature, the decrease in the concentration of the Na_2O in the working electrode corresponds to the decrease in Na_2O activity, leading to a decrease in cell EMF because the gradient of the chemical potential of Na_2O across the NASICON decreases[198]. The stability was also confirmed by examining the sample using XRD before and after the high temperature thermodynamic measurements. This is shown in Figure 6.7.

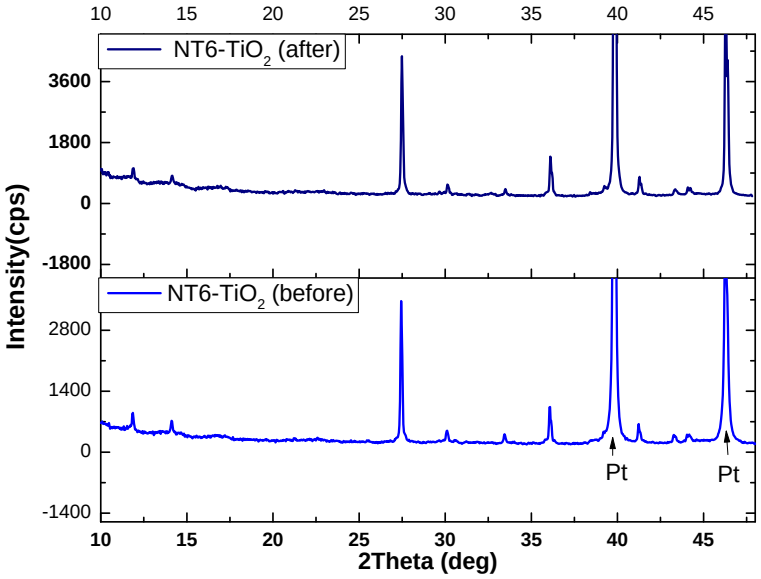

Figure 6.7 – NT6-TiO_2 before and after the EMF measurements. The side analysed was one that was in contact with NASICON pellet.

Generally, all electrochemical cells have a concentration gradient of conducting species across the solid electrolyte. Semipermeability flux of the conduction ions can result when there is a large chemical potential gradient resulting in mass transport across the electrolyte from one electrode to another subsequently resulting in a small compositional change in the electrode and electrolyte. However, in this research, the cell is buffered by the presence of the two phase mixture in the reference.

The standard Gibbs energy of reaction, $\Delta G^{\circ}_{r,\mathrm{NT6}} = RT \ln a_{\mathrm{Na_2O(NT6-TiO_2)}}$ (or the change in sodium oxide chemical potential from the anodic cell reaction of Equation (6.10)

$$\mathrm{Na_2O}(c) + 6\mathrm{TiO_2}(c)^1 \rightarrow \mathrm{NaTi_6O_{13}}(c) \tag{6.10}$$

yields

$$\Delta\mu_{\mathrm{Na_2O}} = \Delta G^{\circ}_{r,\mathrm{NT6}}(\mathrm{J/mol}) = \begin{cases} -230497 - 11.55T & \text{for} \quad 523 \leq T(K) < 705 \\ -264422 + 34.46T & \text{for} \quad 800 \leq T(K) < 1073 \end{cases} \tag{6.11}$$

The values are in reasonable agreement with literature from Ferrante [195] except for a $\leq 6\%$ experimental difference from the Gibbs energy of reaction calculated using S°_{298}, ΔH°_{298} obtained from Stuve [199] and Bennington and Brown [200] respectively. Table 6.1 is a comparison with the obtained Gibbs energies in this investigation with literature values.

Non linear dependencies in the EMF as a function of temperature is not uncommon whenever there is some phase transition taking place in the material, as has been observed in other systems by Subasri et al. [191], Balaya and Maier [192], Feng and Taskinen [201], and Kale et al. [202]. In the former and the later, DSC was employed to determine the transition.

[1] Rutile

Table 6.1 – Thermodynamic data for $Na_2O(c) + 6TiO_2(c)$[1] $\rightarrow NaTi_6O_{13}(c)$

T/K	ΔG_r°**(J/mol)** **Ferrante [195]**	ΔG_r°**(J/mol)** **This study**	**% diff.**
298.15	-245530	-233941	4.7
300	-245555	-233962	4.7
400	-247664	-235117	5.1
500	-249718	-236272	5.4
600	-251655	-237427	5.7
700	-252124	-238582	5.4

However, in the NT6-TiO_2, in the present study, it was not possible to resolve it because of the relatively fast heating and cooling rate in high temperature XRD studies which makes it difficult to attain thermal equilibria and capture any transition. However, with EMF being more sensitive and operating at constant temperature, the transition was able to be observed. This can only be explained as a phase transition.

Anatase to rutile transition is ruled out because, (a) the sintering of the pellet of the biphasic mixture of NT6-TiO_2 at 1050 °C implies that irreversible phase transition already occurred since it happens at a temperature lower than 1050 °C. (b) furthermore, the first measurement point was at 800 °C (a temperature higher than the transition temperature $\sim$ 600 °C[203]) down to the lowest temperature and then back to the maximum temperature, therefore any transition that may have taken place while heating to that temperature would not not be detected when EMF measurements are taken. (c) since the EMF measurements are shown to be

[1] Rutile

reversible/reproducible both in the heating and cooling runs, the non-linearity in the data may not be due to the anatase/rutile transition.

The reversible non linearity of the EMF observed in the the temperature range $705 < T \leq 800$ (K) may be explained in light of phase transitions in the NT6 system. There is information on the existence of high titanium rich phases of $Na_2Ti_7O_{15}$ (NT7)[204, 205, 206] or $Na_2Ti_9O_{19}$(NT9)[207, 208] reported in the literature implying that there may exist these phases between the NT6 and TiO_2 in the phase diagram of Figure 6.1 and very close to the TiO_2.

Further, Wadsley and Mumme [204] states that NT7 does not form by simple expedience of mixing and heating of oxides in a sealed system but through the transformation of NT6 through $7\,Na_2Ti_6O_{13} \rightarrow 6\,Na_2Ti_7O_{15} + Na_2O$. Therefore these may have formed in-situ but the amount may be too small to be detected by XRD. This was also observed by Amin [40] in explaining the non equilibriating EMF of his cell.

Furthermore, the fact that the EMF measurement was reversible implies that the formation of the titanium rich sodium titanates was reversible too. This observation may give evidence for the presence of the NT7 or NT9 phases between NT6 and TiO_2 in the phase diagram.

To investigate any phase change in NT6, high temperature XRD (HTXRD) was performed on the powder (Figure 6.8b) as well as subzero quenching in liquid nitrogen of NT6 pellets after 16 h of equilibration at different temperatures(6.8a) as shown in Figure 6.8.

No evidence of any phase transformation was observed, again this could be because any new phase would be too little to be detected by XRD.

Since the phase transition detected in the NT6-TiO_2 in this study has not been considered in the evaluation of free energy functions or other thermodynamic

parameters, by not considering the two linear regimes and ended up extrapolating through the entire temperature range, possibilities of free energies being inaccurate in some temperature ranges are high. A better practice would be to deal with the different linear regimes separately rather than grossly generalising.

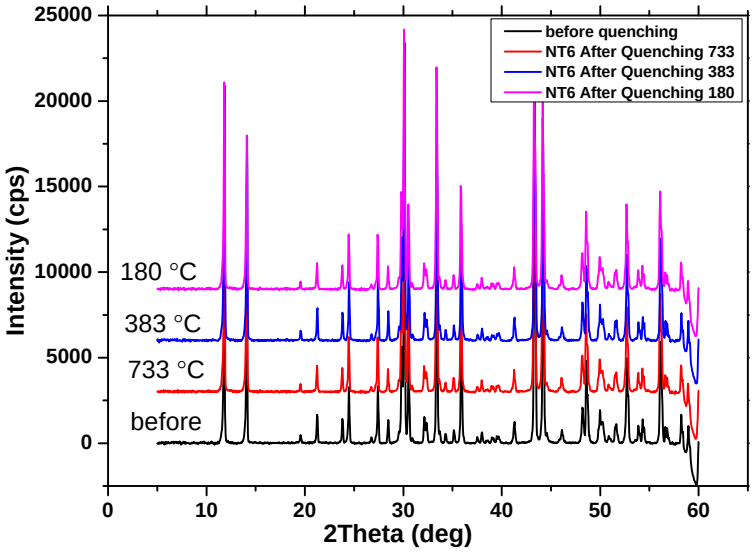

(a) Subzero quenched NT6 pellets.

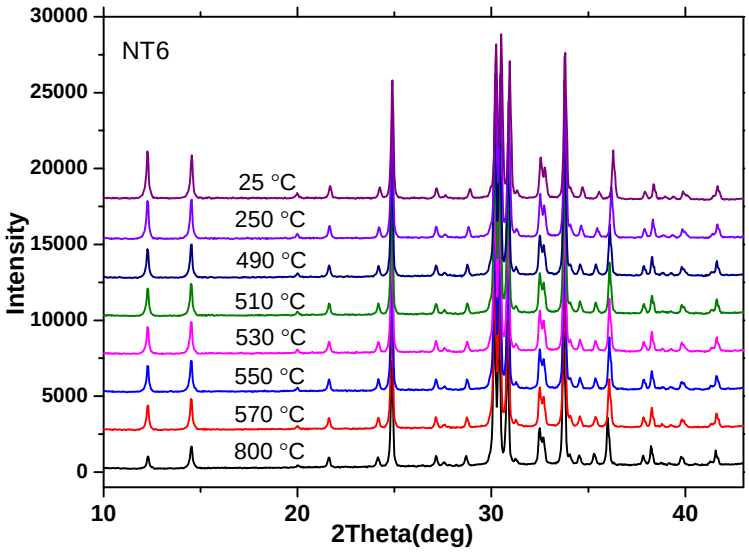

(b) HTXRD on NT6 powder.

Figure 6.8 – Ambient and non ambient XRD for powder and subzero quenched NT6 pellets. No phase change is observed.

Further work is also necessary to substantiate this supposition of an existence of two titanium rich phases between NT6 and TiO_2 and to get a better insight into the details of the phase diagram.

6.4 Cell: (-)NT6-NT3 | NASICON | $\alpha + \beta$

6.4.1 Theoretical Considerations

Similar to the the cell I electrochemical reactions, the cathodic reaction of cell II, at the NASICON/$\alpha-Al_2O_3$ + $Na-\beta-Al_2O_3$ interface in terms of sodium oxide is

$$2\,Na^+ + 2\,e + \frac{1}{2}O_2 \longrightarrow Na_2O(\alpha + \beta). \tag{6.12}$$

while the anodic cell reaction at the NT6-NT3/NASICON interface is

$$Na_2O(NT_6{-}NT_3) \longrightarrow 2\,Na^+ + 2\,e + \frac{1}{2}O_2. \tag{6.13}$$

so that the overall cell reaction from (6.12) and (6.13) becomes

$$Na_2O(NT_6{-}NT_3) \longrightarrow Na_2O(\alpha + \beta). \tag{6.14}$$

and alternatively the equivalent to the overall virtual cell reaction being

$$Na_2Ti_3O_7 + 9.5\,Al_2O_3 \rightarrow Na_2Ti_6O_{13} + 2\,NaAl_{9.5}O_{17}. \tag{6.15}$$

6.4.2 Results

Figure 6.9 is the typical EMF equilibration with time and temperature. As can be seen in Figure 6.9a, the cell equilibriated pretty well confirming the integrity of the thermodynamic equilibrium of the cell. Figure 6.9b is a plot of the equilibrium EMFs as a function of temperature. Both data from the cooling and heating runs are shown and the plot shows to be reproducible in the temperature range $611 \leq T \leq 798$ K.

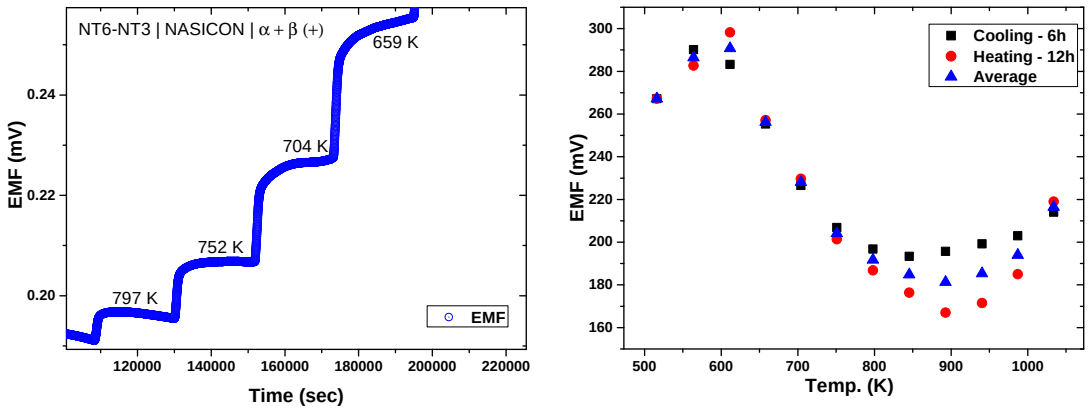

(a) EMF equilibration with time.

(b) Equilibrium EMF with temperature.

Figure 6.9 – EMF equilibration for cell II.

The EMF obtained from Figure 6.9 in the temperature range $611 \leq T \leq 798$ K was

$$E_{II}(\text{mV}) = (667.3263 \pm 25.3896) + (0.6204 \pm 0.03717)T. \tag{6.16}$$

To obtain the activity of Na_2O in the biphasic phase of NT6-NT3, Equation (6.5) is rearranged so that

$$\log a_{Na_2O(\text{NT6-NT3})} = -4.42 - \frac{8024}{T} \tag{6.17}$$

The variation of Na_2O activity in NT6-NT3 with temperature and compared with those of NASICON[48] and $\alpha + \beta$ - Al_2O_3[193] as shown in Figure 6.10. The results show that since the activity of Na_2O in NASICON is lower than in the NT6-NT3, the NASICON is thermodynamically more stable than the working electrode; NT6-NT3 implying NASICON/NT6-NT3 interfacial reaction cannot to take place within the temperature range examined. The temperature dependence of activity in Equation (6.17) obtained by other workers [40] was $\log a_{Na_2O(NT6-NT3)} = -1.6 - \frac{8697}{T}$. The percentage difference in slopes is only 7.5% implying a good agreement with what other workers have obtained.

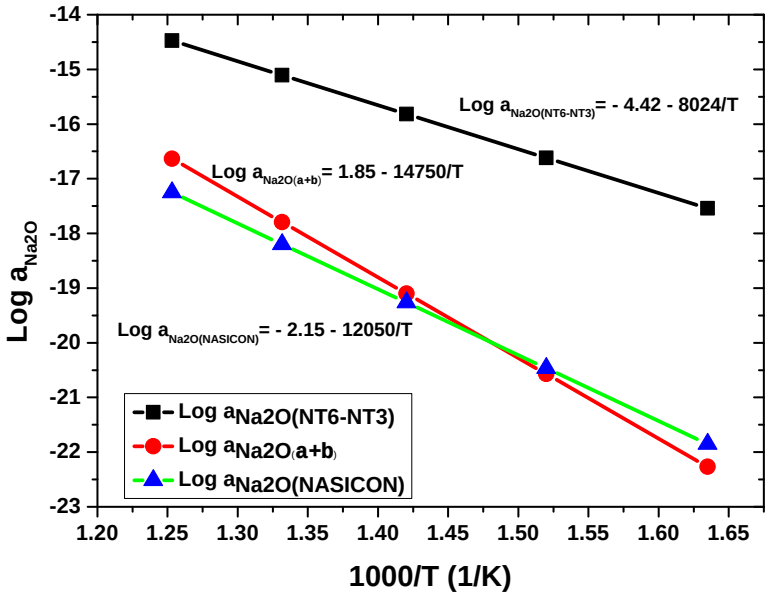

Figure 6.10 – Variation of activity of sodium oxide in NT6-NT3 as a function of temperature.

According to Figure 6.9b, it can be seen that the EMF was quite reproducible and linear in the temperature range; $611 \leq T \leq 798$ K. However, above 798K, non-linearity sets in and in this region the EMFs are not reproducible both in the heating and cooling runs; the deviation is maximum at 900 K. The EMF shows reproducibility again at $T \geq 1034$ K indicating a defined thermodynamic

equilibrium.

It is not clear what is happening within the temperature range of $798 \leq T \leq 1034$ K but metastability and phase transformation may be a plausible explanation. Previous studies by Sahner et al. [14] showed a possible transformation of NT3 into NT6 when in contact with NASICON. Furthermore, as has already been alluded to in Section 6.3.2 of the possible transformation of NT6 to NT7 and NT9[40, 204, 205, 206, 207]. On a good note, the fact that the EMF was reproducible in some temperature range alluded to already, indicates the stability of the biphasic phases in those temperature ranges and this is important in achieving a defined thermodynamic equilibrium information.

To confirm the integrity of the thermodynamic measurements, and to make sure that no reactions took place during the high temperature measurements, XRD was taken before and after measurements on both sides of the interface; NT6-NT3 side and the NASICON side.

Figure 6.11 shows that the biphasic mixture was effectively stable despite the proposed reversible transformation of ; NT3 $\rightarrow$NT6$\rightarrow$NT7(NT9). XRD from the NASICON side that was in contact with the NT6-NT3 also shows that NASICON was well preserved as no interfacial reactions took place.

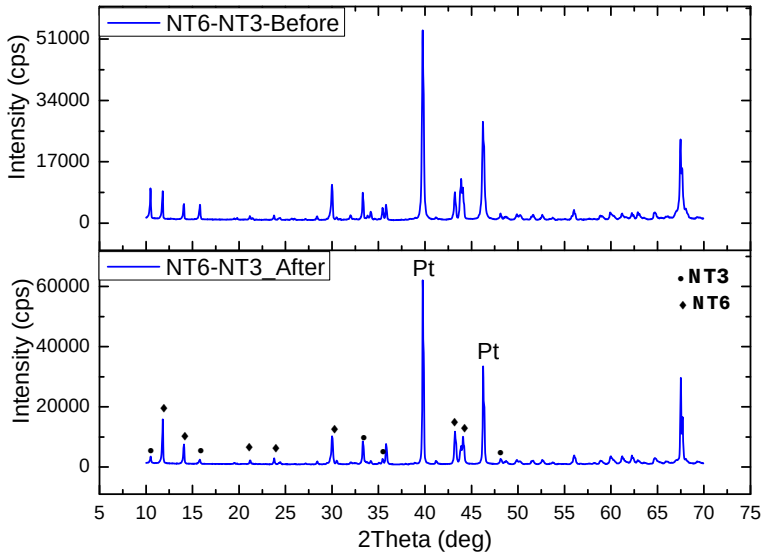

Figure 6.11 – XRD - NT6-NT3 before and after measurements.

XRD from the NASICON side that was in contact with the NT6-NT3 also shows that NASICON was well preserved as no interfacial reactions took place. This is shown in Figure 6.12. The reference side of NASICON was also stable. The two intense peaks (at 40° and 43°) on the reference side are Pt peaks arising from the Pt coating that got stuck on the NASICON after the measurements.

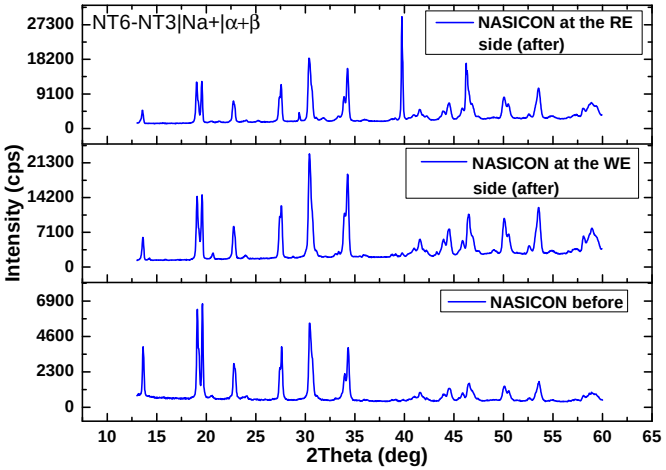

Figure 6.12 – XRD - NASICON before and after measurements.

Using the EMFs of cell II and the sodium oxide activity given by Equation (6.17), the Gibb's energy change (or sodium oxide chemical potential) of reaction

$$Na_2O(c) + Na_2Ti_6O_{13}(c) \rightarrow 2\,Na_2Ti_3O_7(c)$$

can be obtained as,

$$\begin{aligned}\Delta\mu_{Na_2O} = \Delta G^{\circ}_{r,NT3}(J/mol) &= RT \ln a_{Na_2O(NT6\text{-}NT3)} \\ &= -153637 - 84.25T \end{aligned} \tag{6.18}$$

where T is the temperature in Kelvin (K).

6.5 Cell: NT6-NT3 | NASICON | NT6-TiO2

To check the internal consistence of the results, cell III was constructed which is equivalent to cell II and cell I(with reversed polarity) representing EMFs E_{II} and $-E_I$ connected in series. The EMF of cell III, which is directly measured is thus expected to be $E_{III} = E_{II} + (-E_I) = E_{II} - E_I$. The components of this cell were fresh pellets and not reused pellets from cell I and cell II. Below is the cell.

(-)Pt, NT6 - NT3 | NASICON | NT6-TiO_2, Pt(+) III

With these two conditions i.e, fresh pellets, and cell setup, if the measured EMF matches with the cells I and II by virtue of $E_{III} = E_{II} + (-E_I) = E_{II} - E_I$ then the results can be relied upon.

Figure 6.13 is the equilibrium EMF as a function of temperature. As was observed for cell II, with NT6-NT3 working electrode, there exists a non linearity and irreproducibility of the data within the same temperature range and also it is

maximum at around the same temperature. Further away, at higher temperatures above 1000 K, the EMF is reproducible again. This observation alone proves the reliability of cell II results.

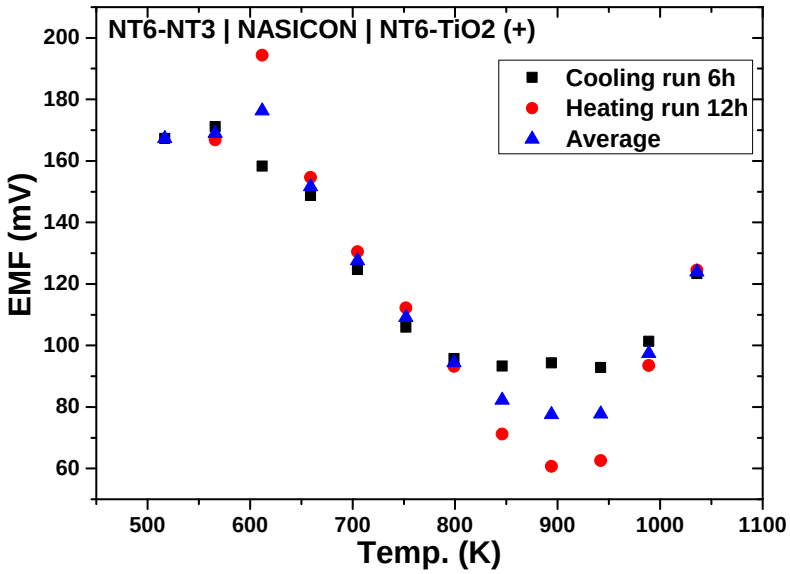

Figure 6.13 – EMF as a function of temperature for the consistent cell III.

Figure 6.14 shows the internal consistence check of the results by comparing the results of cells I and II with the measured EMF of cell III .

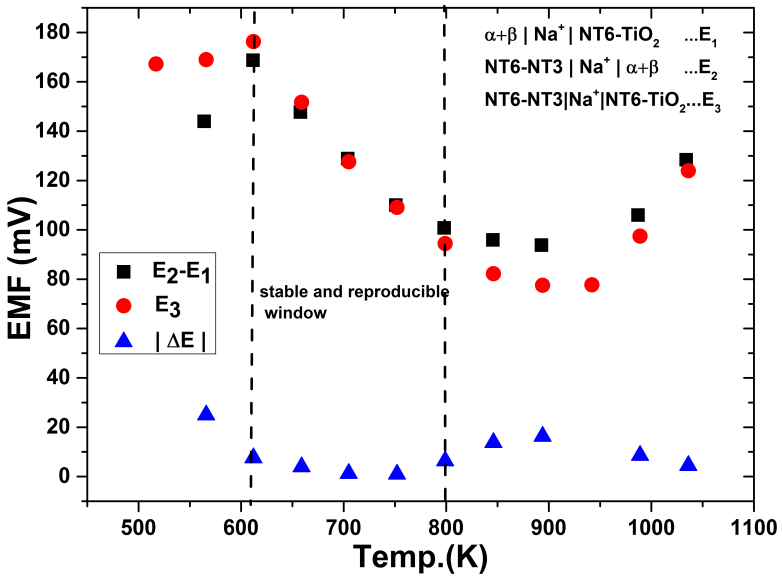

Figure 6.14 – Internal consistence check. The cell do indeed prove that $E_3 = E_2 - E_1$.

It can clearly be seen that the directly measured EMF of cell III is in good agreement with the independently measured EMFs of E_I and E_{II} such that $E_{III} = E_{II} - E_1$ and that the values coincide pretty well within the reproducible window and this is the temperature range which was used for thermodynamic analysis for cell II. Therefore this internal consistence check has shown that the results are reliable between 622-798 K.

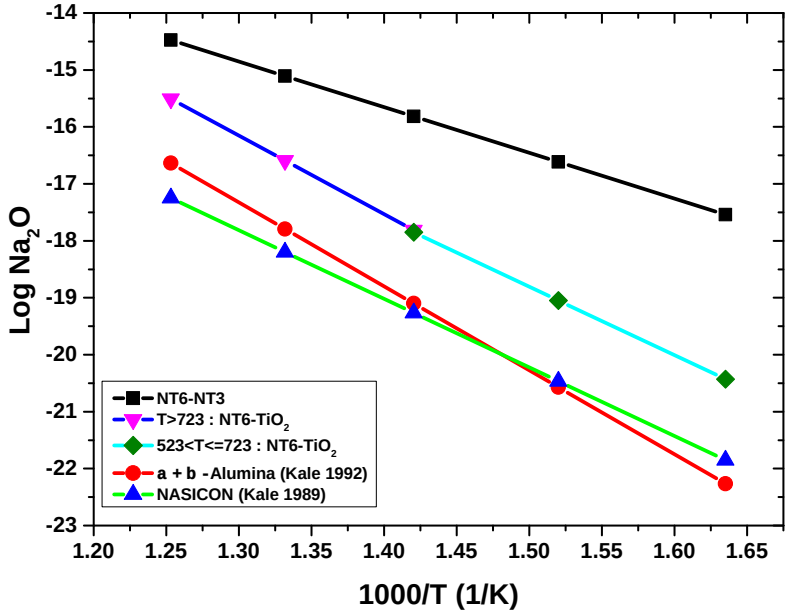

Figure 6.15 – Comparison of temperature dependence of Na_2O activities in NASICON[48], $\alpha-Al_2O_3$ + $Na-\beta-Al_2O_3$ [193], NT6-NT3 and NT6-TiO_2.

Finally, Figure 6.15 is a comparison of activities of Na_2O in NT6-NT3, NT6-TiO_2, NASICON and $\alpha-Al_2O_3$ + $Na-\beta-Al_2O_3$. The result as is expected shows that the activity is much lower in NT6-TiO_2 than in NT6-NT3 and hence more stable than the NT6-NT3. However, the solid electrolytes have lower activities than the the working electrode materials of NT6-NT3 and NT6-TiO_2 implying that they are thermodynamically stable when the biphasic mixtures in the Na_2O-TiO_2 system are used as electrodes.

6.6 Conclusions

- From the revelations of the existence of 2-linear regimes of EMF vs T dependencies of cell I, it is clear that most thermodynamic data of EMFs is grossly oversimplified by extrapolating the linear section investigated to span the whole temperature range, or the second linear regime is ignored. This

represents the first results showing multiple linear regimes that requires that the thermodynamic parameters are dealt with separately and accordingly.

- Due to instrumental limitations, the probable second linear regime in the EMF of cell II ;
  (-)Pt, NT6 - NT3 | NASICON | $(\alpha + \beta)$ - Al_2O_3, Pt(+)
  was not investigated but it would be interesting to conduct the measurements for $T > 1034$ K where the data become reproducible again as was shown in Figure 6.9b.

- The likely reason for the non-linearity in the EMF vs T dependencies is the reversible phase transition of NT6 to higher titanium content NT7 or NT9; whose phase would lie between NT6 and TiO_2 of the phase diagram. This transition is reversible because the data is reproducible both in the heating and cooling runs. This result gives the first experimental indication using the EMF method of the phase transition of NT6 to NT7 or NT9 as was reported by other workers[205, 206, 207, 204].

- The standard Gibb's free energy change of reaction (or sodium oxide chemical potential change) on the working electrode for cell I ; $Na_2O + 6TiO_2 \rightarrow NaTi_6O_{13}$ is

$$\Delta\mu_{Na_2O} = \Delta G^{\circ}_{r,NT6}(\text{J/mol}) = \begin{cases} -230497 - 11.55T & \text{for} \quad 523 \leq T(K) < 705 \\ -264422 + 34.46T & \text{for} \quad 800 \leq T(K) < 1073 \end{cases}$$

- The standard Gibb's free energy change (or sodium oxide chemical potential change) of reaction on the working electrode for cell II; $Na_2O + Na_2Ti_6O_{13} \rightarrow$

$2\,Na_2Ti_3O_7$ is:

$$\Delta\mu_{Na_2O} = \Delta G^{\circ}_{r,NT3}(\text{J/mol}) = -153637 - 84.25T.$$

- The thermodynamic data that are needed for the quantitative characterisation of the sensor signals, the Na_2O activity was obtained as a function of temperature. The following are the relationships:

$$\log a_{Na_2O(NT6-TiO_2)} = \begin{cases} -0.76 - \frac{12031}{T} & \text{for} \quad 523 \leq T(K) < 705 \\ 1.80 - \frac{13810}{T} & \text{for} \quad 800 \leq T(K) < 1073 \end{cases}$$

and

$$\log a_{Na_2O(NT6-NT3)} = -4.42 - \frac{8024}{T}, \quad \text{for } 611 \leq T(K) < 798.$$

- Contrary to the contrasting findings by Amin [40] for the possible NT6/electrolyte reactions which hindered the thermodynamic equilibrium in his findings, and those of Sahner et al. [14] where NT3/NASICON was found to transform to NT6, the present study has shown that actually the solid electrolytes, NASICON and sodium beta alumina have much lower activity values of Na_2O than the NT6-NT3 and NT6-TiO_2 electrodes indicating good stability when in contact with each other. Furthermore, XRD conducted before and after the measurements showed no change in the phases confirming the stability of both the NT6-NT3 and NT6-TiO_2.

- The internal consistency check of the cells passed the test hence all these results can be relied upon.

Chapter 7

Sensor Characterisation

7.1 Introduction

The need for low cost, highly selective, sensitive, portable and stable sensor as an alternative to the highly expensive and complex NDIR sensor can not be over emphasized. This has been discussed Chapter 2.

Also, many attempts have been made in lowering the cost of production through a high throughput deposition technique of screen printing and to improving the general performance of the sensor such as long term stability, fast response times and selectivity. Technological aspects such as sensor modifications have also been attempted. Standing out among the sensor architectures is the planar sensor architecture (PSA) as described by [14, 86] where the solid electrolyte is printed on an alumina substrate and then the electrodes printed side by side, the sensors show a fair sensing performance. Within this architecture, some researchers used solid biphasic reference electrodes while others relied on the gas reference system envisaging a fixed Na potential at the reference electrode.

For a sensor using Na_2CO_3 as a sensing electrode that has a gas reference, provided

there is oxygen pressure, the overall reaction is

$$Na_2CO_3 \rightleftharpoons \underline{Na_2O}_{\text{Nasicon}} + CO_2 \tag{7.1}$$

while the sensor with a solid reference such as NT6-TiO_2 will have an overall reaction of

$$Na_2CO_3 \rightleftharpoons \underline{Na_2O}_{NT6-TiO_2} + CO_2 \tag{7.2}$$

or more importantly as was shown in Equation (2.15) of Chapter 2. $\underline{Na_2O}_{NT6-TiO_2}$ is the sodium oxide in NT6-TiO_2.

All these rely on a fixed Na_2O activity to achieve a uniquely defined equilibrium but this is not always so for the sensor with Equation (2.15). Despite the existence of a known Na_2O activity in NASICON from Kale and Jacob [48] and that for each x in the $Na_{1+x}Zr_2Si_xP_{3-x}O_{12}$: $0 \leq x \leq 3$ system correspond to a unique activity, any progressive deviation will not provide a uniquely defined equilibrium.

Also, sensor calibration would depend uniquely on the exact phase of x that has been used. Since it may not be possible to know the exact composition in-situ due to the degradation factors already discussed, the need to fix the Na_2O can not be over-emphasised.

Furthermore, since NASICON has to undergo high temperature sintering both on bulk or thick films, Na_2O volatisation always takes place including the precipitation of zirconia and these phenomena may also change the activity. As was revealed in this research in Chapter 4, the progressive interfacial reactions between NASICON and the alumina substrate to a large extent does not guarantee a fixed Na_2O activity. The fact that the sensors undergo multiple thermal cycling, the activity would never be fixed.

To redress this, biphasic solid reference systems are used because the activity of Na_2O in the NT6-TiO_2 or NT6-NT3 is fixed. There is however still some reports of EMF drifts and possible explanations are the degradation of NASICON due to humidity. Formation of Na_2CO_3 at the reference electrode at very high CO_2 concentrations may also lead to the establishment of a symmetric cell.

7.2 Procedure

In this research, the materials used for the sensors were as follows; NASICON as solid electrolyte (SE) and NT6-NT3 and NT6-TiO_2 as reference electrodes (RE). The thermodynamic properties and chemical stability of the RE have been studied in Chapter 6.

For the sensing electrodes (working electrode (WE)), eutectic mixtures of Na_2CO_3 : $BaCO_3$ and Na_2CO_3 : $BaCO_3$: Li_2CO_3 in the mass ratio of 1.5 : 1.624 and 0.8056 : 1.5 : 0.5616 respectively were used. The mixtures were weighed appropriately and melted at 800 °C for 30 minutes to homogenise the mixtures. They were then quenched, ground and made into pastes according to the procedure in Chapter 3. A eutectic mixture of the sensing electrode (sodium carbonate) and barium carbonate is used to prevent humidity cross-sensitivity. $BaCO_3$ being far less soluble than Na_2CO_3, studies have found that a eutectic mixture of the two contained unusually high amounts of the former than the later hence the sensor resistance to water vapour[50]. In this study, the sensing electrode Na_2CO_3-$BaCO_3$ and Na_2CO_3 - $BaCO_3$ - Li_2CO_3 will be denoted as NaBa and NaLiBa respectively

The buffer used comprised $CuAlO_2$ - $CuAl_2O_4$ - Al_2O_3. Its synthesis and characterisation was described in Chapters 3 and 5 respectively.

7.2.1 Fabrication

Two sensor architectures of dimensions 10 mm x 9 mm were screen printed; (a) planar sensor architecture (PSA) and (b) multi-layered structure also referred to as stacked sensor architecture (SSA).

7.2.1.1 Planar sensor architecture (PSA)

The PSA is the commonly used architecture but in addition, in this research, the design has been slightly modified by adding an extra layer containing a buffer material whose purpose is not only to fix the oxygen potential but to work as a protective material to shield the reference electrode from any negative effects such as high CO_2 concentrations. To check the performance of new architectures, the conventional PSA was also printed. Figure 7.1 shows the conventional architecture (a) and the modified PSA architecture (M-PSA) (b).

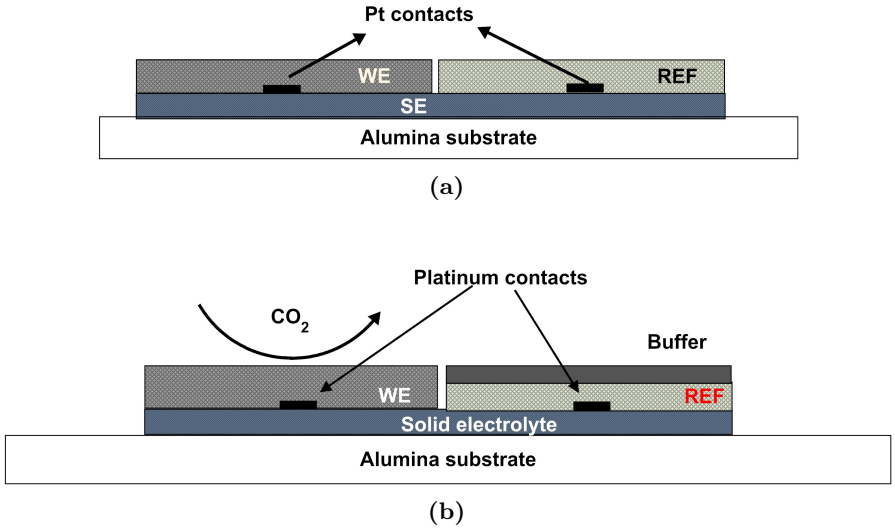

Figure 7.1 – The planar sensor architecture (PSA). (a) conventional PSA (b)modified (M-PSA).

To fabricate the sensors, the following steps were followed:

1. NASICON was firstly printed on alumina substrate and then fired at 1100 °C for 60 minutes.

2. Platinum strips were then printed parallel to each other on the NASICON electrolyte and fired at 850 °C for 30 minutes.

3. On top of one platinum strip, the reference electrode (RE) was printed and then fired at 950 °C for 90 minutes.

4. This stage is for the modified sensor. The buffer was printed on top of the RE and fired at 950 °C for 90 minutes. Note that this was the optimised firing temperature and durations as any temperature above 950 °C or longer duration than 90 minutes was deleterious to the buffer as interfacial reactions were obvious. Since NT3 and NT6 are good ion exchangers [209], especially with copper, it was vital that this process is avoided by firing it at slightly lower temperature than the sintering temperature of the titanates. 950 °C was found to be ideal. After firing for 90 minutes, the ternary mixture of the buffer was preserved.

5. Platinum wires were wire bonded using platinum ink and firing at 850 °C for 30 minutes.

6. Finally on the adjacent side of the sensor, on top of the platinum strip, the sensing (working) electrode was printed and fired at 550 °C for 30 min. The ternary mixture of Na-Li-Ba-CO_3 was fired at 500 °C.

7.2.1.2 Stack Sensor Architecture (SSA)

The SSA sensor was fabricated by printing from the bottom-up approach with firing in between the prints. Figure 7.2 is a schematic of the multilayered SSA. In

this configuration, NASICON is not in direct contact with the alumina substrate and so no electrolyte (phase) deterioration is expected.

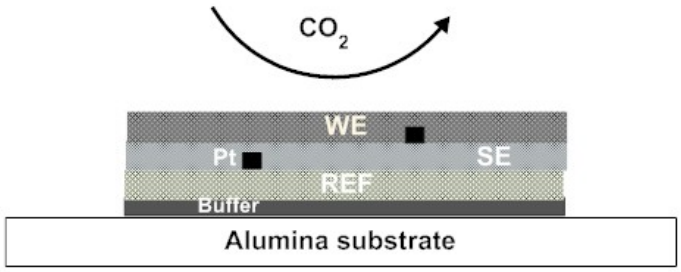

Figure 7.2 – Multilayered stack sensor architecture.

To fabricate the sensor, the following steps were followed;

1. The buffer was printed on alumina substrate and fired at 1200 °C for 120 minutes.

2. The reference electrode of the (Na-Ti-O) system was printed on top of the buffer and fired at 950 °C for 90 minutes. As was stated earlier, this sintering temperature and duration the reference on the buffer is an optimised recipe.

3. Platinum strips were printed on top of the fired RE, and fired at 850 °C for 30 minutes.

4. NASICON was then printed on top and fired at 900 °C for 90 minutes. The film was not fully sintered at this temperature but was still fixed on the RE. Being a superionic conductor, NASICON can still conduct ions enough for sensing purposes.

5. Platinum strips were again printed on top of NASICON, and fired at 850 °C for 30 minutes. At this stage wire bonding was also carried out.

6. Finally the sensing (working) electrode was printed and fired at 550 °C for 30 min. The ternary mixture of Na-Li-Ba-CO_3 was fired at 500 °C.

7.2.2 Sensor Measurements

Figure 7.3 is the schematic of the gas testing rig that was used to characterise the sensing properties of the fabricated planar CO_2 sensors. The gas source was in the form of two cylinders; one containing 500 ppm CO_2 in air and the other synthetic air respectively.

These were mixed appropriately into desired concentrations using the flow meters (Platon, Basingstoke, UK) and then homogeneously mixed through the mixing column containing glass beads. To divert the mixed gas through the bubbler to test for humidity cross-sensitivity, the tube was clamped using clamp D, and then to test for dry gas, it was simply loosened.

The gas mixing proportions are as shown in Table 7.1. The flow rates was in cubic centimetre per minute (ccm).

Table 7.1 – Gas mixing proportions used in the flow meters.

Air/ ccm	**CO_2/ ccm**	**% CO_2**	$P_{CO_2} \times 10^{-4}$**/atm**	P_{CO_2}**/ppm**
200	0	0	0	0
150	50	25	1.25	125
100	100	50	2.5	250
50	150	75	3.75	375
0	200	100	5	500

The temperature of the bubbler was monitored because the water vapour pressure is a function of ambient temperature. The temperature was constant in the room and was found to be 24 °C corresponding to 2975 Pa.

The gas was then fed into the quartz sensor chamber. A K-type thermocouple placed close to the sample ensured the correct and real time sensor temperature.

The NI-TC data acquisition (NI-TC DAQ) was used to acquire the temperature data, while the Keithley 6517A was used as the DAQ for the sensor data. LabView program was coded to collect, analyse and display the data on the PC. Furthermore, the chamber was inserted into a grounded Faraday cage to shield the sensor from any induced voltages.

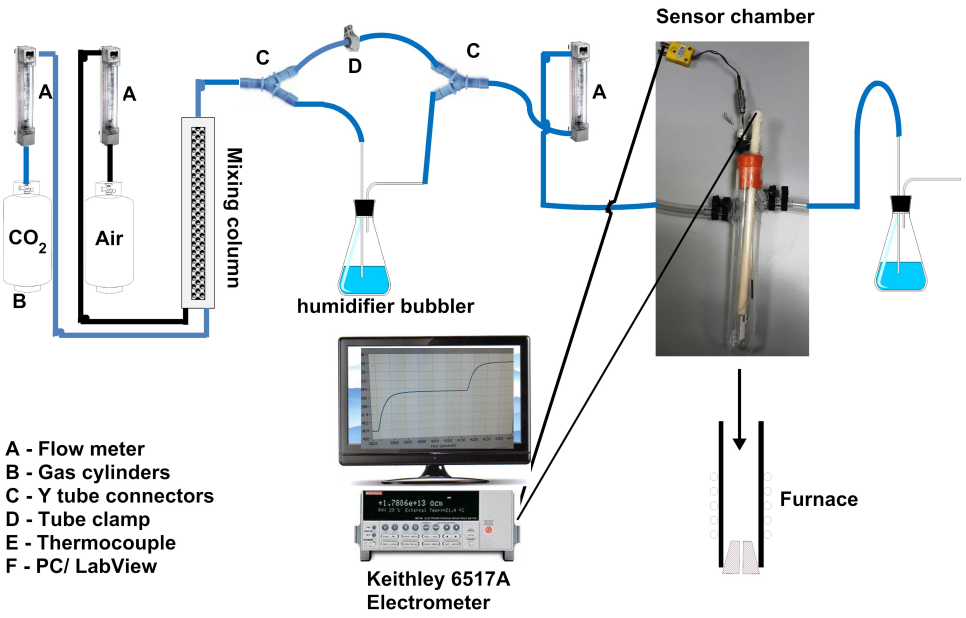

Figure 7.3 – Sensor measurement rig.

The sensor chamber was designed in such a way that it had a small interior volume in order to reduce the dead volume. However, this came at a cost, because, being short, it could not be inserted deep into the tube furnace but was just 10 cm from the edge. This meant that, the furnace temperature was always higher than the sample temperature. Consequently, the sensor testing was only limited up to about 450 °C other wise the tubes attached the chamber would char or burn.

7.3 Theoretical Considerations

The general cells of used in this study are (-)NaBa(Li) | NASICON | NT6-NT3 (NT6-TiO_2) or (-)NaBa(Li) | NASICON | NT6-NT3 (NT6-TiO_2)| Buffer. The anodic reaction taking place at the electrode

$$Na_2CO_3 \rightleftharpoons 2\,Na^+ + 2e + \frac{1}{2}O_2 + CO_2$$

The cathodic reaction when NT6-TiO_2 is used as reference electrode is

$$6\,TiO_2 + 2\,Na^+ + 2e + \frac{1}{2}O_2 \rightleftharpoons Na_2Ti_6O_{13}$$

and when NT6-NT3 is used the reaction is

$$Na_2Ti_6O_{13} + 2\,Na^+ + 2e + \frac{1}{2}O_2 \rightleftharpoons 2Na_2Ti_3O_7$$

so that the overall cell reactions become

$$6\,TiO_2 + Na_2CO_3 \rightleftharpoons Na_2Ti_6O_{13} + CO_2 \tag{7.3}$$

and

$$Na_2Ti_6O_{13} + Na_2CO_3 \rightleftharpoons 2Na_2Ti_3O_7 + CO_2 \tag{7.4}$$

The measured Nernstian EMF becomes

$$E = -\frac{\Delta G^o}{nF} - \frac{RT}{nF}\ln\left(\frac{P_{CO_2}a_{\underline{Na_2O}(\mathrm{Ref})}}{a_{\underline{Na_2CO_3}(\mathrm{NaBa})}}\right)$$

where $a_{\underline{Na_2CO_3}(\mathrm{NaBa})}$ is the activity of Na_2CO_3 in the biphasic mixture, Na_2CO_3-

$BaCO_3$, $a_{\underline{Na_2O(Ref)}}$ is the activity of Na_2O in the biphasic reference electrode and $n = 2$ is the number of electrons transferred in the process. ΔG^o was obtained using the JANAF thermodynamics tables[210].

By using the Raoultian law[121] in an ideal case, the activity assumed to be the mole fraction in the solid solution then taking a ratio of the activity of each component of a solution to its activity as a pure material(this is approximately equal to the mole fraction of the component in the solution). The assumption is on the basis that the activity data as a function of temperature (T) and mole fraction (X) is not available in the literature for binary and tenary metal carbonate systems.

Therefore in the Na_2CO_3-$BaCO_3$ solution, $a_{\underline{Na_2CO_3(NaBa)}} = \gamma X_{Na_2CO_3}$ and $a_{\underline{BaCO_3(NaBa)}} = \gamma X_{BaCO_3} = 1 - \gamma X_{Na_2CO_3}$ so that in an ideal case, $\gamma = 1$ and X being the mole fraction will be the Na_2CO_3 activity in the solution.

For the multi-layered sensor which is some kind of a closed reference, the buffer system fixes the oxygen potential at the reference side by virtue of the reaction of Equation (7.5) or the Gibbs phase rule. The same applies to the modified PSA. A buffer may be the only material that may function as a shield but also prevent oxygen interference by fixing its potential.

$$2CuAlO_2(s) + Al_2O_3(s) + \frac{1}{2}O_2(g) \rightleftharpoons 2CuAl_2O_4(s) \tag{7.5}$$

By using the phase rule $F = C - P + 2 = 1$, for $C = 3$ (O, Al and Cu) and $P = 4$($CuAlO_2$, $CuAl_2O_4$, Al_2O_3 and O_2). The single degree of freedom implies that temperature is the only variable remaining and by fixing the temperature, the oxygen potential is fixed at the reference/buffer interface.

7.4 Sensor Measurement Window

Based on the thermodynamic measurements in Chapter 6, the temperature ranges at which the reference electrodes in the cells gave reproducible and stable EMF as well a linear EMF vs Temperature response were identified and selected. These represented the temperature regimes at which the sensors are expected to work best. For the sake of comparison, the sensors were also tested outside the sensing windows.

Furthermore, the window was narrowed down by the inclusion of the buffer in the modified sensor. Since the transition to intrinsic conduction takes place at 375 °C(from Chapter 5), the reference electrode/buffer couple would conduct more efficiently at $T > 375$ °C.

The temperature ranges(in °C) at which the EMF vs Temperature is linear and reproducible from the thermodynamics measurements of NT6-TiO_2 based cell are

$$T_{ref(NT6-\mathrm{TiO}_2)} \equiv \begin{cases} 250 \leq T \leq 432 \\ \\ T > 527 \end{cases} \tag{7.6}$$

while for the NT6-NT3 electrode, the regime is

$$T_{ref(NT6-NT3)} \equiv \begin{cases} 338 \leq T \leq 525 \\ \\ T > 817 \end{cases} \tag{7.7}$$

Therefore, a PSA sensor has these working temperature regions at which the

response is expected to be Nernstian.

For the modified sensors which use the copper aluminate oxygen buffer, combining the intrinsic conduction range and the thermodynamics range of the reference electrodes reduces the working window to

$$T_{ref(NT6-\mathrm{TiO_2}/p-type)} \equiv \begin{cases} 375 \leq T \leq 432 \\ \\ T > 527 \end{cases} \tag{7.8}$$

and

$$T_{ref(NT6-NT3/p-type)} \equiv \begin{cases} 375 \leq T \leq 432 \\ \\ T > 527 \end{cases} \tag{7.9}$$

for sensors with NT6-TiO_2 and NT6-NT3 electrode respectively. To better represent the ranges in the tables, the following colour codes were used:

Color code	**Representation**
Red	Outside the T_{ref} + T_{p-type} regimes.
Orange	Outside the T_{p-type} but within the T_{ref} regimes.
Green	Within the T_{ref}(for PSA) or T_{ref} + T_{p-type} regimes.

7.5 Planar Sensor Architecture (PSA)

7.5.1 (-)NaBa | NASICON | NT6-TiO_2

Figures 7.4a-d are response transients of planar sensors (PSA) employing Na_2CO_3 - $BaCO_3$ as sensing electrodes. The sensors also had a variation of either having a NT6-TiO_2 or NT6-NT3 as reference electrode. The baseline signal (100% air) is indicated as 0% in the figures.

It can be observed that the sensor responded to step-wise changes in CO_2 concentration. As confirmed in Table 7.2, both the response time (t_{90}) and the recovery time, decreased with temperature due to the corresponding increase in ionic dynamics. Further the recovery time was found to be shorter than the response time.

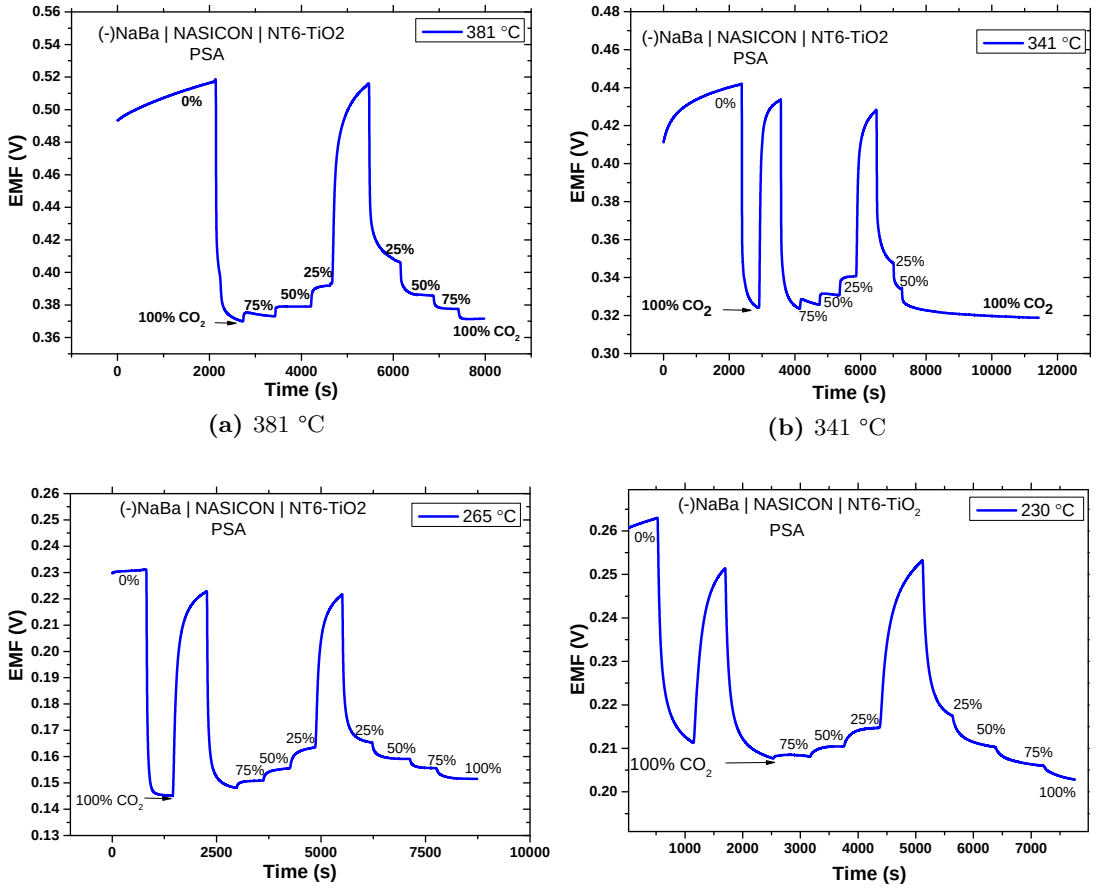

(a) 381 °C **(b)** 341 °C

(c) 265 °C **(d)** 230 °C

Figure 7.4 – Sensor response transients for the cell (-)NaBa | NASICON | NT6-TiO_2 (PSA)

The EMF as a function of temperature is shown in Figure 7.5. The linear relationship between of EMF versus the partial pressure/concentration in a logarithmic scale indicates that the sensor response followed the the Nernst relation $E \propto \ln P_{CO_2}$.

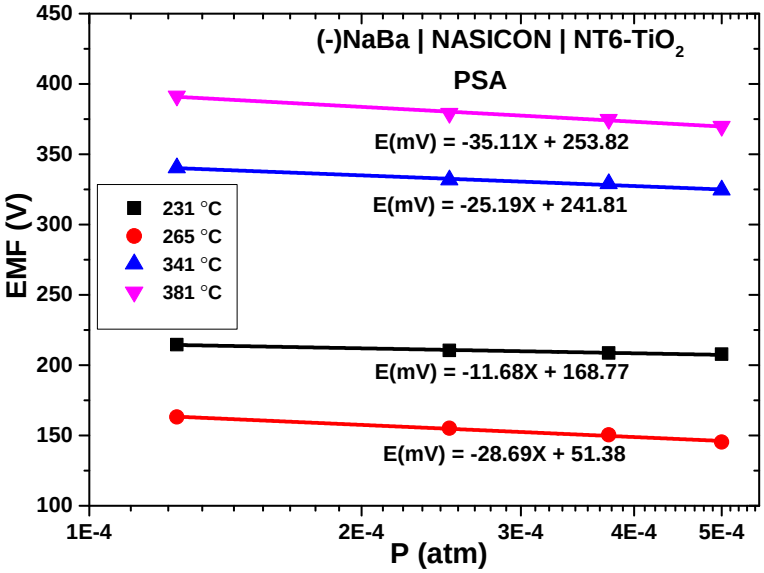

Figure 7.5 – EMF response as function of CO_2 concentration for the cell : (-)NaBa | NASICON | NT6-TiO_2.

Table 7.2 shows the quantitative sensor performance characteristics gathered from Figures 7.4 and 7.5.

Uncharacteristically higher values of n deviant from theory is observed due to a number of reasons; low sensitivity at temperatures under investigations due to low conductivities, slower electrode kinetics making overall equilibrium slower and possible non-Nernstian behavior. This is explained in detail in Section 7.8. Furthermore, there is a general improvement in sensor repeatability with increasing temperature. The source of error in this is the difficulty in the manual control of the flow meters whose values may not be precise. The signal drift(at 100% CO_2) was calculated using $d(\%/day) = \frac{\Delta E \times 100\%}{E_o t}$, where $\triangle E = E_i - E_o$, and E_o, E_i and t are initial EMF, EMF after drifting for a time t and t is the duration in days respectively.

Table 7.2 – Sensor performance characteristics for cell NaBa|NASICON|NT6-TiO_2.

Parameters	**Temperature**			
	231 °C	**265 °C**	**341°C**	**381°C**
Slope (mV/dec)	-11.68	-28.69	-25.19	-35.11
$-\frac{RT}{nF}\ln(10)$	-50.0	-53.4	-60.9	-64.9
n	8.6	3.7	4.8	3.7
t_{90} **(sec)**	272	200	145	133
Recovery (sec)	272	184	27	20
FSO (mV)	54.8	86.06	117.64	146.8
Hysteresis error (%)	5.84	4.83	2.83	4.5
Measured EMF (mV)	-	145.01	319.12	371.5
Theoretical EMF (mV)	-	157.8	243.2	288.8
Signal drift. (%/day)	--	-	12.75	2.16

Figure 7.6 shows the full scale output of the sensor. It can be seen that the full scale signal increases linearly with temperature. This shows that with an increase in temperature the sensor resolution increases which is vital for sensing very low gas concentrations.

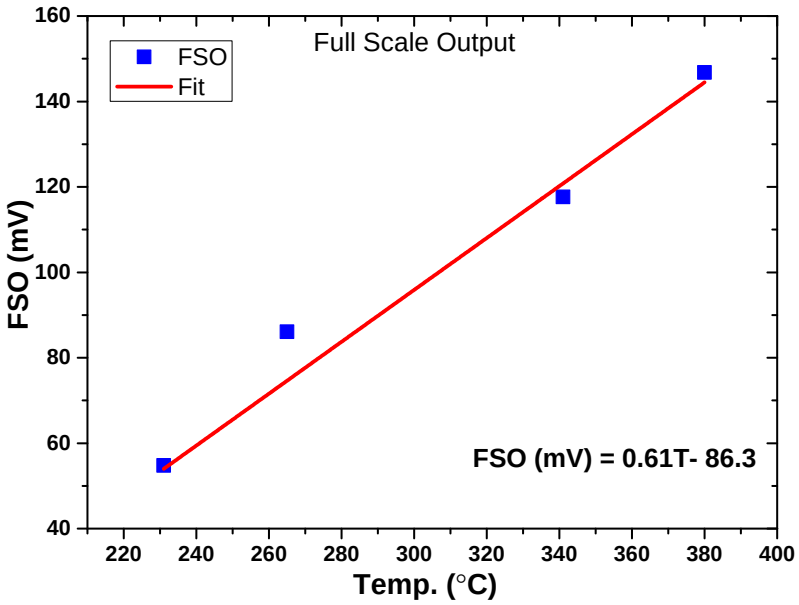

Figure 7.6 – Full scale output as a function of temperature.

Figure 7.7 shows the signal stability and hence the sensor stability after prolonged hours in CO_2 (500 ppm). The signal is quite stable at 341 °C operating temperature with a 2.16% drift per day while lower temperatures are characterised by significant drifts. The magnitudes of the steady signals agree well with the signals in the transients in Figure 7.4.

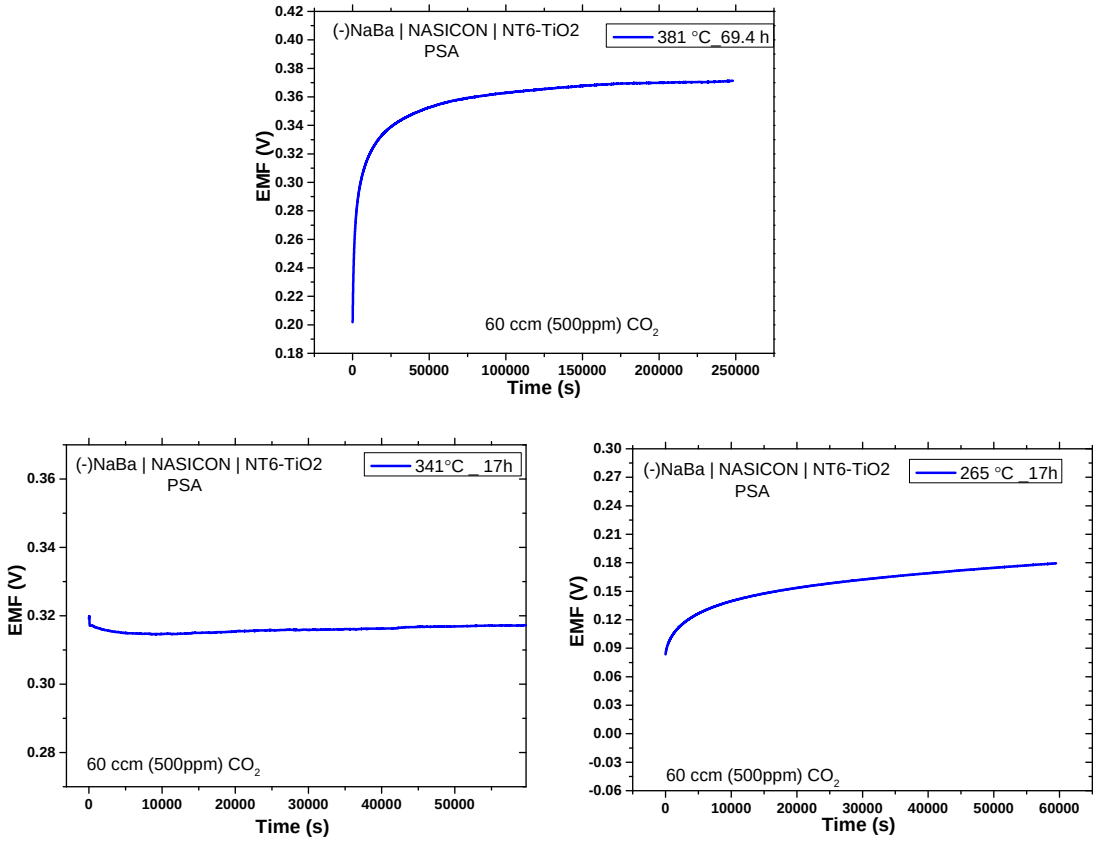

Figure 7.7 – Sensor stability for cell: NaBa | NASICON | NT6-TiO_2.

Figure 7.8 shows the effect of humidity on sensor performance. There is humidity interference at low temperature as can be seen while as the temperature increases the interference reduces. From this trend it is anticipated that at temperature higher 359 °C the sensor may be immune to humidity interference.

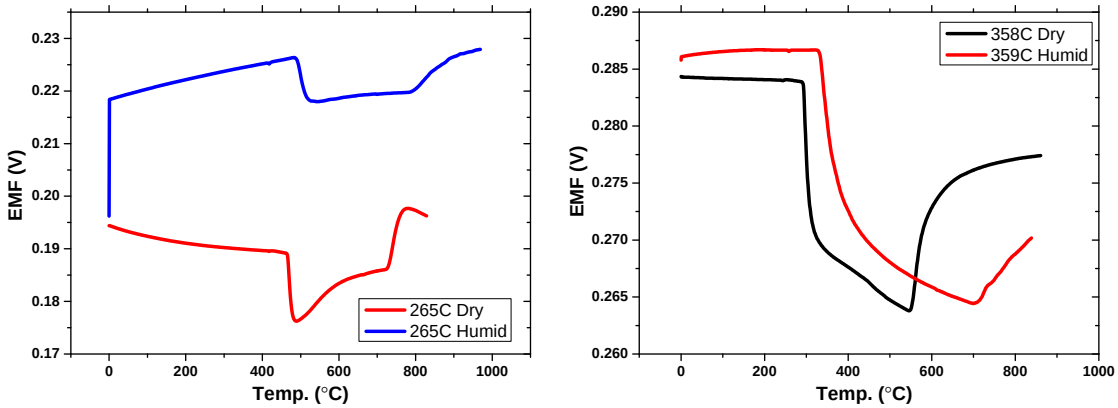

Figure 7.8 – Test for humidity cross-sensitivity for cell NaBa | NASICON | NT6-TiO_2

Figure 7.9 shows Cole Cole plots from AC impedance measurements of the sensor during operation in air and in CO_2. The inset are higher temperature semicircular plots.

As can been there is no change in ion conductivity both in air or CO_2 except a slight deviation for lower temperatures that could be due to extrinsic effects. Furthermore, the two Arrhenius plots, for the sensor device and the NASICON film studied in Figure 4.24 of Chapter 4 are parallel implying same activation energy of 0.57 eV. This is also in agreement with the value obtained by Wang and Kumar [86]. This result shows that the electrolyte in the sensor device exhibits the same intrinsic properties.

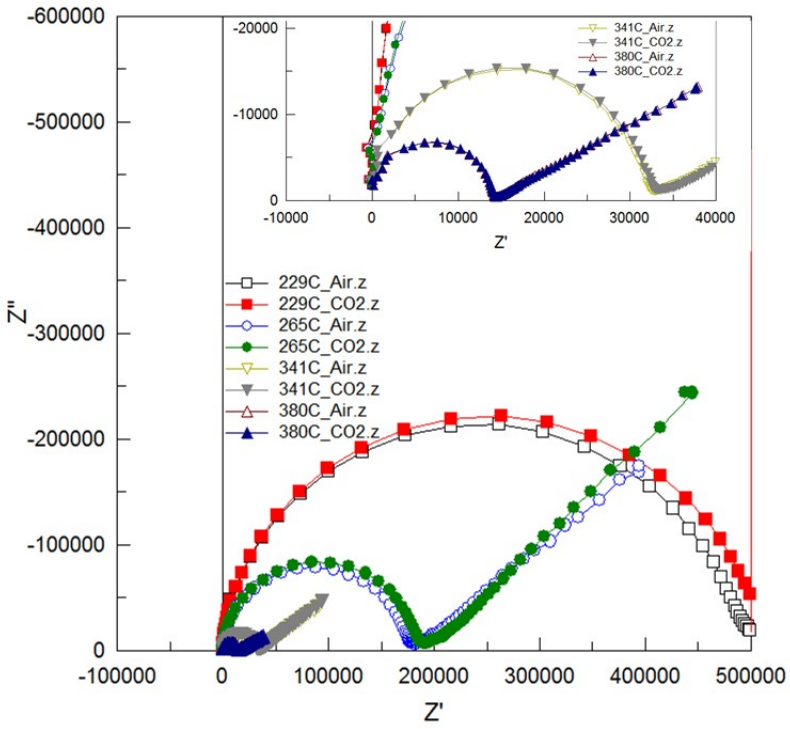

Figure 7.9 – AC sensor impedance in air and CO2 of the sensor at different temperatures. The inset are higher temperature plots.

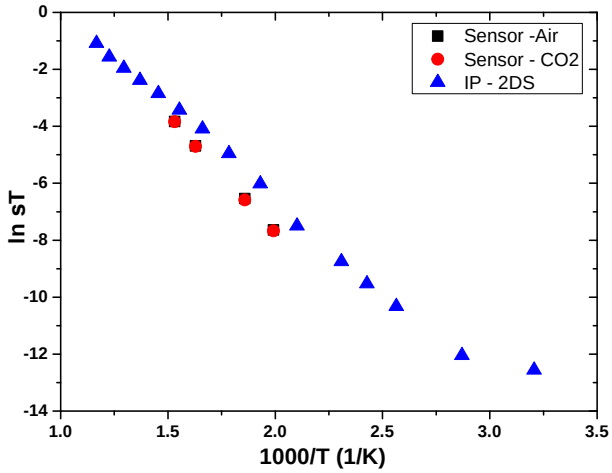

Figure 7.10 – Comparison of Arrhenius plots: in situ (sensor) vs ex situ (NASICON thick film)

7.5.2 (-)NaLiBa | NASICON | NT6-TiO_2

A eutectic melt of ternary phase of NaLiBa carbonates was used as sensing electrode. Figure 7.11 shows the response transients of the sensor. It can be seen that with this sensing material combination, the sensor showed a rapid response. The response time(t_{90}) and the recovery times at 325 °C were 46.8 s and 34.5 s respectively. The sensor signal was stable and repeatable with a hysteresis error of 0.6 % . Furthermore the sensor response was better than the sensor with NaBa carbonates as a sensing electrode.

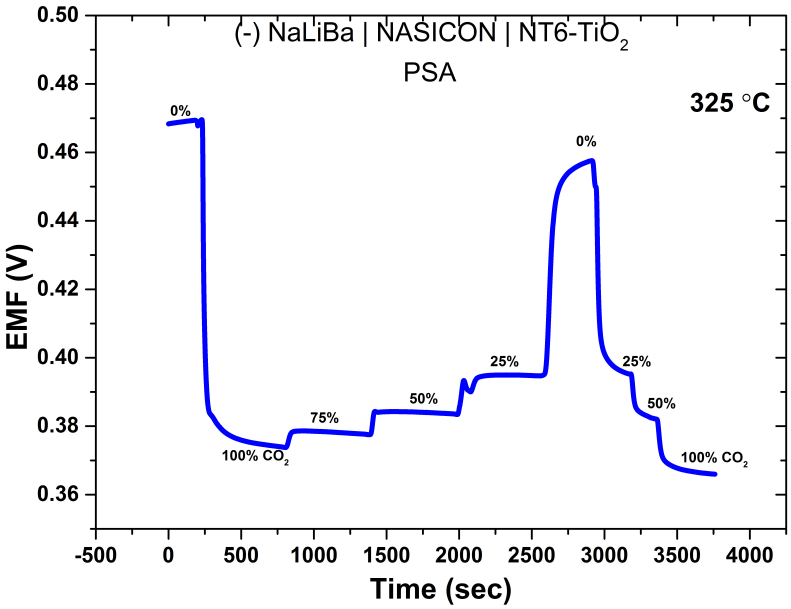

Figure 7.11 – Sensor response transient for the cell NaLiBa | NASICON | NT6-TiO_2

Figure 7.12 is the plot of EMF against CO_2 partial pressure. The plot shows a linear relation akin to the Nernstian type. Using the regression fitting on the data, the EMF relation was $E(\text{mV}) = -41.66X + 232.63$ translating to a sensitivity of 41.66 mV and $n = 2.8$. The data are summarised in Table 7.3.

Table 7.3 – Sensor performance characteristics for cell NaLiBa|NASICON|NT6-TiO_2. E_m= **Measured EMF,** E_T =**Theoretical EMF.**

T (°C)	Slope (mV/dec)	n	t_{90} (sec)	Rec. (sec)	FSO (mV)	Hyst. (%)	E_m mV	E_T mV
325	-41.66	2.8	46.8	34.5	94.9	0.6	374.2	208.1

Figure 7.13 is a plot to test how stable the sensor signal holds. It can be seen that the EMF is pretty stable and its value is exactly as it was recorded in the response transients of Figure 7.11. The drift was found to be 0.45 % /day. This represents a very low signal drift, a requirement for any sensor. This is the very important characteristic for successful application of the sensor.

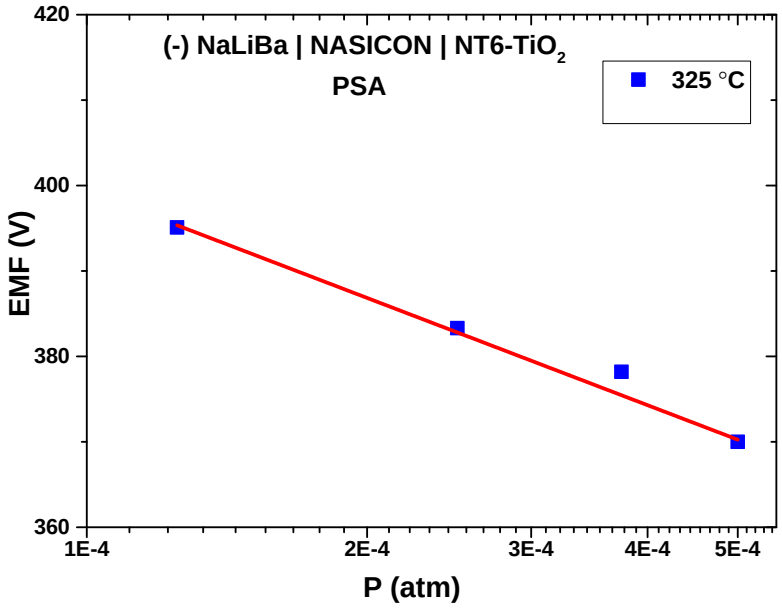

Figure 7.12 – EMF vs partial pressure of CO_2 at 325 for cell (-)NaLiBa | NASICON | NT6-TiO_2 (PSA)

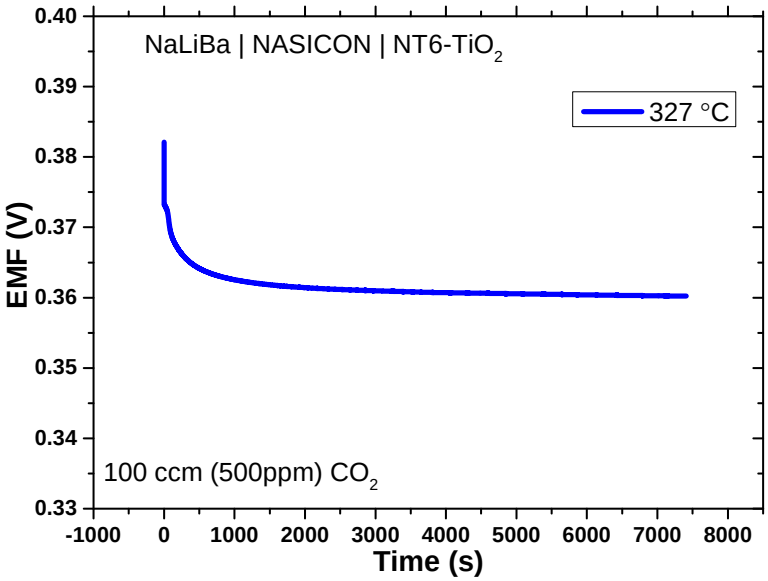

Figure 7.13 – Signal stability for the cell NaLiBa | NASICON | NT6-TiO2 (PSA

7.5.3 (-)NaBa | NASICON | NT6-NT3

Figure 7.14 is a plot of sensor response for the cell NaBa | NASICON | NT6-NT3 at different temperatures when CO_2 concentration is changed in a step-wise sense.

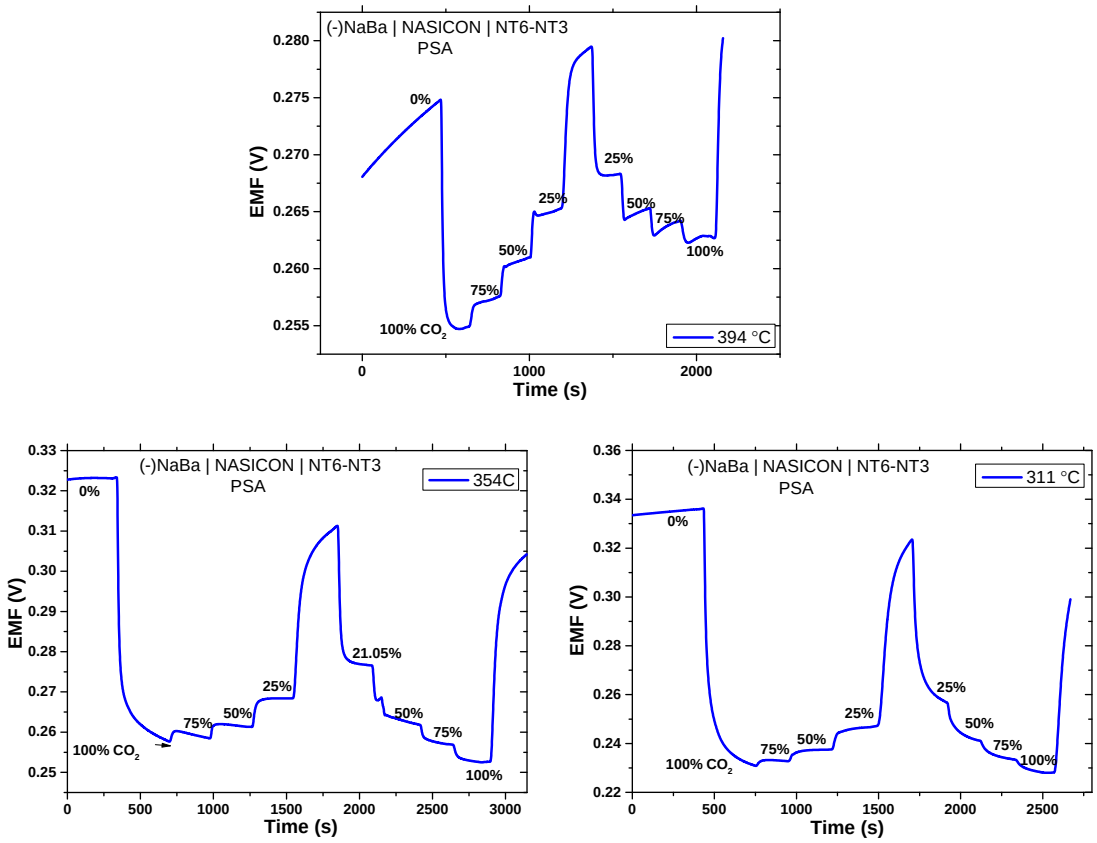

Figure 7.14 – Sensor response transients for the cell (-)NaBa | NASICON | NT6-NT3 (PSA)

The sensor is clearly responding well to the step changes in CO_2 partial pressure. Due to the usual sluggish electrode kinetics at lower temperatures the response was slow as was observed in previous measurements.

Despite its rapid response there is an observed EMF drift when the sensor is operated at 394 °C. One reason was the temperature in the furnace was not stable as it varied from 393 to 395 °C. Stable signals are however observed in the lower operation temperatures and are pretty repeatable.

Figure 7.15 is a plot of EMF as a function of gas concentration. The plots conformed to the Nernstian relation however the sensitivity at 394 °C was not

high enough owing to the reason already discussed.

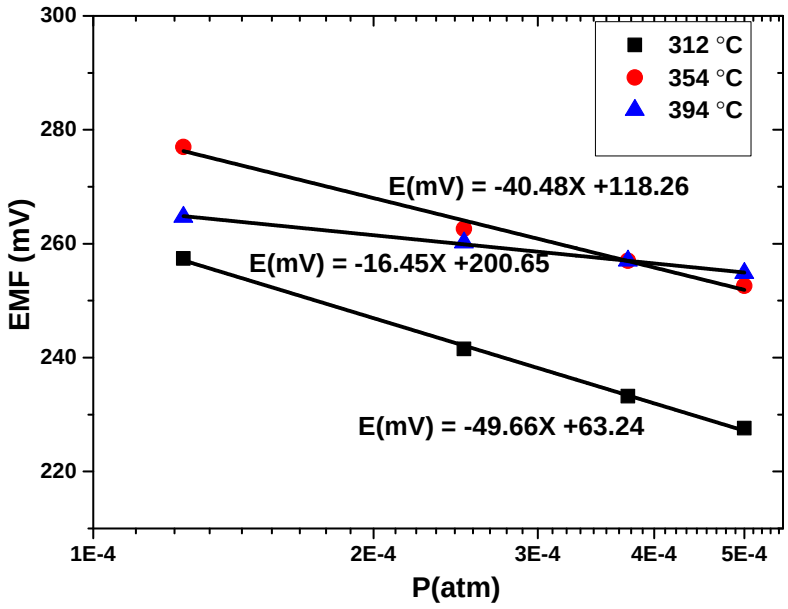

Figure 7.15 – EMF response as function of CO_2 concentration for the cell : (-)NaBa | NASICON | NT6-NT3 (PSA).

Table 7.4 shows the quantitative sensor performance. As has been observed with other sensor structures in this study, signal recovery is more rapid than the response time (t_{90}) and that the rates increase with temperature. The sensor is also repeatable within 1.8 % hysteresis error except the 394 °C operating temperature when the signal kept drifting.

Table 7.4 – Sensor performance characteristics for the cell NaBa | NASICON | NT6-NT3

Parameters	**Temperature**		
	312 °C	**354 °C**	**394°C**
Slope (mV/dec)	-49.66	-40.48	-16.45
$-\frac{RT}{nF}\ln(10)$	-58.0	-53.4	-66.2
n	2.3	3.1	4.8
t_{90} **(sec)**	132.1	35.6	25.9
Recovery (sec)	81	48	14
FSO (mV)	108.2	70.6	20.3
Hysteresis error (%)	1.8	1.8	37.9
Measured EMF (mV)	228.1	257.8	254.7
Theoretical EMF (mV)	-	285.4	249.7
Signal drift. (%/day)	1.83	76.0	137

Figure 7.16 is the stability of the signal with time. The signal (at 312 °C operating temperature) was quite stable, with a drift of 1.83 %/day. This is important for real sensor application in terms of repeatability and long term stability. However, there was considerable higher drift when the sensor was operated high temperature. The possible reason for this drift could be a slight leakage in the rig tubes.

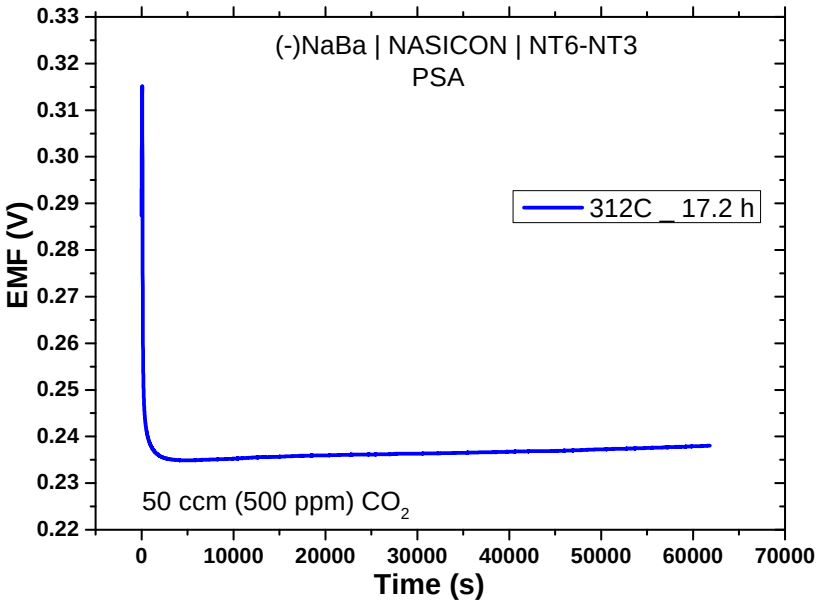

Figure 7.16 – Sensor stability in operation temperature of 312 °C.

Figure 7.17 is a comparison of sensor response to dry and as well as humidified CO_2 to check its cross-sensitivity. The results shows that, in the temperature range investigated the sensor signal was slightly affected by humidity within 1.1-2.8% when CO_2 was passed as shown in Table 7.5. The baseline EMF was always higher in dry CO_2 than in humid CO_2. From the trend, it is clear that the sensor becomes immune to humidity as the operation temperature is increased.

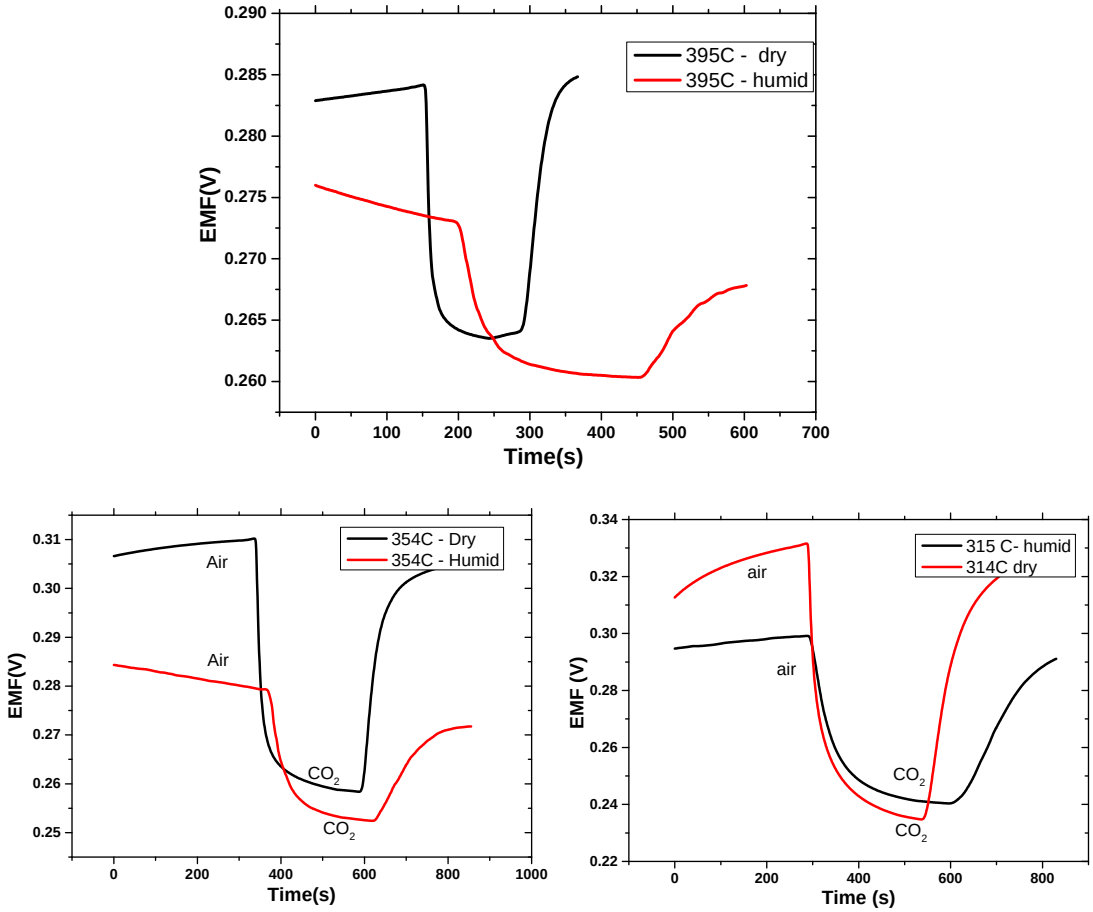

Figure 7.17 – Sensor humidity cross-sensitivity for cell NaBa | NASICON | NT6-NT3 (PSA)

Table 7.5 – EMF deviations in dry and humid conditions.

T/°C	CO_2 (500 ppm)
	△/%
312	2.8
354	2.0
394	1.1

Figure 7.18 are Cole Cole plots of the sensor in air and when CO_2 is passed. As was observed previously, there is no observed change in electrolyte conductivity when CO_2 is passed as dry air or humidified as well in air. This implies that the sensor is immune to humidity and this technique represents a way of checking any electrolyte degradation due to humidity as well as understanding the kinetics during sensing. Therefore it implies that the same ionic kinetics that exist in a pure NASICON film are the existent ones even in the sensor during sensing.

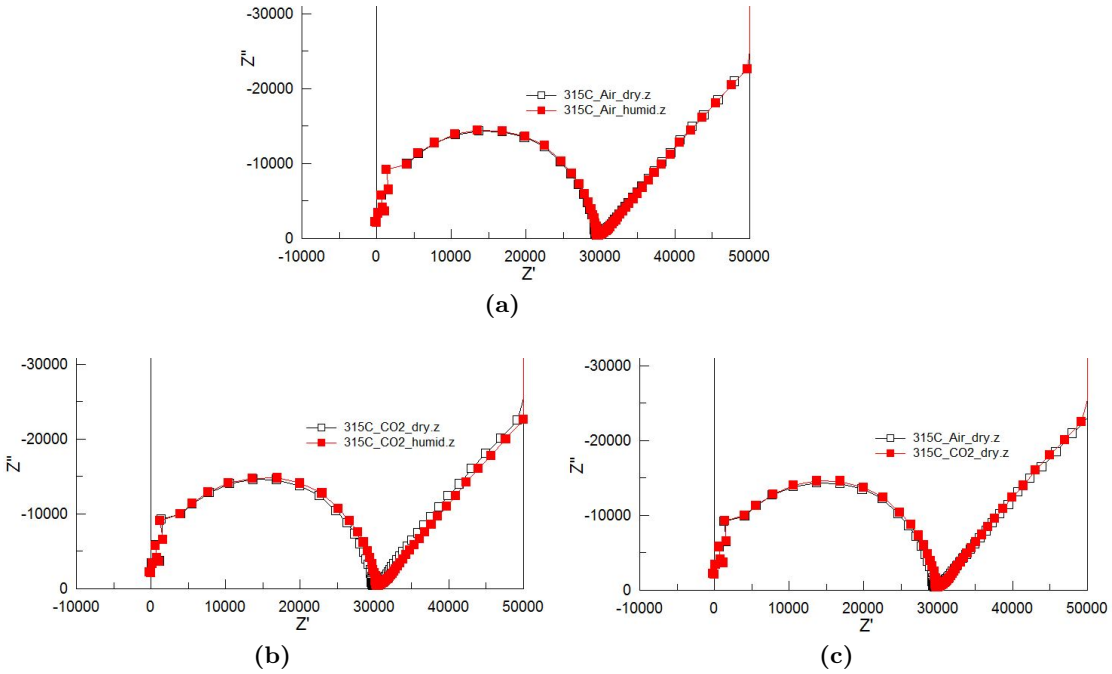

Figure 7.18 – Sensor AC impedance in air and CO_2.(a)Effect of humidity on conductivity in air. (b)Effect of humidity on conductivity in CO_2. (c) Effect of CO_2 gas on conductivity.

7.6 Modified - Planar Sensor Architecture (M-PSA)

7.6.1 (-)NaBa | NASICON | NT6-TiO_2 | Cu-Al-O

Figure 7.19 shows response transients of the modified planar sensors (M-PSA) employing Na_2CO_3 - $BaCO_3$ as sensing electrodes and NT6 - TiO_2 as reference electrodes at different temperatures when a step-wise change of CO_2 gas is introduced.

From the figures, it can be seen that the sensor was responsive to changes in concentrations and the response became more rapid with temperature as expected; due to improved electrical conductivity of the electrolyte as well as rapid equilibrium kinetics.

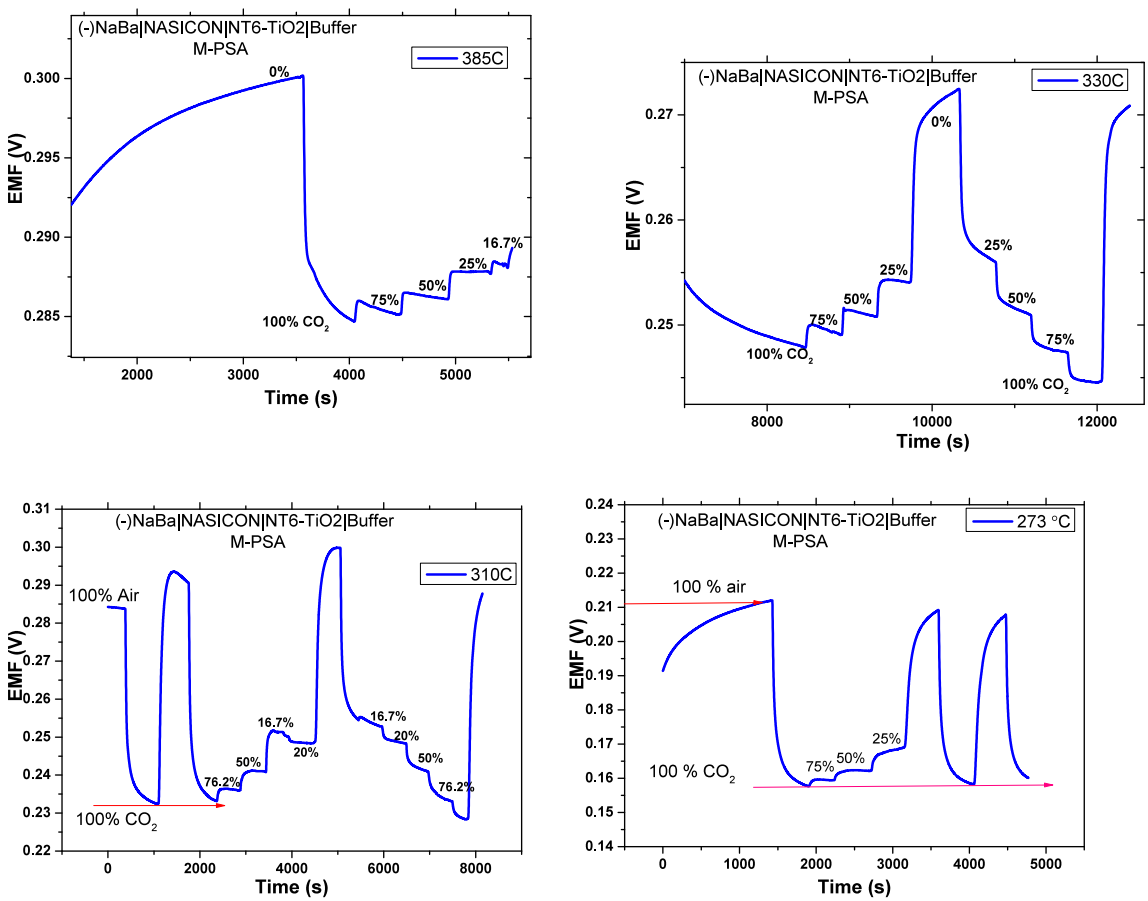

Figure 7.19 – Sensor response transients for the cell (-)NaBa | NASICON | NT6-TiO_2 (M-PSA)

Furthermore the sensor signal was more stable up to 310 °C while above this temperature, the signal was drifting. It is not clear as to the source of this drift as this was exactly opposite to the sensor response of the sensor with NT6-NT3 as reference electrodes discussed in Section 7.6.2. In terms of repeatability, the sensor signal was reproduced for each stepwise decrement or increment of CO_2 concentration.

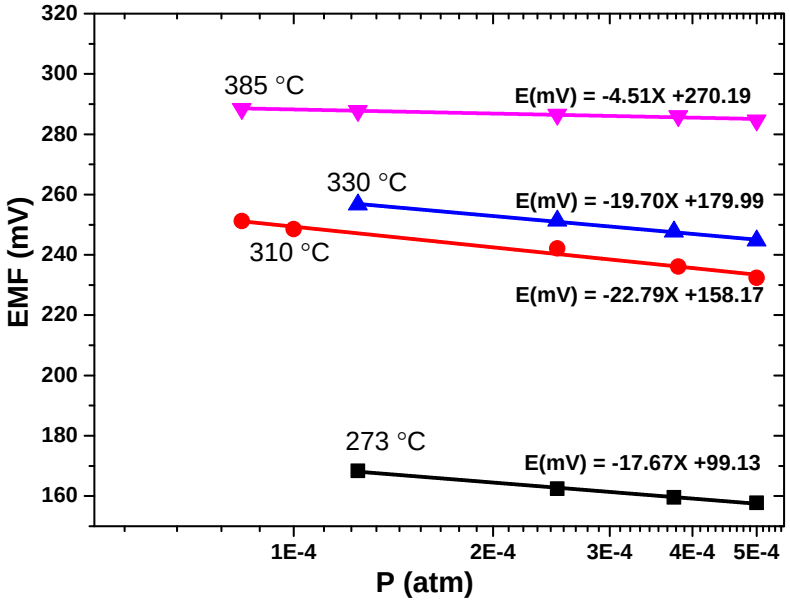

Figure 7.20 – EMF response as function of CO_2 concentration for the cell : (-)NaBa | NASICON | NT6-TiO_2 (M-PSA).

Figure 7.20 confirms the Nernstian relationship of EMF to change in partial pressure. Furthermore, as shown in Figure 7.20 and Table 7.6, the sensor showed lower sensitivities (in mV/decade) in the gas concentration and temperature range investigated. Higher temperature operation may improve the sensitivity. The values of n are uncharacteristically higher than theoretical one. This could be due to the low operating temperature which in turn lowered the sensitivity and produced sluggish electrode kinetics.

Table 7.6 – Sensor characterisation parameters for cell NaBa | NASICON | NT6-TiO_2 (M-PSA)

Parameters	**Temperature**		
	273 °C	**310 °C**	**330°C**
Slope (mV/dec)	-17.67	-22.79	-19.7
$-\frac{RT}{nF}\ln(10)$	-54.1	-57.9	-61.8
n	6.1	5.1	6.2
t_{90} **(sec)**	158	197	87
Recovery (sec)	58	60	40
FSO (mV)	51.8	51.9	27.2
Hysteresis error (%)	3.3	2.2	3.8
Measured EMF (mV)	157.6	232.1	244.6
Theoretical EMF (mV)	166.8	208.4	230.9
Signal drift. (%/day)	10	17.7	31.9

Further, the sensor recovery was more rapid than the response time (t_{90}) and improved with temperature. Figure 7.21 are plots of EMF stability over a time when 500 ppm of gas at 60 ccm of flow-rate is passed in the chamber. As was observed in the transient responses where the response was drifting at higher temperatures, the signal was stable at 273 (°C) but drifting to slightly stable when the operating temperature was 385 (°C), where it was 2.85%/day.

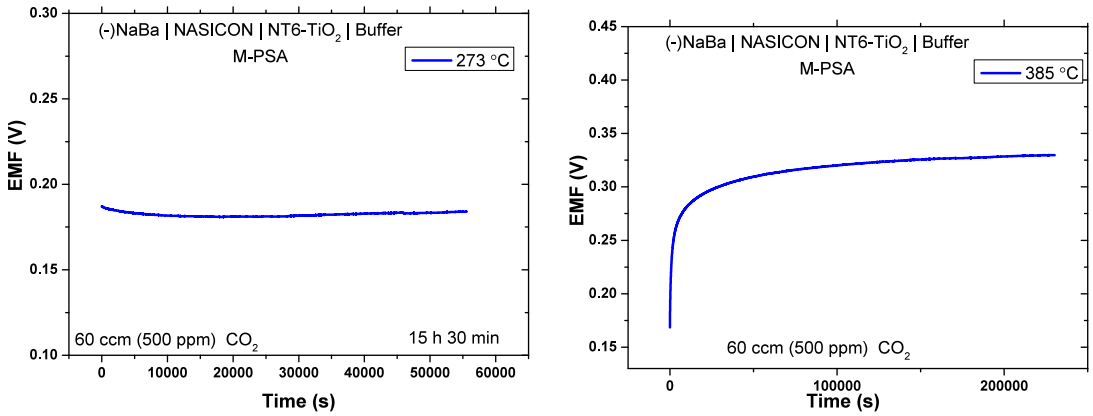

Figure 7.21 – Sensor stability for cell: NaBa | NASICON | NT6-TiO_2 (M-PSA)

Figure 7.22 shows AC impedance measurements of the sensor during operation in air and in CO_2. As was obtained in the previous sensor, there is no significant difference in the impedance when CO_2 or air is passed through the sensor. Similarly in view of the parallel plot, the activation energy is the same for NASICON electrolyte of the sensor and the plane NASICON investigated previously.

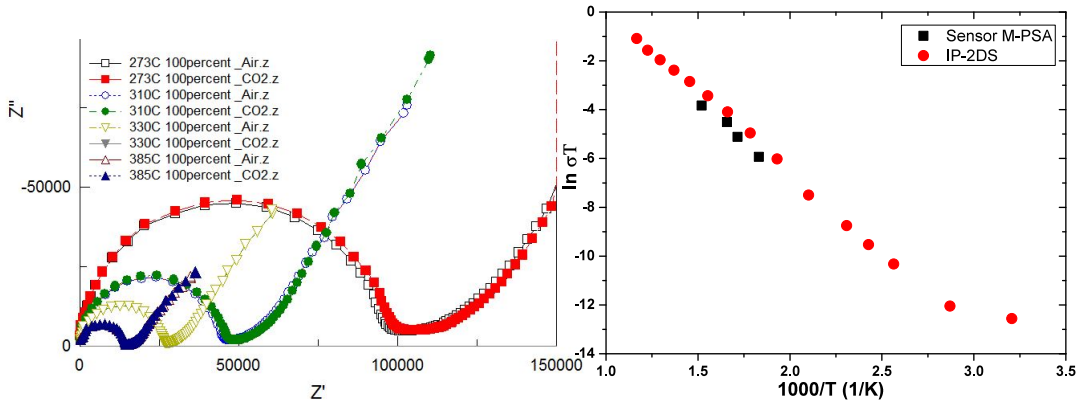

Figure 7.22 – AC sensor impedance and comparison of Arrhenius plots: in situ (sensor) vs ex situ (NASICON thick film)

7.6.2 NaBa | NASICON | NT6-NT3 | Cu-Al-O

Figures 7.23 are response transients of the modified planar sensors (M-PSA) employing Na_2CO_3 - $BaCO_3$ as sensing electrodes while the reference electrodes was the biphasic NT6-NT3. It can be seen that for each step-wise increase in CO_2 concentrations the response is rapid and reproducible except at low temperatures ($< 311°C$) where there is observed drift. Also, as is expected the response time (t_{90}) improved with operating temperature from 276 seconds at 225 °C to 28 seconds at 430 °C.

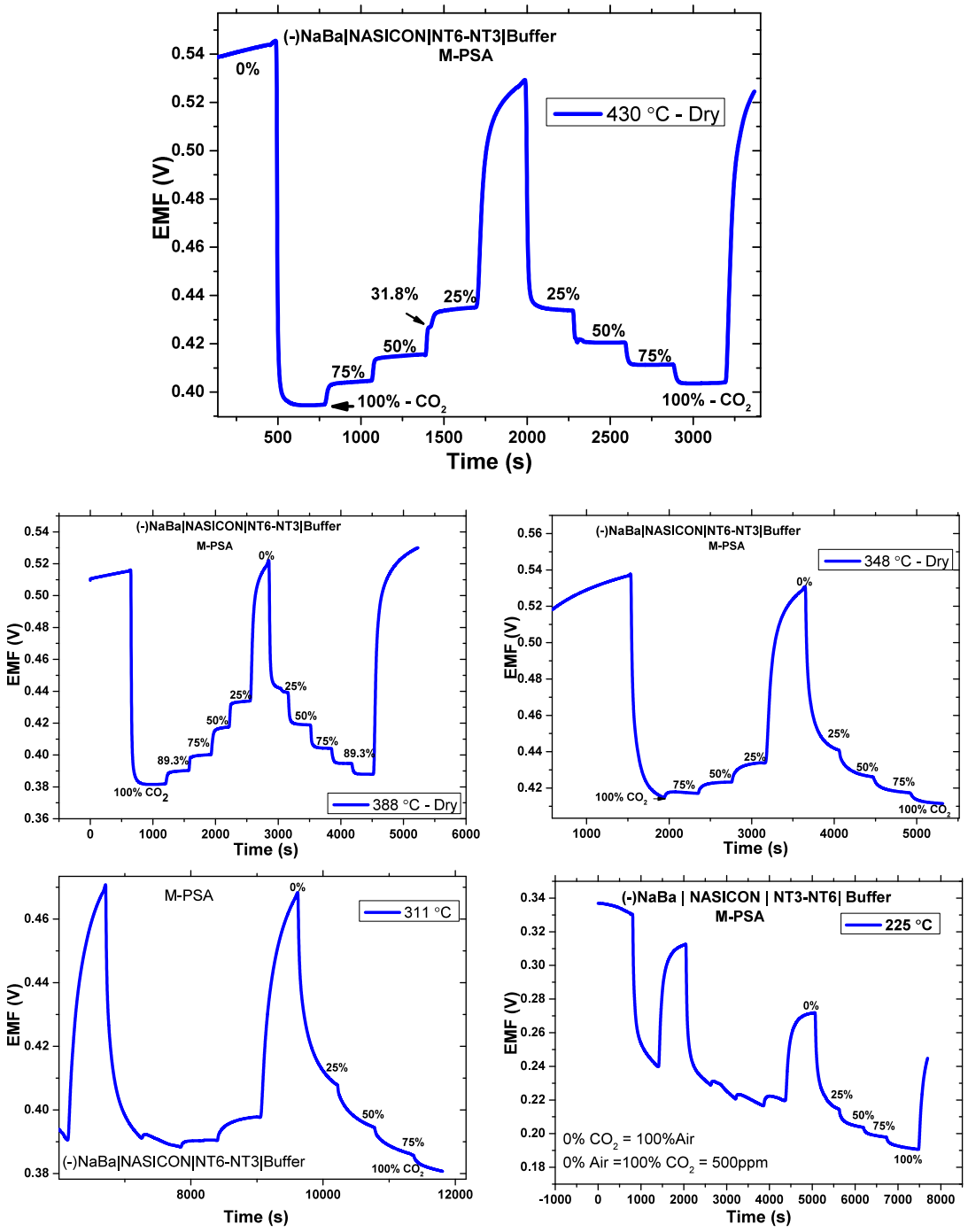

Figure 7.23 – Sensor response transients for the cell (-)NaBa | NASICON | NT6-NT3 (M-PSA)

Figure 7.24 shows the EMF for various temperatures as a function of CO_2 partial pressure. The linearity of the plots are in good agreement with the Nernst equation.

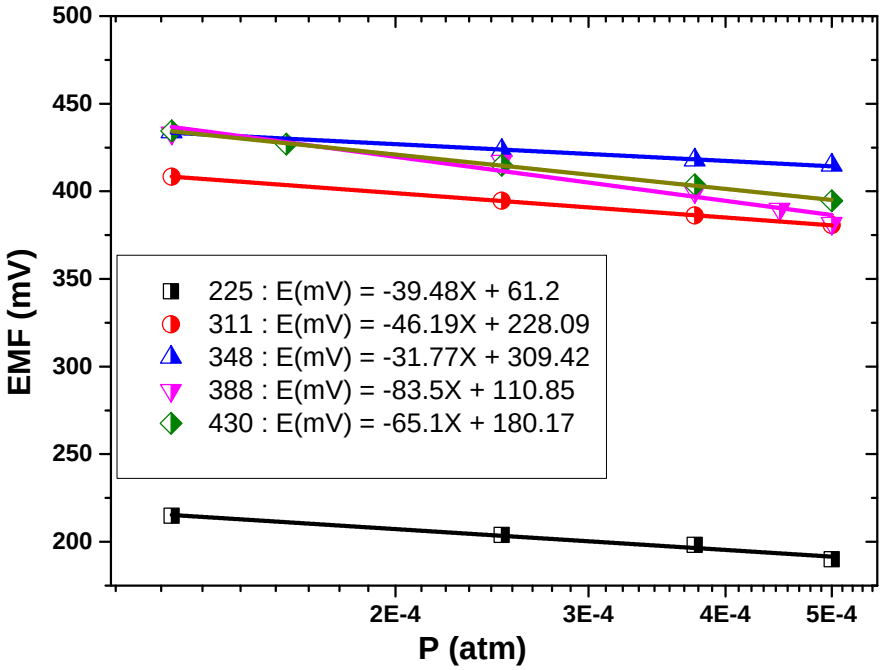

Figure 7.24 – Sensor signal as a function of the CO_2 partial pressure for different temperatures.

Table 7.7 contains the characterised parameters to show sensor performance in detail and how it conforms to the theory within and outside the predicted thermodynamic range. The sensor sensitivity (indicated by slopes) for temperatures (< 311 °C) were not high enough and the reason being obvious, low ion conductivity and sluggish electrode kinetics. Above 311 °C the sensitivity is close to the theoretical value $-\frac{RT}{nF}\ln(10)$. The electron transfer number for sensor operated at 430 was close to the theoretical value $n = 2$. This is also in agreement with studies obtained by Holzinger et al. [12] on bulk pellets were the experiment agreed perfectly with theory at 450 °C and above.

Table 7.7 – Sensor characterisation parameters for cell NaBa | NASICON | NT6-NT3 (M-PSA).

Parameters	**Temperature**				
	225 °C	**311 °C**	**348°C**	**388°C**	**430 °C**
Slope (mV/dec)	-39.48	-46.19	-37.77	-83.5	-65.1
$-\frac{RT}{nF}\ln(10)$	-49.4	-57.9	-61.8	-65.6	-69.8
n	2.50	2.52	3.88	1.57	2.14
t_{90} **(sec)**	276	211	172	49	20
FSO (mV)	81.68	87.95	122.1	134.1	149.0
Hysteresis error (%)	9.7	4.5	2.6	1.4	3.4
Measured EMF (mV)	-	350	412.1	381.6	394.5
Theoretical EMF (mV)	-	-		255.1	217.6
Signal drift. (%/day)	--	11.6	5.2	37.7	80

It terms of hysteresis or repeatability, the operation temperature had a positive effect in that higher the temperature the more repeatable the signals were when measuring from both directions. This property is vital for any successful sensor application because during operation the sensor must be able to sense the test gas accurately and appropriately even when the gas concentrations change from one level to another and back again.

Figure 7.25 shows that the full scale output (FSO) as a function of temperature. The FSO is observed to increase linearly with temperature at the rate of 0.32 mV/°C.

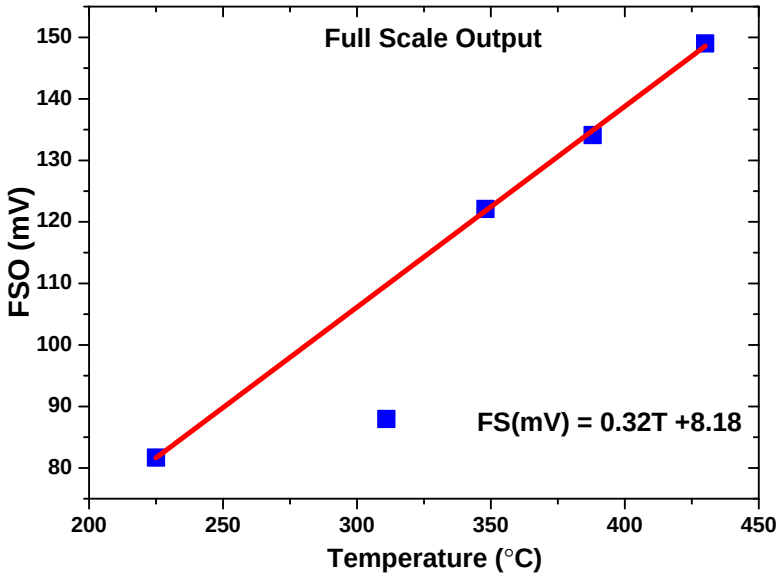

Figure 7.25 – Full Scale response for cell : NaBa | NASICON | NT6-NT3 | Buffer

To check whether the sensor is prone to humidity cross-sensitivity, the tests were run in both humid and dry air for comparison. Figure 7.26 shows the sensor response to humidified test gas at different operating temperature.

From the figures it can be seen that the sensor in air suffers cross interference than when CO_2 is passed. It can be seen that the baseline EMF in dry air is higher than in humid air. However, when the test gas is passed there is little interference and the EMF in dry and humid conditions only differ by $\leq 12\%$. As the operating temperature is increased the sensor is virtually humidity insensitive.

These results imply that for any CO_2 stimuli, the sensor will be able to work and sense accurately irrespective of degree of humidity of the test gas. The sensor will especially be immune in high CO_2 concentrations.

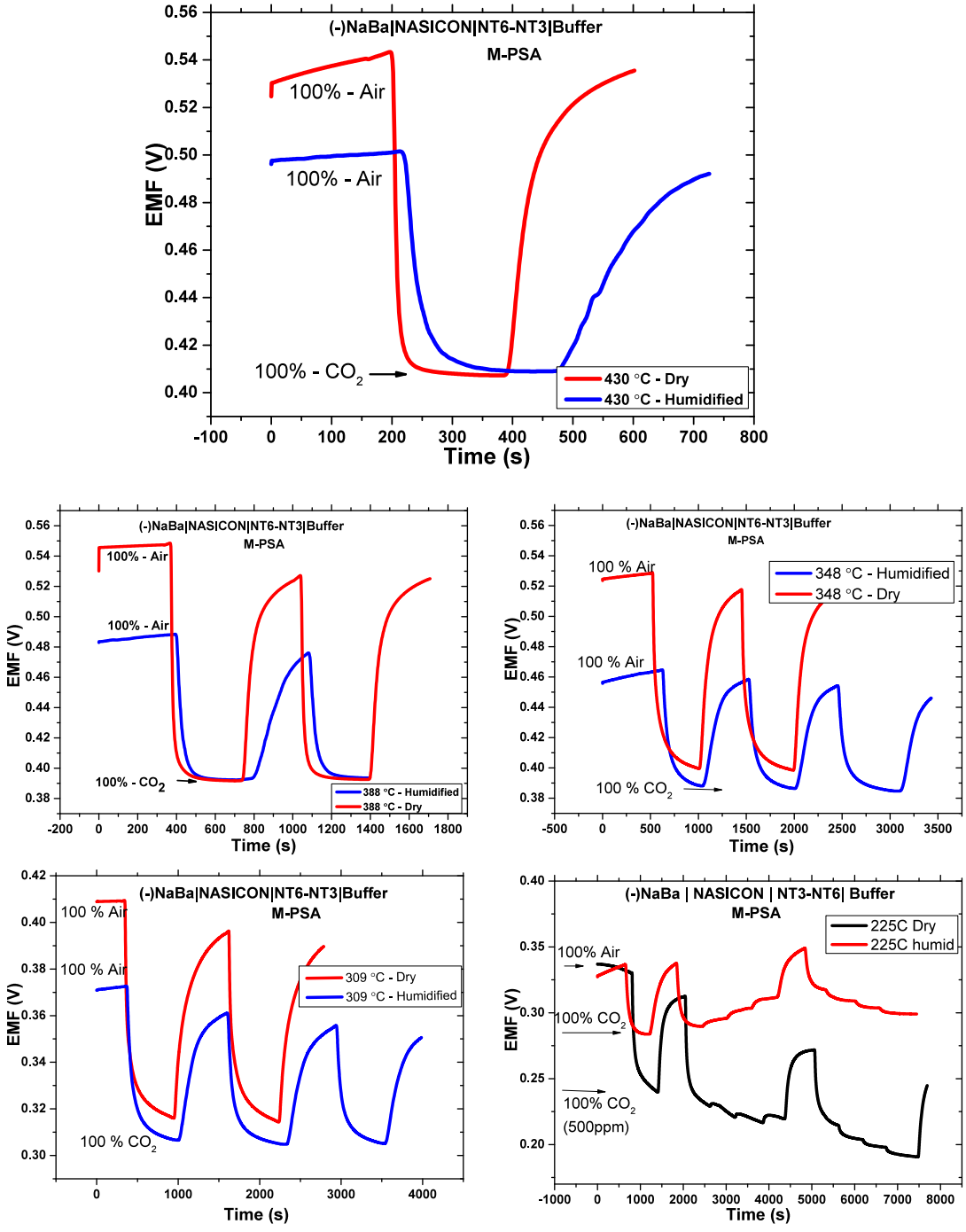

Figure 7.26 – Test for humidity cross-sensitivity.

To quantify the extent of interference given $\triangle = {}^{(EMF_{dry}-EMF_{humid})}/_{EMF_{dry}}$, Table

7.8 tabulates the extent. The slight percentage difference is due to the difficulty in controlling the flow meter to a correspondingly stable and exact reading.

Table 7.8 – EMF deviations in dry and humid conditions.

T/°C	**Air (Baseline)**	**CO_2 (500 ppm)**
	△/%	△/%
225	0	18.2
309	9.0	3.1
348	12.0	3
388	10.7	0.2
430	7.4	0.5

Stability of the sensor signal is shown in Figure 7.27. No significant drift effect is observed over a period of several hours. The drift observed however does decrease with temperature, for instance, the signal drift at 309 °C is 11.6 %/day stabilising duration while at 347 °C the drift reduced to 5.2 %/day which simply means at higher operating temperatures, the sensor signal becomes stable. Inspecting the high temperature data at 388 and 430 °C shows that the signals for each concentration was very stable, and nearly horizontal but when the air was passed in, the pattern was reproduced but there was a significant drift for all the concentrations despite the observed local stability. This result indicates that the sensor works perfectly well and presents one of the best set of device data investigated so far but the drift is akin to an insufficient flashing out of previous gas concentrations in the rig and pipe systems.

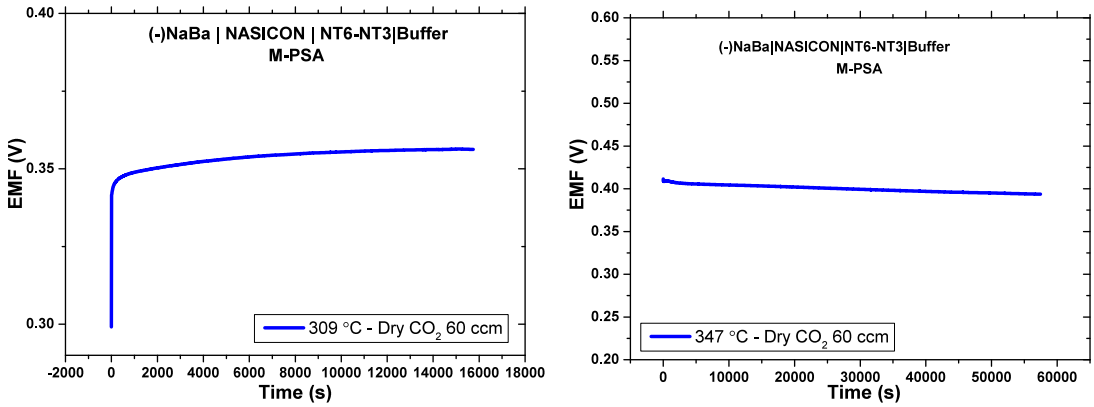

Figure 7.27 – Sensor stability for cell: NaBa | NASICON | NT6-NT3 (M-PSA)

To check any change in ion dynamics in sensors during sensing and compare its ionic conduction properties with pure NASICON thick film studied in Chapter 4, AC impedance was conducted on the sensor both in dry and humid conditions.

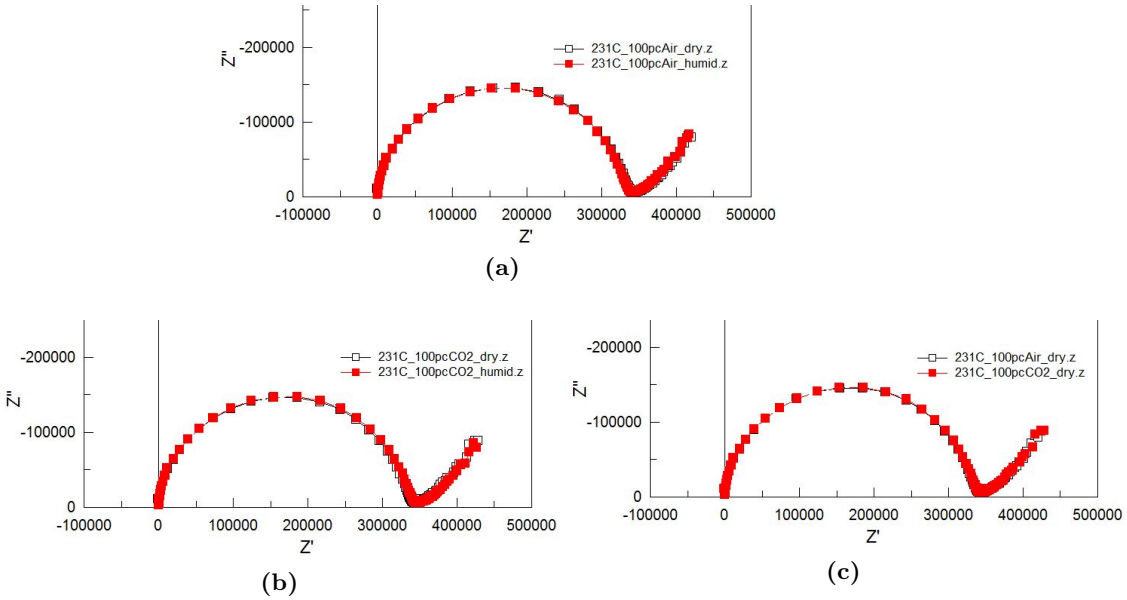

Figure 7.28 – Sensor ion conductivity in air and CO_2.(a)Effect of humidity on conductivity in air. (b)Effect of humidity on conductivity in CO_2. (c) Effect of CO_2 gas on conductivity.

Figure 7.28 shows that the sensor retains its intrinsic conduction even when sensing;

while humidity did not affect the magnitude of conduction implying that the sensor was immune to humidity. Similar results were obtained for measurements at higher temperatures.

Figure 7.29 is a comparison of Arrhenius plots of the sensor and of NASICON thick film studied in Chapter 4. The figure clearly shows a slight decrease in conductivity as compared to the printed NASICON alone. However the activation energy was the same in view of the parallel plots implying the same conductivity mechanism.

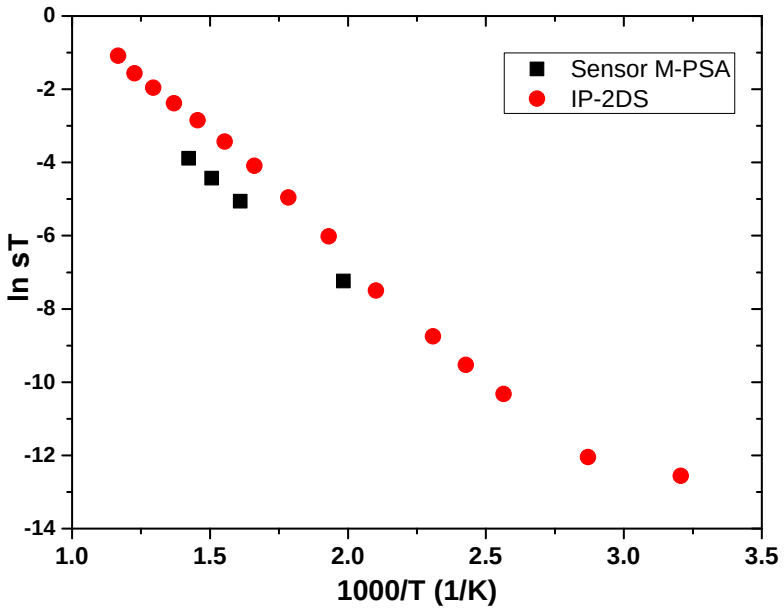

Figure 7.29 – Comparison of Arrhenius plots: in situ (sensor) vs ex situ (NASICON thick film)

7.7 Stacked Sensor Architecture (SSA)

7.7.1 (-)NaLiBa | NASICON | NT6-TiO_2 | Buffer

Figure 7.30 is the sensor response of the multilayered stacked structure.

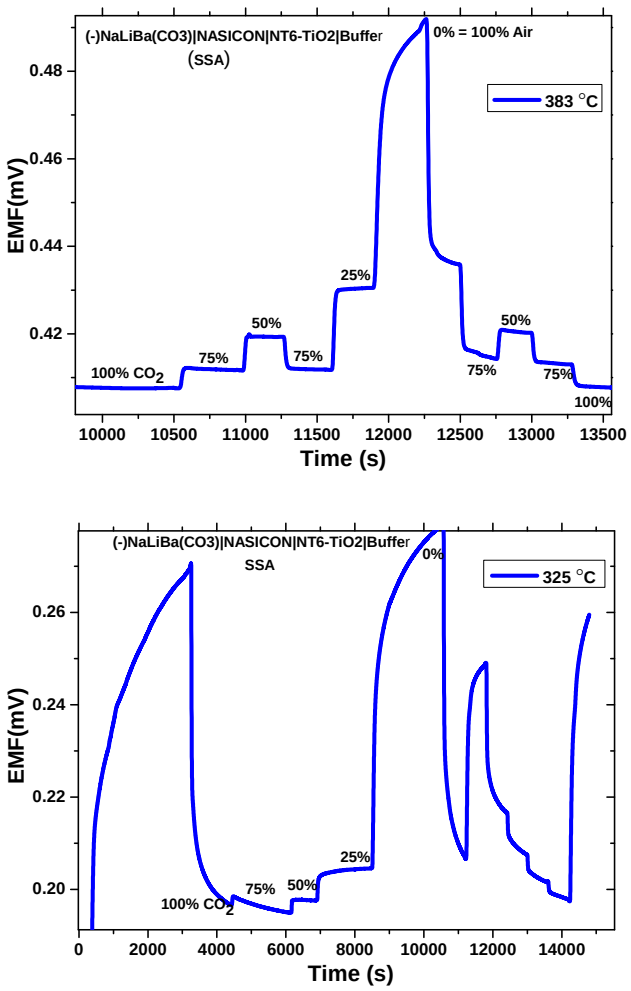

Figure 7.30 – Sensor response transients for the cell: (-)NaLiBa | NASICON | NT6-TiO_2 | Buffer (SSA)

Despite the fact that the electrolyte was never densified when it was fired, it could still conduct and performed well in the sensor. NaLiBa sensing electrode was used in this sensor as it demonstrated rapid response as was shown in Section 7.5.2.

It can be seen that the responses are akin to steps following corresponding step-wise changes to CO_2 concentration. Responses from lower operating temperatures looked to drift because of the longer response times, and longer than the time interval between step changes in CO_2 concentrations.

Table 7.9 shows the sensor characteristics of the multilateral structure. As was observed in the previous tests, recovery time was shorter than the response time (t_{90}). The sensor had one of the shortest response times of the the sensor investigated here. This could be because of the sensing electrode combination that was used. This rapid response was also observed on the planar (PSA) sensor when NaLiBa was used. Furthermore the rapid response also could have been due to the sensor configuration itself; the stacked sensor architecture ensures that the test gas only accesses the sensing electrode.

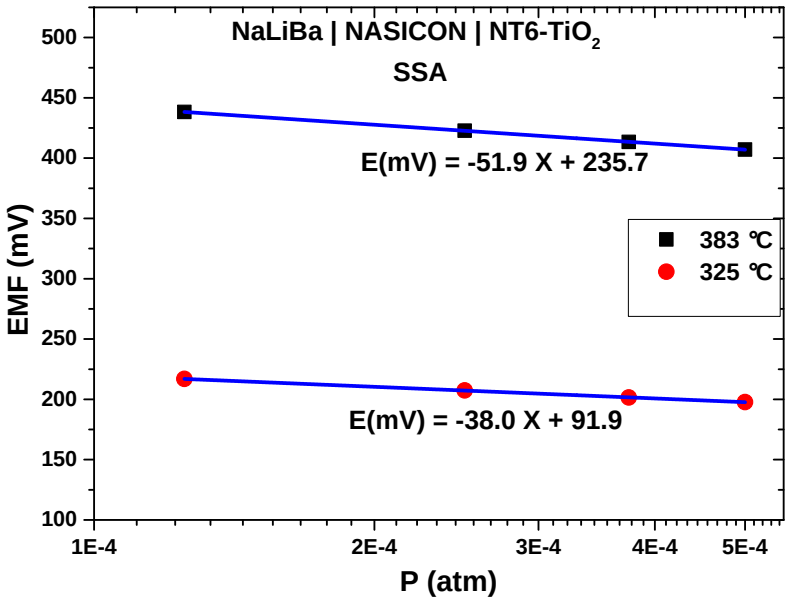

Figure 7.31 – EMF response as function of CO_2 concentration for the cell : (-)NaLiBa | NASICON | NT6-TiO_2 |Buffer (SSA).

Figure 7.31 is a sensitivity plot of EMF against the CO_2 partial pressure. A linear plot is realised which follows the Nernstian law. The sensitivity increased with temperature from 38.0 mV/dec to 51.9 mV/dec at 325 and 383 °C respectively. As was observed previously, sensor response at lower operating temperatures is slightly away from Nernstian behaviour as can be seen from the values of n that has been obtained in Table 7.9. However as the temperature increases, $n \rightarrow 2$.

Furthermore, for ideal application as a sensor, signal stability and reproducibility are the key elements for successful operation and this sensor ticks all the boxes. The knowledge of the value of n may be irrelevant. The sensor reproducibility was 99.1% at 383 °C. Full scale output also increased with operating temperature implying improved sensor resolution with temperature.

Furthermore, looking at the stability of the sensors based on NaLiBa as sensing electrodes (Section 7.5.2 and 7.7.1) it is clear the sensors had superior response times and were more stable as they showed low drift percentages per day as compared to the other sensors.

Table 7.9 – Sensor performance characteristics for the cell NaLiBa | NASICON | NT6-TiO_2 (SSA).

Parameters	**Temperature**	
	325 °C	**383 °C**
Slope (mV/dec)	-38.8	-51.9
$-\frac{RT}{nF}\ln(10)$	-59.3	-65.1
n	3.1	2.5
t_{90} **(sec)**	323	31.9
Recovery (sec)	54	24.7
FSO (mV)	74	91.48
Hysteresis error (%)	12.2	0.9
Measured EMF (mV)	-	407.5
Theoretical EMF (mV)	-	272.0
Signal drift. 100% CO2	-	0
$\Delta E/E$ **(%/day)**		

The influence of humidity on sensor response is shown Figure 7.32. It shows a

reduced EMF response in air when it is humidified, however, importantly there is little or non interference on CO_2 . This result was observed in the previous studies in this work. The implication of this is that sensor as long as a new level of CO_2 is detected, the sensor is immune to humidity.

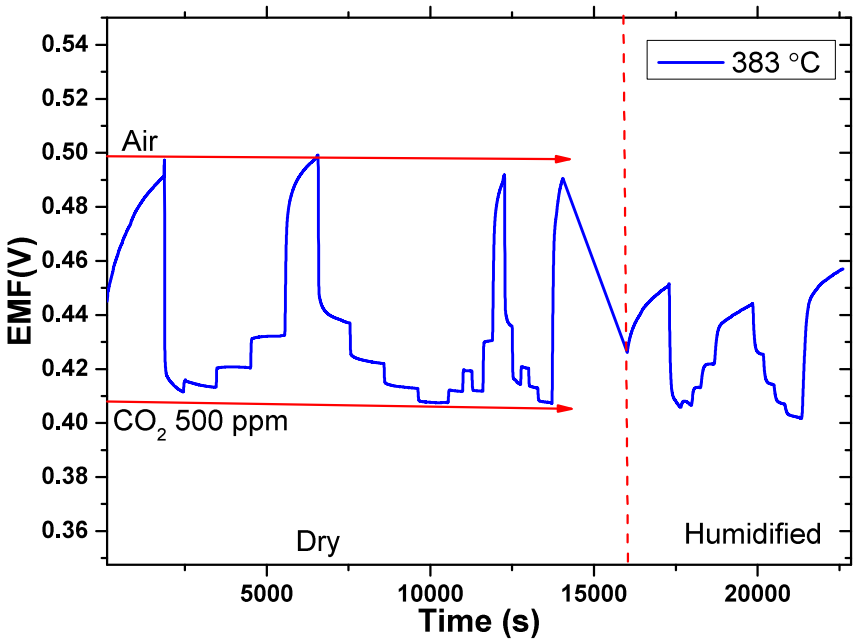

Figure 7.32 – Effect of humidity on sensor performance.

No change in electrolyte conductivity during sensing is observed from AC impedance measurements of Figure 7.33. This implies that the sensor electrical characteristics are the same as a plain NASICON film as studied in Chapter 4.

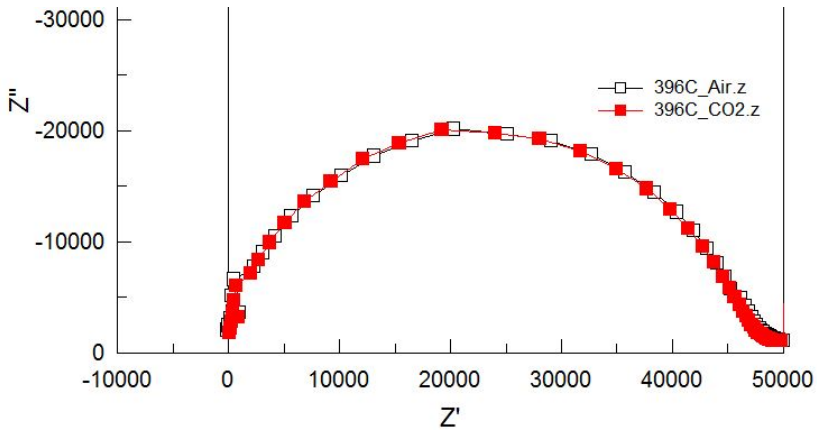

Figure 7.33 – AC impedance of the cell.

7.8 Discussion on some experimental deviations.

From the results, it has been shown that sensors with NaLiBa as the sensing electrode had better sensing properties than the sensors with NaBa as the sensing electrode in terms of sensor stability and response time. The sensors(in Sections 7.5.2 and 7.7.1) had the least drift percentage.

The observed drifts in the sensors could probably be due to insufficient flashing out of the gas/air in the rig and pipe systems where for instance, the EMF at 25% CO_2 is slightly higher than at the same concentration in the previous measurements simply because the gas is diluted. This can be seen clearly on the transient graphs as the signals were drifting towards the high potential end(low CO_2 concentration).

Further, to add more credence to this suggestion, for instance in Figure 7.23, the sensor signals(at 388 and 430 °C) had a perfect local stability but still showed a drift when the measurement was repeated, this could only boil down to slow gas dilution due to insufficient time for flashing out the air and possible slight leakage. Therefore, those drifts in that sensor are just temporal otherwise the sensor can

be drift free looking at how good the local stability is.

In addition to this, from the tables, the measured EMF was mostly higher than the theoretical EMF showing that CO_2 was slightly diluted even at 100% CO_2 flow.

7.8.1 Deviation of n from Theoretical value ($n = 2$) and Theoretical EMF.

The deviation of the measured EMF from the theoretical values as measured at 100% CO_2 flow could be due to a couple of reasons:(a) Insufficient flashing time of gas in the rig before a new measurement is taken and has already been discussed in the preceding subsection, (b) The precise value of the activity of Na_2CO_3 in the Na_2CO_3-$BaCO_3$ eutectic mixture is not known. The value used was just an assumption of an ideal case of the Raoultian law.(c) Even though NASICON (x=2) has a tranference number of close to 1, this number may not be guaranteed for a NASICON thick film that is deposited on alumina substrate due to the interfacial degradation of the NASICON (discussed in Chapter 4).

Furthermore more, there is a possibility of the formation of CUSICONs ($Cu_xZr_2P_3O_{12}$ where $0.5 \leq x \leq 1$) by the virtue of ion exchange in the buffer/NASICON couple. Buffer/NASICON contact could have been established during the printing process as complete isolation of NASICON from the buffer was not possible. This is because the screen printer used was semi automatic and so sub-millimeter precision of film positions was not guaranteed hence the possible contact.

A similar work was reported by Davidson and Fray [211] and Schaffer et al. [212]. CUSICONs are copper ion conductors coupled with low electronic conduction of about 4% at 600 K[212]. Therefore if that is the case, the measured EMF (E_m) would be deviant from the theoretical EMF (E_T), in fact it would be less than

the theoretical value due to the shorting effect. The fact that the results showed $E_m > E_T$ in most cases shows that the leakage effect may have masked this EMF electronic contribution.

Discrepancies from theoretically predicted $E \propto \ln P_{CO_2}$ and hence the value of n may be due to one or a number of reasons:

- At lower temperatures, sluggish kinetics may slow or prevent establishment of local equilibria at the electrodes. Further, the gradual change from non-Nernstain to Nernstian behaviour with temperature as is expected is in agreement with the results obtained in this study, where $n \to 2$.

- Mixed potential phenomenon - more than one competitive reaction may be simultaneously occurring at the sensing electrodes[213].

- The solid electrolyte may exhibit some element of electronic conductivity ($t_{\text{ion}} < 1$) because $E_{\text{exp}} = t_{\text{ion}}E$ where E_{exp} and E are the experimental and theoretical EMFs respectively. When this is the case, n can assume non integral values. Furthermore, the equation is somewhat semi-quantitative because it is assumed that the t_{ion} is constant in the whole of the solid electrolyte when it is not. Näfe and Steinbräck [214] and Näfe [215] indeed confirmed the variation of t_{ion} with n such that even low t_{ion} (5×10^{-3}) led to non-Nernstian behaviour. Also the influence of t_{e} is more significant at lower temperatures[213]. Further, as has been discussed already, the possible formation of CUSICON despite it being in trace amounts(not detected by XRD but blue coloration observed) contributed to the electronic conduction since CUSICONS at 600 K for instance has $T_e = 0.4\%$ and this is within the sensor measurement regime of this work.

The above explanations are in agreement with what was obtained. However, for

real world sensor applications, as long as the sensor EMF is reproducible and stable for prolonged durations, knowing the value of n would be irrelevant as only the calibration would be needed.

7.8.2 Repeatability deviations and cross sensitivity tests.

Despite the fact that sensors were repeatable to within 98% +, the deviation may be systematic because of the manual control of gas flow-meters. The graduation of the meters were too close to be resolved during the flow control. Use of a digital mass flow controller would guarantee an almost 100% repeatability.

The same reason may be applied to humidity cross-sensitivity measurements.

7.9 Summary

The sensors have been successfully fabricated and tested. The following are the findings:

- NaLiBa | NASICON | TiO_2 (PSA)- The eutectic mix of the the NaLiBa-carbonates as sensing electrodes improved sensor response/recovery time and signal stability and proved superior to the NaBa-carbonates sensing electrodes based sensors.

- NaLiBa | NASICON | TiO_2 (SSA) - Because of the success of the electrodes in the planar sensor, it was used in the multi-layered structure and it performed just as well in terms of response and recovery time. The success of the multi-layered structure implies that the NASICON can be protected from any alumina induced degradation using the reference electrode and the buffer thereby guaranteeing a fixed sodium oxide potential as well as

transference number during sensing. Furthermore the sensor showed stability in the presence of humidity except for the baseline which was always lower when humidified. The drawback to this sensor was that it delaminated after several cycles of use. This was due to the fact the integrity of adhesion of the layers was not strong because the NASICON was not fired to full density. This was due to the firing hierarchy which required that the upper film had to be compatible with the thermal budget of the underlying substrate implying that the subsequent film on top be fired at a much lower temperature than the bottom film.

- Comparison of planar structures(PSA) and modified planar structures (M-PSA) show that the modified sensor, NaBa | NASICON | NT6-NT3 performed well in terms of stability in the presence of humidity. The sensor was immune to humidity during sensing as it did not matter whether the test gas was humidified or not. Furthermore, the full scale output increased with operating temperature indicating that the sensor resolution increases with operation temperature.

- The success of the sensors tested herein is that (1) they performed well at lower temperatures (240- 430 °C), which translates to a massive thermal input saving especially when an on-board heater is required to drive the sensor. The sensors have been operated at temperature lower than successful tests reported in literature of $T \geq 500$ °C[12, 14, 86, 94]. (2) sensor resolution was improved as they were able to sense step change in CO_2 concentrations of $\leq$500 ppm, in contrast to tests in literature where the step changes were mostly in decade ranges such as 0, 500, 5000, 50000 ppm as such steps would definitely invoke sensor response.

Chapter 8

Conclusion and Recommendations

8.1 Conclusions

The main achievements of this study are: (a) in the quest to lowering the cost of sensor production new synthesis procedures for sensor components (NASICON and $CuAlO_2$) have been developed which require low thermal input. Sintering schedule for the thick films have been developed(b) thermodynamics of reference electrodes using the EMF method revealed new information that may have been ignored by other workers. The existence of two temperature regimes and phase transformation of NT6 to higher(lower sodium content) titanates (NT7 and NT9). This data presents the first indications from EMF thermodynamic studies for the possible transformation as was proposed by other workers. (c) a new sensing material combination (Na_2CO_3-Li_2CO_3-$BaCO_3$) improved sensing response and recovery times of the sensors. Good sensor performance has been demonstrated by a multilayered sensor that uses a buffer and reference electrode to shield from

any NASICON degradation at the alumina/ NASICON interface. Furthermore the shielding of the reference electrode using the buffer on a planar structure demonstrated good sensor performance as well as immunity from humidity.

Detailed conclusions of the study is in the next sub-sections.

8.1.1 Material synthesis and characterisation.

New synthesis procedures were developed for NASICON and the buffer (Cu-Al-O). The techniques used to characterise these materials were also described. Lastly, pastes were successfully made and the screen printed films were characterised using SEM/EDS, XRD and AC impedance spectroscopy.

NASICON

- The new procedure of NASICON synthesis has produced fine, single phase NASICON powders which need no further cycles of re-calcination, milling and grinding. A single phase is obtained in just one attempt of calcination at 1000 °C for 1h and the powder is ready for thick film slurry making. The end result is a reduced thermal input needed for materials synthesis and this would overall lead to a reduction in the cost of sensor.

- The maltose-pectin incorporated NASICON procedure was able to obtain very fine powders but the explosive nature of the calcination process limited its use because a lot of powder was wasted.

- Optimisation of sintering schedules of NASICON thick film on alumina substrate revealed a narrow window in which a well densified, sintered film and an almost phase pure NASICON is obtained. On either side of the window, the film won't sinter or, the film will sinter but the NASICON phase would

be denuded leaving a precipitation of zirconia and other phases. Therefore a sintering schedule of 1100 °C for 60 minutes was found appropriate.

- Effect of electrode configuration on electrical conductivity showed no significant difference in conductivity when the electrodes were in a basal/planar configuration(IP and IPB) but much lower conductivity values were obtained than in the planar when the electrodes are placed across the thickness of the film(AP).

- Effect of film thickness on electrical conductivity: Varying film thickness as well showed no difference in surface conductivity in the intrinsic regions (high temperature region) while at lower temperatures thinner films possessed higher conductivity than thicker films(because thinner films sintered better than thicker films) This work was published in [216].

- Spectral conductivity studies showed that Na^+ conduction was of long range hopping while scaling studies showed that surface ion conductivity and relaxation were independent of temperature and thickness. Skin effect due to high frequency alternating electric-field also had no effect on surface conductivity because of the magnitudes of the conductivity values involved.

- Thick film surface conduction activation energy ($E_a = 0.46 - 0.89$ eV) is much higher than the bulk activation energy ($E_a = 0.21$ eV) reported in literature [150]. The values of conductivity and relaxation activation energies suggest that ions whilst conducting and relaxing overcome the same energy barrier.

- SEM investigation showed that there is a minimum thickness (7 μm) for which NASICON can be printed on alumina substrate and used in high temperature applications (up to 1100 °C) successfully and less than that,

the entire film may undergo phase change, zirconia being the dominant secondary phase.

$CuAlO_2$

- Synthesis of a phase pure delaffosite $CuAlO_2$ through the conventional high temperature processing of mixed component oxides, Cu_2O and Al_2O_3 has always been obtained after prolonged reaction time some as long as 4 days. In this research a process of pelletising component oxides followed by isothermal calcination in argon environment and quenching under graphite crucible which can be employed to reduce the reaction time down to 1.5 h has been achieved. A single phase $CuAlO_2$ can be easily synthesized from mixed component oxides as long as the powder has been pelletised regardless of the amount of load applied.

- Electrical characterisation has revealed for the transition to intrinsic type conduction (T_{trans}) of $CuAlO_2$ and this work reports for the first time the T_{trans} for the delaffosite, being $T_{trans} \simeq 375$ °C which has been reported in [183].

- It has also been shown for the first time that Pt can catalyse the inadvertent formation of $CuAl_2O_4$ spinel from $CuAlO_2$, former being an insulator whereas the latter is a good *p*-type conductor.

8.1.2 Thermodynamic measurements

The thermodynamic cells consisting (-)Pt, NT6 - NT3(and NT6-TiO_2) | NASICON | $(\alpha + \beta)$ - Al_2O_3, Pt(+) were successfully constructed and EMF vs T dependency measurements revealed two temperature regimes separated by a non linear knee akin to a second order phase transition.

1. From the revelations of the existence of 2-linear regimes of EMF vs T dependencies, it is clear that most thermodynamics data of EMFs is grossly oversimplified by extrapolating the linear section investigated to span the whole temperature range, or the second linear regime is ignored. This represents the first results showing multiple linear regimes that requires that the thermodynamic parameters are dealt with separately and accordingly.

2. The likely reason for the non-linearity in the EMF vs T dependencies is the reversible phase transition of NT6 to higher titanium content NT7 or NT9; whose phase would lie between NT6 and TiO_2 of the phase diagram. This data using the EMF method presents the first indication of the transition.

3. The standard Gibb's energy change of reaction on the working electrode for cell I ; $Na_2O + 6TiO_2 \rightarrow NaTi_6O_{13}$ is

$$\Delta G^{\circ}_{r,\mathrm{NT6}}(\mathrm{J/mol}) = \begin{cases} -230497 - 11.55T & \text{for} \quad 523 \leq T(K) < 705 \\ -264422 + 34.46T & \text{for} \quad 800 \leq T(K) < 1073 \end{cases}$$

4. The standard Gibb's energy change of reaction on the working electrode for cell II; $Na_2O + Na_2Ti_6O_{13} \rightarrow 2\,Na_2Ti_3O_7$ is:

$$\Delta G^{\circ}_{r,\mathrm{NT3}}(\mathrm{J/mol}) = -153637 - 84.25T.$$

5. The thermodynamic data that is needed for the quantitative characterisation of the sensor signals, the Na_2O activity was obtained as a function of temperature. The following are the relationships:

$$\log a_{\mathrm{Na_2O}(NT6-\mathrm{TiO_2})} = \begin{cases} -0.76 - \frac{12031}{T} & \text{for} \quad 523 \leq T(K) < 705 \\ 1.80 - \frac{13810}{T} & \text{for} \quad 800 \leq T(K) < 1073 \end{cases}$$

and

$$\log a_{\mathrm{Na_2O}(NT6-NT3)} = -4.42 - \frac{8024}{T}, \quad \text{for } 611 \leq T(K) < 798.$$

8.1.3 Sensor fabrication and characterisation

The sensors were successfully printed both as a stacked structure and as modified planar structure. A conventional planar structure was also printed for comparison including the use of a new sensing material combination. The use of a eutectic melt of the Na_2CO_3-Li_2CO_3-$BaCO_3$(NaLiBa) is the first time it has been used as sensing material. The study revealed the following:

1. NaLiBa | NASICON | NT6-TiO_2 (PSA)-The eutectic mix of the the NaLiBa-carbonates as sensing electrodes improved sensor response and recovery time and performed better than the NaBa-carbonates sensing electrodes.

2. NaLiBa | NASICON | NT6-TiO_2 (SSA) - Because of the success of the the electrodes in the planar sensor, it was used in the multi-layered structure and it performed just as well in terms of response and recovery time (see Table 7.9). The success of the multi-layered structure implies that the NASICON can be protected from any alumina induced degradation using the reference electrode and the buffer thereby guaranteeing a fixed sodium oxide potential as well as transference number during sensing. Furthermore the sensor showed stability in the presence of humidity except for the baseline which was always lower when humidified (see Figure 7.32). Sensor repeatability

was 99% + (see Figure 7.30) demonstrating the applicability of the sensor. Despite all these good sensing characteristics, the sensor was was

3. Comparison of planar structures(PSA) and modified planar structures (M-PSA) show that the modified sensor, NaBa | NASICON | NT6-NT3 performed well in terms of stability in the presence of humidity. The sensor was was immune to humidity during sensing as it did not matter whether the test gas was humidified or not. Furthermore, the full scale output increased with operating temperature indicating that the sensor resolution increases with operation temperature.

4. The success of the sensors tested herein is that (1) they performed well at lower temperatures (240- 430 °C), which translates to massive thermal input saving especially when an on-board heater is required to drive the sensor. The sensor have been operated at temperature lower than successful tests as reported in literature of $T \geq 500$ °C[12, 14, 86, 94]. (2) sensor resolution was improved as they were able to sense step change in CO_2 concentrations of $\leq$500 ppm, in contrast to tests in literature were the step changes were mostly in decade ranges such as 0, 500, 5000, 50000 ppm as such steps would definitely invoke sensor response.

8.2 Recommendations

1. More research on the choice of the buffer that is very stable at high temperature during fabrication when in contact with other sensor components.

2. Investigation on the choice of substrate. This in virtue of the findings in this study for the NASICON degradation at the alumina substrate - NASICON interface.

3. The need for sensors that work in extreme harsh environments such as high temperatures (> 600 °C) in automotive engines, gas turbines, geothermal plants, aircraft engines, hypersonic spacecrafts, planatory gas sensing is an ongoing research. A solid state based potentiometric sensor can actually work in such high temperatures because the higher the temperature the more conductive the solid electrolyte will be and hence the better the sensing performance. However, the sensing is only limited by the type of sensing material that is used and its stability at high temperatures when in contact with the solid electrolyte. More research should be focused on the identification of new sensing material that can withstand high temperatures in the excess of 600 °C without melting.

4. Explore better materials for on-board heaters to be integrated with the planar sensor to enable it work as a standalone device.

5. Due to the emergence of the internet of things, there is need for interfacing the miniaturised sensors with wireless technology for ubiquitous sensing and monitoring. Low cost and low power wireless modules such as ZigBee from Texas Instruments should be explored for possible sensor handshaking.

6. Development of sensor arrays that may utilise the same electrolyte but different auxiliary electrodes for difference gases printed at different positions on the electrolyte.

7. Transfer of planar technology to other other gases such as H_2S for high undersea sensing were there is extreme high pressure environment and low temperatures.

References

[1] M. Tucker. Analysis: Carbon dioxide emissions and global GDP. *Ecological Economics*, 15:215, 1995.

[2] A.G Florides and P. Christodoulides. Global warming and carbon dioxide through sciences. *Environment Internation*, 35:390, 2009.

[3] Atmospheric carbon dioxide for June 2015. http://co2now.org/, 2015. URL `http://co2now.org/`. Accessed on 10 June 2015.

[4] S. A. Rice. Human health risk assessment of CO_2: Survivors of acute high level exposure and populations sensitive to prolonged lo level exposure. In *Third Annual Conference on carbon Sequestration*, Alexander, Virginia, USA, May 2004.

[5] *Code of Federal Regulations; The Superintendent of Documents,*. U.S. Government Printing Office: Washington, DC, USA., 1994.

[6] W.L. Grosshandler. Towards the developement of a Universal Fire Emulator-Detector Evaluator. *Fire safety J.*, 29:113, 1997.

[7] Sheikh Akbar, Prabir Dutta, and Chonghoon Lee. High-Temperature Ceramic Gas Sensors: A Review. *Int. J. Appl. Ceram. Technol*, 3(4):302, 2006.

[8] M. Gauthier and A. Chamberland. Solid-State detectors for the potentiometric determination of gaseous oxides. *J. Electrochem. Soc*, 124:1579, 1977.

[9] T. Maruyama, S. Sasaki, and Y. Saito. Potentiometric gas sensor for carbon dioxide using solid electrolytes. *Solid State Ionics*, 23:107, 1987.

[10] G.M Kale, A.J Davison, and D.J. Fray. Investigation into an Improved Design of CO_2 Sensor. *Solid State Ionics,*, 86-88:1107, 1996.

[11] N. Miura, S. Yao, Y. Shimizu, and N. Yamazoe. High-performance solid electrolyte carbon dioxide sensor with a binary carbonate electrode. *Sensors and Actuators*, B9:165, 1992.

[12] M. Holzinger, J. Maier, and W. Sitte. Fast CO_2 - Selective Potentiometric Sensor with Open Reference Electrode. *Solid State Ionics*, 86-88:1055, 1996.

[13] C. Belda, M. Fritsch, C. Feller, D. Westphal, and G. Jung. Stability of solid electrolyte based thick-film CO_2 sensors. *Microelectronics Reliability*, 49(6): 614–620, 2009.

[14] K. Sahner, A. Schulz, J. Kita, R. Merkle, J. Maier, and R. Moos. CO_2 Selective Potentiometric Sensor in Thick-film Technology. *Sensors*, 8:4774, 2008.

[15] Sven Wiegartner, Jaroslaw Kita, Gunter Hagen, Christa Schmaus, Andre Kiebig, Eckard Glaser, Armin Bolz, and Ralf Moos. Development and application of a fast solid-state potentiometric CO_2-sensor in thick-film technology. *Procedia Engineering*, 87:1031–1034, 2014.

[16] Nak-Jin Choi, Hyung-Kun Lee, Seung Eon Moon, Woo Seok Yang, and Jong-

dae Kim. Stacked-type potentiometric solid-state co2 gas sensor. *Sensors and Actuators B: Chemical*, 187:340–346, 2013.

[17] Han Byel Shim, Ju Hyun Kang, Jung Woon Choi, and Kwang Soo Yoo. Characteristics of thick-film co2 sensors based on nasicon with Na_2CO_3-$CaCO_3$ auxiliary phases. *Journal of Electroceramics*, 17:971–974, 2006.

[18] J. Fraden. *Handbook of Modern Sensors: Physics, Designs and Applications*. AIP Press, 3rd edition, 2003.

[19] K. Arshak, E. Moore, G. M. Lyons, J. Harris, and S. Clifford. A review of gas sensors employed in electronic nose application. *Sensor Review*, 24(2): 181, 2004. Review.

[20] C.O. Park, S.A. Akbar, and W. Weppner. Ceramic Electrolytes and Electrochemical Sensors. *J. Mater. Science*, 38:4639, 2003. review.

[21] Christopher M. A. Brett and ANA M. O.Brett. *Electrochemistry- Principles, methods and Applications*. Oxford University Press Inc, Oxford University Press Inc, New York, USA, 1994.

[22] C.B. Alcock. Solid state sensors and process control. *Solid State Ionics*, 53-56:3, 1992.

[23] Ulrich Guth, Winfried Vonau, and Jens Zosel. Recent developements in electrochemical sensor application and technology - a review. *Meas. Sci. Technol.*, 20:042002, 2009. URL `http://iopscience.iop.org/0957-0233/20/4/042002/`.

[24] Michael B Heaney. *The Measurement, Instrumentation and Sensors Handbook*, chapter Electrical Conductivity and Resistivity. CRC Press, 1999.

[25] Ghenadii Korotcenkov, editor. *Chemical Sensors: Fundamentals of Sensing Materials- General Approaches*, volume 1. Momentum Press, New York, USA, 1st edition, 2010.

[26] C.C. Liu. Electrochemical Sensors. In *Electrical Engineering Handbook*, pages 48–1–48–6–. CRC Press, April 2006. doi: 10.1201/9781420003864.ch48. URL `http://dx.doi.org/10.1201/9781420003864.ch48`.

[27] Xiao Liu, Sitian Cheng, Hong Liu, Daqiang Zhang, and Huansheng Ning. A survey on gas sensing technology. *Sensors*, 12:9635–9665, 2012.

[28] Joseph R. Stetter and Jing Li. Amperometric gas sensors - a review. *Chem. Rev*, 108:352–366, 2008.

[29] Richard Cote, Christopher W. Bale, and Michel Gauthier. K_2CO_3 Solid Electrolyte as a CO_2 Probe: Decomposition Measurements of $CaCO_3$. *J. Electrochem. Soc.*, 131:67, 1984.

[30] Nelson R. Stradiotto, Hideko Yamanaka, and Maria Valnice B. Zanoni. Electrochemical Sensors: A Powerful Tool in Analytical Chemistry. *J. Braz. Chem. Soc.*, 14(2):159, 2003.

[31] Takehiko Takahashi, Katsumi Kuwabara, and Masahiro Shibata. Solid State Ionics - Conductivities of Na^+ Ion Conductors based on NASICON. *Solid State Ionics*, 1:163, 1980.

[32] R. Stevens and J.P.G. Binner. Review structure, properties and production of β-alumina. *J. Mater. Science*, 19:695, 1984.

[33] H.Y.P. Hong. Crystal Structures and Crystal Chemistry in the System $Na_{1+x}Zr_2Si_xP_{3-x}O_{12}$. *Materials Research Bulletin*, 11:173, 1976.

[34] N. Anantharamulu, K. Koteswara Rao, G. Rambabu, B. Vijaya Kumar, and Velchuri Radha. A wide ranging review on NASICON type materials. *J. Mater. Science*, 46:2821, 2011.

[35] P. Perthius and Ph. Colomban. Sol-gel routes leading to nasicon ceramics. *Ceramics International*, 12:39, 1986.

[36] N.G Bukun. Superionic Transitions in NASICON-Type Solid Electrolytes. *Ionics*, 2:63, 1996.

[37] U. von Alpen. Phase transition in NASICON ($Na_3Zr_2Si_2PO_{12}$). *Materials Research Bulletin*, 14:1317, 1979.

[38] J.P. Boilot and Ph. Colomban. Stoichiometry , structure, fast ion conduction in NASICON solid solution. *Solid State Ionics*, 28-30:403, 1988.

[39] Parul Yadav and M.C Bhatnagar. Structural studies of NASICON materials of different compositions by solgem method. *Ceramics International*, 38: 1731, 2012. Short Communication.

[40] Md. Rahul Amin. *Solid state electrochemical characterization of thermodynamic properties of sodium-metal-oxygen systems.* PhD thesis, University of Stuttgart, 2005.

[41] E. C Subbarao, editor. *Solid Electrolytes and Theory Applications.* Plenum Press, 1980.

[42] H. Kohler, H Schulz, and O Melnikov. Structural investigations of NASICON ($Na_{1+x}Zr_2Si_xP_{3-x}O_{12}$; $x = 3$) with X-ray diffraction at 298 and 403K. *Materials Research Bulletin*, 18:589, 1983.

[43] G. Collin and J.P Boilot. *Superionic Solids and Solid Electrolytes.* Academic Press, 1989.

[44] H. Sato. *Solid Electrolytes.* Springer-Verlag, 1977.

[45] J.B. Goodenough, H.Y.P. Hong, and J.A. Kafalas. Fast Na^+ Ion Transport in Skeleton Structures. *Materials Research Bulletin*, 11:203, 1976.

[46] Nalamudayan Arul Dhas and Kashinath C. Patil. Controlled Combustion Synthesis and Properties of Fine-particle NASICON Materials. *J. Mater. Chem.*, 4(3):491, 1994.

[47] Hee Bog Kang and N.H Cho. Phase formation, sintering behavior, and electrical characteristics of NASICON compounds. *J. Mater. Science*, 34: 5005, 1999.

[48] G. M. Kale and K.T Jacob. Thermodynamic Partial Pressures of Na_2O in Nasicon Solid Solution, $Na_{1+x}Zr_2Si_xP_{3-x}O_{12}$. *Journal of Materials Research*, 4:417, 1989.

[49] M. Holzinger, J. Maier, and W. Sitte. Potentiometric detection of complex gases: Application to CO_2. *Solid State Ionics*, 94:217, 1997.

[50] N. Miura, S. Yao, Y. Shimizu, and N. Yamazoe . 139 (1992)1384. Carbon Dioxide Sensor Using Sodium Ion Conductor and Binary Carbonate Auxiliary Electrode. *J. Electrochem. Soc*, 139:1384, 1992.

[51] G. M. Kale, L. Wan, and Y. R Hong. Planar SO_x sensor incorporating a bi-electrolyte couple. *Solid State Ion.*, 161:155–163, 2003.

[52] N. Miura, S. Yao, Y. Shimizu, and N. Yamazoe. Development of high-performance solid-electrolyte sensors for NO and NO_2. *Sensors and Actuators*, B13-14:387, 1993.

[53] J.E Hayes. *Synthesis, Characterisation and Applications of Solid electrolytes*

for SO_x *and* NO_x *gas sensors*. PhD thesis, School of Process, Environmentals and Materials Engineering, University of Leeds, 2001.

[54] Ling Wang and R V Kumar. Cross-sensitivity effects on a new carbon dioxide gas sensor based on solid bielectrolyte. *Meas. Sci. Technol.*, 15:1005, 2004. IOP.

[55] G. H´otzel and W. Weppner. Potentiometric gas sensors based on fast solid electrolytes. *Sensors and Actuators*, 12(4):449 – 453, 1987. ISSN 0250-6874.

[56] J. Liu and W. Weppner. Beta alumina solid electrolytes for solid state electrochemical CO2 gas sensors. *Solid Sate Communications*, 76(3):311–313, 1990.

[57] David W. Richerson. *Modern Ceramic Engineering-Properties, Processing and Use in Design*. CRC Taylor and Francis Group, 2006.

[58] S. Crouch-Baker, G. Deublein, H-C. Tsai, L.Z. Zhou, and R.A. Huggins. Materials considerations related to sodium-based rechargeable cells for use above room temperature. *Solid State Ionics*, 42:109 – 115, 1990. ISSN 0167-2738.

[59] H. Schettler, J. Liu, W. Weppner, and R. A. Huggins. Investigation of solid sodium reference electrodes for solid-state electrochemical gas sensors. *Journal of applied Physics*, A57:31–35, 1993.

[60] Pradeep Puligundla, Junho Jung, and Sanghoon Ko. Carbon dioxide sensors for intelligent food packaging applications. *Food Control*, 25:328, 2012.

[61] www.vaisala.com. URL `www.vaisala.com`. **Accessed on 20th July 2012**.

[62] http://www.figarosensor.com/products/4161pdf.pdf. electronic. URL `http:`

//www.figarosensor.com/products/4161pdf.pdf. **Accessed on 7 June 2012**.

[63] Alphasense. http://www.alphasense.com/index.php/products/ndir-air/. URL http://www.alphasense.com/index.php/products/ndir-air/. **Accessed on 22 May 2015**.

[64] S. Neethirajan, D.S Jayas, and S. Sadistap. Carbon dioxide (CO_2) sensors for the agri-food industry - A review. *Food Bioprocess Technol*, 2:115, 2009.

[65] S. Herber, J. Bomer, W. Olthuis, P. Bergveld, and A.V. Berg. A miniaturised carbon dioxide gas sensor based on sensing of PH-sensitive hydrogel swelling with a pressure sensor. *Biomed. Microdevices*, 7:197, 2005.

[66] Florence Colin, Timothy J.N. Carter, and John D. Wright. Modification of a piezo-optical gas dosimeter system towards continuous gas sensing: a feasibility study with carbon dioxide. *Sensors and Actuators B: Chemical*, 90(1-3):216, 2003.

[67] Hiroyo Segawa, Eiji Ohnishi, Yasuhiko Arai, and Kazuaki Yoshida. Sensitivity of fiber-optic carbon dioxide sensors utilizing indicator dye. *Sensors and Actuators B: Chemical*, 94(3):276 – 281, 2003.

[68] Jim Mulrooney, John Clifford, Colin Fitzpatrick, and Elfed Lewis. Detection of carbon dioxide emissions from a diesel engine using a mid-infrared optical fibre based sensor. *Sensors and Actuators A: Physical*, 136(1):104 – 110, 2007.

[69] T. Ishihara, K Kometani, M Hashida, and Y Takita. Application of mixed oxide capacitor to the selective carbon dioxide sensor. *J. Electrochem. Soc*, 138:173, 1991.

[70] A. Haeusler and J. Meyer. A novel thick film conductive type carbon dioxide sensor. *Sensors an*, 34(1-3):388, 1996.

[71] D. Kim, J. Yoon, H. Park, and K. kim. CO_2 sensing of SnO_2 thick film by coating lanthanum oxide. *Sensors and Actuators*, 62:61, 2000.

[72] M.S. Lee and J.U. Meyer. A new process for fabricating CO_2-sensing layers based on $BaTiO_3$ and additives. *Sensors and Actuators*, 68:293, 2000.

[73] E.H.A Diagne and M. Lumbreras. Elaboration and characterization of tin oxide - lanthanum oxide mixed layers prepared by the electrostatic spray pyrolysis technique. *Sensors and Actuators*, 78:98, 2001.

[74] Carlos R. Michel, Alma H. Martinez-Preciado, Rodrigo Parra, Celso M. Aldao, and Miguel A. Ponce. Novel CO_2 and CO gas sensor based on nanostructured Sm_2O_3 hollow microspheres. *Sensors and Actuators B: Chemical*, 202:1220 – 1228, 2014.

[75] Ya Xiong, Guozhu Zhang, Shunping Zhang, Dawen Zeng, and Changsheng Xie. Tin oxide thick film by doping rare earth for detecting traces of CO_2: Operating in oxygen-free atmosphere. *Materials Research Bulletin*, 52:56 – 64, 2014.

[76] G.G. Mandayo, F. Gonzalez, I. Rivas, I. Averdi, and J. Herran. $BaTiO_3$-CuO sputtered thin film for carbon dioxide detection. *Sensors and Actuators*, 118(1-2):305, 2006.

[77] D. Mutschall and E. Obermeier. A capacitive CO_2sensor with on-chip heating. *Sensors and Actuators B: Chemical*, 25:412 – 414, 1995.

[78] Travis Anderson, Fan Ren, Stephen Pearton, Byoung Sam Kang, Hung-Ta Wang, Chih-Yang Chang, and Jenshan Lin. Advances in Hydrogen,

Carbon Dioxide, and Hydrocarbon Gas Sensor Technology Using GaN and ZnO-Based Devices. *Sensors*, 9:4669, 2009. Review.

[79] Keat G. Ong and Craig A. Grimes. A Carbon Nanotube-based Sensor for CO_2 Monitoring. *Sensors*, 1:193, 2001.

[80] Bernard John V. Tongol, Christina A. Binag, and Fortunato B. Sevilla. Surface and electrochemical studies of a carbon dioxide probe based on conducting polypyrrole. *Sensors and Actuators B: Chemical*, 93:187 – 196, 2003.

[81] Tonosaki T. Oho, K. Isomura, and K. Ogura. A CO_2 sensor operating under high humidity. *Synthetic Metals*, 522:173, 2002.

[82] S. Neethirajan, M.S. Freund, D.S. Jayas, C. Shafai, D.J. Thomson, and N.D.G. White. Development of carbon dioxide (CO2) sensor for grain quality monitoring. *Biosystems engineering*, 106:395, 2010.

[83] Duk Dong Lee, Soon Don Choi, and Kwang Woo Lee. Carbon dioxide sensor using NASICON prepared by the sol-gel method. *Sensors and Actuators B: Chemical*, 25:607–609, 1995.

[84] Andreas Dubbe, Hans-Dieter Wiemhofer, Yoshihiko Sadaoka, and Wolfgang Gopel. Microstructure and response behaviour of electrodes for CO_2 gas sensors based on solid electrolytes. *Sensors and Actuators B: Chemical*, 25: 600 – 602, 1995. Proceedings of the Fifth International Meeting on Chemical Sensors.

[85] A. Dubbe, M. Wake, and Y. Sadaoka. Yttria/carbonate composite solid electrolytes for potentiometric CO_2 sensors. *Solid State Ionics*, 96:201 – 208, 1997.

[86] Ling Wang and R V Kumar. Thick film CO_2 sensors based on Nasicon solid electrolyte. *Solid State Ionics*, 158:309, 2003.

[87] C. Lee, S.A. Akbar, and C.O. Park. Potentiometric CO_2 gas sensor with lithium phosphorous oxynitride electrolyte. *Sensors and Actuators B: Chemical*, 80(3):234 – 242, 2001.

[88] C.O Park, C Lee, S.A Akbar, and J Hwang. The origin of oxygen dependence in a potentiometric CO_2 sensor with Li-ion conducting electrolytes. *Sensors and Actuators B: Chemical*, 88(1):53 – 59, 2003.

[89] Hidekazu Narita, Zhang Yi Can, Junichiro Mizusaki, and Hiroaki Tagawa. Solid state CO_2sensor using an electrolyte in the system Li_2CO_3-Li_3PO_4-Al_2O_3. *Solid State Ionics*, 79:349 – 353, 1995. Proceedings of the 20th Commemorative Symposium on Solid State Ionics in Japan.

[90] Joachim Maier and Udo Warhus. Thermodynamic investigations of Na_2ZrO_3 by electrochemical means. *The Journal of Chemical Thermodynamics*, 18 (4):309 – 316, 1986.

[91] Joachim Maier, Michael Holzinger, and Werner Sitte. Fast potentiometric CO2 sensors with open reference electrodes. *Solid State Ionics*, 74:5 – 9, 1994.

[92] K Kaneyasu, K Otsuka, Y Setoguchi, S Sonoda, T Nakahara, I Aso, and N Nakagaichi. A carbon dioxide gas sensor based on solid electrolyte for air quality control. *Sensors and Actuators B: Chemical*, 66:56 – 58, 2000.

[93] F. Salam, S. Bredkhin, P. Birke, and W. Weppner. Effect of thickness of the gas sensitive layer on the response of solid state electrochemical CO_2 sensors. *Solid State Ionics*, 110:319, 1998.

[94] Tetsuya Kida, Yuji Miyachi, Kengo Shimanoe, and Noboru Yamazoe. NASICON thick film-based CO_2 sensor prepared by a sol-gel method. *Sensors and Actuators B: Chemical*, 80(1):28 – 32, 2001.

[95] Piotr Lorenc, Anna Strzelczyk, Bogdan Chachulski, and Grzegorz Jasinski. Properties of nasicon-based CO_2 sensors with $Bi_8Nb_2O_{17}$ reference electrode. *Solid State Ionics*, 271:48–55, 2015.

[96] J. Zosel, W. Oelβner, M. Dekker, G. Gerlach, and U. Guth. The measurement of dissolved and gaseous carbon dioxide concentration. *Meas. Sci. Technol.*, 22:072001, 2011.

[97] T. Kida, K. Shimanoe, N. Miura, and N. Yamazoe. Stability of NASICON-based CO_2 sensor under humid conditions at low temperaturea. *Sensors and Actuators*, B75:179, 2001.

[98] P. Pasierb, S. Komornicki, S. Kozinski, R. Gajerski, and M. Rekas. Long-term stability of potentiometric CO_2 sensors based on Nasicon as a solid electrolyte. *Sensors and Actuators B: Chemical*, 101:47 – 56, 2004.

[99] Yuji Miyachi, Go Sakai, Kengo Shimanoe, and Noboru Yamazoe. Fabrication of CO_2 sensor using NASICON thick film. *Sensors and Actuators B: Chemical*, 93:250 – 256, 2003.

[100] R.O. Fuentes, F. Figueiredo, F.M.B. Marques, and J.I. Franco. Reaction of NASICON with water. *Solid State Ionics*, 139:309 – 314, 2001.

[101] Xiaowen Xu, Jing Wang, and Yingcai Long. Zeolite-based Materials for Gas Sensors. *Sensors*, 6:1751, 2006.

[102] L.Wang and R.V. Kumar. A novel carbon dioxide sensor based on solid bielectrolyte. *Solid State Ionics*, 158:309, 2003.

[103] S. Yao, S. Hosohura, Y. Shimizu, N. Miura, H. Futata, and N. Yamazoe. Solid electrolyte CO_2 sensor using NASICON and Li-based binary carbonate electrode. *Chem. Lett.*, page 2069, 1990.

[104] N. Yamazoe. Toward innovations of gas sensor technology. *Sensors and Actuators*, B108:2, 2005.

[105] Heng-Yao Dang and Xing-Min Guo. Characteristics of NASICON-Based Thick-Film CO_2 Sensor Attached with Integrated Auxiliary Electrode. *IEEE Sensors Journal*, 12(7):2430–2434, July 2012.

[106] Youichi Shimizu and Takashi Ushijima. Sol-gel processing of NASICON thin film using aqueous complex precursor. *Solid State Ionics*, 132:143 – 148, 2000.

[107] Y. Shimizu, Y. Azuma, and S. Michishita. Sol-gel synthesis of NASICON discs from aqueous Solution. *J. Mater. Chem.*, 7-8:1487, 1997.

[108] Zihua Wang, Tim P. Comny, Mojtaba Ghadiri, and Girish M. Kale. Maltose and Peptin Assisted sol-gel production of $Ce_{0.8}Gd_{0.2}O_{1.9}$ Solid Electrolyte Nanopowders for Solid Oxide Fuel Cell. *J. Mater. Chem.*, 21:16494, 2011.

[109] Zihua Wang, Girish M. Kale, and Mojtaba Ghadiri. Sol-Gel Production of $Ce_{0.8}Gd_{0.2}O_{1.9}$ Nanopowders Using Sucrose and Pectin as Organic Precursors. *Journal of the American Ceramic Society*, 2012.

[110] K.T Jacob and C.B Alcock. Thermodynamics of $CuAlO_2$ and $CuAl_2O_4$ and Phase Equilibria in the System Cu_2O-CuO-Al_2O_3. *J.Amer. Ceram. Soc.*, 58:5–6, 1975.

[111] Steven Mudenda. Development and characterization of bioceramic coatings

for medical and dental applications. Master's thesis, University of the Western Cape, 2007.

[112] D. Dimos, P. Chaudhari, J. Mannhart, and F. K. LeGoues. Orientation Dependence of Grain-Boundary Critical Currents in $YBa_2Cu_3O_{7-x}$ bicrystals. *Phys. Rev. Lett.*, 61:219, 1988.

[113] H. Sumino, O. Sakurai, K. Shinozaki, M. Kato, and N. Mizutani. A New Instruement to Measure the Electrical Properties in Very Narrow Regions in Ceramics. *J. Mater. Sci. Lett*, 10:1026, 1991.

[114] John T. S. Irvine, Derek C. Sinclair, and Anthony R. West. Electroceramics : Characterization by Impedance Spectroscopy. *Advanced Materials*, 2: 132–138, 1990.

[115] Derek C. Sinclair. Characterization of electro-materials using ac impedance spectroscopy. *Boletin de La Sociedad Espanola de Ceramica y vidrio*, 34: 55–65, 1995.

[116] Wei Lai. *Impedance Spectroscopy as a Tool for the Electrochemical Study of Mixed Conducting Ceria.* PhD thesis, California Institute of Technology, 2007.

[117] Evgenij Barsoukov and J. Ross Macdonald, editors. *Impedance Spectroscopy Theory, Experiment, and Applications.* Wiley-Interscience, 2005.

[118] Giovanni Capurso. *Innovative Materials and Systems for Solid State Hydrogen Storage.* PhD thesis, University of Padova, 2013.

[119] Hohne Gunther, Hemminger F. Wolfgang, and H. J Flammersheim. *Differential Scanning Calorimetry.* Springer, New York, 2nd edition, 2003.

[120] Alan Hobby. Printing Thick Film Hybrids. Online, 1997. URL $www.gwent.org/gem_thick_film.html$. **Accessed on 14 December 2014**.

[121] Hae-Geon Lee. *Chemical thermodynamics for Metals and Materials*. Imperial College Press, 1999.

[122] Peter Tsolov Ivanov. *Design, fabrication and Characterisation of Thick Film Gas Sensors*. PhD thesis, Universitat Rovira i Virgili, 2004.

[123] Tiegang Zhong, Baofu Quan, Xishuang Liang, Fengmin Liu, and Biao Wang. SO_2-sensing characteristics of NASICON sensors with $ZnSnO_3$ sensing electrode. *Mater. Sci. Eng. B*, 151(2):127 – 132, 2008.

[124] James Alamo and Roy Rustum. Ultra low -expansion ceramics in the system Na_2O-ZrO_2-P_2O_5-SiO_2. *J. Am. Ceram. Soc.*, 67(5):78–80, 1984.

[125] Noriya Izu, Gunter Hagen, Daniela Schonauer, Ulla Roder-Roith, and Ralf Moos. Planar potentiometric SO_2 gas sensor for high temperatures using NASICON electrolyte combined with $V_2O_5/WO_3/TiO_2$+Au or Pt electrode. *J.Ceram Soc. Japan*, 119(9):687–691, 2011.

[126] N B Desai, K Byrappa, A B Kulkarni, and G S Gopalakrishna. Ionic Conductivity and Hopping rate for some NASICON Analogues. *Bull. Mater. Sci*, 9:117–121, 1987.

[127] K. Funke. Jump relaxations in solid electrolytes. *Prog. Solid State Chem.*, 22:111–195, 1993.

[128] D P Almond., C C Hunter, and A R West. The extraction of ionic conductivities and hopping rates from a.c. conductivity data. *J. Mater. Sci.*, 19: 3236–3248, 1984.

[129] W. Bogusz, R. Sobiestuanskas, J. R. Dygas, F. Krok, A. Orliukas, E. Kozakievicius, and A. Kezionis. Electrical properties of nasicon at radio frequencies. *Molecul. Phys. Rep.*, 27:11–17, 2000.

[130] Grzegorz Pasciak, Wiltod Mielcarek, Krystyna Prociow, and Joanna Warycha. Structural and electrical studies of NASICON material for NO_x sensing. *Ceram. Int.*, 40:12783 – 12787, 2014.

[131] S. Wiegartner, G. Hagen, J. Kita, R. Moos, M. Seufert, E. Glaser, K. Grimmel, A. Bolz, C. Schmaus, and A. Kiessig. Solid-state potentiometric CO_2-sensor in thick film technology for breath analysis. *IEEE Sensors Proc.*, pages 1014–1016, 2001.

[132] James C. Rautio and Veysel Demir. Microschip conductor loss models for electromagnetic analysis. *IEEE Transactions on Microwave Theory and Techniques*, 51:915–921, 2003.

[133] Potassium nitrate and sodium nitrate mixture. **Accessed on 28 May 2012** . URL `cameochemicals.noaa.gov/chemical/4510`.

[134] J.P Boilot, G. Collin, and P.h. Colomban. Relation structure fast ion conduction in the NASICON solid solution. *J. Solid State Chem.*, 73:160, 1988.

[135] Minghua Zhou and Aftab Ahmad. Synthesis, Processing and Characterisation of nasicon Solid Electrolytes for CO_2 Sensing Applications. *Sensors and Actuators B*, 122:419–426, 2007.

[136] Fabin Qiu, Qifeng Zhu, Xiaotian Yang, Yujun Quan, and Liangyan Sun. Investigation of CO_2 sensor based on NASICON synthesized by a new sol-gel process. *Sensor Actuat. B - Chem*, 93:237–242, 2003.

[137] William A. Maryniak, Toshio Uehara, and Maciej A. Noras. Surface resistivity and surface resistance measurements using a concentric ring probe technique. Trek Application Note 1005, Trek, 2013.

[138] A.S Nowick and Wing-Kit Lee. *The Conductivity Pre-Exponential of Solid Electrolytes*, pages 381–405. Academic Press, 1989.

[139] R.O. Fuentes, F.M.B. Marques, and J.I. Franco. Synthesis and properties of nasicon prepared from different zirconia-based precursors. *Boletin de La Sociedad Espanola de Ceramica y vidrio*, 38:631–634, 1999.

[140] R.O Fuentes, F.M Figueiredo, F.M.B Marques, and J.I Franco. Processing and electrical properties of NASICON prepared from yttria-doped zirconia precursors. *Journal of the European Ceramic Society*, 21(6):737 – 743, 2001.

[141] AK Jonscher. The 'universal' dielectric response. *Nature*, 267:673–679, 1977.

[142] C.R. Mariappan, G. Govindaraj, and B. Roling. Lithium and potassium ion conduction in $A_3TiB'P_3O_{12}$ (A=Li, K; B'=Zn, Cd) NASICON-type glasses. *Solid State Ionics*, 176:723–729, 2005.

[143] G Govindaraj and C.R Mariappan. Synthesis, characterization and ion dynamic studies of NASICON type glasses. *Solid State Ionics*, 147:49 – 59, 2002. ISSN 0167-2738.

[144] C.R. Mariappan, G. Govindaraj, S. Vinoth Rathan, and G. Vijaya Prakash. Preparation, characterization, ac conductivity and permittivity studies on vitreous $M_4AlCdP_3O_{12}$ (M= Li, Na, K) system. *Mater. Sci. Eng. B*, 121: 2–8, 2005.

[145] T Prakash. Influence of Temperature on AC Conductivity of Nanocrystalline $CuAlO_2$. *International Nano Letters*, 2:1–3, 2012.

[146] M. Vijaykumar, S. Selvasekarapandian, M.S Bhuvaneswari, G.K. Hiran, G. Ramprasad, R. Subramanian, and P.C Angelo. Synthesis and ion dynamics studies of nanocrystalline Mg stabilized zirconia. *Physica B*, 334: 390–397, 2003.

[147] Harry E. Green. A simplified derivation of the capacitance of a two-wire transmission line. *IEEE Transactions on Microwave Theory and Techniques*, 47(3):365–366, 1999.

[148] S. Basu and H.S Maiti. Ion dynamics study of $La_2Mo_2O_9$. *Ionics*, 16: 111–115, 2010.

[149] B. Roling, A. Happe, K. Funke, and M.D. Ingram. Carrier concentrations and relaxation spectroscopy: New information from scaling properties of conductivity spectra in ionically conducting glasses. *Phys. Rev. Lett.*, 78: 2160–2163, 1997.

[150] F. Lalere, J.B. Leriche, M. Courty, S. Boulineau, V. Viallet, C. Masquelier, and V. Seznec. An all solid state NASICON sodium battery operating at 200řc. *J. Power Sources*, 247:975–980, 2014.

[151] L. Torkian and M.M Amini. Low Temperature Synthesis of Delafossite $CuAlO_2$ Using Aluminium Nitrate. *Mater. Lett.*, 63:587–588, 2009.

[152] H Kawazoe, H Yasakawa, H Hyodo, M Kurita, H Yanagi, and H Hosono. p-Type Electrical Conduction in Transparent Thin Films of $CuAlO_2$. *Nature*, 389:939–942, 1997.

[153] Zanhong Deng, Xuebin Zhu, Ruhua Tao, Weiwei Dong, and Xiadong Fang. Synthesis of $CuAlO_2$ Ceramics Using Sol-Gel. *Materials Letters*, 61:686–689, 2007.

[154] R.G. Gordon. Criteria for Choosing Transparent Conductors. *Materials Research Bulletin*, 25:52–57, 2000.

[155] Masayoshi Ohashi, Yasuo Iida, and Hisashi Morikawa. Preparation of $CuAlO_2$ Films by Wet Chemical Synthesis. *Journal of American Ceramic Society*, 85(1):270–272, 2002.

[156] David O Scanlon and Graeme W Smith. Conductivity limits in $CuAlO_2$ from Screened-Hybrid Density Function Theory. *Journal of Physical Chemical Letters*, 1:3195–3199, 2010.

[157] D.O Scanlon, A Walsh, and G.W Watson. Understanding the p-Type Conduction Properties of the Transparent Conducting Oxide $CuBO_2$: A Density Functional Theory Analysis. *Chem. Mater*, 21:4568–4576, 2009.

[158] A Kudo, A Walsh, and G.W Watson. $SrCu_2O_2$: A p-Type Conductive Oxide with a Wide Band Gap. *Appl.Phys.Lett.*, 73:220–222, 1998.

[159] X. G Zheng, K. Taniguchi, A. Takahashi, Y. Liu, and C. N Xu. Room temperature sensing of ozone by transparent p-type semiconductor $CuAlO_2$. *Applied Physics Letters*, 75(10):1728–1729, 2004.

[160] C. Baratto, R. Kumara, G. Faglia, K. Vojisavljevic, and B. Malic. *p*-type copper aluminum oxide thin films for gas-sensing applications. *Sensors and Actuators B: Chemical*, 209:287–296, 2015.

[161] Hsin-Chun Lu, Jo-Ling Lu, Chun-Lung Chu, Chi-You Lai, and Gwo mei Wu. Preparation of Nano-Powders of p-Type Transparent Conductive Copper Aluminum Oxide by Co-precipitation method. In *IEEE International Nanoelectronics Conference*, pages 485–488. IEEE Xplore, 2008.

[162] Dehua Xiong, Xianwei Zeng, Wenjun Zhang, Huan Wang, Xiujian Zhao, Wei Chen, and Yi-Bing Cheng. Synthesis and characterization of $CuAlO_2$ and $AgAlO_2$ delafossite oxides through low temperature hydrothermal methods. *Inorg.Chem*, 53:4106–4116, 2014.

[163] Jahangeer Ahmed, Colin K. Blakely, Jai Prakash, Shaun R. Bruno, Mingzhe Yu, Yiying Wu, and Viktor V. Poltavets. Scalable synthesis of delafossite cualo2 nanoparticles for p-type dye-sensitized solar cells applications. *Journal of Alloys and Compounds*, 591:275–279, 2014.

[164] A.N Banerjee, S. Kundoo, and K.K Chattopadhyay. Synthesis and Characterisation of p-Type Transparent Conducting $CuAlO_2$ Thin Film by DC Sputtering. *Thin Solid Films*, 440:5–10, 2003.

[165] Brian J. Ingram, Gabriela B. Gonzalez, and Thomas O. Mason. Transport and Defect Mechanism in Cuprous Delafossites. Comparison of Hydrothermal and Standard Solid State Synthesis in $CuAlO_2$. *Chemical Materials*, 16: 5616–5622, 2004.

[166] Amol P. Amrute, Zbigniew Lodziana, Cecilia Mondelli, Frank Krumeich, and Javier Perez-Ramirez. Solid-state chemistry of cuprous delafossites: Synthesis and stability aspects. *Chem. Mater*, 25:4423–4435, 2013.

[167] Tran V. Thu, Pham D. Thanh, Koichiro Suekuni, Nguyen H. Hai, Derrick Mott, Mikio Koyano, and Shinya Maenosono. Synthesis of delafossite $CuAlO_2$ p-type semiconductor with a nanoparticle-based Cu(i) acetate-loaded boehmite precursor. *Mater.Res.Bull*, 46:1819–1827, 2011.

[168] K. Vojisavljevic, B. Malic, M. Senna, S. Drnovsek, and M. Kosec. Solid state synthesis of nano-boehmite-derived $CuAlO_2$ powder and processing of the ceramics. *Journal of the European Ceramic Society*, 33:3231–3241, 2013.

[169] Richard H. Jarman, Julie Bafia, Tsige Gebreslasse, Brian J. Ingram, and J. David Carter. Synthesis of the p-type semiconducting ternary oxide $CuAlO_2$ using the Pechini method. *Materials Research Bulletin*, 48(10): 3916 – 3918, 2013.

[170] T. Ishiguro, A. Kitazawa, N. Mizutani, and M. Kato. Single Crystal Growth and Crystal structure Refinement. *Journal of Soild State Chemistry*, 40: 170–174, 1981.

[171] C.K Ghosh, S.R Popuri, T.U Maheshi, and K.K Chattopadhyay. Preparation of Nanocrystalline $CuAlO_2$ through Sol-Gel Route. *Journal of Sol-Gel Science and Technology*, 52:75–81, 2009.

[172] Hiroshi Yanagi, Shin-Ichiro Inoue, Kazushige Ueda, Hiroshi Kawazoe, Hideo Hosono, and Noriaki Hamada. Electronic structure and optoelectronic properties of transparent p-type conducting $CuAlO_2$. *Journal of Applied Physics*, 88(7):4159–4163, 2000.

[173] T. Prakash, K. Padma Prasad, R. Kavitha, and S. Ramasamyand B. S. Murty. Dielectric relaxation studies of nanocrystalline $CuAlO_2$ using modulus formalism. *J. Appl. Phys.*, 102:104104, 2007.

[174] C.T Su, H.Y Lee, and M.Y Chern. Development of Phase Pure $CuAlO_2$ Thin films Grown on c-plane Sapphire Substrates Prepared by RF Sputtering. *J.Cryst. Growth*, 328:25–29, 2011.

[175] F. B. Benko and F. P. Koffyberg. Opto-electronic properties of $CuAlO_2$. *Journal of Physics and Chemistry of Solids*, 45(1):57–59, 1984.

[176] M.S. Lee., T.Y Kim, and D. Kim. Anisotropic electrical conductivity of delafossite-type $CuAlO_2$ laminar crystal. *Applied Physics Letters*, 79(13): 2028–2030, 2001.

[177] A.N. Banerjee, R. Maity, and K.K. Chattopadhyay. Preparation of p-type transparent conducting $CuAlO_2$ thin films by reactive DC sputtering. *Materials Letters*, 58:10 – 13, 2004.

[178] O.J. Dura, R. Boada, A. Rivera-Calzada, C. Leon, E. Bauer, M.A. Lopez de la Torre, and J. Chaboy. Tranport, electronic, and structural properties of nanocrystalline $CuAlO_2$ delafossites. *Physical Review B*, 83:045202 (1–9), 2011.

[179] B.J. Ingram, T.O Mason, R. Asahi, K.T. Park, and A.J. Freeman. Electronic Structure and Small Polaron Hole Transport of Copper Aluminate. *Physical Review B*, 64:155114, 2001.

[180] Z. Q. Yao, B. He, L. Zhang, C. Q. Zhuang, T. W. Ng, S. L. Liu, M. Vogel, A. Kumar, W. J. Zhang, C. S. Lee, S. T. Lee, , and X. Jiang. Energy band engineering and controlled p-type conductivity of $CuAlO_2$ thin films by nonisovalent Cu−O alloying. *Appl.Phys. Lett.*, 100:0621021, 2012.

[181] Lev I. Berger. *Semiconductor Materials*. CRC Press, 1997.

[182] Helmut F Wolf. *Semiconductors*. Wiley-Interscience, 1971.

[183] Steven Mudenda, Girish M. Kale, and Yotamu R. S. Hara. Rapid synthesis and electrical transition in p-type delafossite $CuAlO_2$. *J. Mater. Chem. C*, 2:9233–9239, 2014.

[184] M. Neumann-Spallart and R. Pinto. Growth conditions of $CuAlO_2$ films -Thermodynamic considerations. *Thin Solid Films*, 520(4):1299 –1302, 2011.

[185] D.P. Almond, G.K Duncan, and A.R West. The determination of hopping rates and carrier concentrations in ionic conductors by a new analysis of ac conductivity. *Solid State Ion.*, 8:159–164, 1983.

[186] K T Jacob, G M Kale, and G N K Iyengar. Oxygen potentials, gibbs' energies and phase relations in the Cu-Cr-O system. *J. Mater. Science*, 21: 2753–2758, 1986.

[187] K T Jacob, G M Kale, and Y Waseda. Gibbs energy of formation of $CuCrO_4$ and phase relations in the system Cu-Cr-O below 735 k. *Thermochimica Acta*, 208:341–348, 1992.

[188] Girish M. Kale and K T Jacob. Gibbs energies of formation of $CuYO_2$ and $Cu_2Y_2O_5$ and phase relations in the system Cu-Y-O. *Chem. Mater*, 1: 515–519, 1989.

[189] Zbigniew Moser and Krzysztof Fitzner. The use of Experimental Thermodynamic Data in the Phase Equilibria Verification. *Thermochimica Acta*, 332:1–19, 1999.

[190] Herbert Ipser, Adolf Mikula, and Iwao Katayama. Overview: The emf method as a source of experimental thermodynamic data. *CALPHAD: Computer Coupling of Phase Diagrams and Thermochemistry*, 34:271–278, 2010.

[191] R. Subasri, T. Mathews, K. Swaminathan, and O.M. Sreedharan. Thermodynamic Stability of Na_2ZrO_3 using the Solid Electrolyte Galvanic Cell Technique. *Journal of Nuclear Materials*, 300:237–241, 2002.

[192] Palani Balaya and Joachim Maier. Thermodynamics of Nano- and Macrocrystalline Anatase using Cell Voltage Measurements. *Physical Chemistry Chemical Physics*, 12:215–219, 2010.

[193] G.M Kale. $Na_2O-AI_2O_3$ System Activity of Na_2O in $(\alpha+\beta)$ and $(\beta+\beta")$ − Alumina. *Metallurgical Transactions B*, 23B:839, 1992.

[194] Robert S. Roth, Taki Negas, and Lawrence P. Cook. *Phase Diagrams for Ceramists*, volume IV. American Ceramic Society, INC, 1981.

[195] M. J. Ferrante. High Temperature Relative Enthalpies and Related Thermodynamic Properties of $Na_2Ti_6O_{13}$. Technical report, US Department of Interior Bureau of Mines, 1986.

[196] M. Holzinger, A. Benisek, W. Schnelle, E. Gmelin, J. Maier, and W. Sitte. Thermodynamic Properties of $Na_2Ti_6O_{13}$ and $Na_2Ti_3O_7$: Electrochemical and Calorimetric Determination. *J. Chem. Thermodynamics*, 35:1469–1487, 2003.

[197] Gunnar Eriksson and Arthur D Pelton. Critical Evaluation and Optimization of the Thermodynamic Properties and Phase Diagrams of the MnO-TiO_2, MgO-TiO_2, FeO−TiO_2, Ti_2O_3-TiO_2, Na_2O-TiO_2, and K_2O-TiO_2 systems. *Metallurgical Transactions B*, 24B:795–805, 1993.

[198] Girish Madhav Kale and Srinivasan Srikanth. Electrochemical determination of the activity of Na_2O in the pyrochlore phase of the Sb_2O_4-$NaSbO_3$ system. *Journal of American Ceramic Society*, 82(8):2161–2165, 1999.

[199] J. M Stuve. Low-temperature heat capacities of sodium hexatitanate. *Journal of Chemical Engineering data*, 27:391–392, 1982.

[200] K.O Bennington and R. R Brown. Thermodynamic properties of three sodium titanates. Technical report, US Department of Interior Bureau of Mines, 1973.

[201] Dawei Feng and Pekka Taskinen. Thermodynamic properties of Ag_3AuSe_2 from 300 to 500 K by a Solid State Galvanic Cell. *Journal of Alloys and Compounds*, 583:176–179, 2014.

[202] G. M. Kale, S. S. Pandit, and K.T Jacob. Thermodynamics of Cobalt (ii,iii) Oxide (Co_3O_4 : Evidence of Phase Transition. *Transactions of the Japan Institute of Metals*, 29(2):125–132, 1988.

[203] Dorian A. H. Hanaor and Charles C. Sorrell. Review of the anatase to rutile phase transformation. *Journal of Materials Science*, 46:855–874, 2011.

[204] A.D Wadsley and W. G. Mumme. The crystal structure of $Na_2Ti_7O_{15}$, and an ordered intergrowth of $Na_2Ti_6O_{13}$ and '$Na_2Ti_8O_{17}$'. *Acta Crystallographica Section B*, 24(3):392–396, Mar 1968.

[205] H. Okamoto. O-Ti (oxygen-titanium). *Journal of Phase Equilibria*, 22(4): 515–515, 2001.

[206] H. Okamoto. O-Ti (oxygen-titanium). *Journal of Phase Equilibria and Diffusion*, 32(5):473–474, 2011.

[207] Y. Bando, M. Watanabe, and Y. Sekikawa. Structure analysis of $Na_2Ti_9O_{19}$ by 1 MV high-resolution electron microscopy. *Acta Crystallographica Section B*, 35(7):1541–1545, Jul 1979.

[208] M. Watanabe, Y. Bando, and M. Tsutsumi. A new member of sodium titanates, $Na_2Ti_9O_{19}$. *Journal of Solid State Chemistry*, 28(3):397–399, 1979. ISSN 0022-4596.

[209] M. Vithal, S. Rama Krishna, G. Ravi, Suresh Palla, Radha Velchuri, and Someshwar Pola. Synthesis of Cu^{2+} and Ag^{+} doped $Na_2Ti_3O_7$ by a facile ion-exchange method as visible-light-driven photocatalysts. *Ceramic International*, 39:8429–8439, 2013.

[210] Ihsan Barin. *Thermochemical data of pure substances*. VCH, Weinheim ; New York, 3rd edition, 1995.

[211] A.J Davidson and D.J Fray. Measurement of high concentrations of copper in molten phases. *Solid State Ionics*, pages 613–620, 2000. ISSN 0167-2738. Proceedings of the 12th International Conference on Solid State Ionics.

[212] R.J. Schaffer, R.V. Kumar, and A.E. Ingham. Thermodynamics of cusicon oxidation. *Materials Research Bulletin*, 34(7):1153–1164, 1999. ISSN 0025-5408.

[213] P. Pasierb and M. Rekas. Solid-state potentiometric gas sensors current status and future trends. *J. Solid State Electrochem.*, 13:3–25, 2009.

[214] H. Näfe and M. Steinbräck. Electronic conductivity of polycrystalline Na - β-alumina at high temperatures. *J. Electrochem. Soc*, 141:2779, 1994.

[215] H. Näfe. The feasibility of a potentiometric CO_2 sensor based on Na-beta-alumina in the light of the electronic conductivity of the electrolyte. *Sensor Actuat. B - Chem*, 21:79–82, 1994.

[216] Steven Mudenda and Girish M. Kale. New insight into the electrical properties and ion dynamics of screen printed NASICON thick films. *Journal of Materials Chemistry A*, 3:12268–12275, 2015.

Chapter 9

Publications, Conferences and Recognition

9.1 Conferences

1. Steven Mudenda, Development of a Solid State Based Planar CO_2 Sensor. *Postgraduate Researcher Conference 2014, University of Leeds , UK.*

2. Steven Mudenda and Dr. Girish M Kale, Performance of a Multilayered Screen Printed CO_2 Sensor Using NASICON as a Solid Electrolyte, *International Symposium on Sensor Science (I3S) 2015, Basel, Switzerland.*

3. Steven Mudenda and Dr. Girish M Kale, Effect of Film Thickness of NASICON and Electrode Configuration on Electrical Properties, *International Symposium on Sensor Science (I3S) 2015, Basel, Switzerland*

9.2 Publications

9.2.1 Published Articles

1. S. Mudenda and Dr. Girish M. Kale and Yotamu R.S. Hara. *Rapid synthesis and electrical transition in p-type delafossite $CuAlO_2$, Journal of Materials Chemistry C, 2014, 2,9233.*

2. S. Mudenda and Dr. Girish M. Kale. *New insight into the electrical properties and ion dynamics of screen printed NASICON thick films, Journal of Materials Chemistry A, 2015,3, 12268.*

9.2.2 Potential Publications

1. S. Mudenda and Dr. Girish M. Kale. *CO_2 sensors; Challenges and Opportunities - A review*- from Chapter *2.*

2. S. Mudenda and Dr. Girish M. Kale. *Effect of Film Thickness of NASICON and Electrode Configuration on Electrical Properties* (In preparation)- from Chapter 3-4.

3. S. Mudenda and Dr. Girish M. Kale. *Choice of platinum based electrical contacts to devices: Issues that may arise in high temperature applications*(In preparation)- from Chapter *3&5.*

4. S. Mudenda and Dr. Girish M. Kale. *New revelations on the thermodynamic Stability of $Na_2Ti_6O_{13}$-TiO_2 System using EMF Measurements* (In preparation) - from Chapter 3&6.

5. S. Mudenda and Dr. Girish M. Kale. *Thermodynamic activity of Na_2O in $Na_2Ti_6O_{13}$-$Na_2Ti_3O_7$ System: An Electrochemical Metho*d(In preparation) - from Chapter 3&6.

6. S. Mudenda and Dr. Girish M. Kale. *Performance of a Modified Screen Printed CO_2 Sensor Using NASICON as a Solid Electrolyte*(In preparation)-from Chapter 3&7.

9.3 Recognition

1. Postgraduate researcher **student of the year nominee** (School of Chemical and Process Engineering) (2014).

2. School of Chemical and Process Engineering **Best Student Paper Award 2014** (for the article : Journal of Materials Chemistry C, 2014, 2,9233)

Appendix A

$CuAlO_2$/Pt interface at high temperatures

A.1 Cole Cole plots

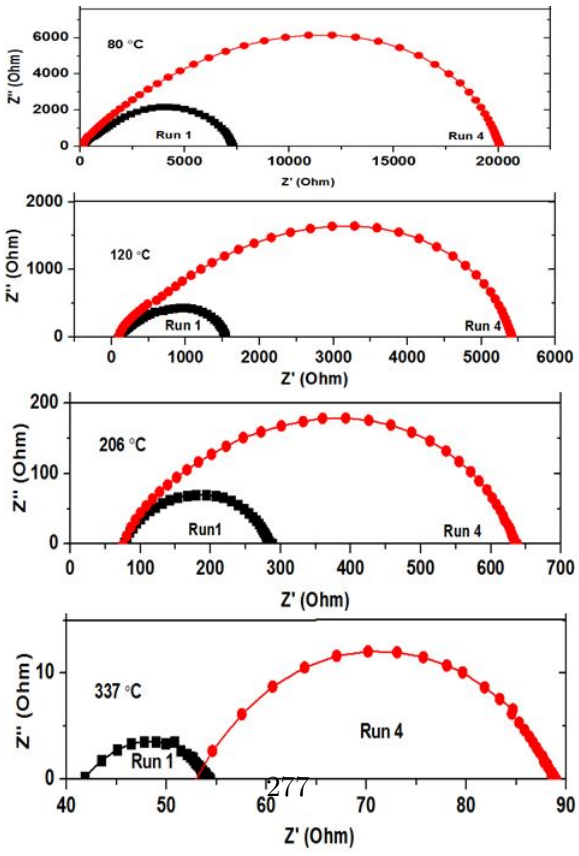

Figure A.1 – Cole-Cole plots from high temperature impedance measurements showing increase in resistivity of the material as the experiment proceeded.There was a progressive blockage of electrical transport at each run of the experiment. The material responsible for this blockage is believed to have been formed during the firing of platinum film on the pellet and high temperature electrical measurements.

A.2 XRD

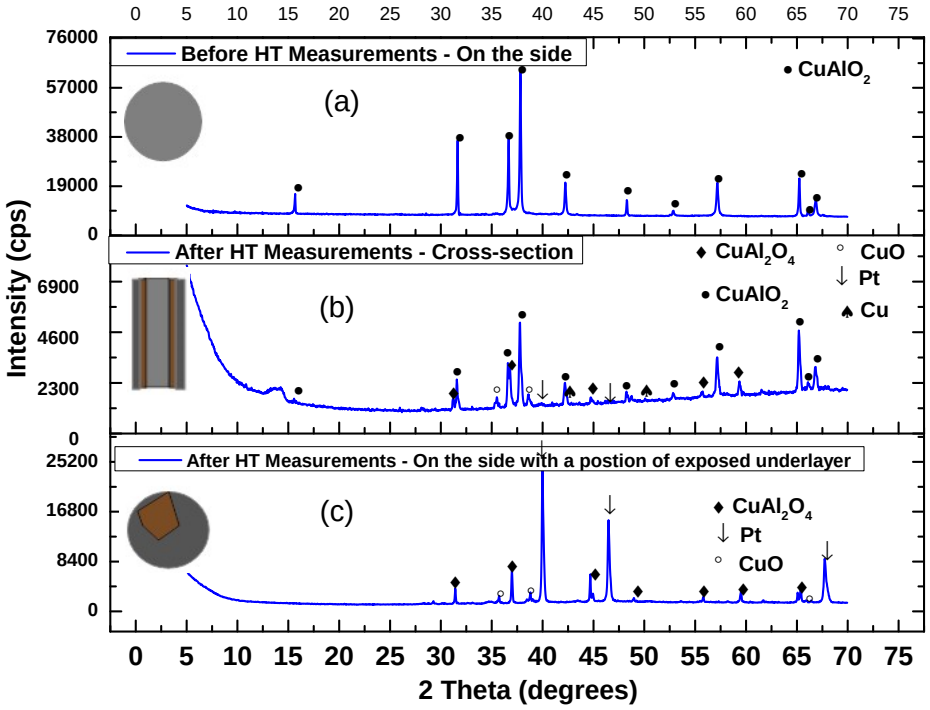

Figure A.2 – XRD reflections for pellet before Pt coating and AC measuremements (a), cross-section of the pellet after measurements(b) and on top of the Pt with an underlayer exposed after AC measurement (c).

A.3 SEM/EDS

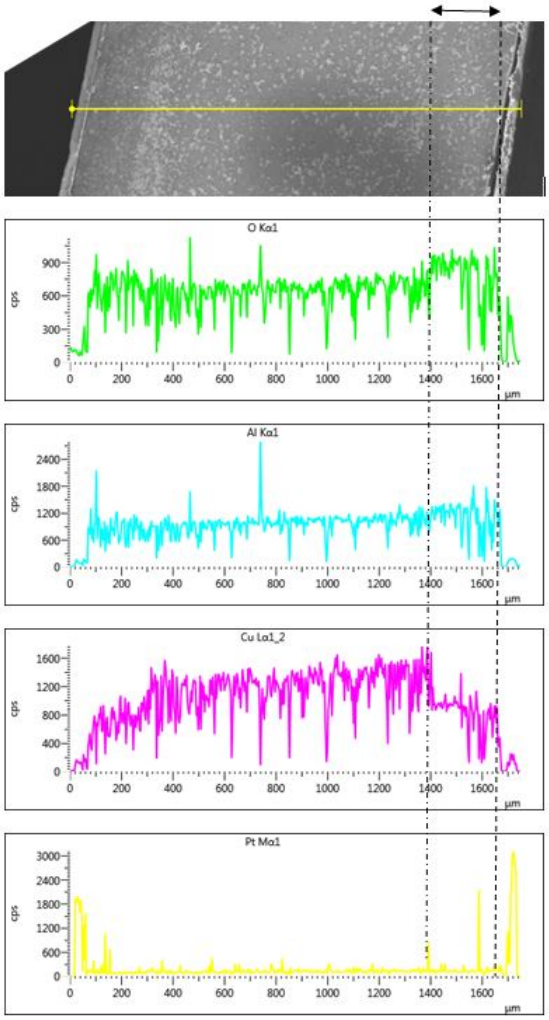

Figure A.3 – EDX Line scan across the who pellet. Elemental counts in each region is displayed. The interface shows a decrease in Cu amounts.

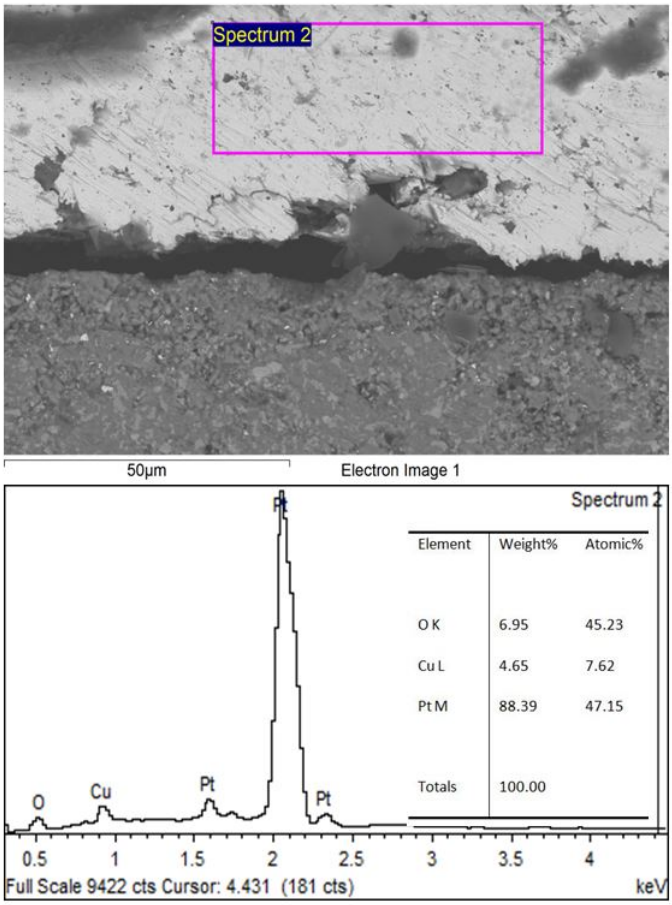

Figure A.4 – EDX quantification within the Pt coating. The decreased Cu at the interface was as a result of the Cu diffusion into Pt leaving a $CuAl_2O_4$ rich phase.

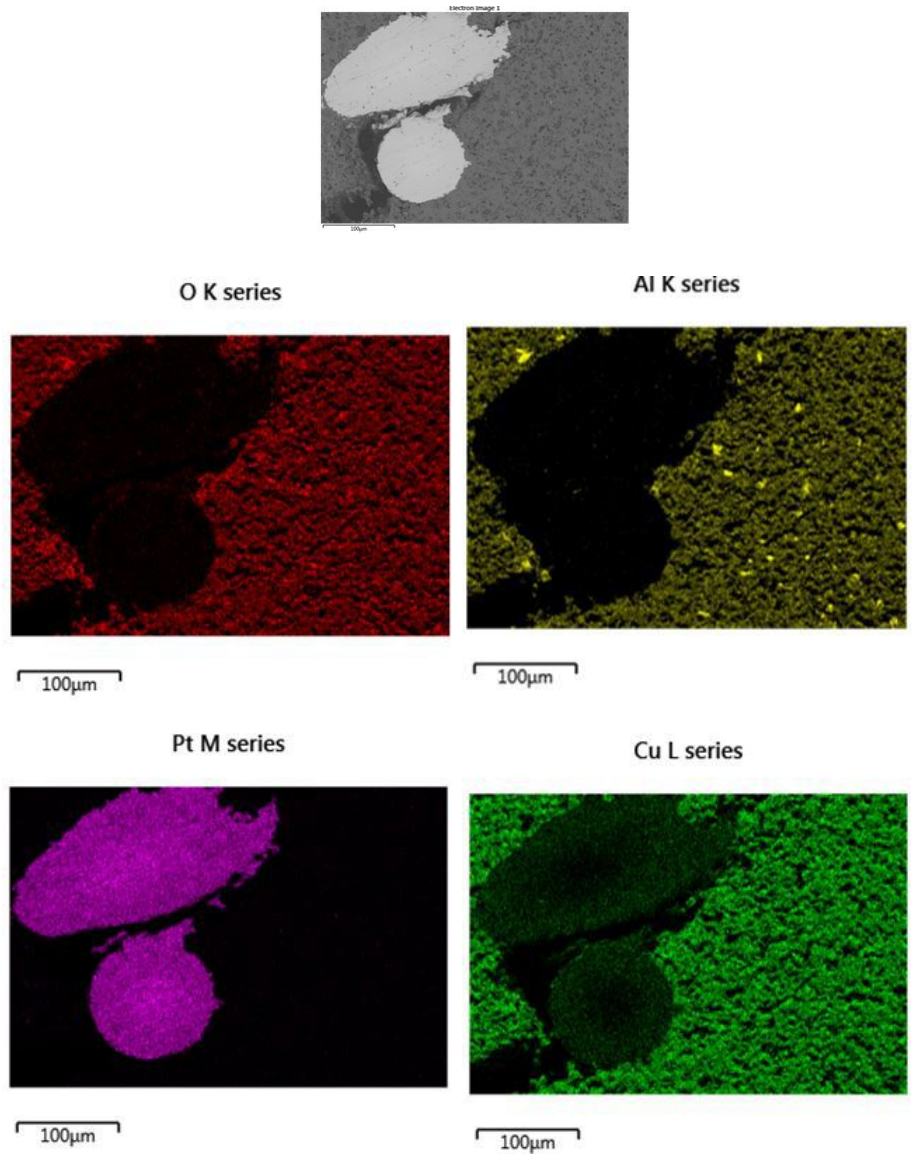

Figure A.5 – EDS mapping of the CAO with embedded Pt mesh. Significant amounts of Cu from the CAO diffused into the Pt.

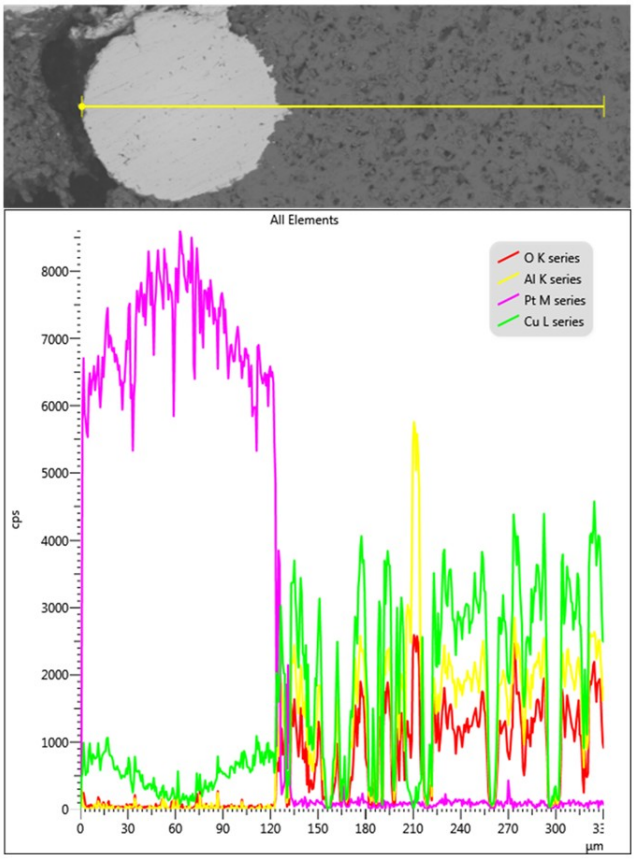

Figure A.6 – EDS line scan on the Pt and CAO to tract the elements.